



Summary of Activities 2020



CANADA-NUNAVUT
GEOSCIENCE OFFICE

ᑕᑕᑕᑕᑕᑕᑕᑕᑕᑕ
ᑕᑕᑕᑕᑕᑕᑕᑕᑕᑕᑕᑕ

BUREAU GÉOSCIENTIFIQUE
CANADA-NUNAVUT

KANATAMI-NUNAVUMI
GEOSCIENCE TITIGAKVIIT



CANADA-NUNAVUT
GEOSCIENCE OFFICE

ᑲᑲᑕᐅᑦ-ᑭᑲᑦᑕᑦ
ᐅᑭᑲᑲᑲᑦ ᑭᑲᐅᑭᑭᑲᑲᑦ

BUREAU GÉOSCIENTIFIQUE
CANADA-NUNAVUT

KANATAMI-NUNAVUMI
GEOSCIENCE TITIGAKVIIT

SUMMARY OF ACTIVITIES 2020

© 2021 by Canada-Nunavut Geoscience Office.
All rights reserved. Electronic edition published 2021.

This publication is also available, free of charge, as colour digital files in Adobe Acrobat® PDF format from the Canada-Nunavut Geoscience Office website: <https://cngo.ca/>.

Every reasonable effort is made to ensure the accuracy of the information contained in this report, but the Canada-Nunavut Geoscience Office does not assume any liability for errors that may occur. Source references are included in the report and users should verify critical information.

When using information from this publication in other publications or presentations, due acknowledgment should be given to Canada-Nunavut Geoscience Office. The recommended reference is included on the title page of each paper. The complete volume should be referenced as follows:

Canada-Nunavut Geoscience Office (2021): Canada-Nunavut Geoscience Office Summary of Activities 2020; Canada-Nunavut Geoscience Office, 100 p.

ISSN 2291-1235 Canada-Nunavut Geoscience Office Summary of Activities (Print)
ISSN 2291-1243 Canada-Nunavut Geoscience Office Summary of Activities (Online)

Front cover photo: Surface rock sampling on glacial boulder for cosmogenic isotope geochronology, Jungersen River area, Nunavut. Photo by Serge Basso, Canada-Nunavut Geoscience Office.

Back cover photo: Photograph from an unmanned aerial vehicle of the glacier-influenced fiord-head delta of Southwind Fiord, Nunavut. Photo by Angus Robertson and Alexandre Normandeau, Geological Survey of Canada.

Foreword

It again gives me great pleasure to introduce the 2020 *Summary of Activities*. It represents the work of the Canada-Nunavut Geoscience Office's researchers, and includes papers from other researchers conducting work in Nunavut.

The Canada-Nunavut Geoscience Office (CNGO), Nunavut's de facto geological survey, was established in 1999, the same year that Nunavut became Canada's third territory. In the twenty years that the office has been open, its managerial structure has remained unchanged, in that the CNGO is co-managed and co-funded by three partners—two federal departments and the territorial Government of Nunavut (GN). The federal departments are Natural Resources Canada (NRCan) and Crown-Indigenous Relations and Northern Affairs Canada (CIRNAC), and the territorial department is Economic Development and Transportation (GN-EDT). Nunavut Tunngavik Incorporated (NTI) is an ex officio member of the CNGO Management Board that provides operational oversight for the office.

However, the governments of Nunavut and Canada signed an Agreement-in-Principle (AIP) in mid-August 2019; this AIP will devolve Crown lands, and oil, gas and mineral resources from the Government of Canada to the Government of Nunavut. The final devolution agreement will be in place in the near future (1–2 years), followed by drafting of the legislation needed to bring devolution into effect in the next 4–5 years (2025). At that time, professionals from the CNGO, CIRNAC and the GN will likely amalgamate and form the Nunavut Geological Survey, under the aegis of the GN.

The discovery and development of Nunavut's mineral and petroleum resources has significant potential to generate economic benefits for the territory, its communities and its people. To date, Nunavummiut have benefited from past and present mine development and mineral-resource production (e.g., gold, iron, lead, zinc) and mineral-resource exploration. Research, data and knowledge of Nunavut's geology will allow all stakeholders in Nunavut to make sound and informed decisions on mineral-resource development, land-use planning and infrastructure development for the territory's economy and betterment.

The mandate of the CNGO is to provide accessible geoscience information and expertise to support responsible resource exploration and development, infrastructure development, and public geoscience education and awareness in Nunavut. Staff in the office initiate and conduct a wide range of geoscience research—mapping, interpreting and reporting on Nunavut's geological features and resources. This work is conducted commonly through collaborations with other governments, universities, industry and communities. The resultant geoscience data and interpretations are equally accessible to all.

The CNGO and its office partners co-manage and disseminate data through two websites (<https://cngo.ca/> and <https://NunavutGeoscience.ca/>). Work to migrate the websites to a new hosting platform was completed in 2019; updating of the websites is now a focus for the office. The *Summary of Activities* volumes and the accompanying Geoscience Data Series and Open File Map Series disseminate the results of geological mapping (bedrock and surficial) and analytical results from sampling (rock, till, soil, lake sediment and stream sediment).

The year 2020 is one unlike any year that most of us have experienced in our lifetime. In mid-March 2020, the world ground to a halt with the appearance of the Coronavirus disease (COVID-19), an infectious disease caused by a newly discovered coronavirus. On March 15, offices and schools across Canada shut down to prevent the spread of this sometimes-fatal disease. For CNGO, the office shut down; all employees worked, and continue to work, remotely; and travel (i.e., to the field) was nonexistent. There were several projects planned for the summer of 2020 that involved fieldwork; these projects have been postponed and hopefully can be resumed in the future (summer 2021?). Without this fieldwork, the CNGO focused on planning for the future and taking this opportunity to write up past research.

With devolution on the horizon, priorities for the CNGO and for Nunavut include

- a greater emphasis on public geoscience that highlights the economic potential of Nunavut and supports mineral-resource development;
- a greater focus on improving access to Nunavut's public geoscience information;
- a focus on smaller, more targeted geological mapping activities, particularly in areas with high mineral potential; and
- adapting to a changing climate and permafrost degradation in Nunavut.

Four papers in this volume are from researchers involved in the Fury and Hecla Geoscience Project (2017–2020), led by the CNGO, that comprised bedrock and stratigraphic mapping and sampling of the Archean, Proterozoic and Paleozoic rocks, and mapping of the Quaternary surficial deposits and features north and south of Fury and Hecla Strait on Baffin Island and

Melville Peninsula, respectively, in the Qikiqtaaluk Region. These papers discuss different aspects of this project, which started with an aeromagnetic survey (2017–2019) and continued with bedrock, stratigraphic and surficial mapping. The bedrock mapping components (Bovingdon et al. and Dufour et al.) were carried out in collaboration with geoscientists from two universities. As part of the mapping component, banded iron formation (BIF) rocks were discovered in the study area, leading the researchers (Lebeau and Mercier-Langevin) to undertake a preliminary territory-wide look at known gold deposits hosted by BIF rocks. Their intent for 2021 is to conduct fieldwork from an exploration camp established near BIF-hosted gold occurrences in western Kitikmeot Region, and assist the company geologists in interpreting and understanding further the geology of these rocks and deposits. Tremblay, in 2019, discovered corundum and kimberlite-indicator minerals in the glacial till overlying the Fury and Hecla study area, and discusses the significance on these in the fourth paper.

Under the theme of ‘Geoscience for Infrastructure’, one paper discusses work results in central Nunavut. LeBlanc and Oldenborger, colleagues at the Geological Survey of Canada (GSC) in Ottawa, present results on ground temperature, active-layer thickness and ground-ice conditions in the vicinity of Rankin Inlet. Bennett et al. and Normandeau et al., also GSC colleagues but with GSC-Atlantic in Nova Scotia, discuss active marine geohazards by providing assessments, respectively, of the distribution of submarine slope failures in Baffin Island fiords and of modern turbidity currents, submarine landslides and iceberg scouring in Baffin Bay.

The final paper in the volume deals with a geological database initiative driven by the CNGO; the authors (Tremblay and Basso) report on the compilation of data from the analysis of surficial materials in Nunavut.

These papers report on work carried out by scientists of the CNGO and partners and collaborators from other organizations, as well as by other researchers who were invited to report on their work in Nunavut. I am proud of the work that CNGO and our colleagues do, particularly in this unprecedented year of a worldwide pandemic that has necessitated creative and original ways to conduct and report on field-based studies when field travel was not permitted. I am also proud of the work that Celine Gilbert, CNGO’s GIS Specialist, does from start to finish with this annual publication. Everyone (our partners, collaborators and supporters) involved in, and with, the CNGO can share in this pride of the high-quality research presented in this volume.

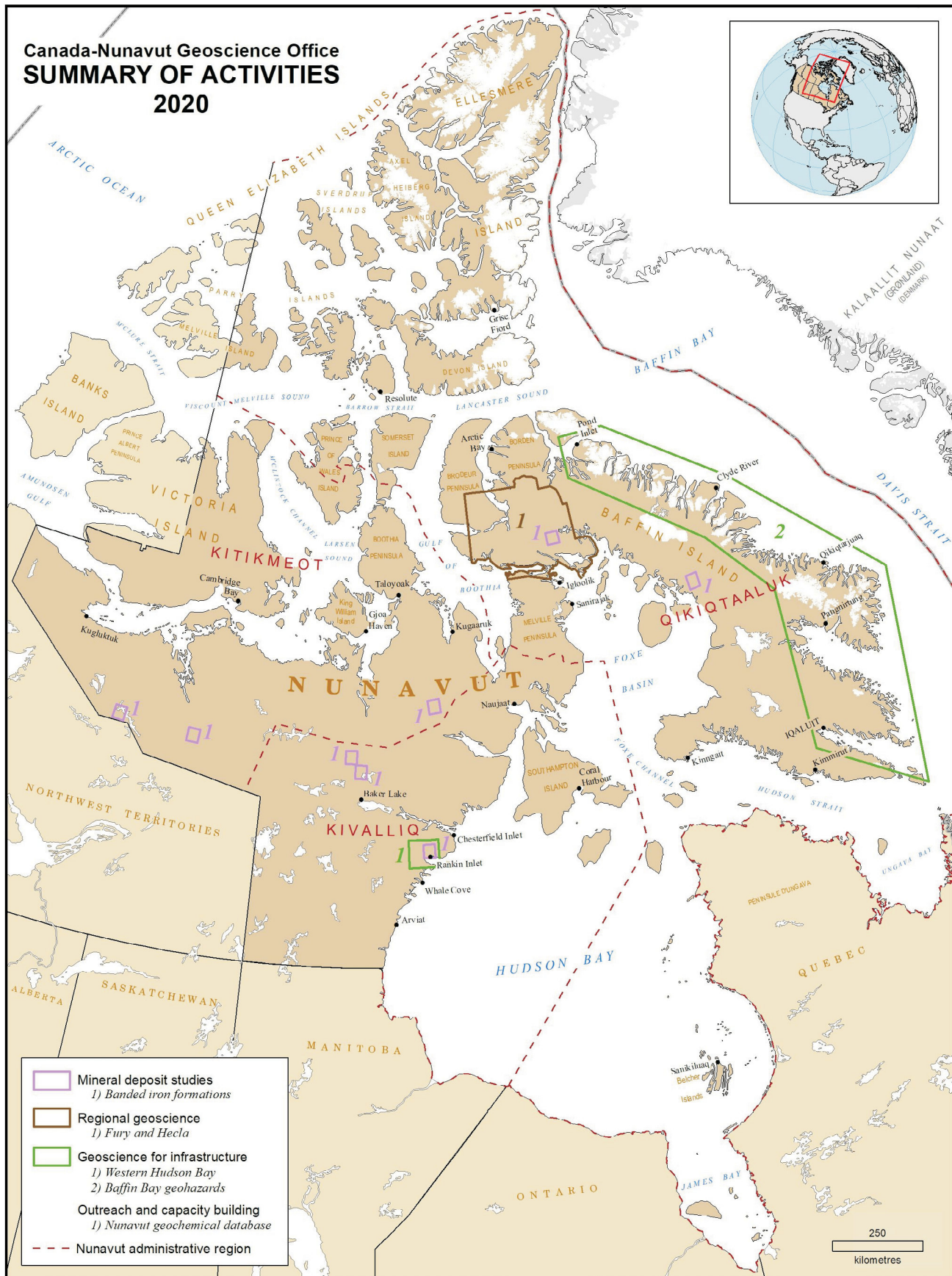
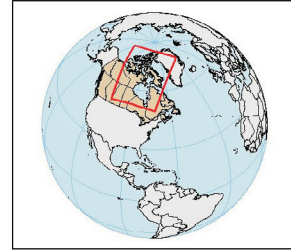
Acknowledgments

The CNGO staff thank all authors of papers in this *Summary of Activities*. Their dedication is greatly appreciated, and, year after year, is critical in helping the CNGO deliver such a quality product. RnD Technical is also thanked for their technical editing and assembling of the volume. In addition, special thanks are extended to reviewers of papers:

Stephen Adcock	Geological Survey of Canada
Jean Bédard	Geological Survey of Canada
Ken Buchan	Geological Survey of Canada (emeritus)
Sébastien Castonguay	Geological Survey of Canada
David Corrigan	Geological Survey of Canada
Jordan Eamer	Geological Survey of Canada
Pierre-Marc Godbout	Geological Survey of Canada
Brendan O’Neill	Geological Survey of Canada
Tommy Tremblay	Canada-Nunavut Geoscience Office

Linda Ham
Chief Geologist
Canada-Nunavut Geoscience Office
<https://cngo.ca/>

Canada-Nunavut Geoscience Office
SUMMARY OF ACTIVITIES
2020



Contents

Mineral deposit studies

Review of banded iron formation–hosted gold deposits in Nunavut and preliminary data on a new prospect <i>L.E. Lebeau, and P. Mercier-Langevin</i>	1
---	---

Regional geoscience

Mineralogy, geochemistry and field relationships in the Gifford River area, northwestern Baffin Island, Nunavut <i>P.J. Bovingdon, D. Tinkham and L.E. Lebeau</i>	19
Geochemical comparison of Mackenzie and Franklin igneous mafic rocks in Nunavut, Northwest Territories and northwestern Greenland <i>F. Dufour, R. Stevenson and T. Skulski</i>	33
Geochemistry and mineralogy of glacial sediments and geomorphology of the Jungersen River area, northwestern Baffin Island, Nunavut <i>T. Tremblay</i>	47

Geoscience for infrastructure

Ground temperature, active-layer thickness and ground-ice conditions in the vicinity of Rankin Inlet, Nunavut <i>A.-M. LeBlanc and G.A. Oldenborger</i>	63
Preliminary assessment of the distribution of submarine slope failures in Baffin Island fiords, Nunavut <i>R. Bennett, A. Normandeau, and D.C. Campbell</i>	73
Southwind Fiord, Baffin Island, Nunavut: a natural laboratory to explore modern turbidity currents, submarine landslides and iceberg scouring in an Arctic environment <i>A. Normandeau, K. Mackillop, M. Macquarrie, G. Philibert and R. Bennett</i>	81

Outreach and capacity building

Compiling data from the analysis of surficial materials in Nunavut into a database at the Canada-Nunavut Geoscience Office <i>T. Tremblay and S. Basso</i>	93
---	----



Review of banded iron formation–hosted gold deposits in Nunavut and preliminary data on a new prospect

L.E. Lebeau¹ and P. Mercier-Langevin²

¹Canada-Nunavut Geoscience Office, Iqaluit, Nunavut, Iorraine.lebeau2@canada.ca

²Natural Resources Canada, Geological Survey of Canada, Québec, Québec

Lebeau, L.E. and Mercier-Langevin, P. 2021: Review of banded iron formation–hosted gold deposits in Nunavut and preliminary data on a new prospect; in *Summary of Activities 2020*, Canada-Nunavut Geoscience Office, p. 1–18.

Abstract

Banded iron formation (BIF)–hosted gold is a highly sought-after gold deposit type due to its potential for high-grade and high-tonnage deposits, and prospect of a long mine life. All three regions of Nunavut (i.e., Kivalliq, Kitikmeot and Qikiqtaaluk) host such deposit types. In this paper, seven of Nunavut’s mines and exploration properties are briefly reviewed, including: Agnico Eagle Mines Limited’s Meadowbank complex (Portage, Goose and Amaruq deposits) and the Meliadine mine district (Kivalliq Region); Fury Gold Mines Limited’s Three Bluffs project, Mandalay Resources Corporation’s Lupin former mine and Sabina Gold and Silver Corporation’s Back River project (Kitikmeot Region); and ValOre Metals Corporation’s Baffin Gold project (Qikiqtaaluk Region). In studying BIF-hosted gold deposits in Nunavut, recurring characteristics emerge that can be very useful for future exploration. These include a thick BIF unit (oxide and silicate facies, at least decametres in thickness); strong deformation and dominant structural controls on ore (faults and folds); greenschist- to amphibolite-facies metamorphism; and a sulphide-mineral assemblage dominated by pyrrhotite, with possible arsenopyrite±loellingite and lesser chalcopyrite and pyrite along quartz-carbonate veins and/or as stratabound replacements. The Precambrian rocks of Nunavut are very prospective but remain underexplored despite recent major discoveries; hence the need for detailed regional surveys to assist in better assessing the potential of this vast territory. During the 2019 fieldwork for the Fury and Hecla Geoscience Project led by the Canada-Nunavut Geoscience Office, a previously unknown, deformed BIF unit of significant thickness and lateral extent was discovered. In this paper, preliminary field observations, petrography and geochemistry of this BIF unit are presented. Although this work is preliminary, further exploration of this BIF may be warranted.

Introduction

Banded iron formation (BIF) represents one of many rock types that are common in Archean to early Proterozoic greenstone belts across Nunavut (Berman, 2010). This formation is characterized as laminated sedimentary rock that contains at least 15 wt. % Fe and is commonly present among deformed volcanic and clastic sedimentary successions (James, 1954). Banded iron formation is classified genetically as one of two types: either Algoma type, formed from the local deposition of iron-rich sediment from submarine hydrothermal vents, or Superior type, formed in a shelf environment from the deposition of iron-rich chemical muds (Cloud, 1973). In addition, BIF is classified descriptively as one of oxide, sulphide, carbonate or silicate facies based on the dominance of magnetite/hematite, Fe-Cu-Zn-Pb sulphide, carbonate minerals (e.g., dolomite, ankerite, siderite) or Fe-Mg-Mn bearing silicate minerals, respectively (James, 1954).

Banded iron formation is a highly sought-after target for gold exploration because of its potential to host high-grade, large-tonnage deposits. Gold preferentially concentrates in BIF because of its affinity to trap gold (structurally and chemically) from migrating gold-bearing hydrothermal fluids of metamorphic origin (Phillips and Powell, 2010). In addition, BIF units can be very thick and laterally extensive with the Superior type generally being much more voluminous than the Algoma type (James, 1954), and its layered texture, contrasted rheology and ability to easily deform create favourable pathways, in which hydrothermal fluids can circulate and deposit gold. There are two subtypes of BIF-hosted gold deposits based on empirical features: 1) large deposits where the ore is entirely hosted in the BIF (typically Algoma type) and which tend to have a subtle alteration footprint; and 2) deposits that are only partially hosted in the BIF (Dubé and Mercier-Langevin, 2015), and which generally have the large iron carbonate-sericite alteration footprint of typical quartz-carbonate

This publication is also available, free of charge, as colour digital files in Adobe Acrobat® PDF format from the Canada-Nunavut Geoscience Office website: <https://cngo.ca/summary-of-activities/2020/>.

orogenic gold systems. The Homestake deposit in South Dakota, one of the largest gold deposits of the world with over 1130 t Au (40 million oz.), produced at an average grade of 8.4 g/t between 1876 and 2002 (Morelli et al., 2010; Bell, 2013) and is the archetype of BIF-hosted gold deposits.

Although none as large as Homestake, Nunavut also hosts numerous highly economical BIF-hosted gold deposits of both types (Figure 1); the largest are located in the central Kivalliq Region of Nunavut, near the communities of Rankin Inlet and Baker Lake. Agnico Eagle Mines Limited owns two mining complexes: 1) Meadowbank produced over 90 t Au (3.3 million oz.) from the Portage, Goose and Vault deposits between 2010 and 2019, and now gets ore from the Amaruk deposit (discovered in 2013) with an estimated 77 t Au (2.7 million oz.) in open pit and 16 t Au (0.6 million oz.) underground (Agnico Eagle Mines Limited, 2020a); and 2) Meliadine, where production from the Tiriganiaq deposit began in 2019, with an estimated mine life of 12 years and gold reserves of over 130 t Au (4.7 million oz.) in the Meliadine district (Agnico Eagle Mines Limited, 2020b). In the Kitikmeot Region of Nunavut, the BIF-hosted gold deposits include: 1) the Lupin former mine located in the northern Slave Province, currently owned by Mandalay Resources Corporation, which produced approximately 95 t Au (3.4 million oz.) between 1982 and 2005 (Crown-Indigenous Relations and Northern Affairs

Canada, 2019); 2) the Back River project, a planned gold mine approximately 520 km northeast of Yellowknife (Northwest Territories) owned by Sabina Gold and Silver Corporation (Sabina Gold and Silver Corporation, 2020), which, although it has not started production, contains an estimated 182 t Au (6.4 million oz.) in the Goose and George deposits combined (Crown-Indigenous Relations and Northern Affairs Canada, 2019); and 3) the Three Bluffs deposit located in the Committee Bay greenstone belt in eastern Kitikmeot. Three Bluffs is owned by Fury Gold Mines Limited and has an indicated resource total of 15 t Au (0.52 million oz.) and an inferred total of 20 t Au (0.72 million oz.; Fury Gold Mines Limited, 2020). In the Qikiqtaaluk Region, there are no developed BIF-hosted gold deposits; however, BIF-hosted gold was discovered by Commander Resources Limited on central Baffin Island in 2001 within silicate- and sulphide-facies iron formation. Today, ValOre Metals Corporation owns the gold property; although the resource is not yet fully defined, approximately four prospects have been delineated, with over \$25 million worth of work conducted by ValOre Metals and previous owners (Crown-Indigenous Relations and Northern Affairs Canada, 2019).

The Canada-Nunavut Geoscience Office (CNGO) conducted fieldwork in 2018 and 2019 on northwestern Baffin Island, within the Qikiqtaaluk Region. Fieldwork was part of the Fury and Hecla Geoscience Project, which was a

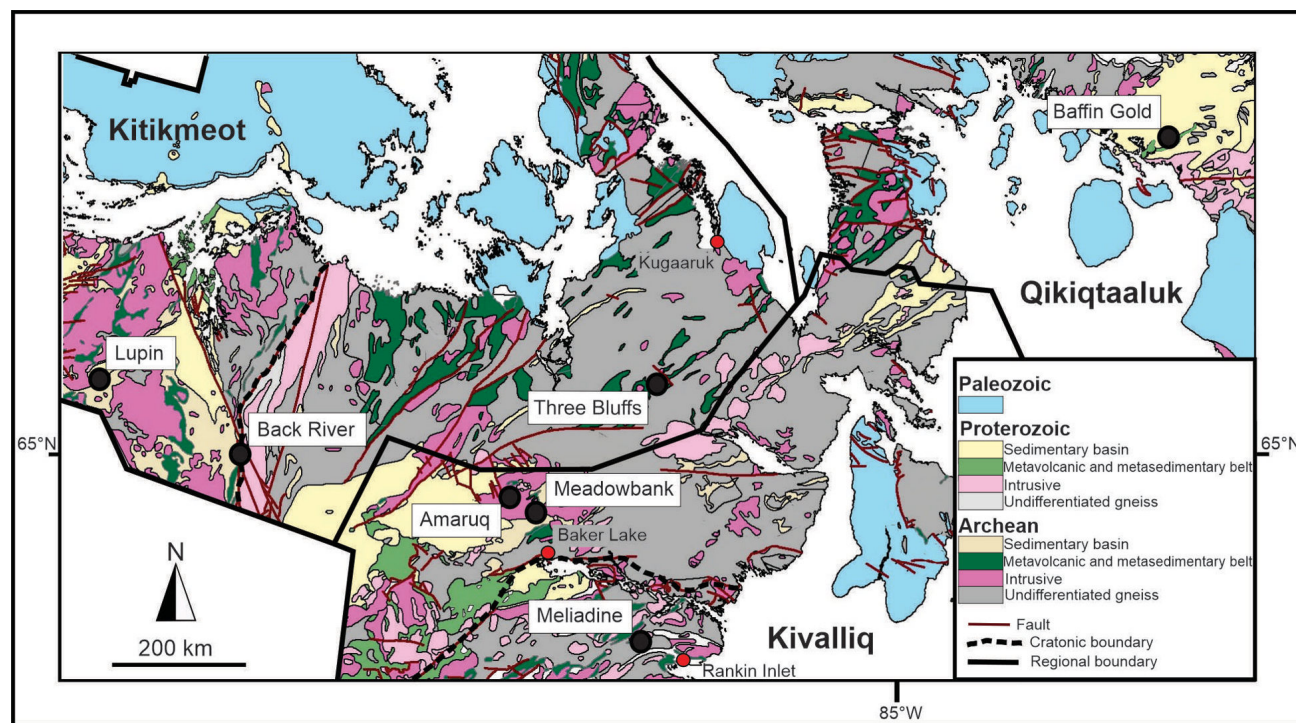


Figure 1: Generalized geology of Nunavut with locations of BIF-hosted gold properties indicated by the black dots (modified from Wheeler et al., 1996). The three regions of the territory (Kitikmeot, Kivalliq and Qikiqtaaluk) are separated by solid black lines. The major geological cratons are separated by dotted lines (i.e., the Slave craton in the west, where Lupin and Back River are located; the Rae craton (central) that hosts the Three Bluffs, Amaruk, Meadowbank and Baffin Gold properties; and the Hearne craton, where the Meliadine complex is located).

joint endeavour between the CNGO, Crown-Indigenous Northern Affairs Canada and Canadian universities. A magnetic geophysical survey was flown over the project area in 2017 and again in 2019. This survey effectively completed coverage of one of the last remaining areas in Nunavut without regional-scale magnetic data. The data collected in 2019 revealed a highly contrasting magnetic anomaly (residual total field) approximately 3 by 15 km in size, which was identified as BIF on the ground. Although the BIF was not studied in detail due to the regional nature of the mapping project, it demonstrated prospective characteristics for gold.

In this paper, a summary of the current knowledge of the major BIF-hosted gold deposits in Nunavut is presented, largely based on work by the Geological Survey of Canada (GSC) and its collaborators from industry and academia. In addition, new petrographic and geochemical data of the new prospective BIF discovered as part of the Fury and Hecla project led by the CNGO on northwestern Baffin Island are presented.

BIF-hosted gold in the Kivalliq, Kitikmeot and Qikiqtaaluk regions

The BIF-hosted gold deposits throughout Nunavut have been, and are still being, studied to various degrees by different groups. The information presented below is from this research and is all publicly available. A summary is presented for each deposit, with a focus on the most relevant features in each case. This section is organized into three parts by region and further subdivided to describe each mine or project within that region, starting with geological setting. Generally, each mine or exploration project is described by location with property or target names, economic values, geochronological aspects and mineralization style, with structural controls and geochemistry (when applicable), respectively.

Kivalliq Region

Geological setting of the Woodburn Lake and Rankin Inlet Archean greenstone belts

The Kivalliq Region is located in central Nunavut within the western Churchill Province. Specifically, the region is divided into the Rae craton, the Hearne craton and the Chesterfield block (Hoffman, 1988). Regional sutures such as the Snowbird Tectonic Zone separate these domains (Berman et al., 2007). It is widely recognized that crustal-scale sutures such as these are conduits from the mid-to upper crust, by which gold can be transported and deposited to form syndeformation orogenic gold deposits (Pehrsson et al., 2014). Orogenic gold deposits are generally formed a few tens of millions of years after hostrock formation (Goldfarb et al., 2004). However, based on available geochronology, some orogenic gold deposits in the western Churchill Province (e.g., Meadowbank and Meliadine) are

even magnitudes of years younger than their hostrocks (i.e., up to one billion years) and were deposited during the superimposition of major Paleoproterozoic orogenesis (cf. the Paleoproterozoic gold metallotect in Carpenter et al., 2005) such as the Trans-Hudson (Pehrsson et al., 2013; Janvier et al., 2015; Lawley et al., 2016).

The Meadowbank and Amaruq deposits of the Meadowbank complex are located north of Baker Lake (Figure 1), in the Woodburn Lake greenstone belt of the Rae craton (Sherlock et al., 2004; Pehrsson et al., 2013; Valette et al., 2018). The mineralized zones are within the Woodburn Lake group (ca. 2.71 Ga), which is characterized by komatiitic and tholeiitic mafic metavolcanic rocks, with associated intermediate tuffs and flows intercalated with iron formation, and wacke to mudstone (Pehrsson et al., 2013; Jefferson et al., 2015). The Meliadine mine (Figure 1) is located near the community of Rankin Inlet, in the Rankin Inlet greenstone belt (RIGB; >2.66 Ga), which follows the inferred boundary between the Hearne craton and the Chesterfield block (Lawley et al., 2015a, b, 2016). The RIGB comprises two distinct volcanic assemblages, a lower and an upper assemblage, that are separated by discontinuous conglomerate (≤ 2.15 Ga; Davis et al., 2008). These assemblages predominantly encompass mafic volcanic rocks interbedded with siliciclastic and carbonate sedimentary rocks, including oxide-facies BIF (Lawley et al., 2016). The crustal-scale Pyke Fault crosscuts the RIGB and hosts numerous gold deposits and prospects (Carpenter and Duke, 2004).

Meadowbank mine

The Meadowbank mine encompasses the Portage, Goose and Vault deposits, from which a total of 92.7 t Au (3.3 million oz.) has been produced from 2010 to 2019 (Crown-Indigenous Relations and Northern Affairs Canada, 2019). The Portage and Goose zones are hosted in thick magnetite and chert BIF, and lesser volcanoclastic units, whereas the Vault zone, 7 km to the north, is mostly hosted in sheared intermediate volcanoclastic rocks. The Portage and Goose zones are hosted in the central BIF, whereas otherwise similar BIF units to the east and west are barren. Careful geological mapping, core logging and U-Pb zircon ages indicate that the central BIF is located along a structural boundary that separates two distinct lithological domains that are aged ca. 2717 Ga and ca. 2711 Ga, possibly a key controlling factor in gold endowment (Janvier et al., 2015). The property has two main mineralization styles: one that contains the bulk of the gold and is dominated by pyrrhotite and largely associated with the magnetite and chert layers in the BIF (Figure 2a, b); and the other, which is hosted in quartz-pyrrhotite-pyrite veins in volcanoclastic units in proximity to the BIF's pyrrhotite-rich zones (Janvier et al., 2015). The mineralized Algoma-type, oxide-facies BIF is polydeformed and metamorphosed at greenschist to amphibolite

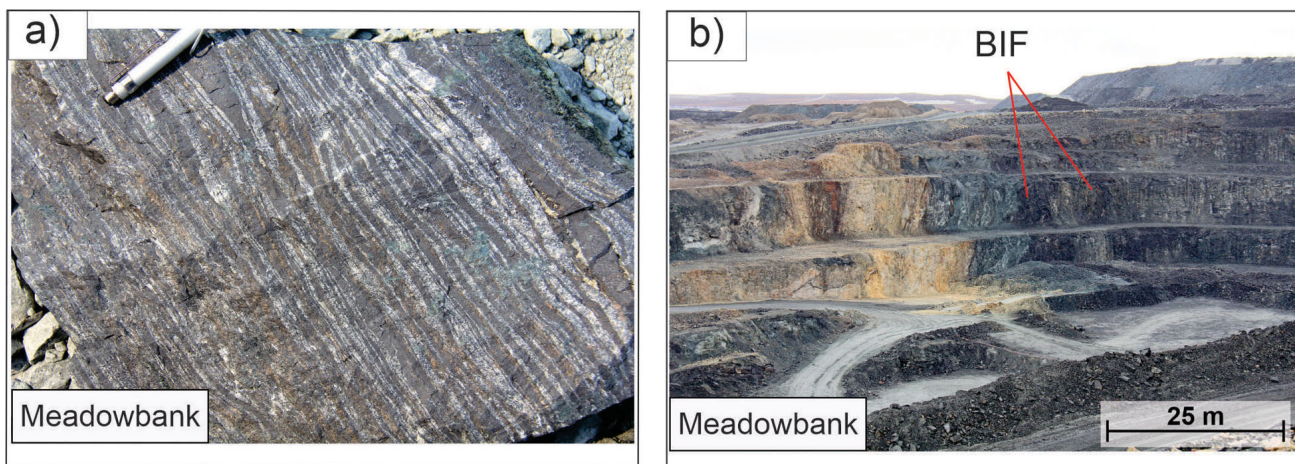


Figure 2: **a)** Mineralized, thinly bedded magnetite-chert iron formation of the Portage pit at the Meadowbank mine. Pyrrhotite replacement is better developed along deformed magnetite layers and locally associated with irregular quartz veining or 'silica-flooding'. **b)** View looking northwest of the northern end of the Portage open pit at the Meadowbank mine, showing the folded and sheared BIF (dark grey) in contact with intermediate volcanoclastic units to the right and with ultramafic rocks (dark green) structurally overlain (left) by quartzite (yellowish unit).

facies (Sherlock et al., 2004; Pehrsson et al., 2013). Gold is associated with pyrrhotite±pyrite that replace magnetite layers, with secondary chalcopyrite and very local arsenopyrite. Grunerite is common in chert bands along with chlorite alteration. Elements, including As, S, Cu, Pb, Ni, Co and Te, are anomalous in gold-bearing BIF, whereas Ca is leached (Janvier et al., 2015). Janvier et al. (2015) suggested that gold was introduced and structurally controlled by D₁ faults and was overprinted and partly remobilized by D₂ deformation along shear zones and F₂ fold limbs. Gold-bearing BIF is texturally disaggregated with fragmented, folded and transposed chert and magnetite layers in high-strain zones.

Amaruq property

The Amaruq property comprises the Whale Tail and IVR deposits totalling an estimated 172.93 t Au (6.1 million oz.), including precommercial production, reserves and resources (Valette et al., 2020). Both the Whale Tail and IVR BIFs are Algoma type, silicate facies, polydeformed and hosted in a mafic to ultramafic sliver intercalated with thin chert and argillite. This sliver is bounded both to the south and north by ≤2.65 Ga greywacke (Pehrsson et al., 2013; Valette et al., 2020). Whale Tail and IVR have distinct mineralization styles. The Whale Tail deposit is characterized by pyrrhotite-rich and arsenopyrite (±loellingite) stratabound replacement zones with silica flooding and veining in the silicate-facies BIF, chert, and along contacts with mafic-ultramafic rocks in F₂ fold hinges and high strain zones (Figure 3a; Valette et al., 2020). Gold was exsolved from loellingite during retrograde metamorphism (Mercier-Langevin et al., 2018; Lauzon et al., 2020). In contrast, gold from the IVR orebody is associated with sulphide-poor quartz veins in the volcanosedimentary package, whereby gold placement is interpreted as contempora-

neous with early to syn-D₂ deformation. Overall, at Amaruq, orebodies are present along shallow, east-plunging (20°) ore shoots that are subparallel to collinear F₂ and F₃ fold axes, and L₂₋₃ intersection lineation. Geochemical analysis of the host units, stratigraphic correlations, deformation and metamorphism, and geochronology (U-Pb, Re-Os and Ar/Ar) are currently the subjects of a major research activity at the GSC (Targeted Geoscience Initiative-5, Gold Project; Mercier-Langevin et al., 2020), which also includes the funding of a doctoral thesis (cf. Valette et al., 2020).

Meliadine mine

The Meliadine mine encompasses seven deposits, the largest known and only one currently being mined is the Tiriganiaq zone. The other deposits include Wolf North, Discovery, F Zone, Pump, Wolf Main, Wesmeg and Normeg. All deposits are associated with the Pyke Fault and occur within 5 km of the Tiriganiaq deposit, except for the Discovery deposit located at a distance of 17 km away. The Meliadine district is estimated to have a 12-year mine life with gold reserves of 132.39 t Au (4.67 million oz.; Agnico Eagle Mines Limited, 2020b). The Tiriganiaq deposit is hosted in a turbidite and BIF sequence along a west-trending splay of the Pyke Fault (Lower fault). The results of U-Pb radiometric dating conducted on a sensitive high-resolution ion microprobe (SHRIMP) suggest that the Tiriganiaq hanging wall and footwall are the same age (≤2.66 Ga; Lawley et al., 2016). At the Tiriganiaq deposit, mineralization resides in large fault-fill veins and associated extension veins (i.e., lodes), with arsenopyrite replacement of magnetite-rich layers in folded BIF along vein selvages (Figure 3b; Carpenter et al., 2005; Lawley et al., 2015a, b, 2016; St. Pierre et al., 2020). The highest gold grades are present where folded BIF is cut by quartz (±ankerite) vein networks

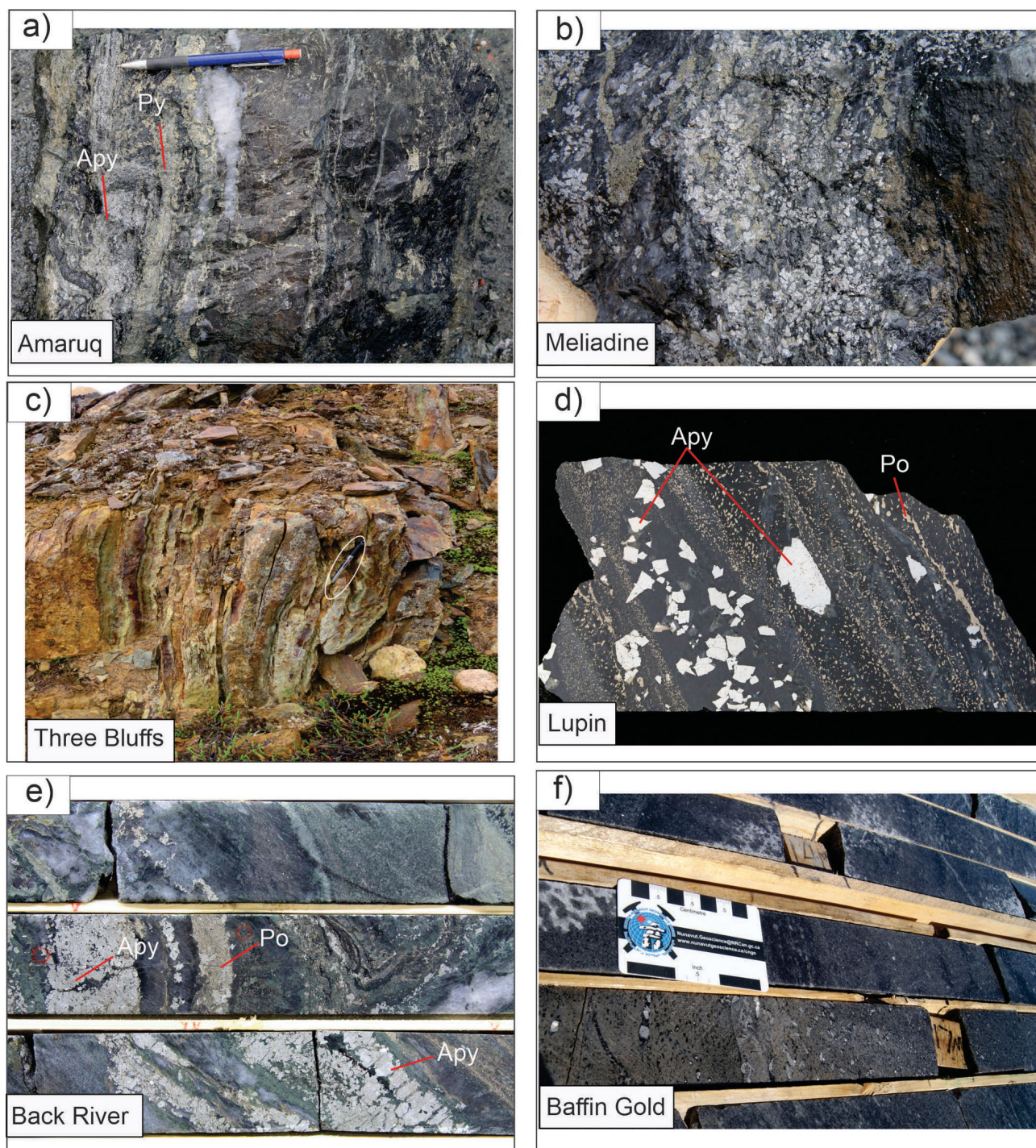


Figure 3: Field photographs showing **a)** thinly-bedded chert and silicified siltstone with stratabound arsenopyrite (Apy) replacement, locally weathered to pyrite (Py), and dismembered quartz veins with fracture-controlled pyrrhotite remobilization in the Whale Tail open pit at the Amaruq mine (mechanical pencil for scale); **b)** heavily mineralized sample from the laminated, quartz-ankerite shear vein referred to as the '1000 lode' of the Tiriganiaq deposit at the Meliadine mine, consisting of a grey quartz vein with pyrrhotite and coarse-grained arsenopyrite in a siltstone unit; **c)** discovery outcrop at Three Bluffs, heavily weathered, nearly vertical and folded chert and magnetite bedding (marker for scale circled in white, photo courtesy of Crown-Indigenous Relations and Northern Affairs Canada); **d)** close-up view of a mineralized, thinly bedded magnetite-chert iron formation at the Lupin deposit, with the sample showing finely disseminated pyrrhotite (Po) and large arsenopyrite in a partly silicified BIF unit; **e)** mineralized BIF interval from the Umwelt zone in the Vault area at the George property of the Back River deposit, with strongly deformed silicified sulphide-facies iron formation and (amphibole-rich and chert layers) cut by diffuse quartz veins or 'silica flooding' associated with stratabound to discordant coarse-grained arsenopyrite and fine-grained pyrrhotite replacement; **f)** mineralized drillcore from the Kanosak prospect, Baffin Gold project (photo courtesy of Crown-Indigenous Relations and Northern Affairs Canada).

(Lawley et al., 2016; St. Pierre et al., 2020). The U-Pb ages of monazite and xenotime and Re-Os ages of arsenopyrite suggest a protracted ore-forming history, with part of the gold perhaps as old as 2.3 Ga and some related to the Trans-Hudson Orogen at ca. 1.85 Ga (Carpenter et al., 2005; Lawley et al., 2016).

Kitikmeot Region

Geological setting of the Committee Bay Belt and the Slave structural province

The Kitikmeot Region of Nunavut spans the Rae craton and Slave structural province (SSP). The Three Bluffs deposit occurs in the Rae craton of eastern Kitikmeot Region (Figure 1); the Lupin and Back River deposits are in the SSP of western Kitikmeot Region.

The Three Bluffs deposit is located approximately 200 km southwest of Kugaaruk and 350 km northeast of Baker Lake (Figure 1). Although previously believed to be hosted in the Prince Albert Group, as part of the Committee Bay Belt (Skulski et al., 2003; Davies et al., 2011), recent findings indicate the Prince Albert Group and Committee Bay Belt are not correlated (Wodicka et al., 2011; Corrigan et al., 2013). Thus, the Three Bluffs deposit is now considered to be hosted in the south-central supracrustal domain of the Committee Bay Belt, specifically in the Three Bluffs supracrustal strand (Sanborn-Barrie et al., 2014). The south-central supracrustal domain comprises semipelite, psammite and secondary quartzite, with a thick unit of mafic and ultramafic metavolcanic rocks (MacHattie, 2002, 2008) intercalated with felsic metavolcanic rocks. Oxide-, silicate- and sulphide-facies iron formation occur as discontinuous layers up to 50 m in thickness that are interstratified with komatiite (Sanborn-Barrie et al., 2014).

The SSP, where the Lupin and Back River deposits are located (Figure 1), is an Archean granite-greenstone meta-sedimentary terrane spanning the area between Great Slave Lake and the Coronation Gulf. The SSP borders the Thelon Orogen (ca. 2020–1910 Ma) to the east and the Wopmay Orogen (ca. 1950–1840 Ma) to the west (Hoffman, 1988; Hoffman and Hall, 1993; Sherlock et al., 2012). Two types of iron formation have been identified throughout the SSP and classified as amphibolitic iron formation, consisting of quartz+grunerite+hornblende+graphite±garnet+ilmenite±pyrrhotite±pyrite±chalcopyrite, or pelitic iron formation, consisting of quartz+garnet+biotite+cummingtonite-grunerite+hornblende+ilmenite (Ford, 1988). The Lupin former mine is located 400 km northeast of Yellowknife in the central SSP of Nunavut, where ore is hosted in amphibolitic iron formation. It lies within an Archean metaturbidite and iron formation sequence comprising the Contwoyo Formation as part of the Yellowknife Supergroup (Geusebroek and Duke, 2005). The Back River project is located 520 km northeast of Yellowknife, also in the central

SSP of Nunavut. Specifically, it lies within the Beechey Lake Group, which onlaps the Back River volcanic complex (2708.5 ± 0.8 Ma; Villeneuve et al., 2001), also part of the Yellowknife Supergroup (Henderson, 1970). The Beechey Lake Group comprises oxide- and silicate-facies BIF, with interbedded turbidite, greywacke and mudstone (Crown-Indigenous Relations and Northern Affairs Canada, 2019).

Three Bluffs project

The Three Bluffs deposit (Figure 3c) is currently in the exploration stages along many promising drill targets named Inuk, West Plains, Raven, Shamrock and Aiviq (Fury Gold Mines Limited, 2020). The highest-grade intercept was found in the Raven target with 36.22 g/t Au over 2.43 m. The Three Bluffs deposit has an indicated resource total of contained gold of 14.86 t Au (0.52 million oz.) and an inferred total of 20.41 t Au (0.72 million oz.) as of 2017 (Fury Gold Mines Limited, 2020). Results of SHRIMP U-Pb zircon dating of a conformable dacite and a crosscutting diorite intrusion suggest a ca. 2.7 Ga depositional age for the Beechey Lake Group. In contrast, timing of gold endowment is placed at ca. 1815 Ma using U-Pb monazite methods, Re-Os of arsenopyrite, and Pb-Pb secondary errorchron age for pyrite and arsenopyrite (Davies et al., 2011). Thus, it was found that gold predates the high-grade metamorphism in the area (upper-amphibolite facies). This is consistent with the timing of gold emplacement at the Meliadine mine, suggesting a regional gold-emplacement event during the Trans-Hudson orogeny (1.86–1.85 Ga; Lawley et al., 2015a). In Three Bluffs, gold is associated with sulphide replacement of iron formation and is best developed in F_2 fold hinges, and to a lesser extent along fold limbs. More specifically, the highest grades are associated with silica-rich flooding (ubiquitous quartz veinlets) and muscovite-rich (altered) intervals in the sulphide-facies BIF. Sulphide assemblages are mainly pyrrhotite, with lesser pyrite, arsenopyrite and chalcopyrite (Davies et al., 2011).

Lupin former mine

The Lupin former mine consists of the Lupin dome, and the McPherson M1 and M2 ore zones. The mine was in production from 1982 to 2004, except for re-engineering periods in 1998 and 1999, and intermittently between care and maintenance from 2004, until its definitive closure and remediation in 2013 (Crown-Indigenous Relations and Northern Affairs Canada, 2019). Approximately 91.29 t of Au (3.22 million oz.) were produced at the mine between 1982 and 2004 (Geusebroek and Duke, 2005; Harron, 2012). The supracrustal host sequence has not been dated, but it is assumed to be ca. 2700–2660 Ma based on regional crosscutting relationships. Timing of gold emplacement remains undated despite a recent tentative Re-Os study of arsenopyrite (R. Creaser, pers. comm., 2019) but is consid-

ered as Archean based on regional constraints on the controlling structures. Research has focused on structural, geochemical and sulphide distribution aspects. The Lupin orebody is controlled by a domical structure, where gold resides in the western, central and eastern limbs of a doubly folded BIF (Gardiner, 1986). The dome is interpreted as an F_2/F_3 hammerhead-shaped interference fold structure (Geusebroek and Duke, 2005). Several genetic models for gold emplacement at Lupin have been proposed: 1) a syngenetic model (i.e., primary deposition during basin development) based on the extensive stratiform habit of the sulphides (Bostock, 1980; Gardiner, 1986; Padgham and Atkinson, 1991; Kerswill et al., 1992); 2) an epigenetic model (i.e., gold entirely coming from an external source and reconcentrated during metamorphism) based on isotopic analyses of Pb and Sr on the network of mineralized quartz veins and field relationships (Lhotka, 1988; Geusebroek and Duke, 2005); or 3) a multiphase model, which hypothesizes a mixed contribution of syngenetic gold with the addition of epigenetic processes (e.g., Bullis et al., 1994). The BIF at Lupin is considered to be silicate facies (grunerite and hornblende rich) and locally sulphide facies. Gold commonly occurs as finely disseminated inclusions in pyrrhotite and along grain boundaries between arsenopyrite and loellingite (Figure 3d; Bullis et al., 1994). The McPherson zone has a similar mode of mineralization as the Lupin dome, although with a higher degree of deformation. Pyrrhotite and arsenopyrite are both abundant, with hedenbergite in silicified domains marginal to quartz veins.

Back River project

The Back River project consists of six properties: the Goose property, which includes the Goose Main, Llama, Echo, Nuvuyak and Umwelt deposits; the George property, with the Locale 1 and Locale 2 mineral deposits; and several secondary properties named Boulder, Boot, Del and Bath (Sabina Gold and Silver Corporation, 2020). The Back River project, once in production, is estimated to have a 10-year mine life with an estimated resource total of 182.29 t Au (6.43 million oz.) for the Goose and George properties combined. Studies conducted using U-Pb zircon and arsenopyrite Re-Os geochronology are currently underway as part of a Sabina Gold and Silver Corporation and GSC collaboration, but field relationships indicate that gold mineralization is probably associated with the main phase of deformation (F_1 folding in the local nomenclature, correlated with D_2 at SSP scale) and overprinted (remobilized and/or upgraded) by D_2 (local nomenclature) open folds. Most of the gold occurs in silicified sulphide-facies BIF, with quartz veins and shears in F_1 -fold hinges and locally along F_1 -fold limbs. Sulphide assemblages include pyrite, coarse arsenopyrite and pyrrhotite, along with accessory chlorite, carbonate, hornblende and grunerite (Figure 3e). The gold-bearing sulphides are associated with dif-

fuse quartz veins ('silica flooding') and locally with shear veins preferentially developed in fold hinges, with sulphides replacing the folded BIF layers. Preliminary (unpublished) arsenopyrite Re-Os dating results suggest that the main phase of mineralization is Archean in age.

Qikiqtaaluk Region

Geological setting of central Baffin Island and the Piling Group

Central Baffin Island, located within the Qikiqtaaluk Region of Nunavut, at the northwestern margin of the Trans-Hudson Orogen (Corrigan et al., 2001; Stacey and Pattison, 2003), comprises Archean basement of the Rae domain to the north and the Foxe fold belt to the south. The main stratigraphic unit, named the Piling Group, consists of a lower passive-margin sequence (lower Dewar Lakes and Flint Lake formations) composed of basal muscovite schist, quartzite with interbedded iron formation, and overlying dolomitic and calcareous marble with chert. This transitions into an upper foredeep sequence (Astarte River and Longstaff Bluff formations), which consists of a basal unit of ferruginous psammite, black shale and sulphide-facies iron formation, overlain by psammite and feldspathic wacke interbedded with semipelite and pelite. The volcanic Bravo Lake formation encompasses ultramafic and mafic flows as well as sills intercalated in the lower sequence of the Piling Group (Henderson and Henderson, 1994; Corrigan et al., 2001).

Baffin Gold project

The Baffin Gold project is the least explored prospect among all other deposits previously mentioned. ValOre Metals Corporation and previous owners Commander Resources Limited have located key gold-bearing areas named Malrock, Brent, Ridge, Kanosak and Durette. The property spans over 100 km of the Piling Group, with auriferous units mainly in the Bravo Lake and Dewar Lakes formations. The gold resources for the property remain to be determined. However, anomalous gold has been identified in key areas, including 107.1 g/t Au over 0.6 m (channel sample) in iron formation at Ridge, and 114.5 g/t Au (grab sample) at Brent along a quartz-filled shear zone (ValOre Metals Corporation, 2020). Results from U-Pb detrital zircon analysis of the Dewar Lakes quartzite are reported to have a bimodal age distribution, yielding an Archean age at 2.85–2.84 Ga and a Paleoproterozoic age at 2.18–2.16 Ga (Henderson and Parrish, 1992; Wodicka et al., 2002). The younger population provides a maximum depositional age of ca. 2.16 Ga for the entire Piling Group. In addition, the Bravo Lake formation has been dated by U-Pb zircon methods, yielding a maximum age of 1883.3 ± 4.7 Ma from a crosscutting diorite sill (Henderson and Parrish, 1992; Wodicka et al., 2002). The Dewar Lakes and Bravo Lake formations are the auriferous hostrocks on the property, specifically within silicate- and sulphide-facies BIF with

grunerite alteration, along major shear zones and quartz veins, and altered gabbro. Structural controls and deformation phases of gold are unknown at the property scale. A petrographic study by Garzon (2010) delineated sulphide relationships within BIF-hosted gold at the Malrock and Ridge prospects. Results indicated a textural association of gold and loellingite, suggesting that arsenic could be a good pathfinder element for regional gold exploration, as for most other BIF-hosted gold deposits of Nunavut. Pyrrhotite was found to be the most abundant sulphide, with chalcopyrite inclusions. Pyrrhotite shows replacement textures of pyrite, magnetite and ilmenite. An example of mineral-

ized drillcore from the Kanosak prospect is shown in Figure 3f.

The Fury and Hecla Geoscience Project: BIF on northwestern Baffin Island

Field observations

The Fury and Hecla Geoscience Project was a multiyear enterprise led by the Canada-Nunavut Geoscience Office in collaboration with Crown-Indigenous Relations and Northern Affairs Canada, Laurentian University, McGill University and Université du Québec à Montréal (outline of study area shown on inset map of Figure 4). The aim of

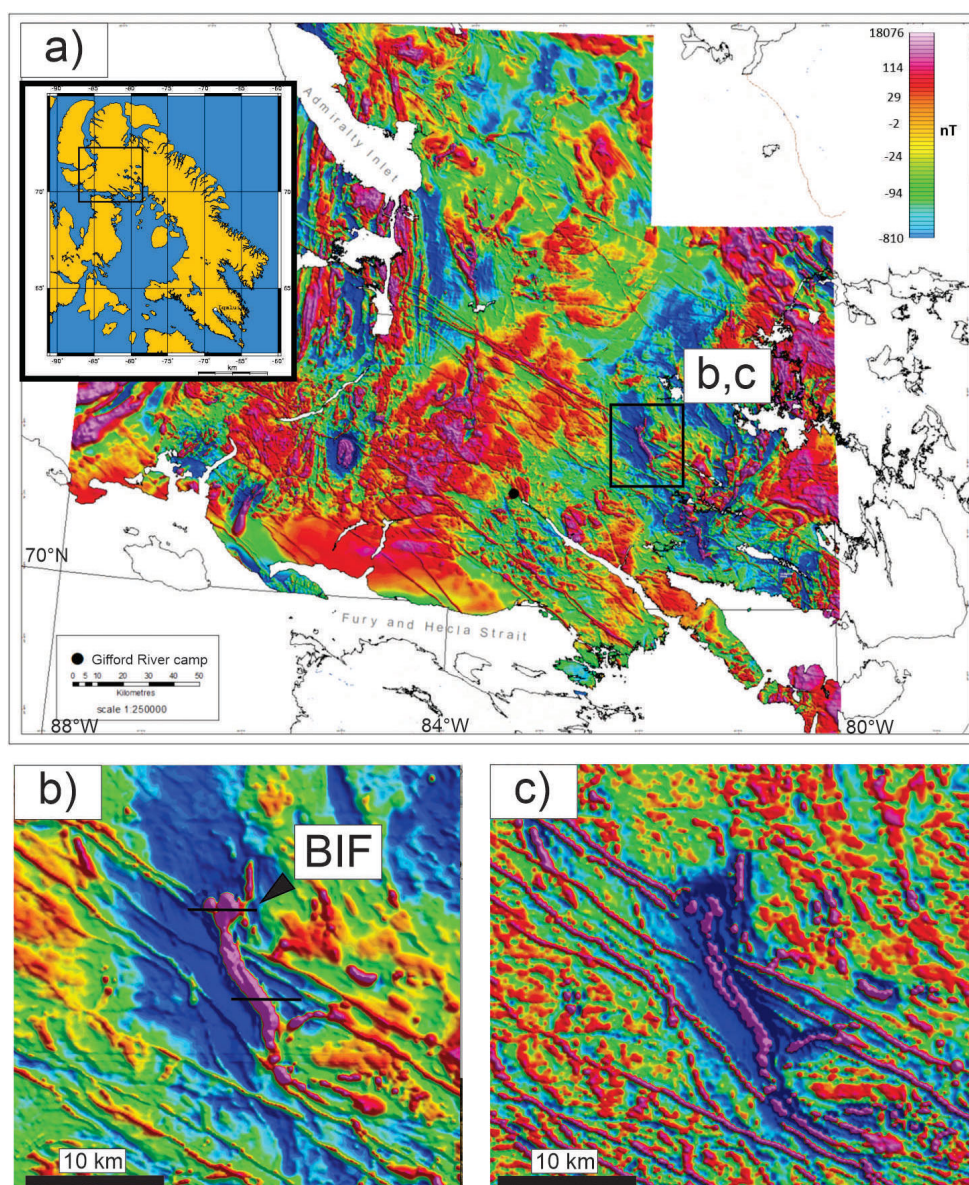


Figure 4: Residual total-field magnetic data from the 2017 and 2019 airborne geophysical surveys, showing the measure of magnetism of the rock in nanoteslas (nT; Steenkamp, 2018a–h; Lebeau, 2019a–g): **a)** coverage of all or parts of NTS areas 47D–H, with outline of the general borders of the study area on Baffin Island, Nunavut (inset map); **b)** close-up of the BIF in residual total-field magnetic data (BIF is pink) with the northern and southern traverse lines (black horizontal lines); **c)** same image as in (b) but in first vertical derivative of the magnetic field.

this study was to contribute new geoscience information at a regional scale for a largely unmapped area of northern Baffin Island, which also happened to be one of the last remaining areas in Nunavut without geophysical magnetic data.

A fixed-wing geophysical magnetic survey collected data in 2017 and 2019; the geological survey was conducted in 2018 and 2019. Papers summarizing field observations and analytical results have been published on the following topics: Precambrian crystalline bedrock (Bovingdon et al., 2018, 2021; Steenkamp et al., 2018; Dufour et al., 2020, 2021; Lebeau et al., 2020), Precambrian Fury and Hecla sedimentary basin (Greenman et al., 2018, 2020; Patzke et al., 2018), Palaeozoic bedrock (Zhang, 2018) and Quaternary geology (Tremblay and Godbout, 2018; Tremblay et al., 2020; Tremblay, 2021). General bedrock geology of the area dominantly comprises Archean granodioritic, monzogranitic, tonalitic and quartz dioritic metaluminous gneiss with local migmatization, and secondary granodioritic weakly to strongly peraluminous gneiss. Felsic plutons are intruded throughout the area, including foliated granodiorite-monzogranite and porphyritic to porphyroclastic (locally megacrystic) monzogranite to quartz monzonite plutons. Supracrustal metasedimentary rock units are scarce in the area: a small garnet-pelite panel was located west-northwest of the Fury and Hecla Basin, as well as some small, centrally located slivers. A thick, sulphide-bearing BIF was located in the area (NAD 83, UTM Zone 17N, 461347E, 7837589N). Younger mafic to ultramafic intrusions, weakly foliated to massive syenogranite dykes, gabbroic dykes and syenogranite pegmatite dykes also intrude throughout the project area. A preliminary geological bedrock map of the area is illustrated in Lebeau et al. (2020) and drafting of the final map is in progress.

Magnetic data indicate a highly contrasting north-trending rock package measuring approximately 3 by 15 km (Figure 4), which was confirmed as BIF on the ground (referred to later in the paper as the ‘Fury and Hecla BIF’). The geophysical signature of the magnetic field, as shown in Figure 4b (residual magnetic field) and Figure 4c (first vertical derivative), demonstrates two separate, side-by-side limbs that meet, suggesting an isoclinally folded package. An aerial view at the suspected fold nose further supports this interpretation (Figure 5). Two field traverses were completed over the BIF, one at the northern extent (at the suspected fold nose) and another along strike that confirmed the BIF was continuous southward (see Figure 4b).

Along the northern traverse line, the BIF is adjacent to a thickly banded orthogneiss with porphyroclastic granodiorite and monzogranite layers (Figure 5). The contact is not exposed. The BIF outcrop is very blocky, with little outcrop that can be confidently considered in place (Figure 6a). Overall, the outcrop is dark grey with patches of gossanous

rock that are more sulphide rich. Outcrop that is in place comprises finely laminated quartz, magnetite and specularite (Figure 6b), with a well-defined, steeply plunging crenulation lineation (Figure 6c). Some sections of the exposure are dominated by massively textured and coarse-grained magnetite with secondary specularite (Figure 6d). Float samples in the gossanous patches demonstrate asymmetrically folded quartz layering in a fine dark grey mass. The sulphide minerals are anhedral to euhedral, fine to coarse grained (up to 2 mm) and stratiform, occurring as strings of sulphides that are parallel to the quartz-layered fabric (Figure 6e). Other gossanous float samples demonstrate higher degrees of deformation, with disaggregated layers of quartz and oxidized sulphide minerals (Figure 6f). Several milky quartz veins crosscut the banded iron formation, but they are not laminated, nor do they present any alteration.

Along the southern traverse line (Figure 4b), the BIF forms a tall rubbly ridge in the landscape, with no in situ outcrop or visible contacts with the adjacent rock units (Figure 7a, b). The adjacent rock is the same monzogranitic and granodioritic orthogneiss; however, the gneiss is locally silicified with dense, fine, net-textured quartz veinlets (Figure 7c). Highly silicified float rock of banded red chert, with crosscutting white quartz veinlets and pervasive quartz alteration with a sugary appearance, was observed on the BIF ridge (Figure 7d). The net-textured quartz veinlets in the adjacent orthogneiss and the presence of pervasively silica-altered BIF suggest late quartz flooding of the area. In addition to silica-altered BIF, the exposure is dominantly composed of finely banded, magnetite-dominated oxide-facies BIF (Figure 7e) and lesser silicate-facies BIF, consisting of banded maroon-red and medium green amphibole (Figure 7f). Massive milky quartz veins are again present, although there are less gossanous patches.

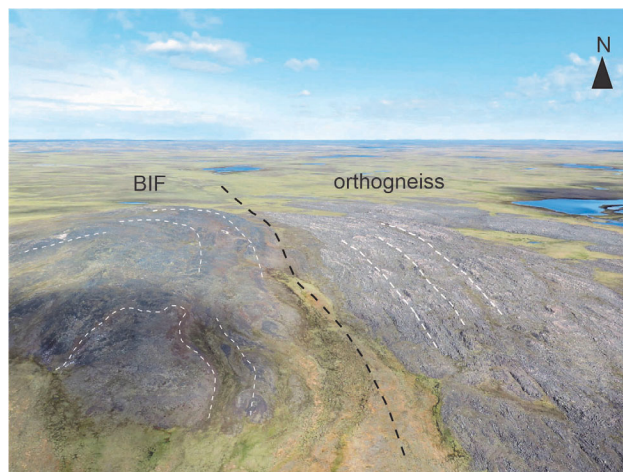


Figure 5: Aerial photograph looking northward of the Fury and Hecla banded iron formation (BIF) outcrop on northern Baffin Island showing the lithological contact (dotted black line) and the rock fabric (dotted white lines).

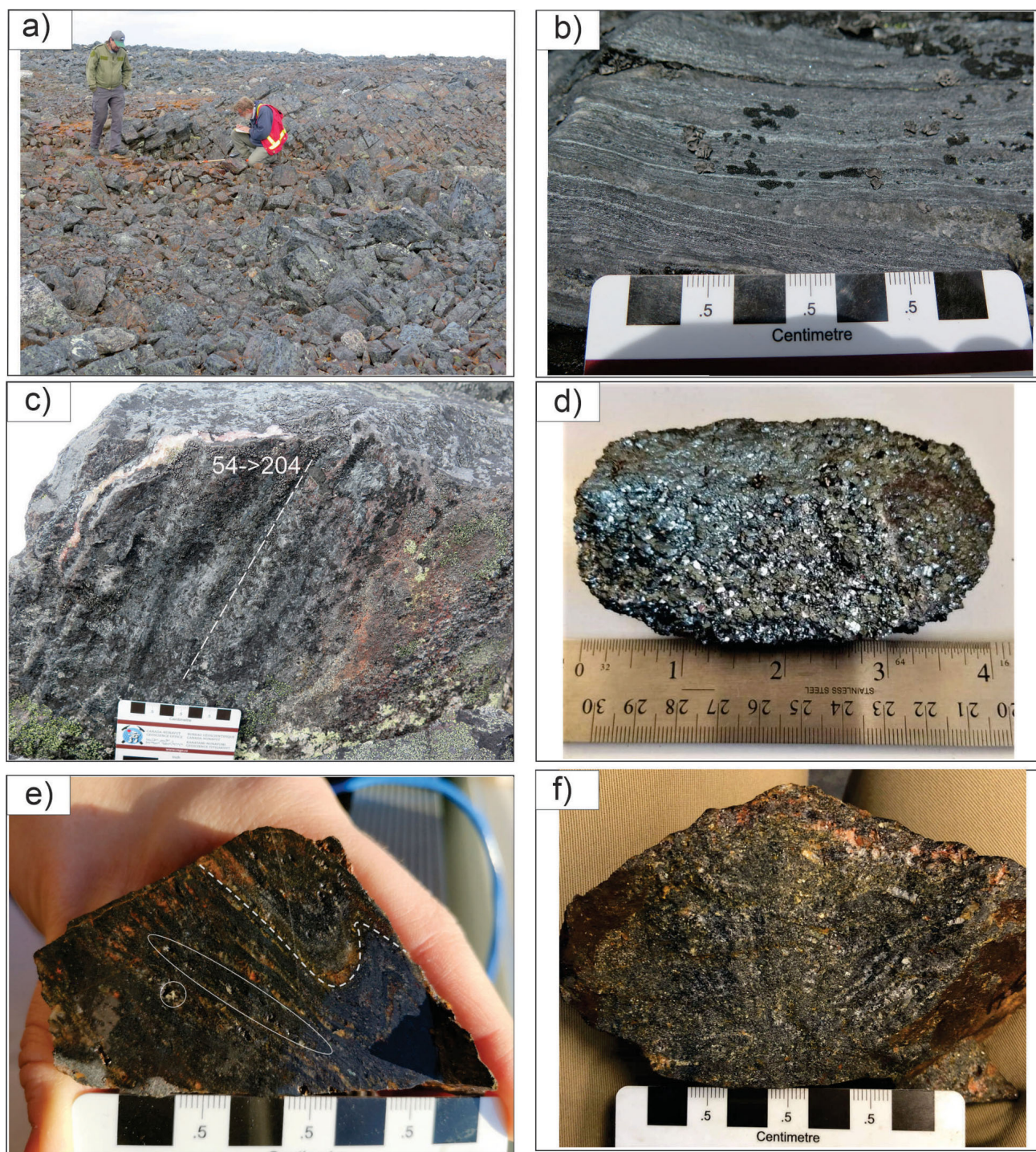


Figure 6: Field photographs from the northern traverse line along the Fury and Hecla banded iron formation (BIF), on northern Baffin Island, showing **a)** an overview of the outcrop (standing helicopter pilot for scale is 176 cm tall); **b)** laminated BIF with quartz, magnetite and specularite; **c)** crenulation lineation (dotted white line), indicating trend and plunge along the bedding plane of the BIF; **d)** float sample of massive and coarse-grained magnetite with specularite; **e)** float sample from gossanous BIF, with folded fabric (dotted white lines) and coarse-grained sulphides (circled); **f)** float sample from gossanous BIF, characterized by a higher degree of deformation with disaggregated layers of quartz and sulphide minerals.

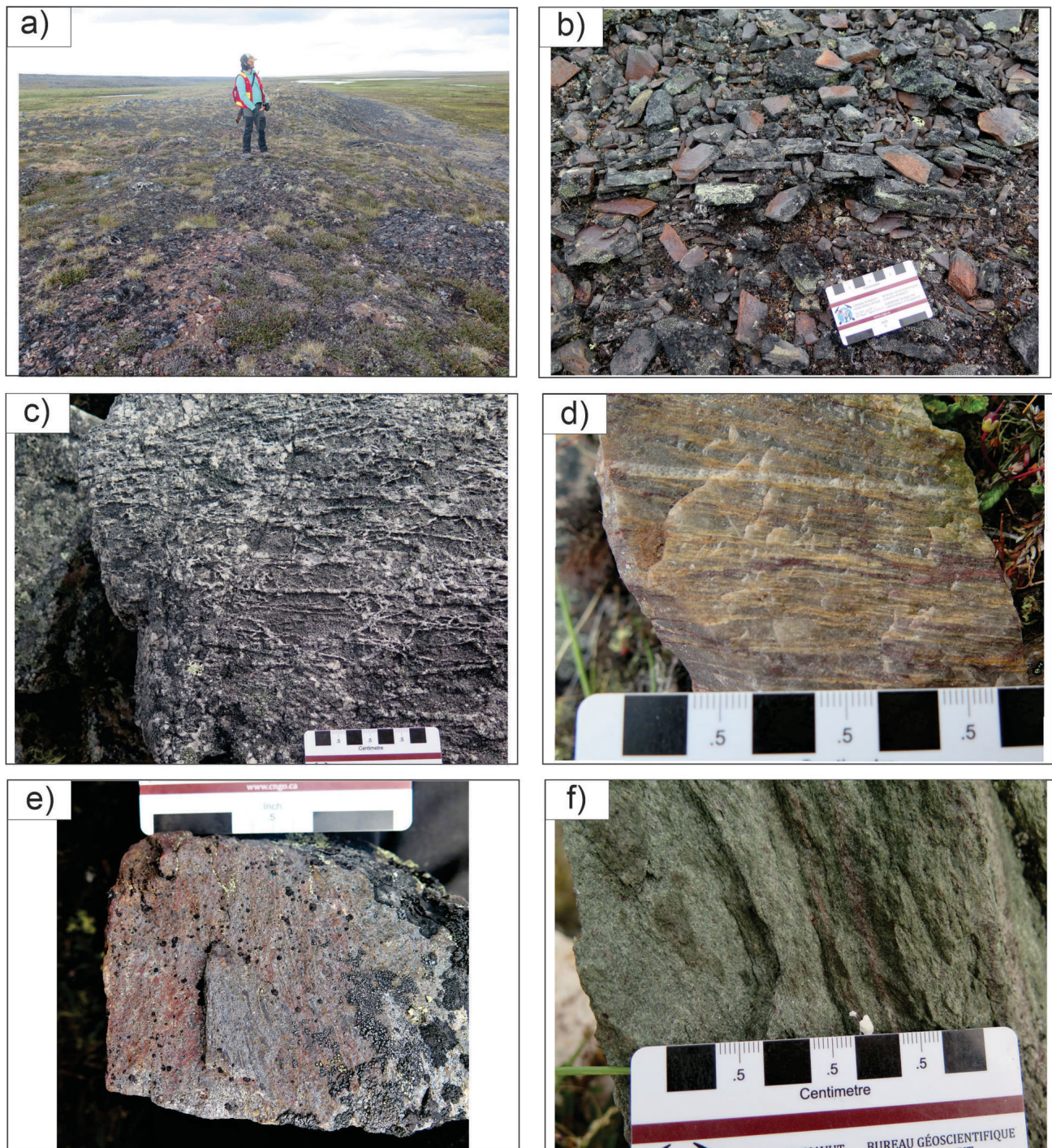


Figure 7: Field photographs from the southern traverse line along the Fury and Hecla banded iron formation (BIF), on northern Baffin Island, showing **a)** the rubbly ridge of the BIF (geologist for scale is 170 cm tall); **b)** BIF rubble; **c)** ubiquitous quartz veinlets in adjacent gneiss; **d)** float sample of silicified and quartz-veined BIF; **e)** float sample of finely layered magnetite-dominated, oxide-facies BIF; **f)** amphibolitic BIF.

Petrography and assays

The petrographic analysis and assay interpretation of the Fury and Hecla BIF are preliminary because of the regional-scale nature of the Fury and Hecla Geoscience Project. During fieldwork, the BIF was not studied in detail and was only investigated for mapping purposes. Although the CNGO is not planning further work in the area based on its current programming, additional exploration of this BIF by industry or academia may be warranted.

As part of this preliminary assessment, thin sections were prepared from two samples from the Fury and Hecla BIF: sample L050A01 is a finely laminated quartz-magnetite-specularite rock sampled from the outcrop (Figure 8a) and sample L050A02 is from a float sample of a gossanous patch (Figure 8b–f). Both samples are from the northern traverse (hinge zone). The finely laminated quartz-magnetite-specularite BIF (Figure 8a) possesses quartz-dominated laminations interlayered with magnetite and hematite (specularite) bands, approximately 1–3 mm in thickness. Mineral modal abundance is approximately 70% quartz and 30% Fe-oxide. Quartz grains are fine to coarse grained and largely equant, with some interfingering grain boundaries most likely due to recrystallization. Other noteworthy characteristics are undulose extinction and polycrystalline grains. The second thin section from the gossanous BIF sample possesses fine- to medium-grained minerals consisting of 50% quartz (highly recrystallized), 15% magnetite, 12% alteration minerals (i.e., sericite, epidote and hematite), 10% Ca-amphibole, 8% sulphide minerals (i.e., 5% pyrite, 2% pyrrhotite, 1% chalcopryrite) and 5% biotite. Modal abundance is variable across the thin section. In parts of the thin section (Figure 8b), biotite and quartz show a well-developed foliation, which is not as penetrative in the amphibole-rich bands. The aggregated texture of the amphibole (not lineated) suggests that peak metamorphism is late- to post-peak deformation. In addition to silicate minerals, sulphide minerals also present interesting textures and relationships. Although in hand sample some sulphide minerals appear subhedral to euhedral, they are mostly anhedral and flattened, showing only some crystal faces, in thin section. Anhedral pyrrhotite and chalcopryrite are the only sulphide minerals observed to share grain boundaries (Figure 8c). Pyrite generally occurs as aligned and flattened grains that follow the fabric of the rock (Figure 8d). It is possible that the other sulphide minerals also follow the same fabric, but their scarcity makes it impossible to confirm. Chalcopryrite is also observed surrounded by colloform-textured magnetite and weathered Fe-oxide that has replaced the chalcopryrite along fractured surfaces (Figure 8e). Lastly, pyrrhotite is also present in close association with magnetite as small anhedral inclusions (Figure 8f), possibly reflecting the start of sulphidization or a primary feature.

Samples assayed for this study consist of a gossanous sample that was thin sectioned from the northern field traverse (L050A02) and a milky quartz vein crosscutting the BIF from the southern field traverse (L064B01). The samples were cut and crushed at Laurentian University and sent to Activation Laboratories Ltd. (Ancaster, Ontario) for analysis. Both samples were analyzed using the 1E3 (aqua regia partial digestion multichannel scan) and 1A2 (fire-assay fusion) methods for gold as well as for other trace metals and elements (Table 1). The gossanous sample contains 26.1 wt. % Fe, well over the necessary 15 wt. % necessary to be considered an iron formation. Although no anomalous results were obtained, the presence of pyrrhotite in the BIF remains an interesting feature and more sampling is required to further evaluate the potential of this new BIF occurrence. Similarly, additional and more systematic sampling from the various gossanous patches is necessary to appropriately interpret the geochemistry of the BIF unit and its various components. Analytical results are presented in Table 1, although no interpretation is suggested because of the limited data.

Table 1: Assay results of two samples from traverse lines along the Fury and Hecla banded iron formation (BIF) outcrop on northern Baffin Island. Both the samples were analyzed at Activation Laboratories Ltd. (Ancaster, Ontario) using the aqua-regia partial digestion method followed by inductively coupled plasma–mass spectrometry, unless otherwise noted.

Element	Detection limit	Sample no.	
		L050A01 (BIF)	L064B01 (quartz vein)
Au (ppb) ¹	5	<5	<5
Ag (ppm)	0.2	0.2	<0.2
Cd (ppm)	0.5	<0.5	<0.5
Cu (ppm)	1	<1	2
Mn (ppm)	5	54	38
Mo (ppm)	1	4	<1
Ni (ppm)	1	7	<1
Pb (ppm)	2	<2	<2
Zn (ppm)	2	<2	<2
Al (%)	0.01	0.1	<0.01
As (ppm)	2	3	<2
B (ppm)	10	<10	<10
Be (ppm)	0.5	<0.5	1.3
Bi (ppm)	2	3	<2
Co (ppm)	1	<1	<1
Cr (ppm)	1	4	2
Fe (%)	0.01	26.1	0.34
S (%)	0.01	0.52	<0.01
Sb (ppm)	2	9	<2
Te (ppm)	1	5	<1
U (ppm)	10	<10	<10
V (ppm)	1	8	<1
W (ppm)	10	<10	<10
Y (ppm)	1	3	<1
Zr (ppm)	1	7	<1

¹Fire assay followed by atomic absorption spectrometry

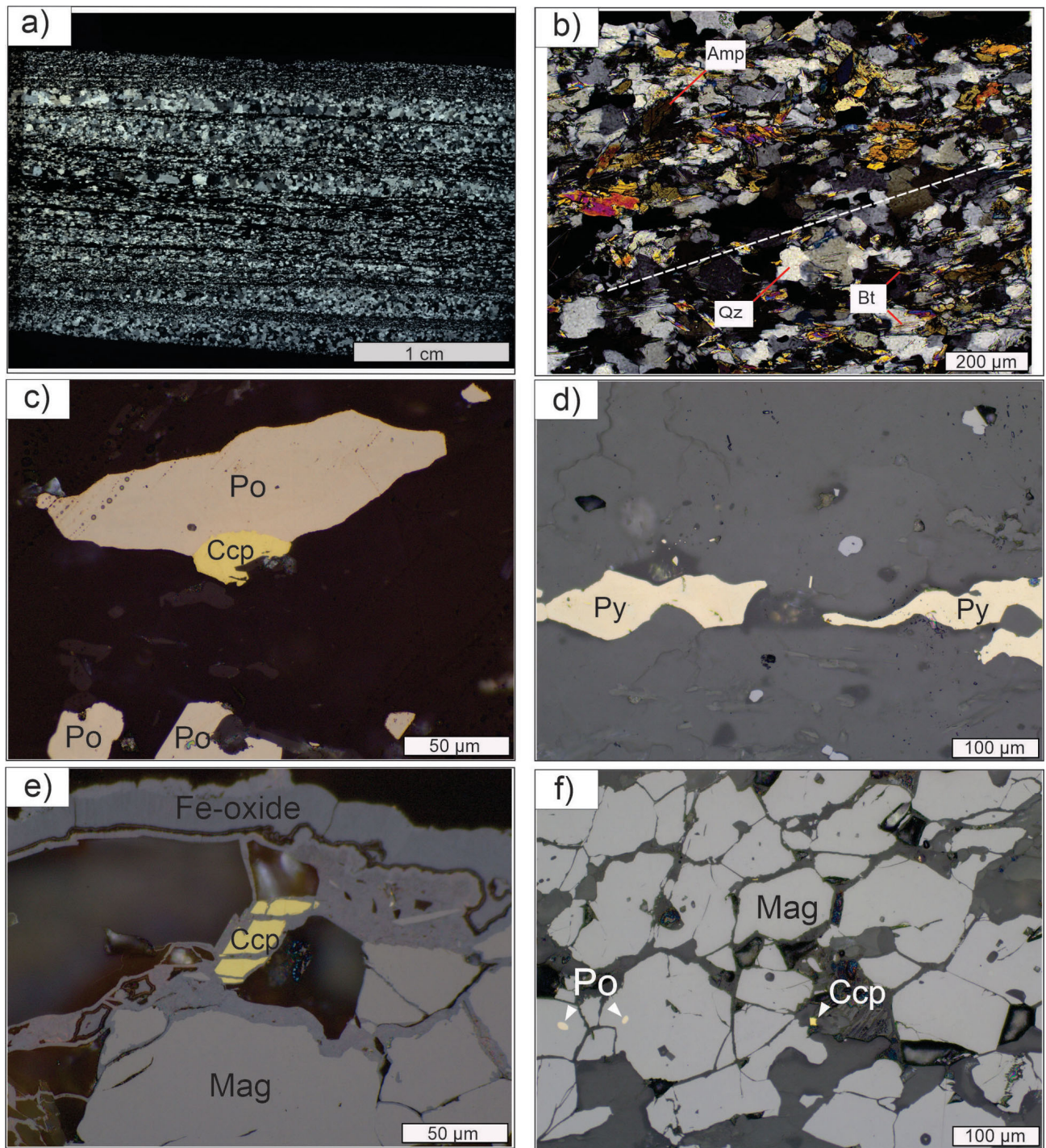


Figure 8: Photomicrographs of samples from the study area: **a)** thin-section scan of laminated quartz-magnetite-specularite banded iron formation (BIF), showing quartz grains (grey) and iron oxides (black) under cross-polarized light (XPL); **b)** BIF (dotted line illustrates general foliation) with quartz (Qz), foliated biotite (Bt) and amphibole (Amp) under XPL (10x magnification); **c)** anhedrall pyrrhotite (Po) in grain-to-grain contact with chalcopyrite (Ccp) and some subhedral pyrrhotite grains in the lower section of the photo seen under reflected light (RFL; 50x magnification); **d)** anhedrall and aligned pyrite (Py) under RFL (20x magnification); **e)** magnetite (Mag) and Fe-oxide forming colloform texture with fractured chalcopyrite under RFL (50x magnification); **f)** aggregate of magnetite with fine inclusions of anhedrall pyrrhotite and free chalcopyrite under RFL (20x magnification).

Economic considerations

Nunavut has many examples of BIF-hosted gold deposits, as summarized herein, and due to the underexplored nature of the territory, there is a good potential for other undiscovered deposits. Nunavut's BIF-hosted gold deposits show many recurring geological characteristics including

- silicate- and oxide-facies, metre- to decametre-thick and laterally continuous BIF units,
- metamorphic grade along the boundary at greenschist to amphibolite facies,
- a high degree of deformation, where BIF layering can be intensely folded or disaggregated proximal to major lithotectonic boundaries,
- silicification (silica flooding) in the form of diffuse to dense quartz veining,
- a mineral assemblage comprising varying amounts of pyrrhotite, pyrite, chalcopyrite, arsenopyrite, loellingite and gold, along with other common occurrences of grunerite, chlorite, biotite and hornblende.

The Fury and Hecla BIF shares many of these characteristics, including a metre- to decametre-thick and laterally continuous BIF, amphibolite-grade metamorphism, a high degree of deformation including tight folding, indications of hydrothermal fluid circulation (zones of silica flooding) and some of the typical sulphide assemblage including pyrite, pyrrhotite and chalcopyrite. Most of the BIF-hosted gold deposits in Nunavut contain significant arsenopyrite, except for Meadowbank, which has rare occurrences. Therefore, arsenopyrite is not necessarily an indicator of gold in all BIF-hosted deposits. However, pyrrhotite is a recurring mineral in each deposit and is typically abundant in gold-rich areas. Pyrrhotite in the Fury and Hecla BIF occurs both as discrete grains and as inclusions in magnetite; pyrrhotite inclusions in magnetite have also been observed in Meadowbank. Although assay results of the Fury and Hecla BIF showed no anomalous gold, more systematic sampling is required for a proper assessment of the prospectivity of this occurrence. Research by the GSC, CNGO, industry and academia on BIF-hosted gold in Nunavut continues, and may very well enter a new phase with the recent renewal of Natural Resources Canada's Targeted Geoscience Initiative and GEM-GeoNorth programs, which could provide an opportunity to look at the Fury and Hecla BIF, as well as other occurrences, more closely.

Acknowledgments

The Fury and Hecla Geoscience Project was funded by the Canadian Northern Economic Development Agency's Strategic Investments in Northern Economic Development program and through a Strategic Partnership Grant (#506660) from the Natural Sciences and Engineering Research Council of Canada. The authors thank P. Bovingdon,

M.Sc. student from Laurentian University, for taking photomicrographs for this paper; they are also grateful to A. Bigio and M. Senkow of the Mineral Resources Division of Crown-Indigenous Relations and Northern Affairs Canada for supplying some mine site photos. The authors thank P. Bovingdon, F. Dufour, W. Greenman, M. Muckpah-Gavin, M. Patzke and I. Theriault for their help in the field during the 2019 Fury and Hecla Geoscience Project. They are also grateful to S. Castonguay for his comments on an earlier version of the manuscript.

Natural Resources Canada, Lands and Minerals Sector contribution 20200594

References

- Agnico Eagle Mines Limited 2020a: Meadowbank Complex, north of Baker Lake, Kivalliq District, Nunavut Territory, Canada; Agnico Eagle Mines Limited, URL <<https://www.agnicoeagle.com/English/operations/operations/meadowbank/default.aspx>> [November 2020].
- Agnico Eagle Mines Limited 2020b: Meliadine, Rankin Inlet area, Kivalliq District, Nunavut Territory, Canada; Agnico Eagle Mines Limited, URL <<https://www.agnicoeagle.com/English/operations/operations/meliadine/default.aspx>> [November 2020].
- Bell, C.C. 2013: Structural controls on gold mineralization at the Homestake mine and their implications for the geology of the Black Hills; Ph.D. thesis, James Cook University, Townsville, Australia, 232 p.
- Berman, R.G. 2010: Metamorphic map of the western Churchill Province, Canada; Geological Survey of Canada, Open File 5279, 49 p., 3 sheets, scale 1:2 500 000.
- Berman, R.G., Davis, W.J. and Pehrsson, S. 2007: Collisional Snowbird tectonic zone resurrected: growth of Laurentia during the 1.9 Ga accretionary phase of the Hudsonian orogeny; *Geology*, v. 35, no. 10, p. 911–914, URL <<https://doi.org/10.1130/G23771A.1>>.
- Bostock, H.H. 1980: Geology of the Itchen Lake area, District of Mackenzie; Geological Survey of Canada, Memoir 391, 101 p.
- Bovingdon, P.J., Tinkham, D. and Lebeau, L.E. 2021: Mineralogy, geochemistry and field relationships in the Gifford River area, northwestern Baffin Island, Nunavut; *in* Summary of Activities 2020, Canada-Nunavut Geoscience Office, p. 19–32, URL <<https://cngo.ca/summary-of-activities/2020/>>.
- Bovingdon, P.J., Tinkham, D. and Steenkamp, H.M. 2018: Mafic-ultramafic rocks north of Fury and Hecla Strait, Baffin Island, Nunavut; *in* Summary of Activities 2018, Canada-Nunavut Geoscience Office, p. 63–74, URL <https://m.cngo.ca/wp-content/uploads/Summary_of_Activities_2018-P05-Bovingdon.pdf> [January 2021].
- Bullis, H.R., Hureau, R.A. and Penner, B.D. 1994: Distribution of gold and sulfides at Lupin, Northwest Territories; *Economic Geology*, v. 89, p. 1217–1227, URL <<https://doi.org/10.2113/gsecongeo.89.6.1217>>.
- Carpenter, R.L. and Duke, N.A. 2004: Geological setting of the West Meliadine gold deposits, western Churchill Province, Nunavut, Canada; *Exploration and Mining Geology*, v. 13, p. 49–65.

- Carpenter, R.L., Duke, N.A., Sandeman, H.S. and Stern, R. 2005: Relative and absolute timing of gold mineralization along the Meliadine Trend, Nunavut, Canada: evidence for Paleoproterozoic gold hosted in an Archean greenstone belt; *Economic Geology*, v. 100, p. 567–576, URL <<https://doi.org/10.2113/GSECONGEO.100.3.567>>.
- Cloud, P.E. 1973: Paleoeological significance of banded iron-formation; *Economic Geology*, v. 68, p. 1135–1143.
- Corrigan, D., Nadeau, L., Brouillette, P., Wodicka, N., Houlé, M.G., Tremblay, T., Machado, G. and Keating, P. 2013: Overview of the GEM multiple metals – Melville Peninsula project, central Melville Peninsula, Nunavut; *Geological Survey of Canada, Current Research 2013-19*, 21 p., URL <<https://doi.org/10.4095/292862>>.
- Corrigan, D., Scott, D.J. and St-Onge, M.R., 2001: Geology of the northern margin of the Trans-Hudson Orogen (Foxe Fold Belt), central Baffin Island, Nunavut; *Geological Survey of Canada, Current Research 2001-C23*, 17 p., URL <<https://doi.org/10.4095/212249>>.
- Crown-Indigenous Relations and Northern Affairs Canada 2019: Nunavut, Mineral Exploration, Mining and Geoscience: overview 2019; Crown-Indigenous Relations and Northern Affairs Canada, Government of Nunavut, Nunavut Tunngavik Incorporated, Canada-Nunavut Geoscience Office, 60 p., URL <https://m.cngo.ca/wp-content/uploads/Exploration_Overview_2019-English.pdf> [January 2021].
- Davies, T., Richards, J.P., Creaser, R., Heaman, L., Chacko, T., Simonetti, A., Williamson, J. and McDonald, D. 2011: Paleoproterozoic age relationships in the Three Bluffs Archean iron formation-hosted gold deposit, Committee Bay greenstone belt, Nunavut, Canada; *Exploration and Mining Geology*, v. 19, p. 55–80, URL <<https://doi.org/10.2113/gsemg.19.3-4.55>>.
- Davis, W.J., Ryan, J.J., Sandeman, H.A. and Tella, S. 2008: A Paleoproterozoic detrital zircon age for a key conglomeratic horizon within the Rankin Inlet area, Kivalliq Region, Nunavut: implications for Archean and Proterozoic evolution of the area; *Geological Survey of Canada, Current Research 2008-08*, p. 8.
- Dubé, B., Mercier-Langevin, P., Castonguay, S., McNicoll, V. J., Bleeker, W., Lawley, C.J.M., De Souza, S., Jackson, S.E., Dupuis, C., Gao, J.-F., Bécu, V., Pilote, P., Goutier, J., Beakhouse, G.P., Yergeau, D., Oswald, W., Janvier, V., Fontaine, A., Pelletier, M., Beauchamp, A.-M., et al. 2015: Precambrian lode gold deposits – a summary of TGI-4 contributions to the understanding of lode gold deposits, with an emphasis on implications for exploration; *in Targeted Geoscience Initiative 4: Contributions to the Understanding of Precambrian Lode Gold Deposits and Implications for Exploration*, B. Dubé and P. Mercier-Langevin (ed.), Geological Survey of Canada, Open File 7852, p. 1–24.
- Dufour, F., Stevenson, R. and Halverson, G.P. 2020: Timing of emplacement of mafic rocks of the Fury and Hecla Group and younger mafic intrusions, northwestern Baffin Island, Nunavut; *in Summary of Activities 2019, Canada-Nunavut Geoscience Office*, p. 27–36, URL <https://m.cngo.ca/wp-content/uploads/Summary_of_Activities_2019-Paper_03.en_.pdf> [January 2021].
- Dufour, F., Stevenson, R. and Skulski, T. 2021: Geochemical comparison of Mackenzie and Franklin igneous mafic rocks in Nunavut, Northwest Territories and northwestern Greenland; *in Summary of Activities 2020, Canada-Nunavut Geoscience Office*, p. 33–46, URL <<https://cngo.ca/summary-of-activities/2020/>>.
- Ford, R.C. 1988: Comparative geology of gold-bearing Archean iron-formation, Slave structural province, Northwest Territories; M.Sc. thesis, University of Western Ontario, London, Ontario, 137 p.
- Fury Gold Mines Limited 2020: Committee Bay; Fury Gold Mines Limited, URL <<https://furygoldmines.com/projects/committee-bay/>> [November 2020].
- Gardiner, J.J. 1986: Structural geology of the Lupin mine, Northwest Territories; M.Sc. thesis, Acadia University, Wolfville, Nova Scotia, 206 p.
- Garzon, G.G. 2010: Petrographic characterization of two gold-rich banded iron formations (BIFs) in the Foxe fold belt, Baffin Island, Canada; M.Sc. thesis, University of Arizona, Tucson, Arizona, 51 p.
- Geusebroek, P.A. and Duke, N.A. 2005: An update on the geology of the Lupin gold mine, Nunavut, Canada; *Exploration and Mining Geology*, v. 13, p. 1–13, URL <<https://doi.org/10.2113/gsemg.13.1-4.1>>.
- Goldfarb, R.J., Frowes, D.I., Bierlein, F.P., Dubé, B. and Vielreicher, R. 2004: Orogenic gold deposits – where are the giants formed?; SEG 2004: Predictive mineral discovery under cover, September 27–October 1, 2004, Perth, Australia, University of Western Australia, Geology Department and Extension Service, Publication no. 33, extended abstracts, p. 41–44.
- Greenman, J.W., Patzke, M., Halverson, G.P. and Ielpi, A. 2018: Refinement of the stratigraphy of the late Mesoproterozoic Fury and Hecla Basin, Baffin Island, Nunavut, with a specific focus on the Agu Bay and Autridge formations; *in Summary of Activities 2018, Canada-Nunavut Geoscience Office*, p. 85–96, URL <https://m.cngo.ca/wp-content/uploads/Summary_of_Activities_2018-P08-Greenman.pdf> [January 2021].
- Greenman, J.W., Patzke, M., Halverson, G.P. and Ielpi, A. 2020: Updated stratigraphy of the Fury and Hecla Group of Melville Peninsula and northwestern Baffin Island, Nunavut; *in Summary of Activities 2019, Canada-Nunavut Geoscience Office*, p. 37–50, URL <https://m.cngo.ca/wp-content/uploads/Summary_of_Activities_2019-Paper_04.en_.pdf> [January 2021].
- Harron, G.A. 2012: NI 43-101 technical report on the Lupin mine property Kitikmeot Region, Nunavut; NI 43-101 technical report prepared for Elgin Mining Inc.
- Henderson, J.B. 1970: Stratigraphy of the Archean Yellowknife Supergroup, Yellowknife Bay–Prosperous Lake area, District of Mackenzie; *Geological Survey of Canada, Paper 70-26*, 12 p., URL <<https://doi.org/10.4095/100647>>.
- Henderson, J.R. and Henderson, M.N. 1994: Geology of the Dewar Lakes area, central Baffin Island, District of Franklin, N.W.T. (parts of 27B and 37A); *Geological Survey of Canada, Open File 2924*, scale 1:100 000, URL <<https://doi.org/10.4095/194767>>.
- Henderson, J.R. and Parrish, R.R. 1992: Geochronology and structural geology of the Early Proterozoic Foxe-Rinkian orogen, Baffin Island, N.W.T.; *Geological Survey of Canada, Current Activities Forum, Program with Abstracts*, p. 12.
- Hoffman, P.F. 1988: United plates of America, the birth of a craton: early Proterozoic assembly and growth of Laurentia; *Annual Review of Earth and Planetary Sciences*, v. 16, p. 543–

- 603, URL <<https://doi.org/10.1146/annurev.ea.16.050-188.002551>>.
- Hoffman, P. and Hall, L. 1993: Geology, Slave Craton and environs, District of Mackenzie, Northwest Territories; Geological Survey of Canada, Open File 2559, 1 sheet; 1 CD-ROM, scale 1:1 000 000, URL <<https://doi.org/10.4095/183951>>.
- James, H.L. 1954: Sedimentary facies of iron-formation; *Economic Geology*, v. 49, p. 235–293.
- Janvier, V., Castonguay, S., Mercier-Langevin, P., Dubé, B., Malo, M., McNicoll, V.J., Creaser, R.A., de Chavigny, B. and Pehrsson, S.J. 2015: Geology of the banded iron formation-hosted Meadowbank gold deposit, Churchill Province, Nunavut; *in* Targeted Geoscience Initiative 4: Contributions to the Understanding of Precambrian Lode Gold Deposits and Implications for Exploration, B. Dubé and P. Mercier-Langevin (ed.); Geological Survey of Canada, Open File 7852, p. 255–269, URL <<https://doi.org/10.4095/296646>>.
- Jefferson, C.W., White, J.C., Young, G.M., Patterson, J., Tschirhart, V., Pehrsson, S.J., Calhoun, L., Rainbird, R.H., Peterson, T.D., Davis, W.J., Tella, S., Chorlton, L.B., Scott, J.M.J., Percival, J.A., Morris, W.A., Keating, P., Anand, A., Shelat, Y. and MacIsaac, D. 2015: Outcrop and remote predictive geology of the Amer Belt and basement beside and beneath the northeast Thelon Basin, in parts of NTS 66-A, B, C, F, G and H, Kivalliq Region, Nunavut; Geological Survey of Canada, Open File 7242, 1 sheet, 2 maps, scale 1:133 333 and 1:50 000, URL <<https://doi.org/10.4095/296825>>.
- Kerswill, J.A. 1992: Gold metallogeny of the Contwoyto Lake, Russell Lake and Courageous Lake areas, Slave Province, NWT; *in* Project Summaries, Canada-Northwest Territories Subsidiary Agreement 1987–1991, D.G. Richardson and M. Irving (ed.), Geological Survey of Canada, Open File 2484, p. 161–167, URL <<https://doi.org/10.4095/133346>>.
- Lauzon, M.-C., Mercier-Langevin, P., Valette, M., Beaudoin, G., De Souza, S., Côté-Mantha, O. and Simard, M. 2020: Ore mineralogy and mineral chemistry of the Whale Tail zone, Amaruq gold deposit, Nunavut; *in* Targeted Geoscience Initiative 5: Contributions to the Understanding of Canadian Gold Systems, P. Mercier-Langevin, C.J.M. Lawley and S. Castonguay (ed.), Geological Survey of Canada, Open File 8712, p. 267–279, URL <<https://doi.org/10.4095/326044>>.
- Lawley, C.J.M., Creaser, R., Jackson, S., Yang, Z., Davis, B., Pehrsson, S., Dubé, B., Mercier-Langevin, P. and Vaillancourt, D. 2015a: Unravelling the Western Churchill Province Paleoproterozoic gold metallotect: constraints from Re-Os arsenopyrite and U–Pb xenotime geochronology and LA-ICP-MS arsenopyrite geochemistry at the BIF-hosted Meliadine gold district, Nunavut, Canada; *Economic Geology*, v. 110, p. 1425–1454, URL <<https://doi.org/10.2113/econgeo.110.6.1425>>.
- Lawley, C.J.M., Dubé, B., Mercier-Langevin, P., Kjarsgaard, B., Knight, R. and Vaillancourt, D. 2015b: Defining and mapping hydrothermal footprints at the BIF-hosted Meliadine gold district, Nunavut, Canada; *Journal of Geochemical Exploration*, v. 155, p. 33–55, URL <<https://doi.org/10.1016/j.jexplo.2015.04.001>>.
- Lawley, C.J.M., McNicoll, V., Sandeman, H., Pehrsson, S., Simard, M., Castonguay, S., Mercier-Langevin, P. and Dubé, B. 2016: Age and geological setting of the Rankin Inlet greenstone belt and its relationship to the gold endowment of the Meliadine gold district, Nunavut, Canada; *Precambrian Research*, v. 275, p. 471–495, URL <<https://doi.org/10.1016/j.precamres.2016.01.008>>.
- Lebeau, L.E. 2019a: Geophysics, airborne geophysical survey of the Jungersen River area, Baffin Island, Nunavut, NTS 47G (southeast); Canada-Nunavut Geoscience Office, Open File Map 2019-03, 2 sheets, scale 1:100 000, URL <<https://cngo.ca/cngo-ofm/2019-03/>> [January 2021].
- Lebeau, L.E. 2019b: Geophysics, airborne geophysical survey of the Jungersen River area, Baffin Island, Nunavut, NTS 47H (northwest); Canada-Nunavut Geoscience Office, Open File Map 2019-04, 2 sheets, scale 1:100 000, URL <<https://cngo.ca/cngo-ofm/2019-04/>> [January 2021].
- Lebeau, L.E. 2019c: Geophysics, airborne geophysical survey of the Jungersen River area, Baffin Island, Nunavut, NTS 47H (southwest); Canada-Nunavut Geoscience Office, Open File Map 2019-05, 2 sheets, scale 1:100 000, URL <<https://cngo.ca/cngo-ofm/2019-05/>> [January 2021].
- Lebeau, L.E. 2019d: Geophysics, airborne geophysical survey of the Jungersen River area, Baffin Island, Nunavut, NTS 47E (northwest); Canada-Nunavut Geoscience Office, Open File Map 2019-06, 2 sheets, scale 1:100 000, URL <<https://cngo.ca/cngo-ofm/2019-06/>> [January 2021].
- Lebeau, L.E. 2019e: Geophysics, airborne geophysical survey of the Jungersen River area, Baffin Island, Nunavut, NTS 47H (southeast); Canada-Nunavut Geoscience Office, Open File Map 2019-07, 2 sheets, scale 1:100 000, URL <<https://cngo.ca/cngo-ofm/2019-07/>> [January 2021].
- Lebeau, L.E. 2019f: Geophysics, airborne geophysical survey of the Jungersen River area, Baffin Island, Nunavut, NTS 47E (northeast); Canada-Nunavut Geoscience Office, Open File Map 2019-08, 2 sheets, scale 1:100 000, URL <<https://cngo.ca/cngo-ofm/2019-08/>> [January 2021].
- Lebeau, L.E. 2019g: Geophysics, airborne geophysical survey of the Jungersen River area, Baffin Island, Nunavut, NTS 47G (northeast); Canada-Nunavut Geoscience Office, Open File Map 2019-02, 2 sheets, scale 1:100 000, URL <<https://cngo.ca/cngo-ofm/2019-02/>> [January 2021].
- Lebeau, L.E., Russer, M., Theriault, I., Bovingdon, P.J., Dufour, F., Greenman, J.W. and Patzke, M. 2020: Regional Precambrian bedrock mapping of the Jungersen River area, north-western Baffin Island, Nunavut; *in* Summary of Activities 2019, Canada-Nunavut Geoscience Office, p. 11–26, URL <https://m.cngo.ca/wp-content/uploads/Summary_of_Activities_2019-Paper_02.en_.pdf> [January 2021].
- Lhotka, P.G. 1988: Geology and geochemistry of goldbearing iron-formation in the Contwoyto Lake region, Northwest Territories, Canada; Ph.D. thesis, University of Alberta, Edmonton, Alberta, 223 p., URL <<https://doi.org/10.7939/R3MK65F2F>>.
- MacHattie, T. 2002: Physical volcanology of komatiite in the Laughland and Walker Lake areas, Committee Bay belt, Nunavut; Geological Survey of Canada, Current Research 2002-C14, p. 1–9. URL <<https://doi.org/10.4095/213191>>.
- MacHattie, T.G. 2008: Geochemistry and geochronology of the late Archean Prince Albert group (PAG), Nunavut, Canada; Ph.D. thesis, University of Alberta, Edmonton, Alberta, 340 p.
- Mercier-Langevin, P., Valette, M., De Souza, S., Creaser, R.A., McNicoll, V.J., Grondin-LeBlanc, P., St.Pierre, B., Lauzon, M.-C., Malo, M., Côté-Mantha, O. and Simard, M. 2018: Lithologic controls on Paleoproterozoic BIF-hosted/associated gold: overview of Re-Os geochronology and Pb isotopes preliminary results; *in* Targeted Geoscience Initiative:

- 2017 Report of Activities, Volume 1, N. Rogers (ed.), Geological Survey of Canada, Open File 8358, p. 147–152, URL <<https://doi.org/10.4095/306466>>.
- Morelli, R.M., Bell, C.C., Creaser, R.A. and Simonetti, A. 2010: Constraints on the genesis of gold mineralization at the Homestake gold deposit, Black Hills, South Dakota from rhenium–osmium sulfide geochronology; *Mineralium Deposits*, v. 45, p. 461–480, URL <<https://doi.org/10.1007/s00126-010-0284-9>>.
- Padgham, W.A. and Atkinson, D., ed. 1991: Mineral deposits of the Slave Province, Northwest Territories; 8th Iagod Symposium, Field Trip 13, August 12–18, 1990, Ottawa, Ontario, Geological Survey of Canada, Open File 2168, 136 p., URL <<https://doi.org/10.4095/132310>>.
- Patzke, M., Greenman, J.W., Ielpi, A. and Halverson, G.P. 2018: Sedimentology of the sandstone-dominated units in the Fury and Hecla Basin, northern Baffin Island, Nunavut; *in* Summary of Activities 2018, Canada-Nunavut Geoscience Office, p. 75–84, URL <https://m.cngo.ca/wp-content/uploads/Summary_of_Activities_2018-P07-Patzke.pdf> [January 2021].
- Pehrsson, S.J., Berman, R.G., and Davis, W.J. 2013: Paleoproterozoic orogenesis during Nuna aggregation: a case study of reworking of the Rae craton, Woodburn Lake, Nunavut; *Precambrian Research*, v. 232, p. 167–188, URL <<https://doi.org/10.1016/j.precamres.2013.02.010>>.
- Pehrsson, S.J., Coyle, M. and Berman, R. 2014: The GEM Chesterfield gold project: understanding controls on western Churchill gold endowment from the bottom up; Geological Survey of Canada, Open File 7490, 31 p., URL <<https://doi.org/10.4095/293763>>.
- Phillips, G.N. and Powell R. 2010: Formation of gold deposits: a metamorphic devolatilization model; *Journal of Metamorphic Geology*, v. 28, p. 689–718, URL <<https://doi.org/10.1111/j.1525-1314.2010.00887.x>>.
- Sabina Gold and Silver Corporation 2020: Projects/ Back River gold project; Sabina Gold and Silver Corporation, URL <<https://www.sabinagoldsilver.com/projects/nunavut/back-river-gold>> [November 2020].
- Sanborn-Barrie, M., Davis, W.J., Berman, R.G., Rayner, N., Skulski, T. and Sandeman, H. 2014: Neoproterozoic continental crust formation and Paleoproterozoic deformation of the central Rae craton, Committee Bay belt, Nunavut; *Canadian Journal of Earth Sciences*, v. 51, no. 6, p. 635–667, URL <<https://doi.org/10.1139/cjes-2014-0010>>.
- Sherlock, R., Pehrsson, S., Logan, A.V., Hrabi, R.B. and Davis, W.J. 2004: Geological setting of the Meadowbank gold deposits, Woodburn Lake Group, Nunavut; *Exploration and Mining Geology*, v. 13, p. 67–107, URL <<https://doi.org/10.2113/gsemg.13.1-4.67>>.
- Sherlock, R., Shannon, A., Hebel, M., Lindsay, D., Madsen, J.K., Sandeman, H., Hrabi, B., Mortensen, J., Tosdal, R. and Friedman, R.M. 2012: Volcanic stratigraphy, geochronology, and gold deposits of the Archean Hope Bay greenstone belt, Nunavut, Canada; *Economic Geology*, v. 107, p. 991–1042, URL <<https://doi.org/10.2113/econgeo.107.5.991>>.
- Skulski, T., Sandeman, H., Sanborn-Barrie, M., MacHattie, T., Young, M., Carson, C., Berman, R., Brown, J., Panagapko, D., Byrne, D. and Deyell, C. 2003: Bedrock geology of the Ellice Hills map area and new constraints on the regional geology of the Committee Bay area, Nunavut; Geological Survey of Canada, Current Research 2003-C22, 11 p.
- Stacey, J.R. and Pattison, D.R. 2003: Stratigraphy, structure, and petrology of a representative klippe of the Bravo Lake Formation, Piling Group, central Baffin Island, Nunavut; Geological Survey of Canada, Current Research 2003-C13, 11 p., URL <<https://doi.org/10.4095/214195>>.
- Steenkamp, H.M. 2018a: Geophysics, airborne geophysical survey of the Gifford River area, Baffin Island, Nunavut, NTS 47F (northwest); Canada-Nunavut Geoscience Office, Open File Map 2018-01 (2nd edition), 2 sheets, scale 1:100 000, URL <<https://cngo.ca/cngo-ofm/2018-01-v2/>> [January 2021].
- Steenkamp, H.M. 2018b: Geophysics, airborne geophysical survey of the Gifford River area, Baffin Island, Nunavut, NTS 47F (southwest); Canada-Nunavut Geoscience Office, Open File Map 2018-02 (2nd edition), 2 sheets, scale 1:100 000, URL <<https://cngo.ca/cngo-ofm/2018-02-v2/>> [January 2021].
- Steenkamp, H.M. 2018c: Geophysics, airborne geophysical survey of the Gifford River area, Baffin Island, Nunavut, NTS 47F (northeast); Canada-Nunavut Geoscience Office, Open File Map 2018-03, 10 sheets, scale 1:100 000, URL <<https://cngo.ca/cngo-ofm/2018-03>> [January 2021].
- Steenkamp, H.M. 2018d: Geophysics, airborne geophysical survey of the Gifford River area, Baffin Island, Nunavut, NTS 47F (southeast) and 47C (part); Canada-Nunavut Geoscience Office, Open File Map 2018-04 (2nd edition), 10 sheets, scale 1:100 000, URL <<https://cngo.ca/cngo-ofm/2018-04-v2/>> [January 2021].
- Steenkamp, H.M. 2018e: Geophysics, airborne geophysical survey of the Gifford River area, Baffin Island, Nunavut, NTS 47E (southwest); Canada-Nunavut Geoscience Office, Open File Map 2018-05, 10 sheets, scale 1:100 000, URL <<https://cngo.ca/cngo-ofm/2018-05/>> [January 2021].
- Steenkamp, H.M. 2018f: Geophysics, airborne geophysical survey of the Gifford River area, Baffin Island, Nunavut, NTS 47D (northwest); Canada-Nunavut Geoscience Office, Open File Map 2018-06, 10 sheets, scale 1:100 000, URL <<https://cngo.ca/cngo-ofm/2018-06/>> [January 2021].
- Steenkamp, H.M. 2018g: Geophysics, airborne geophysical survey of the Gifford River area, Baffin Island, Nunavut, NTS 47E (southeast); Canada-Nunavut Geoscience Office, Open File Map 2018-07, 2 sheets, scale 1:100 000, URL <<https://cngo.ca/cngo-ofm/2018-07/>> [January 2021].
- Steenkamp, H.M. 2018h: Geophysics, airborne geophysical survey of the Gifford River area, Baffin Island, Nunavut, NTS 47D (northeast); Canada-Nunavut Geoscience Office, Open File Map 2018-08, 2 sheets, scale 1:100 000, URL <<https://cngo.ca/cngo-ofm/2018-08/>> [January 2021].
- Steenkamp, H.M., Bovingdon, P.J., Dufour, F., G  n  reux, C.-A., Greenman, J.W., Halverson, G.P., Ielpi, A., Patzke, M. and Tinkham, D.K. 2018: New regional mapping of Precambrian rocks north of Fury and Hecla Strait, northwestern Baffin Island, Nunavut; *in* Summary of Activities 2018, Canada-Nunavut Geoscience Office, p. 47–62, URL <https://m.cngo.ca/wp-content/uploads/Summary_of_Activities_2018-P04-Steenkamp.pdf> [January 2021].
- St. Pierre, B., Mercier-Langevin, P., Simard, M., C  t  -Mantha, O., Blais, J.-C., Servelle, G. and Malo, M. 2020: Structural controls and relative timing of gold mineralization of the banded iron formation-associated Tiriganiaq deposit, Meliadine district, Ranking Inlet greenstone belt, Nunavut; *in* Targeted Geoscience Initiative 5: Contributions to the Understanding of Canadian Gold Systems, P. Mercier-Langevin,

- C.J.M. Lawley and S. Castonguay (ed.), Geological Survey of Canada, Open File 8712, p. 237–250, URL <<https://doi.org/10.4095/326041>>.
- Tremblay, T. 2021: Geochemistry and mineralogy of glacial sediments and geomorphology of the Jungersen River area, northwestern Baffin Island, Nunavut; *in* Summary of Activities 2020, Canada-Nunavut Geoscience Office, p. 47–62, URL <<https://m.cngo.ca/summary-of-activities/2020/>>.
- Tremblay, T. and Godbout, P.M. 2018: Surficial geology of the north coast of Fury and Hecla Strait, northwestern Baffin Island, Nunavut; *in* Summary of Activities 2018, Canada-Nunavut Geoscience Office, p. 107–120, URL <https://m.cngo.ca/wp-content/uploads/Summary_of_Activities_2018-P10-Tremblay.pdf> [January 2021].
- Tremblay, T., Sasseville, C. and Godbout, P.M. 2020: Geochemistry and mineralogy of glacial sediments, north of Fury and Hecla Strait, northwestern Baffin Island, Nunavut; *in* Summary of Activities 2019, Canada-Nunavut Geoscience Office, p. 51–64, URL <https://m.cngo.ca/wp-content/uploads/Summary_of_Activities_2019-Paper_05.en_.pdf> [January 2021].
- Valette, M., De Souza, S., Mercier-Langevin, P., Côté-Mantha, O., Simard, M., Wodicka, N., McNicoll, V.J. and Barbe, P. 2020: Lithological and tectonic controls on banded iron formation-associated gold at the Amaruq deposit, Churchill Province, Nunavut, and implications for exploration; *in* Targeted Geoscience Initiative 5: Contributions to the Understanding of Canadian Gold Systems, P. Mercier-Langevin, C.J.M. Lawley and S. Castonguay (ed.), Geological Survey of Canada, Open File 8712, p. 251–266, URL <<https://doi.org/10.4095/326042>>.
- Valette, M., De Souza, S., Mercier-Langevin, P., McNicoll, V.J., Grondin-LeBlanc, P., Côté-Mantha, O., Simard, M. and Malo, M. 2018: Lithological, hydrothermal, structural and metamorphic controls on the style, geometry and distribution of the auriferous zones at Amaruq, Churchill Province, Nunavut; *in* Targeted Geoscience Initiative: 2017 Report of Activities, Volume 1, N. Rogers (ed.), Geological Survey of Canada, Open File 8358, p. 153–156, URL <<https://doi.org/10.4095/306467>>.
- ValOre Metals Corporation 2020: Baffin Gold; ValOre Metals Corporation, URL <<http://valoremets.com/assets/baffin-gold/>> [November 2020].
- Villeneuve, M.E., Lambert, M.B., van Breemen, O. and Mortensen, J. 2001: Geochronology of the Back River volcanic complex, Nunavut-Northwest Territories; *in* Radiogenic Age and Isotopic Studies, Report 14, Geological Survey of Canada, Current Research 2001-F2, 8 p.
- Wheeler, J.O., Hoffman, P.F., Card, K.D., Davidson, A., Sanford, B.V., Okulitch, A.V. and Roest, W.R. 1996: Geological map of Canada; Geological Survey of Canada, Map 1860A, scale 1:5 000 000, 3 sheets, 1 CD-ROM, URL <<https://doi.org/10.4095/208175>>.
- Wodicka, N., Corrigan, D., Nadeau, L. and Erdmann, S. 2011: New U-Pb geochronological results from Melville Peninsula: unravelling the Archean and early Paleoproterozoic magmatic history of the north-central Rae craton; Geological Association of Canada–Mineralogical Association of Canada–Society of Economic Geologists–Society for Geology Applied to Mineral Deposits, Joint Annual Meeting (Ottawa 2011), May 25–27, 2011, Ottawa, Ontario, Program with Abstracts, v. 34, p. 236.
- Wodicka, N., St-Onge, M., Scott, D. and Corrigan, D. 2002: Preliminary report on the U-Pb geochronology of the northern margin of the Trans-Hudson orogen, central Baffin Island; *in* Radiogenic Age and Isotopic Studies, Report 15, Geological Survey of Canada, Current Research 2002-F7, 12 p., URL <<https://doi.org/10.4095/213623>>.
- Zhang, S. 2018: Ordovician stratigraphy on the unnamed peninsula (southwestern NTS area 37F and northwestern NTS area 37C) northeast of Fury and Hecla Strait on northern Baffin Island, Nunavut; *in* Summary of Activities 2018, Canada-Nunavut Geoscience Office, p. 97–106, URL <https://m.cngo.ca/wp-content/uploads/Summary_of_Activities_2018-P09-Zhang.pdf> [January 2021].



Mineralogy, geochemistry and field relationships in the Gifford River area, northwestern Baffin Island, Nunavut

P.J. Bovingdon¹, D. Tinkham² and L.E. Lebeau³

¹Harquail School of Earth Science, Laurentian University, Sudbury, Ontario, pbovingdon@laurentian.ca

²Harquail School of Earth Science, Laurentian University, Sudbury, Ontario

³Canada-Nunavut Geoscience Office, Iqaluit, Nunavut

The Fury and Hecla Geoscience Project (FHGP) was led by the Canada-Nunavut Geoscience Office in collaboration with Crown-Indigenous Relations and Northern Affairs Canada, and researchers and students from Laurentian University, McGill University and Université du Québec à Montréal. The multiyear project involved mapping and sampling of Archean, Proterozoic and Paleozoic rocks, and Quaternary surficial deposits and features. The study area comprised all or parts of nine 1:250 000 scale NTS map areas north and south of Fury and Hecla Strait on Baffin Island and Melville Peninsula, respectively (NTS 37C, F, 47C–H and 48A).

Bovingdon, P.J., Tinkham, D. and Lebeau, L.E. 2021: Mineralogy, geochemistry and field relationships in the Gifford River area, northwestern Baffin Island, Nunavut; in Summary of Activities 2020, Canada-Nunavut Geoscience Office, p. 19–32.

Abstract

The Gifford River area, on northwestern Baffin Island, is located in the western Churchill Province (Rae craton) and consists of Archean to Paleoproterozoic crust that experienced multiple tectonothermal events. Recorded in these rocks are poorly constrained events before 2.7 Ga and subsequent regional-scale orogenic events spanning the period 2.7–1.8 Ga. Previous geological mapping initiatives in the area resulted in the production of reconnaissance-scale maps. New geological mapping during the 2018 field season aids in advancing geological knowledge of the area, resulting in a preliminary map that documents the major geological units in the study area. A representative suite of samples from the intensely deformed Precambrian basement, granitic and intermediate intrusions, and the supracrustal rocks was collected to study variation in mineral composition, deformational fabric, geochemistry and geochronology. Highlighted in this paper are new mineralogical, geochemical and field relationships that refine the lithological units of the 2018 preliminary map.

A representative suite of 16 samples from major lithological units was collected for U-Pb zircon geochronology. The geochronological data will constrain the timing of crystallization of the basement gneiss and granitoid intrusions, and the timing of deposition of metasedimentary units. Additionally, metamorphic assemblages and fabrics related to deformational events are integrated into a regional-scale analysis of the extent of tectonometamorphic overprint across the study area.

Introduction

The Gifford River study area (Figure 1) is located on northwestern Baffin Island in the northern Rae craton (Jackson and Berman, 2000; Pehrsson et al., 2013). This area was previously mapped at a reconnaissance scale during the late 1950s to early 1960s (Blackadar, 1958, 1963, 1964), and was revisited by Ciesielski and Maley (1980) to refine descriptions on the predominant gneiss, granite and Franklin dykes in the area. The majority of the area north of the Fury and Hecla Basin nonconformity is relatively unstudied. Scott and de Kemp (1998) compiled a regional bedrock map (1:500 000) of northern Baffin Island and northern Melville Peninsula, including part of the study area, using maps produced by Chandler et al. (1980) and Ciesielski and Maley (1980) of the Fury and Hecla Basin and adjacent

basement gneiss. Despite the previous mapping, large areas of the Gifford River area remain described as undifferentiated Archean gneiss.

The Canada-Nunavut Geoscience Office (CNGO) led this multiyear and multidisciplinary Fury and Hecla Geoscience Project (FHGP), which was focused on mapping both north and south of Fury and Hecla Strait. The focus during the 2018 field season was on mapping the Gifford River area. This paper aims to refine field relationships and petrographic and geochemical characteristics of the orthogneiss basement, felsic intrusions and supracrustal units (Figure 2) described in Steenkamp et al. (2018). The results presented here are part of an M.Sc. study of the first author that focuses on the magmatic and thermal history of the Fury

This publication is also available, free of charge, as colour digital files in Adobe Acrobat® PDF format from the Canada-Nunavut Geoscience Office website: <https://cngo.ca/summary-of-activities/2020/>.

and Hecla project area. Field relationships, thin-section photomicrographs and geochemical interpretations of the dominant units are presented.

Regional geology

Much of Melville Peninsula and northwestern Baffin Island lie within the 3.0–2.5 Ga northern Rae craton (Hoffman, 1988; Jackson and Berman, 2000; Corrigan et al., 2013). The northern Rae craton, in the western Churchill Province, formed part of the Paleoproterozoic supercraton Nunavutia that amalgamated ca. 2.55–2.45 Ga (Berman et al., 2013; Pehrsson et al., 2013). The northeastern extent of the northern Rae craton consists of reworked granodiorite to tonalite orthogneiss with granitoid intrusions. Metamorphic grade increases from greenschist to upper-amphibolite facies toward the northeast, closer to the Trans-Hudson Orogen (Jackson et al., 1990; Jackson and Berman, 2000).

Three Archean crust-building episodes characterize the northern Rae craton (Jackson and Berman, 2000). These three magmatic episodes span ca. 3.0–2.5 Ga and consist of 3.0–2.8 Ga felsic plutonism, 2.76–2.71 Ga felsic plutonism and paragneiss formation (Mary River Group, Prince Albert Group), and 2.62–2.58 Ga (Pehrsson et al., 2013) felsic plutonism (Jackson and Berman, 2000).

The northern Rae craton experienced four episodes of orogenesis, including the ca. 2.55–2.50 Ga MacQuoid Orogen (Jackson and Berman, 2000; Bethune and Scammel, 2003a; Berman et al., 2010), the ca. 2.50–2.30 Ga Arrowsmith Orogen (Berman et al., 2013; Pehrsson et al., 2013), the ca. 2.0–1.9 Ga Taltson-Thelon Orogen (Bostock et al., 1990) and the ca. 1.87–1.80 Ga Trans-Hudson Orogen (St-Onge et al., 2007; Corrigan et al., 2009; Berman et al., 2015).

The Melville Peninsula south of the study area is composed of Archean amphibolite- to granulite-grade orthogneiss in three distinct lithological blocks hosting greenstone belts that include voluminous basaltic to ultramafic flows and sills, chemical and clastic metasedimentary rocks, and granitic rocks (Machado et al., 2012; Corrigan et al., 2013). These blocks (from southern Melville to northern Melville) are the Repulse Bay block, Prince Albert block and Northern Granulite block. The Prince Albert block consists of upper-greenschist to middle-amphibolite facies Archean supracrustal rocks with granite and orthogneiss (Corrigan et al., 2013). This block hosts the Prince Albert greenstone belt that trends parallel to the Roche Bay greenstone belt (Corrigan et al., 2013). The Penrhyn Group lies between the Prince Albert block and the Repulse Bay block, and comprises metamorphosed, Paleoproterozoic supracrustal and sedimentary rocks. The Repulse Bay block is composed of older Archean tonalite-trondhjemite-granodiorite (TTG) gneiss, two-pyroxene charnockite, monzogranite

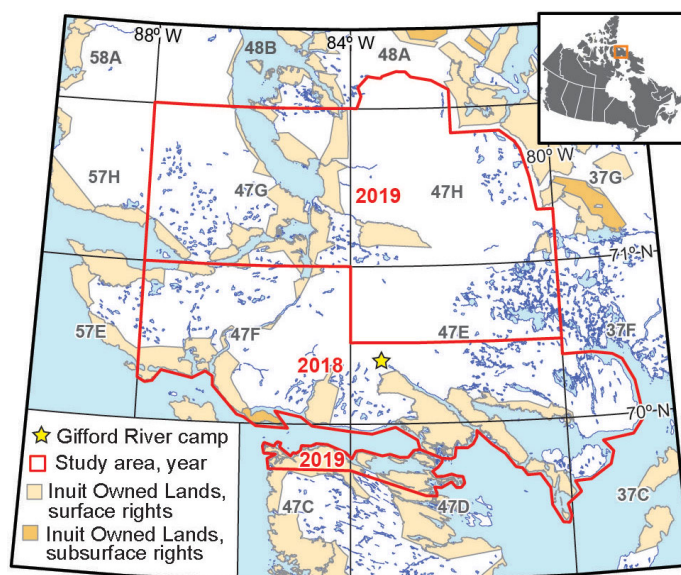


Figure 1: Location of the Fury and Hecla field areas in 2018 and 2019 on northwestern Baffin Island and northern Melville Peninsula.

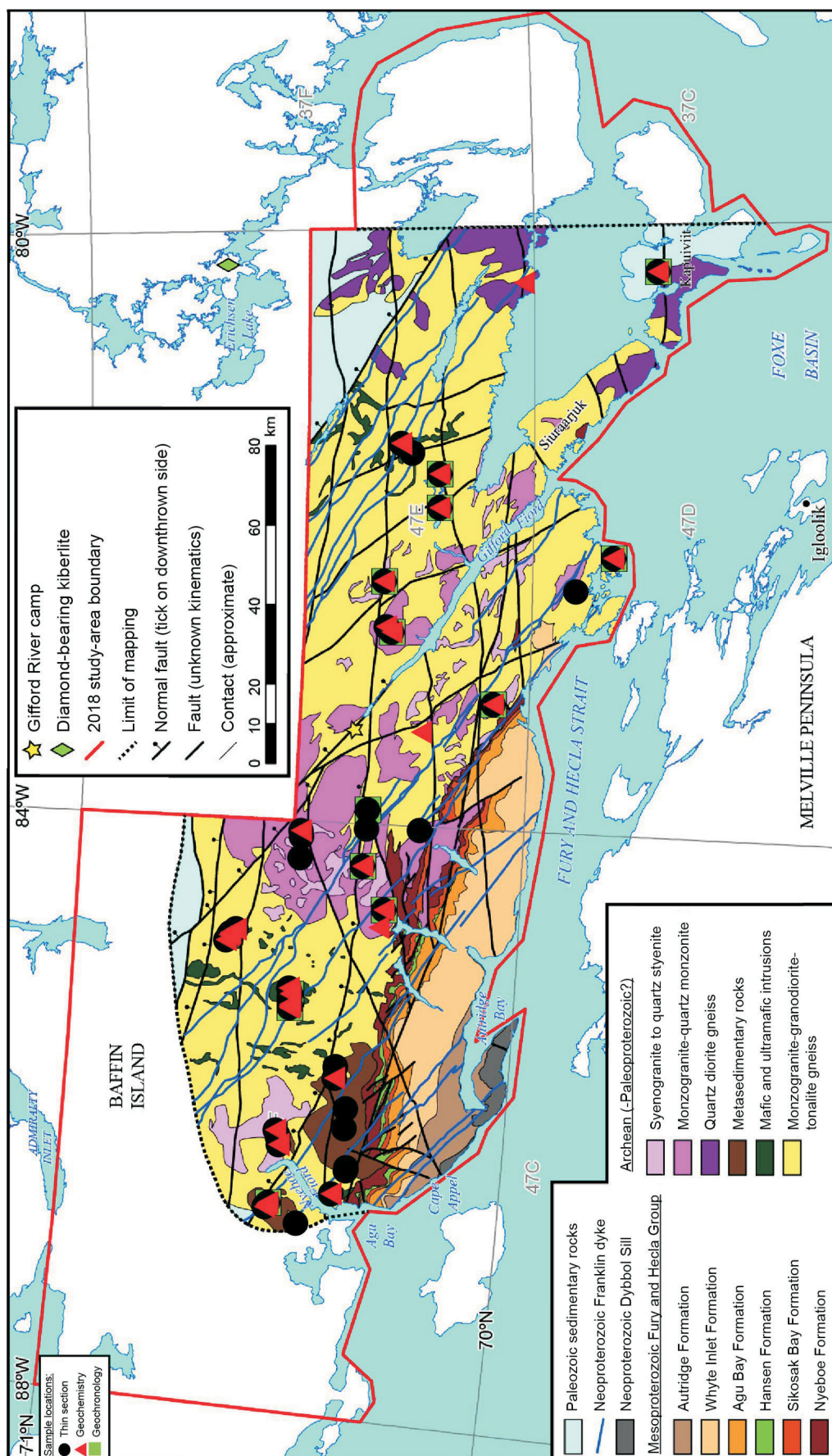
intrusions and minor supracrustal rocks (LaFlamme et al., 2014).

To the northeast of the Gifford River area, the Mary River Group is defined by laterally extensive belts of greenschist-facies mafic metavolcanic rocks associated with banded iron formation, intermediate and ultramafic volcanic rocks, and metasedimentary rocks (Bethune and Scammel, 2003b; Johns and Young, 2006). Skipton et al. (2017) described weakly deformed to massive monzogranite-granodiorite and pegmatitic syenogranite intruding the tonalite-granodiorite basement gneiss and the Mary River Group. Tonalitic gneiss from the Mary River area has been dated at $2851 \pm 20/-17$ Ma (Jackson et al., 1990), whereas preliminary ages of granodioritic gneiss associated with the Mary River area are ca. 2900 Ma (Young et al., 2004). A dacite interlayered with the Mary River iron formation constrains volcanic eruption and sediment deposition at $2718 \pm 5/-3$ Ma (Jackson et al., 1990; Skipton et al., 2019).

Neoarchean–Paleoproterozoic gneiss

Hornblende monzogranite-granodiorite-tonalite orthogneiss

The dominant rock types in the 2018 field area are hornblende-bearing monzogranitic, granodioritic and tonalitic orthogneiss that contain multiple generations of granitoid intrusions and locally contain amphibolite enclaves. These rock types are collectively referred to as the hornblende monzogranite-granodiorite-tonalite gneiss unit (Figure 2) and represent the basement hostrocks to younger intrusive units described below. Contacts between the gneissic rocks and granitoid intrusions are rarely observed in place. The sedimentary rocks of the Fury and Hecla Basin noncon-



formably overlie the gneiss in the southern portion of the study area. Samples from the gneiss were collected for mineralogical, geochemical and zircon U-Pb geochronological investigation.

The hornblende monzogranite-granodiorite-tonalite gneiss unit is variably foliated, with foliation intensity increasing to the northeast. Gneissosity ranges from strong compositional banding at the millimetre to decimetre scale (Figure 3a) to weak banding defined by elongated domains of recrystallized feldspar and quartz (Figure 3b). Biotite and locally lineated amphibole are generally preferentially aligned parallel to gneissosity. Gneissosity is defined by centimetre- to decimetre-scale banding, consisting of leucocratic bands of quartz+plagioclase+K-feldspar and melanocratic bands of amphibole+biotite+magnetite with retrograde chlorite±epidote (Figure 3c). Melanocratic bands are commonly thinner than associated leucocratic bands. Biotite and amphibole are aligned parallel to gneissosity in the melanocratic bands. Mafic enclaves are commonly observed in the basement gneiss and are surrounded by coarser grained hostrocks. These lenses are typically gabbroic in composition, with thin layers enriched in plagioclase and amphibole that define a foliation.

Petrographic observations confirm that the leucocratic bands consist of quartz+plagioclase+K-feldspar, with quartz and plagioclase more abundant than K-feldspar. The K-feldspar is commonly focused around plagioclase grains, with minor sericite replacing rims of K-feldspar and plagioclase. Rocks with a stronger gneissic fabric display fine-grained (0.1–0.3 mm) quartz crystals that are associated with plagioclase crystals in the groundmass (0.2–0.5 mm). Biotite and amphibole occur interstitially between plagioclase and quartz crystals, and have a preferred orientation parallel to gneissosity (Figure 3d). Accessory minerals include clinopyroxene in melanocratic layers. In strongly foliated samples, retrograde epidote+titanite+biotite±white mica replace hornblende (Figure 3e). Magnetite and minor amounts of pyrite and ilmenite are concentrated in melanocratic bands. Sphalerite, rutile or ilmenite are present in some retrograde assemblages.

Samples across the study area were selected for whole-rock geochemistry studies to understand the major, minor and trace-element variations in the basement rock. Rare-earth element (REE) profiles of the basement (Figure 3f) show enrichment of light rare-earth elements (LREE) and depletion in heavy rare-earth elements (HREE). Additionally, tonalitic basement samples with positive Eu anomalies potentially indicate the presence of a cumulate plagioclase phase during crystallization. The silica content of the basement gneiss is considerably higher than that of the younger intrusive rocks (Figure 4). The amounts of MgO, TiO₂ and FeO remain relatively constant in basement samples, which also helps distinguish the basement hornblende monzo-

granite-granodiorite-tonalite gneiss from the younger intrusions, which tend to have higher MgO and FeO.

Granitic to quartz dioritic intrusions

Granitoid intrusions occur as small (<7 km) or large (>10 km) plutons intruding the hornblende monzogranite-granodiorite-tonalite gneiss unit. An intermediate intrusion, ranging from quartz diorite to monzodiorite in composition, is observed along the southeastern portion of the map area (Figure 2). The most voluminous intrusive rock type is a hornblende-biotite monzogranite, located in the centre of the study area. Later syenogranite and quartz syenite intrusions crosscut the monzogranite but also occur as small plutons intruding the basement gneiss unit, indicating that the syenogranite to quartz syenite pluton suite is the youngest identified intrusive suite in the study area.

Quartz diorite gneiss

Along the coastline east of the Fury and Hecla Group (Figure 2), quartz diorite gneiss is in contact with a metagabbro, both of which are crosscut by pink monzogranite stringers (Figure 5a). The quartz diorite contact with the metagabbro is sharp. The monzogranite stringers are also crosscutting discordant to the sharp contact of the metagabbro and quartz diorite. Contacts between the quartz diorite and basement gneiss are sharp, when observed. The contact with the hornblende monzogranite-granodiorite-tonalite gneiss is sharp, when observed. The crosscutting relationship between the quartz diorite, the monzogranite stringers and the metagabbro suggests that the quartz diorite gneiss is the earliest granitic intrusion in the field area.

The quartz diorite gneiss is medium grained (2–4 mm) and has a plagioclase-dominant matrix with minor K-feldspar and quartz (Figure 5b). Hornblende and biotite bands define the foliation, with minor amounts of retrograde epidote concentrated along hornblende-biotite boundaries. The quartz diorite gneiss contains a foliation, defined by aligned hornblende and biotite. Plagioclase laths, ranging from 0.5 to 1 cm, are observed subparallel to foliation. Clinopyroxene is present as medium-grained (1–3 mm) crystals surrounding plagioclase- and hornblende-rich areas. Clinopyroxene is also observed as inclusions in amphibole grains. Magnetite and primary pyrite are concentrated in amphibole-rich rocks. The presence of clinopyroxene being replaced by amphibole is likely a product of the regional amphibolite-grade metamorphism.

Major-element geochemistry indicates that the quartz diorite gneiss has higher MnO, Fe₂O₃, CaO and MgO, and lower K₂O and Na₂O than the monzogranitic-tonalitic basement gneiss unit (Figure 4). This is compatible with the higher proportion of hornblende, pyroxene and anorthitic plagioclase in the quartz diorite gneiss. The REE signature of the quartz diorite gneiss shows depletion in HREE and

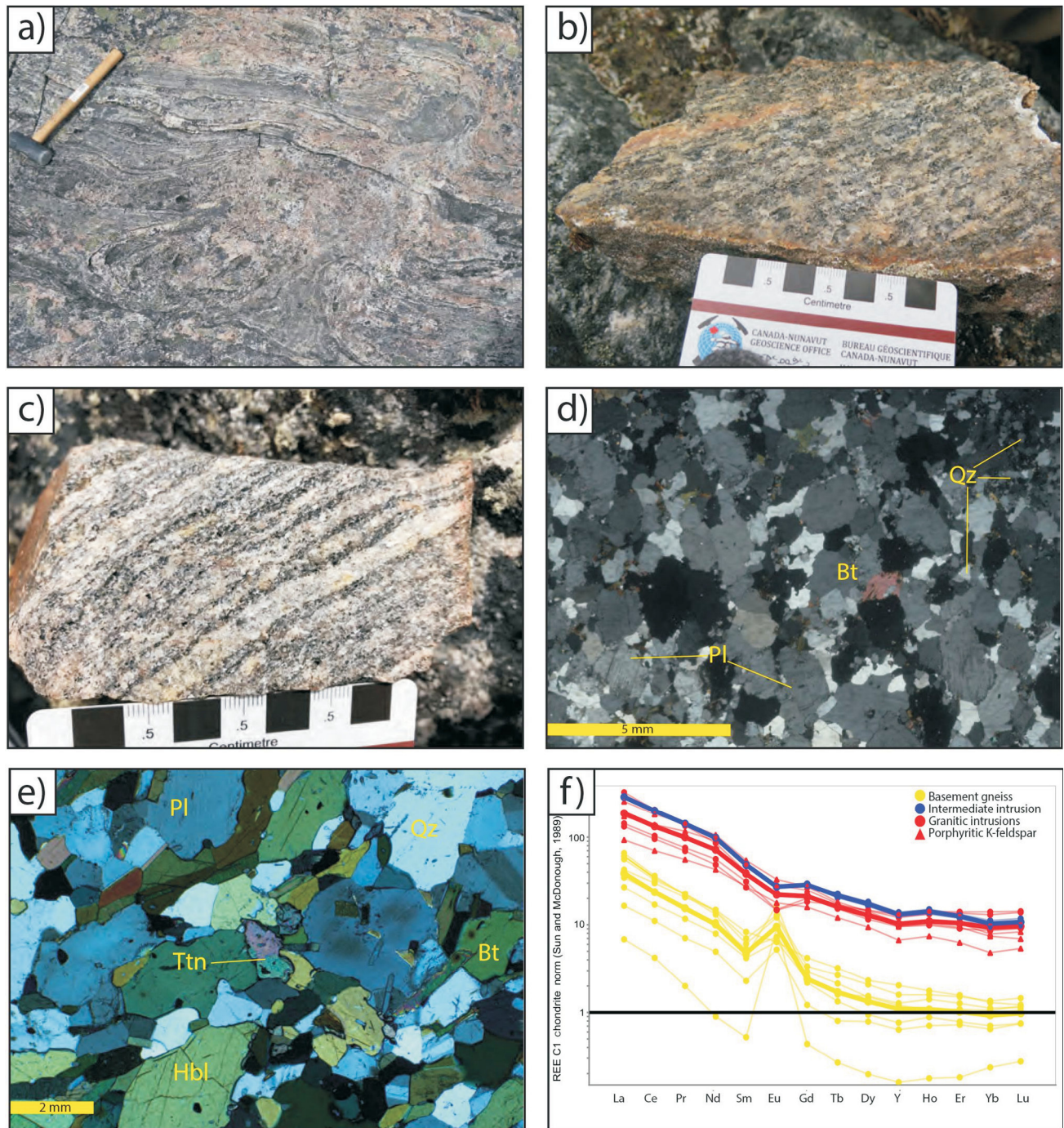


Figure 3: Photographs, thin-section photomicrographs and rare-earth element geochemistry of the hornblende monzogranite-granodiorite-tonalite gneiss: **a)** outcrop photo of intense folding of monzogranite injections in a tonalite gneiss, 30 cm hammer for scale; **b)** hand sample of strongly foliated hornblende granodiorite basement with syenogranite injections concordant with foliation; **c)** gneissic banding observed in hand sample, with melanocratic bands ranging from 3 to 5 mm and leucocratic bands ranging from 7 to 10 mm; **d)** quartz-plagioclase-rich band in tonalite gneiss with minor amounts of K-feldspar and biotite (cross-polarized light, 2.5X magnification); **e)** autometamorphic assemblage of epidote-titanite-magnetite in granodiorite gneiss, with epidote-titanite associated with hornblende (generally along foliation; cross-polarized light, 10X magnification); **f)** rare-earth-element profiles of the basement gneiss, granitic intrusions and intermediate intrusions. Mineral abbreviations: Bt, biotite; Hbl, hornblende; Pl, plagioclase; Qz, quartz; Ttn, titanite.

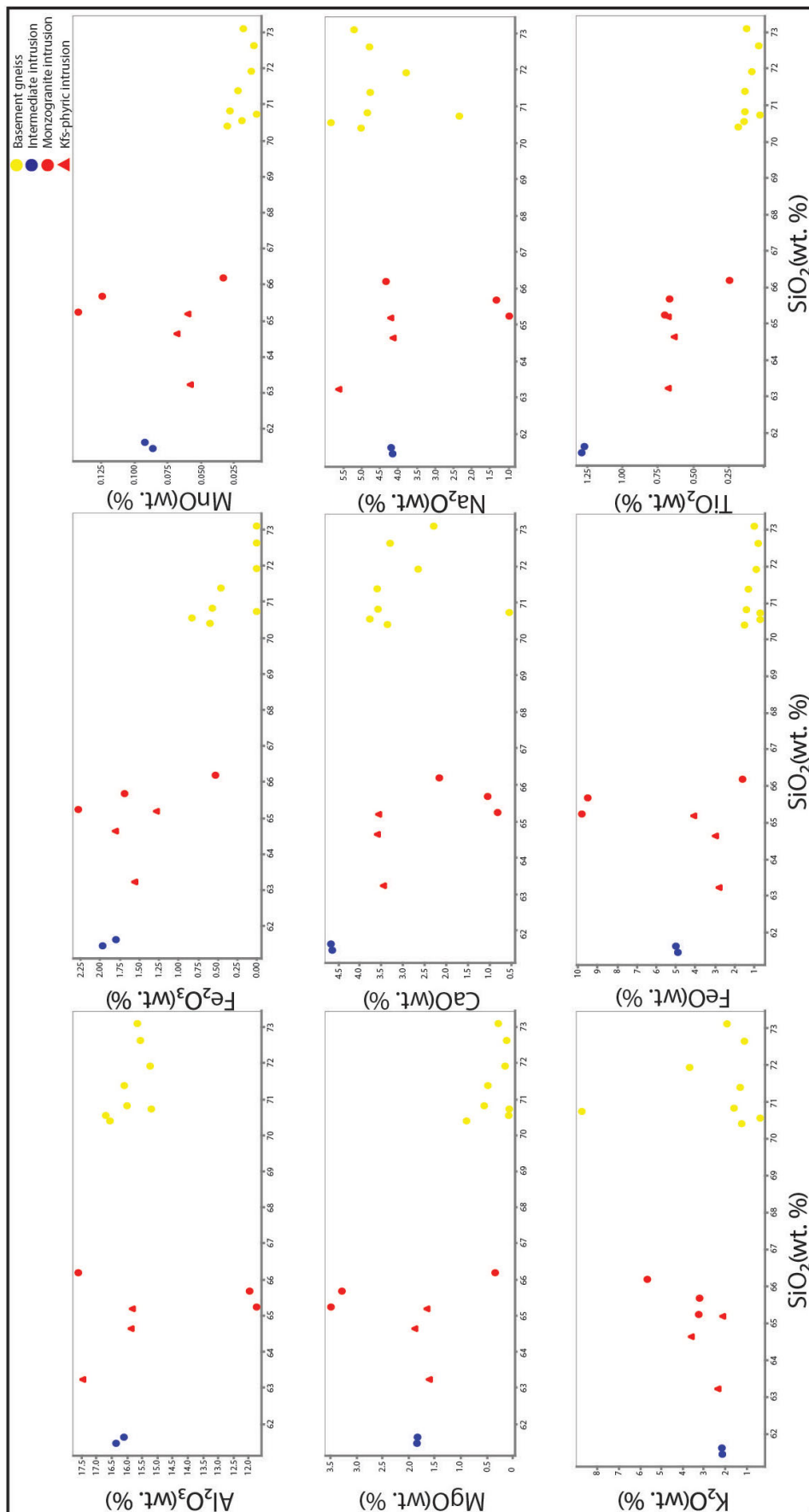


Figure 4: Major-element geochemistry of the hornblende-bearing monzogranite-granodiorite-tonalite gneiss, and intermediate and granitic intrusions.

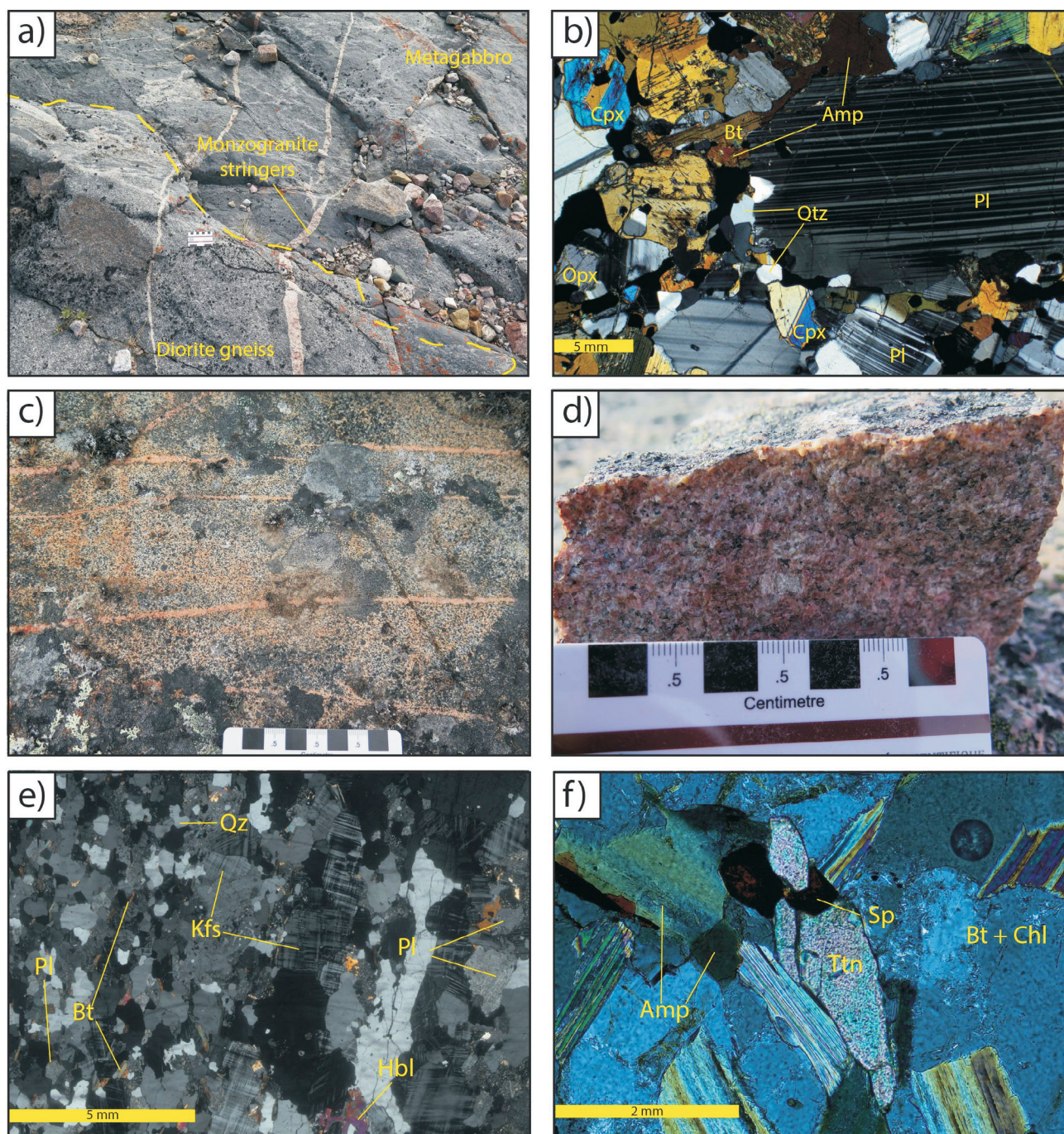


Figure 5: Representative outcrop photos and thin-section photomicrographs of intermediate and granitic intrusions: **a)** contact and cross-cutting relationships in outcrop between an older metagabbro and diorite orthogneiss, both of which are crosscut by later monzogranitic stringers; **b)** diorite gneiss with plagioclase laths (5–15 mm) aligned with biotite and amphibole foliation, and orthopyroxene and clinopyroxene with minor quartz and amphibole around plagioclase lath (cross-polarized light, 5X magnification); **c)** monzogranite outcrop located in centre of study area, crosscut by later syenogranite-monzogranite stringers; **d)** hand sample of massive monzogranite from large monzogranitic intrusion; **e)** hornblende monzogranite gneiss with K-feldspar, quartz and plagioclase in pink bands, and minor amounts of biotite and hornblende (cross-polarized light, 5X magnification); **f)** titanite-sphalerite-chlorite overprinting biotite and amphibole in foliated hornblende-biotite monzogranite (cross-polarized light, 10X magnification). Mineral abbreviations: Amp, amphibole; Bt, biotite; Chl, chlorite; Cpx, clinopyroxene; Hbl, hornblende; Kfs, K-feldspar; Opx, orthopyroxene; Pl, plagioclase; Qz, quartz; Sp, sphalerite; Ttn, titanite.

enrichment in LREE (Figure 3f). The quartz diorite gneiss REE profile is similar to those of other felsic intrusions observed, where a small negative Eu anomaly is present. This differs from what is observed in the basement, where a large positive Eu anomaly is present. On this basis, the quartz diorite gneiss is interpreted to be derived from an intrusion that is different from the protoliths that form the monzogranitic-tonalitic basement gneiss unit.

Hornblende-biotite monzogranite

A hornblende-biotite monzogranite pluton, located in the central and eastern parts of the 2018 field area, is the largest intrusion observed in the area. This intrusion produces a strong magnetic anomaly due to the high abundance of magnetite. Contacts with the basement gneiss are commonly eroded or covered by felsenmeer. The southern contact of the hornblende-biotite monzogranite is an erosional contact with the Fury and Hecla Basin. The intensity of deformation of the hornblende-biotite monzogranite intrusion increases toward the northeast, from weakly foliated to gneissic. Gneissosity increases along some of the eastern margins of the intrusion and is defined by pink bands of K-feldspar+quartz+plagioclase and melanocratic bands consisting primarily of hornblende+biotite+magnetite with retrograde chlorite. The interior of the pluton ranges from strongly foliated with abundant hornblende and biotite to massive with lesser amounts of hornblende and biotite. Massive samples tend to have little deformation and only a weak foliation defined by biotite (Figure 5c). In areas of the pluton that are strongly foliated to gneissic, thin (<3 cm) subconcordant syenogranite stringers follow the foliation defined by biotite (Figure 5d).

The intrusion mineralogy is dominated by coarse-grained K-feldspar (5 mm) and quartz with minor amounts of plagioclase. In more gneissic samples, K-feldspar crystals are coarser grained (5–7 mm) than quartz and plagioclase in leucocratic bands (Figure 5e). Feldspars have slight sericite replacement along crystal edges. Biotite and hornblende are preferentially aligned where foliation is present. Amphibole abundance is 3–15%, increasing in areas that have undergone more deformation. Massive samples have a lower abundance of biotite and hornblende than gneissic and strongly foliated samples. Samples with a higher abundance of amphibole tend to have retrograde mineral assemblages, such as chlorite+titanite±sphalerite (Figure 5f), that are commonly overprinting amphibole and biotite. Magnetite is abundant (1–2%) throughout the amphibole-rich areas.

Two foliated samples and one massive sample were selected for geochemical analysis. The foliated hornblende-biotite monzogranite samples have similar major-element patterns, whereas the massive sample has elevated Al_2O_3 and depleted MgO and FeO (Figure 4). This difference is likely due to the lack of biotite and hornblende in the massive

rocks. The REE profile of the monzogranite is similar to that of the quartz diorite gneiss (Figure 3f). Determining tectonic setting by trace-element geochemistry was first investigated by Pearce et al. (1984). Plotting the granitic intrusions (and other intrusions mentioned) using Yb+Ta vs. Rb shows a trend toward the syncollisional and volcanic-arc fields (Figure 6a). Pearce et al. (1984) stated that similar trends in granitic rock suites likely reflect a post-collisional origin.

Porphyritic K-feldspar quartz monzonite

Small (3–6 km in size) plutons of porphyritic K-feldspar quartz monzonite intrude the hornblende monzogranite-granodiorite-tonalite gneiss. These plutons produce strong magnetic anomalies, similar to the hornblende-biotite monzogranite intrusion in the centre of the map area (Figure 2). Intrusive contacts with the basement are covered by glacial till, but the general location of the contacts can be inferred by their contrasting magnetic signatures as displayed on the geophysical maps of the area, flown as part of this project (see Steenkamp et al., 2018). The K-feldspar phenocrysts range in length from 3 to 6 cm and locally have slight rotation and elongation due to dynamic recrystallization (Figure 6b). Smaller clusters of mafic minerals include biotite and hornblende. A weak mineral foliation is defined by lineated biotite aggregates and amphibole in a quartz+plagioclase+K-feldspar groundmass. Mafic dykes crosscut the intrusion but were not traced into the basement.

Potassium-feldspar phenocrysts are fractured, with sericite and epidote overprinting the K-feldspar (Figure 6c). Sericite also replaces K-feldspar along phenocryst boundaries. Smaller K-feldspar crystals (1–4 mm) within the groundmass are concentrated around plagioclase boundaries. The margins of plagioclase and the K-feldspar in the groundmass are locally altered to sericite. Quartz in the groundmass is fine grained (0.1–0.5 mm) and occurs interstitially between K-feldspar phenocrysts. Quartz is also concentrated along K-feldspar phenocryst fractures, likely as a result of recrystallization. Plagioclase in the groundmass is medium grained (2–5 mm) and generally has stronger sericite alteration than the K-feldspar. Mafic minerals comprise aligned amphibole and biotite that define a foliation. Areas rich in biotite and hornblende commonly contain the retrograde mineral association epidote+titanite+magnetite (Figure 6d). Most fine-grained quartz is likely due to later recrystallization during deformation. The epidote, titanite and magnetite association after amphibole is interpreted to reflect a period of retrograde metamorphism.

Geochemical characteristics of two samples from two separate porphyritic K-feldspar monzonite plutons are relatively similar, with one sample slightly elevated in Na_2O (Figure 4). The REE profiles of the quartz monzonite are

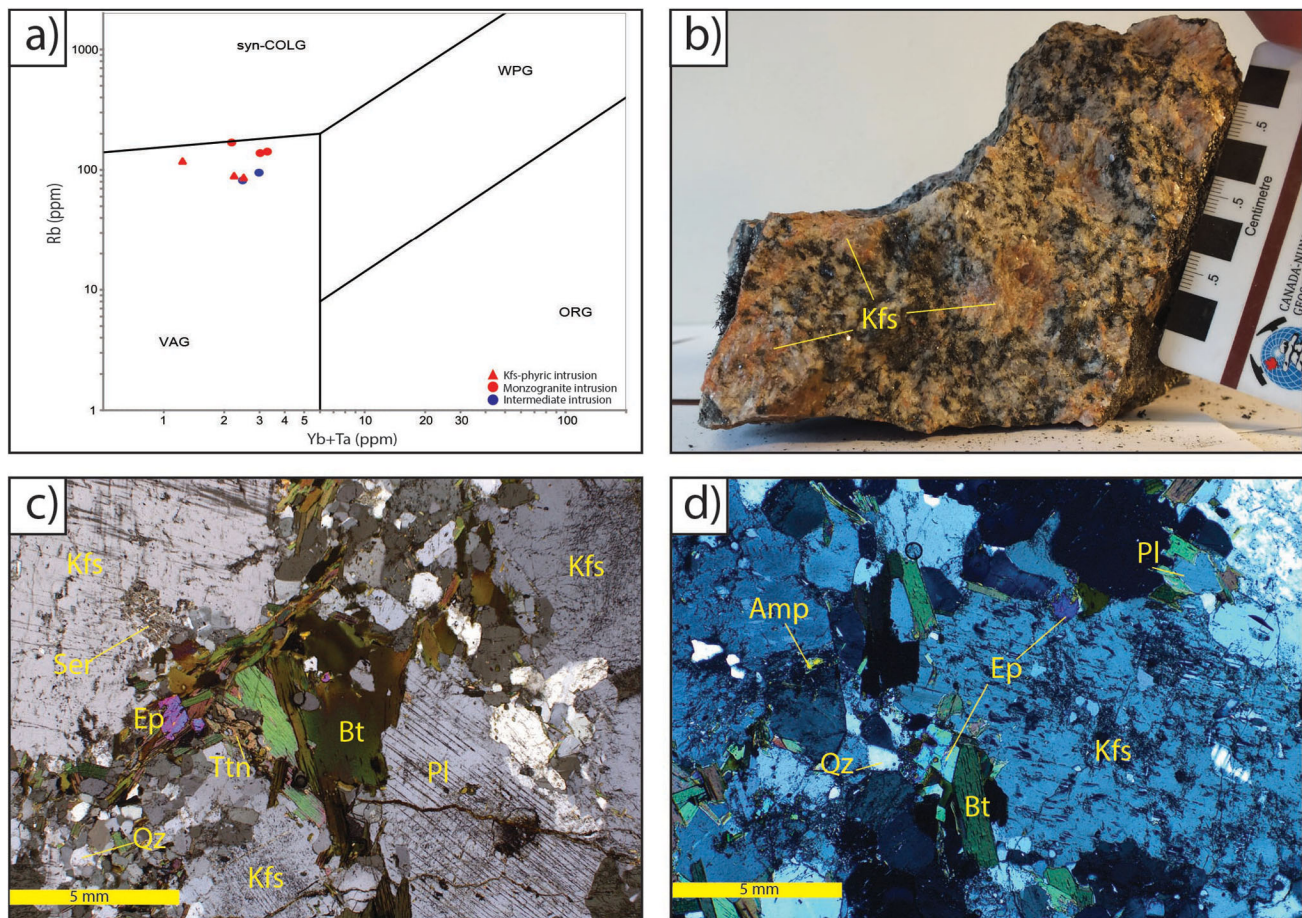


Figure 6: **a)** Representation of tectonic setting for granitic rocks using the Yb+Ta vs. Rb graph described by Pearce et al. (1984), with the intermediate and granite intrusions and basement gneiss plotting off the graph toward the origin. Abbreviations: syn-COLG, syn-collisional; WPG, within-plate granite; VAG, volcanic-arc granite; ORG, orogenic granite. **b)** Hand sample of porphyritic K-feldspar quartz monzonite with slightly deformed K-feldspar crystals ranging from 3 to 5 cm in size. **c)** thin-section photomicrograph of K-feldspar–phyric monzogranite with large, fractured K-feldspar and finer grained quartz patches (cross-polarized light, 5X magnification). **d)** thin-section photomicrograph of slightly deformed K-feldspar–phyric quartz monzonite with fractured and altered K-feldspar, and with biotite concentrated along fractures; plagioclase, quartz and amphibole surround the K-feldspar phenocryst (cross-polarized light, 5X magnification). Mineral abbreviations: Amp, amphibole; Bt, biotite; Ep, epidote; Kfs, K-feldspar; Pl, plagioclase; Qz, quartz; Ser, sericite; Ttn, titanite.

similar to those of the other intrusions but lack a minor negative Eu anomaly (Figure 3f).

Supracrustal rocks

Supracrustal rocks are concentrated in the western portion of the Gifford River study area (Figure 2). They comprise biotite psammite with layers of banded iron formation, metabasite, semipelite and metamorphosed ultramafic flows. The contact between metasedimentary rocks and the monzogranite-granodiorite-tonalite basement gneiss is covered by glacial till, but pods of psammite occur in the basement along inferred margins.

Biotite psammite and semipelite

Biotite psammite, the dominant rock type throughout the metasedimentary unit, has a quartz+biotite+K-feldspar±garnet assemblage. Locally, psammite also contains plagioclase±hornblende. Foliation is defined by biotite alignment

and locally by quartz-biotite bands. Semipelitic rocks locally occur throughout the metasedimentary unit as small pods. These rocks are medium grained and composed of quartz+biotite+plagioclase+K-feldspar+white mica, with some occurrences of garnet±sillimanite. Garnets in both psammite and semipelite are concentrated along biotite-rich layers.

Biotite abundance locally ranges up to 40% in some rocks. Microbands of biotite+garnet±chlorite and quartz are observed in thin section (Figure 7a). Biotite bands are near parallel and range from 1 to 2 mm thick. Quartz bands in the psammite paragneiss contain fine-grained quartz and range from 2 to 4 mm. Biotite crystals have many radiogenic haloes, likely from zircon or monazite inclusions. Where white mica is present, it defines the foliation along with biotite. Where garnet porphyroblasts are present, they are concentrated inside biotite bands. Retrograde chlorite is observed replacing biotite around garnet porphyroblasts.

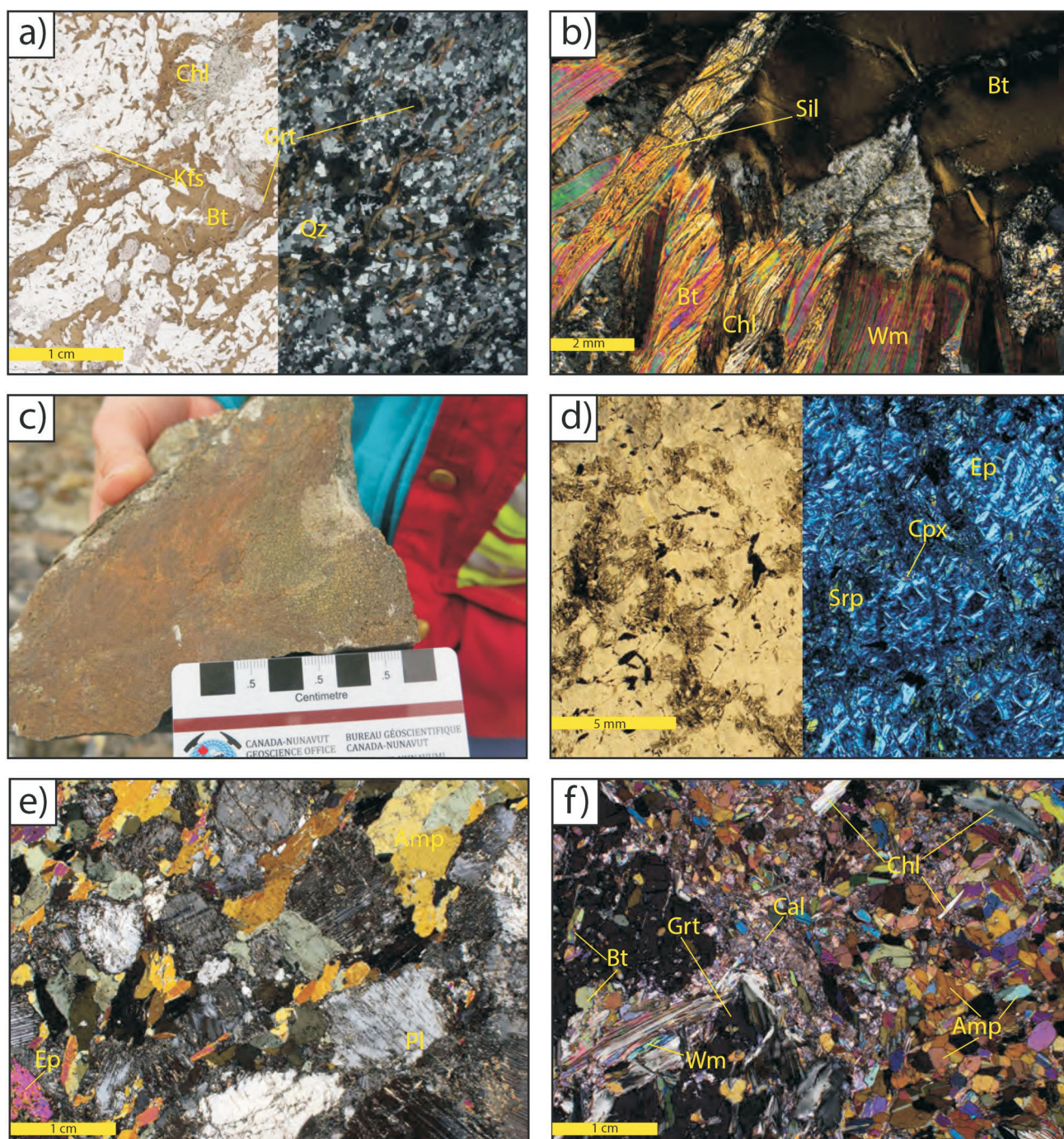


Figure 7: Photo and thin-section photomicrographs of the supracrustal package on the western edge of the Gifford River study area: **a)** biotite-rich psammite with garnet porphyroblasts concentrated in biotite foliation; layers of quartz and biotite are defined (plane-polarized and cross-polarized light); **b)** biotite reacting with white mica and sillimanite in biotite-rich psammite, with retrograde chlorite overprinting biotite (cross-polarized light, 10X magnification); **c)** hand sample of fine-grained olivine cumulate that has been hydrothermally altered to serpentine; **d)** remnant olivine-grain boundaries in altered ultramafic rock with serpentine overprint and interstitial clinopyroxene, serpentine and epidote, (plane-polarized and cross-polarized light, 5X magnification); **e)** plagioclase-rich metabasite with amphibole and rounded plagioclase grains that have slight sericitic alteration and later epidote overprinting amphibole (cross-polarized light, 5X magnification); **f)** garnet-bearing metabasalt with amphibole and clinopyroxene in groundmass and retrograde chlorite concentrated along garnet boundaries and defining foliation in groundmass (cross-polarized light, 5X magnification). Mineral abbreviations: Amp, amphibole; Bt, biotite; Cal, calcite; Chl, chlorite; Cpx, clinopyroxene; Ep, epidote; Grt, garnet; Kfs, K-feldspar; Pl, plagioclase; Qz, quartz; Sil, sillimanite; Srp, serpentine; Wm, white mica.

Semipelitic rocks contain less biotite and more white mica than the psammite. Some semipelite preserves biotite, garnet, sillimanite, quartz and white mica. Sillimanite is commonly observed forming around biotite crystals (Figure 7b), suggesting it is part of the peak assemblage. Retrograde chlorite commonly replaces biotite in both the psammitic and semipelitic rocks. Late sericite and calcite alter much of the very fine grained matrix. Psammite contains a wide range of opaque minerals, including bornite, chalcopyrite, pyrite, sphalerite and graphite, all occurring in minor amounts (<1%) in the fine-grained groundmass. Garnet porphyroblasts are likely a product of prograde metamorphism. Sulphide minerals are concentrated along fracture and foliation planes.

Metamorphosed ultramafic rocks and metabasites

Metabasite and ultramafic rocks are minor constituents within the metasedimentary package and commonly occur as semiconcordant layers that follow the foliation in the biotite psammite and semipelite. These layers range in composition from basalt to olivine websterite and some preserve primary magmatic layering. The layers are coincident with high magnetic anomalies and are typically 3–15 m thick. The metamorphosed ultramafic rocks contain coarse-grained orthopyroxene in a dark fine-grained groundmass. A hand sample of a basal layer from one of the metamorphosed ultramafic layers has a network-like texture with a dark interstitial mineral (Figure 7c). Crystal boundaries of the altered cumulate mineral(s) are surrounded by chlorite and serpentine (Figure 7d).

Metabasite rocks are rich in amphibole and can contain garnet. They are commonly proximal to banded iron formation in the supracrustal unit. Similar to the metamorphosed ultramafic rocks, layers parallel the foliation in the surrounding psammite. The metabasite ranges in composition, with variable plagioclase and garnet abundance. In garnet-free samples, subhedral and partially sericitized plagioclase is the dominant mineral. Hornblende crystals are interstitial to plagioclase crystals, likely reflecting the crystalloblastic series (Figure 7e). Metabasite containing garnet porphyroblasts (5–7 mm) typically contains less plagioclase, can be finer grained, and contains clinopyroxene, orthopyroxene, amphibole, calcite and chlorite. The fabric is defined by lineated amphibole and biotite. Calcite is interpreted as a later phase caused by alteration during retrograde metamorphism. Chlorite is also concentrated around garnet porphyroblasts and is replacing biotite (Figure 7f).

Banded iron formation

Banded iron formation (BIF) occurs both within the supracrustal unit and as pods in the basement gneiss. The BIF in the supracrustal unit occurs as linear layers that range from 5 to 10 m thick and can extend up to 500 m, and is capped by greenish white quartzite. Magnetite bands are 0.5–1 cm in

width, with magnetite crystals displaying oxidation along crystal rims. Bands of microcrystalline quartz range up to 1 cm wide and are clear to white, with minor hematite staining (Figure 8a). Quartz grains are elongated in the direction of banding (Figure 8b). In some locations, quartz bands contain ~5% very fine grained hornblende crystals (Figure 8c).

Economic considerations

Previous studies of the mafic-ultramafic rocks in the Fury and Hecla Geoscience Project area suggested the potential for Ni-Cu-PGE mineralization (Bovingdon et al., 2018). Samples were collected from large mafic bodies ranging in composition from hornblende gabbro to pyroxenite. A large layered mafic intrusion and adjacent ultramafic clinopyroxenite-hornblende intrusion contains locally abundant pyrite and minor amounts of chalcopyrite. Results of platinum-group element (ranging from 7 to 15 ppm Pt and Pd) and gold assays show low mineralization potential, but these rocks may warrant more detailed investigations (Figure 8d; Crocket, 1979).

Chandler et al. (1980) and Ciesielski and Maley (1980) targeted the hornblende-biotite monzogranite nonconformity of the Proterozoic Fury and Hecla sedimentary basin and discovered uranium values along the contact. These anomalies occur along faults and fractures that separate the basin from the Archean basement rocks. Patzke et al. (2018) investigated the basal contact with a handheld gamma-ray spectrometer, obtaining values marginally above background.

Future work

Future work consists of completing U-Pb geochronology of the Archean to Paleoproterozoic basement gneiss, granitoid intrusions and supracrustal rocks. Final refinement of the U-Pb data will allow interpretations and construction of the geological, magmatic and thermal-overprinting history. Additionally, model Hf ages will be obtained from zircon grains. These data will be used to better understand the origin and formation of the magma body that was the source of the basement and granitoid intrusions. Furthermore, Hf isotope determinations on the different populations of detrital zircons in the supracrustal U-Pb samples can reveal crustal-growth episodes.

Samples collected in 2019 in the Jungersen River study area (Lebeau et al., 2020), north of the current study area, will be petrographically and geochemically examined to improve understanding of the basement and granitoid mineralogy and geochemistry of the northern area. Specific samples that encompass aspects of the basement and the granitoid intrusions will be used for U-Pb geochronology to improve understanding of the magmatic and thermal history of the entire Fury and Hecla area.

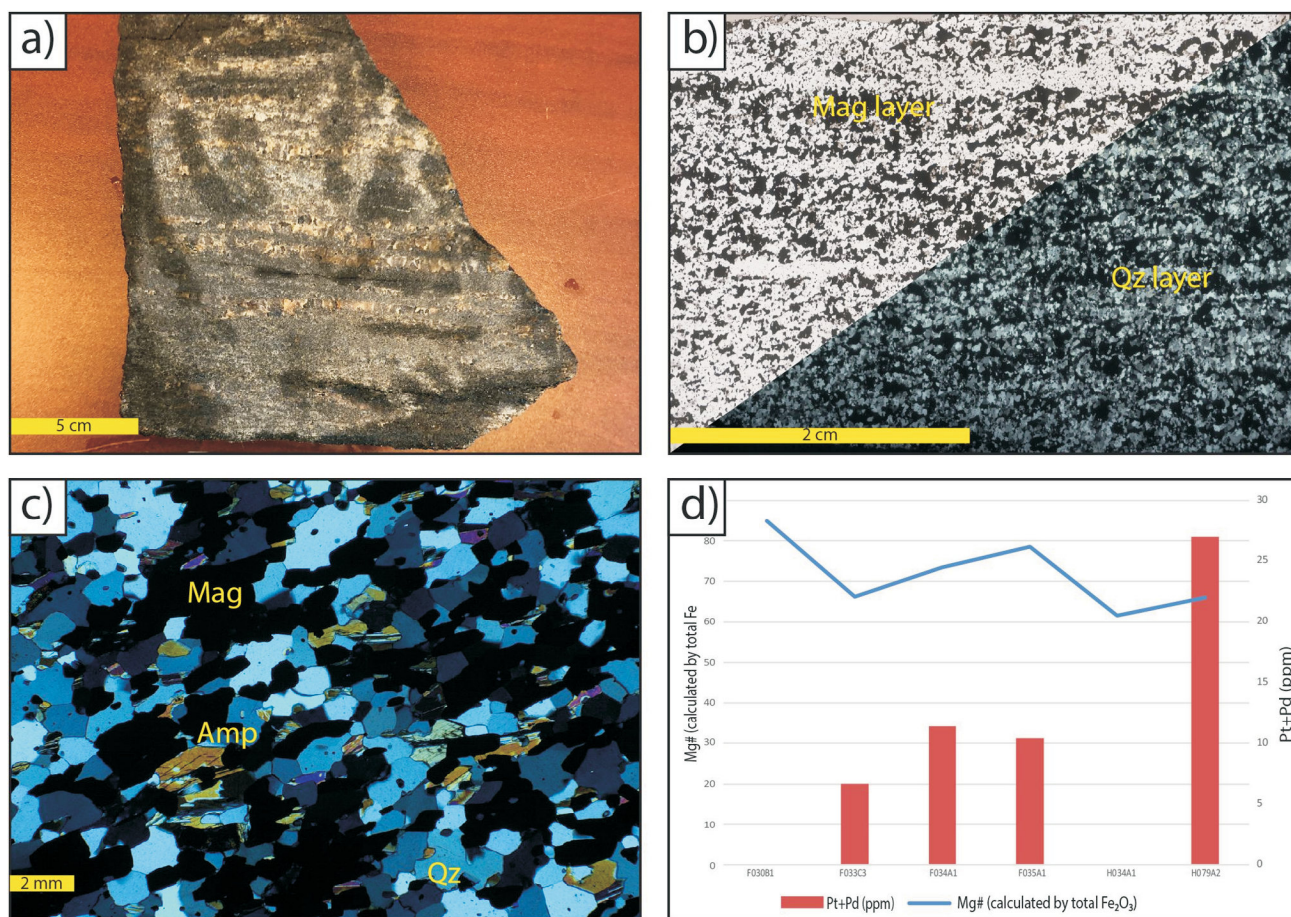


Figure 8: Representative hand sample, thin-section photomicrographs and PGE concentrations of iron formation: **a)** hand sample of banded iron formation pod in supracrustal package, displaying recrystallized quartz bands (1–3 cm) and magnetite- and hematite-rich layers (2–4 cm); **b)** banded iron formation with microscale (1 mm) bands of quartz and magnetite-hematite (plane-polarized and cross-polarized light); **c)** hornblende-bearing banded iron formation, with hornblende and biotite oriented parallel to banding of quartz and magnetite (cross-polarized light, 10X magnification); **d)** Pt-Pd geochemistry of ultramafic units studied by Bovingdon et al. (2018). Mineral abbreviations: Amp, amphibole; Mag, magnetite; Qz, quartz.

Other planned work includes gaining a better understanding of the metasedimentary-mineral assemblages to estimate the pressure-temperature conditions of metamorphism. Further petrographic studies are required to reveal mineral assemblages suitable for pressure-temperature determination. Currently, there is only one thin section containing the assemblage quartz+plagioclase+biotite+garnet+sillimanite in a semipelite and one containing the assemblage garnet+clinopyroxene+hornblende+calcite in a metabasite. These samples will be used for P-T estimates. Based on the mineral assemblages in the supracrustal rocks, the metamorphic grade is middle- to upper-amphibolite facies. This metamorphic grade is compatible with the presence of abundant metamorphic amphibole in metamorphosed banded iron formations and amphibolite lenses in the basement rocks. The metamorphic grade is comparable to adjacent areas such as Pond Inlet and Mary River (Skipiton et al., 2017) and differs from that of rocks directly south of the Fury and Hecla Group on Melville Peninsula that underwent granulite-facies metamorphism. Additionally, U-

Pb geochronology using titanite in metaplutonic rocks can be used to constrain the timing of titanite growth metamorphism if the mineral is metamorphic in origin.

Acknowledgments

The FHGP was funded by the Canadian Northern Economic Development Agency's Strategic Investments in Northern Economic Development program and through a Strategic Partnership Grant (#506660) from the Natural Sciences and Engineering Research Council of Canada. The Canada-Nunavut Geoscience Office and Natural Resources Canada's Research Affiliate Program are thanked for providing funding for research, analytical techniques and logistics for fieldwork. M. Patzke, J.W. Greenman, F. Dufour, C. Gilbert, M. Russer, I. Therriault and M. Muckpaw-Gavin are thanked for field discussions and assistance in the field. C. Gilbert's continual assistance with GIS and technical support before, during and after fieldwork is greatly appreciated. Geochemical analysis was completed by Activation Laboratories Ltd. (Actlabs) and

thin sections were prepared by Vancouver Petrographics Ltd. H. Steenkamp is thanked for continuing discussions on the project, and edits from D. Corrigan are greatly appreciated.

References

- Berman, R.G., Davis, W.J., Corrigan, D. and Nadeau, L. 2015: Insights into the tectonothermal history of Melville Peninsula, Nunavut, provided by in situ SHRIMP geochronology and thermobarometry; Geological Survey of Canada, Current Research 2015-4, 22 p.
- Berman, R.G., Pehrsson, S., Davis, W.J., Ryan, J.J., Qui, H. and Ashton, K.E. 2013: The Arrowsmith orogeny: geochronological and thermobarometric constraints on its extent and tectonic setting in the Rae craton, with implications for pre-Nuna supercontinent reconstruction; *Precambrian Research*, v. 232, p. 44–69.
- Berman, R.G., Sanborn-Barrie, M., Rayner, N., Carson, C., Sandeman, H.A. and Skulski, T. 2010: Petrological and in situ SHRIMP geochronological constraints on the tectonometamorphic evolution of the Committee Bay belt, Rae Province, Nunavut; *Precambrian Research*, v. 181, p. 1–20, URL <<https://doi.org/10.1016/j.precamres.2010.05.009>>.
- Bethune, K.M. and Scammell, R.J. 2003a: Geology, geochronology and geochemistry of Archean rocks in the Ege Bay area, north-central Baffin Island, Canada: constraints on the depositional and tectonic history of the Mary River Group of northeastern Rae Province; *Canadian Journal of Earth Sciences*, v. 40, p. 1137–1167.
- Bethune, K.M. and Scammell, R.J. 2003b: Distinguishing between Archean and Paleoproterozoic tectonism, and evolution of the Isortoq fault zone, Ege Bay area, north-central Baffin Island, Canada; *Canadian Journal of Earth Sciences*, v. 40, p. 1111–1135.
- Blackadar, R.G. 1958: Fury and Hecla Strait, District of Franklin, Northwest Territories; Geological Survey of Canada, Preliminary Series Map 3-1958, 1 map at 1:506 880 scale.
- Blackadar, R.G. 1963: Additional notes to accompany Map 3-1958 (Fury and Hecla Strait map-area) and Map 4-1958 (Foxe Basin north map-area); Geological Survey of Canada, Paper 62-35, 30 p.
- Blackadar, R.G. 1964: Operation Admiralty, northwest Baffin Island; *in* Summary of Activities: Field, 1963, Geological Survey of Canada, Paper 64-1, p. 2–3.
- Bostock, H.H., van Breemen, O. and Loveridge, W.D. 1990: Further geochronology of plutonic rocks in northern Taltson Magmatic Zone, District of Mackenzie, N.W.T.; *in* Radiogenic Age and Isotopic Studies: Report 4, Geological Survey of Canada, Paper 90-2, p. 67–78, 199.
- Bovingdon, P.J., Tinkham, D. and Steenkamp, H.M. 2018: Mafic-ultramafic rocks north of Fury and Hecla Strait, Baffin Island, Nunavut; *in* Summary of Activities 2018, Canada-Nunavut Geoscience Office, p. 63–74, URL <https://m.cngo.ca/wp-content/uploads/Summary_of_Activities_2018-P05-Bovingdon.pdf> [January 2021].
- Chandler, F.W., Charbonneau, B.W., Ciesielski, A., Maurice, Y.T. and White, S. 1980: Geological studies of the Late Precambrian supracrustal rocks and underlying granitic basement, Fury and Hecla Strait area, Baffin Island, District of Franklin; *in* Current Research, Part A, Geological Survey of Canada, Paper 80-1A, p. 125–132.
- Ciesielski, A. and Maley, J. 1980: Basement geology, Agu Bay, Gifford River, Baffin Island, District of Franklin; Geological Survey of Canada, Open File 687, 2 maps at 1:125 000 scale.
- Corrigan, D., Nadeau, L., Brouillette, P., Wodicka, N., Houlié, M.G., Tremblay, T., Machado, G. and Keating, P. 2013: Overview of the GEM Multiple Metals-Melville Peninsula project, central Melville Peninsula, Nunavut; Geological Survey of Canada, Current Research 2013-19, 21 p., URL <<https://doi.org/10.4095/292862>>.
- Corrigan, D., Pehrsson, S., Wodicka, N. and De Kemp, E. 2009: The Palaeoproterozoic Trans-Hudson Orogen: a prototype of modern accretionary processes; *in* Ancient Orogens and Modern Analogues, J.B. Murphy, J.D. Keppie and A.J. Hynes (ed.), Geological Society of London, Special Publications, v. 327, p. 457–479.
- Crocket, J.H. 1979: Platinum group elements in mafic and ultramafic rocks: a survey; *The Canadian Mineralogist*, v. 17, p. 391–402.
- Hoffman, P.F. 1988: United plates of America, birth of a craton – Early Proterozoic assembly and growth of Laurentia; *Annual Review of Earth and Planetary Sciences*, v. 16, p. 543–603.
- Jackson, G.D. and Berman, R.G. 2000: Precambrian metamorphism and tectonic evolution of northern Baffin Island, Nunavut, Canada; *The Canadian Mineralogist*, v. 38, p. 399–421.
- Jackson, G.D., Hunt, P.A., Loverridge, W.D. and Parrish, R.R. 1990: Reconnaissance geochronology of Baffin Island, N.W.T.; *in* Radiogenic Age and Isotopic Studies: Report 3, Geological Survey of Canada, Paper 89-2, p. 123–148.
- Johns, S.M. and Young, M.D. 2006: Bedrock geology and economic potential of the Archean Mary River group, northern Baffin Island, Nunavut; Geological Survey of Canada, Current Research 2006-C5, 13 p., URL <<https://doi.org/10.4095/222954>>.
- LaFlamme, C., McFarlane, C.R.M., Corrigan, D. 2014: U-Pb, Lu-Hf and REE in zircon from 3.2 to 2.6 Ga Archean gneisses of the Repulse Bay block, Melville Peninsula, Nunavut; *Precambrian Research*, v. 252, p. 223–239, URL <<https://doi.org/10.1016/j.precamres.2014.07.012>>.
- Lebeau, L.E., Russer, M., Therriault, I., Bovingdon, P.J., Dufour, F., Greenman, J.W. and Patzke, M. 2020: Regional Precambrian bedrock mapping of the Jungersen River area, north-western Baffin Island, Nunavut; *in* Summary of Activities 2019, Canada-Nunavut Geoscience Office, p. 11–26, URL <https://m.cngo.ca/wp-content/uploads/Summary_of_Activities_2019-Paper_02.en_.pdf> [January 2021].
- Machado, G., Corrigan, D., Nadeau, L. and Rigg, J. 2012: Geology, northern part of Prince Albert Greenstone Belt, Prince Albert Hills, Melville Peninsula, Nunavut; Geological Survey of Canada, Canadian Geoscience Map 81 (preliminary), 1 map at 1:25 000 scale URL <<https://doi.org/10.4095/290088>>.
- Patzke, M., Greenman, J.W., Ielpi, A. and Halverson, G.P. 2018: Sedimentology of the sandstone-dominated units in the Fury and Hecla Basin, northern Baffin Island, Nunavut; *in* Summary of Activities 2018, Canada-Nunavut Geoscience Office, p. 75–84, URL <https://m.cngo.ca/wp-content/uploads/Summary_of_Activities_2018-P07-Patzke.pdf> [January 2021].

- Pearce, J.A., Harris, N.B.W. and Tindle, A.G. 1984: Trace element discrimination diagrams for the tectonic interpretation of granitic rocks; *Journal of Petrology*, v. 25, p. 956–983, URL <<https://doi.org/10.1093/petrology/25.4.956>>.
- Pehrsson, S.J., Berman, R.G., and Davis, W.J. 2013: Paleoproterozoic orogenesis during Nuna aggregation: a case study of reworking of the Rae craton, Woodburn Lake, Nunavut; *Precambrian Research*, v. 232, p. 167–188 URL <<https://doi.org/10.1016/j.precamres.2013.02.010>>.
- Pehrsson, S.J., Berman, R.G., Eglington, B. and Rainbird, R. 2013: Two Neoarchean supercontinents revisited: the case for a Rae family of cratons; *Precambrian Research*, v. 232, p. 27–43.
- Scott, D.J. and de Kemp, E.A. 1998: Bedrock geology compilation, northern Baffin Island and northern Melville Peninsula; Geological Survey of Canada, Open File 3633, 2 maps at 1:500 000 scale and marginal notes, URL <<https://doi.org/10.4095/210024>>.
- Skipton, D.R., Saumur, B.M., St-Onge, M.R., Wodicka, N., Bros, E.R., Morin, A., Brouillette, P., Weller, O.M. and Johnston, S.T. 2017: Precambrian bedrock geology of the Pond Inlet–Mary River area, northern Baffin Island, Nunavut; *in* Summary of Activities 2017, Canada-Nunavut Geoscience Office, p. 49–68, URL <https://m.cngo.ca/wp-content/uploads/Summary_of_Activities_2017-P05-Skipton.pdf> [January 2021].
- Skipton, D.R., Wodicka, N., McNicoll, V., Saumur, B.M., St-Onge, M.R. and Young, M.D. 2019: U-Pb zircon geochronology of Archean greenstone belts (Mary River Group) and surrounding Archean to Paleoproterozoic rocks, northern Baffin Island, Nunavut; Geological Survey of Canada, Open File 8585, 43 p., URL <<https://doi.org/10.4095/314938>>.
- St-Onge, M.R., Wodicka, N. and Ijewliw, O. 2007: Polymetamorphic evolution of the Trans-Hudson Orogen, Baffin Island, Canada: integration of petrological, structural and geochronologic data; *Journal of Petrology*, v. 48, no. 2, p. 217–302.
- Steenkamp, H.M., Bovingdon, P.J., Dufour, F., G  n  reux, C.-A., Greenman, J.W., Halverson, G.P., Ielpi, A., Patzke, M. and Tinkham, D.K. 2018: New regional mapping of Precambrian rocks north of Fury and Hecla Strait, northwestern Baffin Island, Nunavut; *in* Summary of Activities 2018, Canada-Nunavut Geoscience Office, p. 47–62, URL <https://m.cngo.ca/wp-content/uploads/Summary_of_Activities_2018-P04-Steenkamp.pdf> [January 2021].
- Sun, S.-s., McDonough, W.F., 1989. Chemical and isotopic systematics of oceanic basalts: implications for mantle composition and processes; Geological Society of London, Special Publications, v. 42, p. 313–345, URL <<https://doi.org/10.1144/GSL.SP.1989.042.01.19>>.
- Young, M.D., Sandeman, H., Berniolles, F. and Gertzbein, P.M. 2004: A preliminary stratigraphic and structural geology framework for the Archean Mary River Group, northern Baffin Island, Nunavut; Geological Survey of Canada, Current Research 2004 C-1, 17 p.



Geochemical comparison of Mackenzie and Franklin igneous mafic rocks in Nunavut, Northwest Territories and northwestern Greenland

F. Dufour¹, R. Stevenson² and T. Skulski³

¹Département des sciences de la Terre et de l'atmosphère, Université du Québec à Montréal, Montréal, Québec, dufour.frederic.3@courrier.uqam.ca

²Département des sciences de la Terre et de l'atmosphère, Université du Québec à Montréal, Montréal, Québec

³Natural Resources Canada, Geological Survey of Canada, Ottawa, Ontario

The Fury and Hecla Geoscience Project (FHGP) was led by the Canada-Nunavut Geoscience Office in collaboration with Crown-Indigenous Relations and Northern Affairs Canada, and researchers and students from Laurentian University, McGill University and Université du Québec à Montréal. The multiyear project involved mapping and sampling of Archean, Proterozoic and Paleozoic rocks, and Quaternary surficial deposits and features. The study area comprised all or parts of nine 1:250 000 scale NTS map areas north and south of Fury and Hecla Strait on Baffin Island and Melville Peninsula, respectively (NTS 37C, F, 47C–H and 48A).

Dufour, F., Stevenson, R. and Skulski, T. 2021: Geochemical comparison of Mackenzie and Franklin igneous mafic rocks in Nunavut, Northwest Territories and northwestern Greenland; in Summary of Activities 2020, Canada-Nunavut Geoscience Office, p. 33–46.

Abstract

Presented in this paper is a review of the geochemical classification and comparison of the igneous rocks from across the Canadian Arctic and northwestern Greenland, including new data from the Fury and Hecla Basin. These mafic igneous rocks are tentatively associated with the Mesoproterozoic Mackenzie and the Neoproterozoic Franklin igneous events. The majority of these Mackenzie and Franklin igneous rocks fall within the tholeiitic basalt/gabbro fields in the total alkali-silica diagrams with a smaller number of samples falling within the trachybasalt/alkali gabbro and monzogabbro fields. Both the Franklin and Mackenzie suites are enriched in TiO₂, with the Franklin-related rocks having enrichments ranging as high as 5.25 wt. % TiO₂ and the Mackenzie-related rocks ranging as high as 3.75 wt. % TiO₂. However, Mackenzie-related rocks of the eastern Arctic tend to have lower TiO₂ concentrations (<1.25 wt. %) than those of the western Arctic (1.5–3.75 wt. %). The high TiO₂ concentrations and trace element discrimination diagrams (Th/Yb versus Nb/Yb) of the Mackenzie- and Franklin-related rocks of the Fury and Hecla Basin are consistent with enriched mid-ocean-ridge basalts that were derived from an enriched mantle and were subsequently contaminated by crustal sources during emplacement.

Introduction

Presented in this paper are new geochemical data for igneous rocks from the Fury and Hecla Basin that were described and sampled during the 2018 geological mapping season; a program that was led by the Canada-Nunavut Geoscience Office (Steenkamp et al., 2018; Dufour et al., 2020). The sampled igneous rocks are largely mafic in composition and are believed to be formed during the Mesoproterozoic Mackenzie and Neoproterozoic Franklin igneous events. The goal of the study is to classify the igneous rocks from the Fury and Hecla Basin and compare the new data with published data on similar rocks from across the Arctic in Canada and northwestern Greenland.

The Mackenzie and Franklin igneous events are interpreted as large igneous provinces (LIPs) that formed ca. 1268 Ma (LeCheminant and Heaman, 1989) and ca. 723 Ma (Heaman et al., 1992), respectively, with each event pro-

ducing features such as sills, dyke swarms and basalt flows. The petrology and geochemical characteristics of the igneous rocks from the Fury and Hecla Basin will help constrain the magma sources, magmatic evolution and metallogeny in the Bylot basins of the eastern Arctic as has been done in the western Arctic (Bédard et al., 2012; Williamson et al., 2016). Geographic variations in the geochemistry of the Mackenzie and Franklin LIPs, across the Arctic, are also discussed. The data sources for this comparison include

- data for the Coppermine River Group basalt flows extracted from the GEOROC database (Max Planck Institute for Chemistry, 2019) but originally came from Dostal et al. (1983), Griselin et al. (1997) and Day (2013);
- Nauyas Formation basalts compositions, compiled from Dostal et al. (1989);

This publication is also available, free of charge, as colour digital files in Adobe Acrobat® PDF format from the Canada-Nunavut Geoscience Office website: <https://cngo.ca/summary-of-activities/2020/>.

- Mesoproterozoic and Neoproterozoic dykes and sills from Dawes (2006);
- Franklin igneous rock data from Bédard et al. (2016); the data includes Franklin dykes from Somerset Island and Kiluhitquq (formerly Bathurst Inlet), dykes and sills from Coronation Gulf and Brock Inlier and the Natkusiak sills from Victoria Island;
- additional data for the Mackenzie and Franklin dykes and sills compiled from Ernst and Buchan (2010).

Geological setting

Mesoproterozoic Mackenzie igneous suite

The mafic rocks of the Mesoproterozoic Fury and Hecla Basin described here are believed to be associated with the Mackenzie igneous suite (Chandler and Stevens, 1981; Chandler, 1988). The ca. 1268 Ma Mackenzie LIP comprises mafic and lesser ultramafic rocks in the western Canadian Arctic (Figure 1), which include the volcanic rocks of the Ekalulia Formation, the Coppermine River Group, the Muskox intrusion, the East Arm sills, the Mackenzie dyke swarm and the Savage Point sill (Hunting-Aston Basin; Baragar, 1969; Dostal et al., 1983; Hoffman, 1988; LeCheminant and Heaman, 1989; Heaman and LeCheminant, 1993; Baragar et al., 1996; Griselin et al., 1997; Day et al., 2008; Ernst and Buchan, 2010; Day, 2013). Paleomagnetic data show a close correlation of the latter five rock units with the Mackenzie igneous event and no reversal of polarity (Fahrig and Jones, 1969; Jones and Fahrig, 1978; Fahrig et al., 1981). Additional Mackenzie-aged units in the western Arctic include the Tweed Lake volcanic rocks (Figure 1), the Bear River dykes and the Tremblay sills (Sevigny et al., 1991; Hulbert et al., 1993; Schwab et al., 2004). In the eastern Arctic, similar age intrusive rocks (LeCheminant and Heaman, 1989, 1991) are associated with undated volcanic rocks in the Bylot basins (Long and Turner, 2012), including the Fury and Hecla, Borden and Thule basins (Figure 1; Chandler, 1988; Dostal et al., 1989; Dawes, 1997, 2006; Dufour et al., 2020).

Western Arctic

Coppermine River Group

The Mesoproterozoic Coppermine River Group includes approximately 3000 m of continental flood basalts of the Copper Creek Formation overlain by red sandstones and interbedded basaltic lava flows of the Husky Creek Formation (Baragar, 1969; Skulski et al., 2018). The Copper Creek Formation is composed of three stratigraphic members defined on the basis of geochemistry and petrography (Skulski et al., 2018). The September Creek member at the base includes plagioclase-clinopyroxene±orthopyroxene-phyric basalts and, less abundant, olivine-phyric picrite (Skulski et al., 2018). The overlying Stony Creek and Burnt Creek members contain thin basalt flows with microphe-nocrysts of plagioclase, clinopyroxene±titanomagnetite

(Skulski et al., 2018). Native copper is found primarily in these upper two members where it is a minor constituent of amygdules and is locally concentrated in veins (Baragar, 1969; Kindle, 1973). Correlative volcanic rocks of the Ekalulia Formation are found in the Kiluhitquq area (Campbell, 1978).

Muskox intrusion and Mackenzie dyke swarm

The Muskox intrusion is a 125 km long, funnel-shaped plutonic body, which intruded sedimentary strata and crystalline basement rocks beneath the Coppermine River Group (Figure 1; Irvine, 1970). The intrusion comprises a gabbroic to ultramafic marginal zone, enclosing layered peridotite and gabbroic cumulates (LeCheminant and Heaman, 1989). The September Creek member of the Coppermine River Group is comagmatic with the Muskox intrusion (Day, 2013), which has been dated at ca. 1269 Ma (U-Pb baddeleyite analysis; LeCheminant and Heaman, 1989; French et al., 2002; Mackie et al., 2009).

The Mackenzie radiating dyke swarm (Figure 1) can be traced over 2400 km from a focal point on Victoria Island (Jowitt and Ernst, 2013; Blanchard et al., 2017). Two subswarms are recognized on the basis of geochemistry and geometry (Baragar et al., 1996) and include the western swarm and Pitz-Dubawnt lakes swarm in the east. The Mackenzie dykes cut the Muskox intrusion and the Coppermine River Group (September Creek member) and are interpreted to be feeder dykes to the mid and upper lava flows of the Coppermine River Group (Day, 2013; Skulski et al., 2018).

Savage Point sill, Hunting-Aston Basin

The Mesoproterozoic stratigraphy of the Hunting-Aston Basin is considered as one of the Bylot sedimentary basins but is described here as part of the western Arctic (Figure 1; Dixon et al., 1971). The Hunting-Aston Basin is located on Prince of Wales Island and Somerset Island. The lower part of the basin is represented by the 120–300 m thick Savage Point sill, which typically has a columnar-jointed structure and is composed of clinopyroxene, orthopyroxene and plagioclase. South of the Savage Point peninsula, magmatic differentiation within the sill is supported by reports of ultramafic rocks in the lower 8 m of the sill (Mayr et al., 2004) and coarse-grained and granophyric textures in the upper part of the sill (Jones and Fahrig, 1978). The sill is overlain by the Aston Formation, which comprises 800 m of mainly sandstone, and above that the Hunting Formation, which comprises 1000–2000 m of dolostone and sandstone (Dixon et al., 1971; Mayr et al., 2004).

The sill is strongly correlated with the Mackenzie igneous event based on a U-Pb baddeleyite age of ca. 1268 Ma (Heaman and LeCheminant, 1993) and a paleopole position that overlaps with the Mackenzie pole (Jones and Fahrig, 1978; Fahrig et al., 1981).

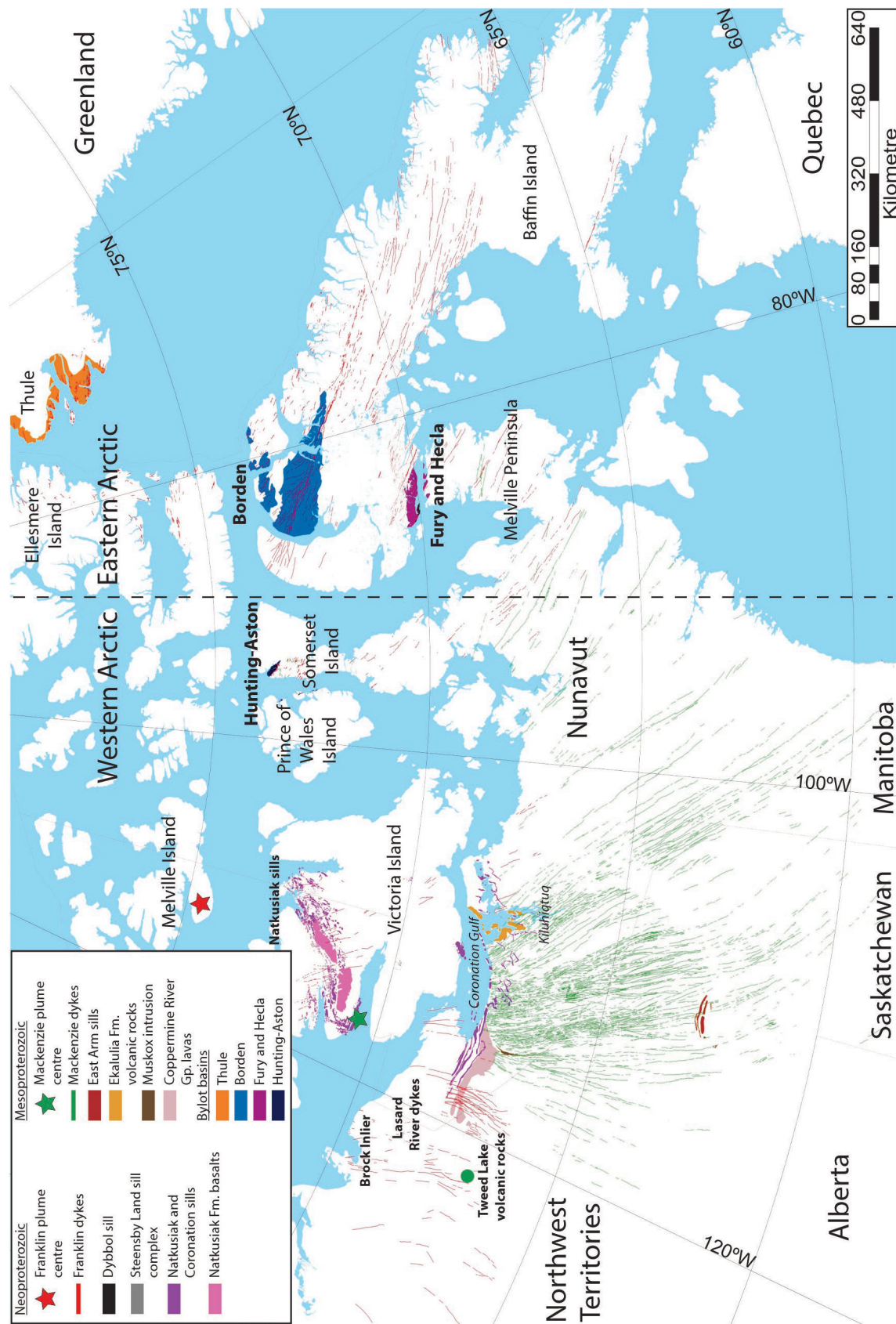


Figure 1: Map of the Mackenzie and Franklin igneous suites of northern Canada and northwestern Greenland. For the purpose of this paper, the eastern Arctic (*sensu lato*) encompasses three of the Bylot basins and the western Arctic (*sensu lato*) encompasses the Hunting-Aston Basin, the Coppermine River and Victoria Island areas. The Mackenzie and Franklin dykes are from Buchanan and Ernst (2013). The Mackenzie mafic rocks (East Arm sills, Ekallua Formation volcanic rocks, Muskox intrusion, Coppermine River Group lavas) and the Coronation sills are adapted from Buchanan et al. (2010), the Borden Basin is from St-Onge et al. (2015), the Fury and Hecla Basin and the Dybbol sill are from Dufour et al. (2020), the Natkusiak Formation basalts, the Natkusiak sills and the Hunting-Aston Basin are from Harrison et al. (2016), the Thule Franklin dykes, the Steensby Land sill complex and the Thule Basin are extracted from the digitized geological map of Greenland (Geological Survey of Denmark and Greenland, 2016).

Eastern Arctic

In the eastern Arctic of Canada and northwestern Greenland, flat-lying Mesoproterozoic sedimentary and volcanic rocks of the Bylot Supergroup (Blackadar, 1970; Jackson and Ianelli, 1981; Dawes, 1997) constitute the three Bylot basins: Fury and Hecla, Borden and Thule basins (Figure 1; Long and Turner, 2012).

Nyeboe Formation, Hansen Formation and Hansen sill, Fury and Hecla Basin

The Fury and Hecla Basin (Figure 1) comprises gently dipping Mesoproterozoic sedimentary and volcanic rocks, which are locally exposed in fault-bounded blocks (Melville Peninsula; Chandler, 1988). The Nyeboe Formation at the base contains siliciclastic units, stromatolites and a few thin (~3 m) locally pillowed to massive basalt flows (Chandler, 1988; Patzke et al., 2018; Dufour et al., 2020). These are overlain by sandstone of the Sikosak Bay Formation and fine-grained massive basalts of the Hansen Formation. The mid and upper reaches of the basin include shale of the Agu Bay Formation and siliciclastic rocks of the Whyte Inlet and overlying Autridge formations (Chandler, 1988; Greenman et al., 2018; Patzke et al., 2018). A fine- to medium-grained, columnar-jointed gabbro sill intrudes the Nyeboe and Sikosak Bay formations (Chandler, 1988; Dufour et al., 2020). This sill is believed to be comagmatic with the Hansen Formation basalts and has a minimum K-Ar whole-rock age of ca. 1.1 Ga (Chandler and Stevens, 1981).

Nauyat Formation, Borden Basin

Volcanic rocks occur in the lower reaches of the Borden Basin (Figure 1) in the Eqaalulik Group (Jackson and Ianelli, 1981). The lower Eqaalulik Group includes the Nauyat Formation, which comprises a lower quartzite member overlain by a volcanic member (Jackson and Ianelli, 1981). The volcanic member (up to 200 m thick) consists of seven tholeiitic basalt flows (Galley, 1978; Jackson and Ianelli, 1981; Galley et al., 1983; Dostal et al., 1989). These are largely massive subaerial flows locally columnar-jointed and may include pillowed amygdaloidal basalts (Long and Turner, 2012). The basalt flows have continental tholeiitic affinity (Dostal et al., 1989). Primary mineralogy consists of Ca-plagioclase, augite and olivine (+titanomagnetite and apatite) and is overprinted by greenschist-facies metamorphic assemblages (prehnite-pumpellyite; Dostal et al., 1989). Overlying the volcanic rocks are siliciclastic sedimentary rocks of the Adams Sound Formation and shale of the Arctic Bay Formation. The Eqaalulik Group is overlain by a carbonate platform (Uluksan Group) and younger siliciclastic rocks (Nunatsiaq Group; Jackson and Ianelli, 1981).

The Mesoproterozoic age of the Nauyat Formation basalts is constrained by a K-Ar whole-rock age of ca. 1.2 Ga (Jackson and Ianelli, 1981), and a minimum age constraint

from a Re-Os isochron age of 1048 ± 0.012 Ma (Gibson et al., 2018) for overlying shale in the Arctic Bay Formation. The Nauyat Formation basalts have a paleopole position that coincides with the Mackenzie pole of 1.27 Ga (Fahrig et al., 1981).

Cape Combermere and Northumberland formations, Thule Basin

The Mesoproterozoic Thule Basin, in northwestern Greenland and eastern Ellesmere Island, Canada (Figure 1), contains 6 km of relatively unmetamorphosed, sedimentary and mafic volcanic rocks (Dawes, 1997, 2006, 2009). The 1200 m thick Nares Strait Group is the lowest stratigraphic unit of the Thule Basin. It contains a lower succession of sandstone of the Northumberland Formation, overlain by a volcanic-red bed sequence of tholeiitic plateau basalts, mafic pyroclastic rocks (tuff and lapilli tuff) and interflow sandstone-shale packages of the Mesoproterozoic Cape Combermere Formation (Dawes, 1997, 2006). Tabular subhorizontal sills outcrop largely in the Inglefield Land area, northwestern Greenland, where they crosscut the Paleoproterozoic basement and the sandstone of the Northumberland Formation (Dawes, 1997). The overlying Josephine Headland and Borden Bugt formations comprise stromatolitic carbonate, sandstone and shale (Dawes, 1997, 2006).

Mafic gabbro sills and associated dykes intrude the Cape Combermere Formation. Dawes (1997) identified both intrusive and extrusive contacts associated with these basalt sills/flows and identified a feeder vent that cut through the carbonate rocks of the Cape Combermere Formation (Dawes, 1997, Figure 61; Dawes, 2006). The gabbroic sills contain plagioclase, clinopyroxene and olivine (usually altered). The sills are up to 100 m thick and are locally columnar-jointed. The Goding Bay sill on Ellesmere Island, part of the Cape Combermere Formation, has a baddeleyite $^{207}\text{Pb}/^{206}\text{Pb}$ age of 1268 Ma (LeCheminant and Heaman, 1991).

Neoproterozoic Franklin igneous suite

The ca. 720 Ma Franklin igneous event in the western Canadian Arctic produced the Natkusiak Formation basalts and the Franklin dyke swarm and sills (Figure 1; Heaman et al., 1992; Denyszyn et al., 2009a, b; Bédard et al., 2012, 2016; Hayes et al., 2015a–c; Williamson et al., 2016; Beard et al., 2018). The 2500 km radiating Franklin dyke swarm is found across mainland Nunavut and the Northwest Territories, as well as in the Arctic Archipelago and northwestern Greenland (Figure 1; Heaman et al., 1992; Bédard et al., 2016; Williamson et al., 2016; Beard et al., 2018). The main dyke swarm fans from northeast-striking in the west, to northwest-striking on Baffin Island to west- to southwest-striking on Ellesmere Island and Greenland (Chandler, 1988; Heaman et al., 1992; Pehrsson and Buchan, 1999; Dawes, 2006; Denyszyn et al., 2009a, b). The Neoproterozoic

zoic mafic dykes and sill from the Fury and Hecla Basin described below are tentatively correlated with the Franklin LIP (Chandler and Stevens, 1981; Chandler, 1988). The intrusions in the eastern Arctic are well correlated with the Franklin igneous event by U-Pb baddeleyite ages and by a similarity in the paleopoles to the Franklin pole (Heaman et al., 1992; Denyszyn et al., 2009a, b). The convergence point of the Franklin igneous event is located on Melville Island (Denyszyn et al., 2009a, b).

Western Arctic

In the western Arctic, Franklin-age mafic rocks include the Natkusiak Formation basalts and other occurrences, such as the Natkusiak sills, the Coronation sills in the Coronation Gulf area, the Aston dykes (Figure 1), the Mount Harper Complex and the Kikiktat volcanic rocks (Heaman et al., 1992; Shellnutt et al., 2004; Macdonald et al., 2010; Cox et al., 2015). The south-southeastern-trending Lasard River dykes, found in the Brock Inlier area, are considered to be associated with the Franklin igneous event and possibly part of the younger Franklin dyke subswarm emplaced in eastern Arctic (Figure 1; Buchan and Ernst, 2006; Denyszyn et al., 2009a). Investigations by Cox et al. (2018) tried to link the Pleasant Creek volcanic rocks and associated Tatonduk dykes (western Yukon–eastern Alaska) to the Franklin LIP but they concluded that the relationships remain uncertain. The Natkusiak and Coronation sills, the Natkusiak Formation basalts and the Franklin Aston dykes from the Hunting-Aston Basin are described below.

Natkusiak and Coronation sills

About 13 Natkusiak sills intrude the Shaler Group and the lower Natkusiak Formation basalts on Victoria Island and they range from 5 to 100 m thick (Figure 1; Heaman et al., 1992; Bédard et al., 2012, 2016; Hayes et al., 2015a–c; Beard et al., 2018). The sills are characterized by homogeneous compositions and thicknesses over tens of kilometres and are generally composed of pyroxene, plagioclase and olivine. The sills are commonly differentiated, with olivine-rich cumulates at the base and pegmatitic–granophyric textures at the top (Heaman et al., 1992; Bédard et al., 2012).

Fifteen Coronation sills, ranging from 20 to 100 m thick, intrude the Proterozoic Rae Group in mainland Northwest Territories and occur in southern Victoria Island (Figure 1; Heaman et al., 1992; Shellnutt et al., 2004). They are mainly composed of clinopyroxene, plagioclase and Fe-Ti oxides.

Six U-Pb ages derived from baddeleyites and zircons indicate an age of 716.33 ± 0.54 Ma for the Natkusiak lower sill (Macdonald et al., 2010) and 723 Ma for the Natkusiak middle and upper sills and Coronation sills (Heaman et al., 1992).

Natkusiak Formation basalts

The Natkusiak Formation is composed of 1100 m of tholeiitic flood basalt flows (Figure 1; Heaman et al., 1992; Williamson et al., 2016; Beard et al., 2018). Palmer and Hayatsu (1975) tentatively correlated the Natkusiak Formation with the Franklin igneous event, reporting a K-Ar age of 625 Ma and supportive paleomagnetic data from the basalt flows. The compositions of these basalts are not used in the ensuing geochemical comparison because no equivalent Franklin volcanic rocks have been observed in the eastern Arctic.

Franklin Aston dykes, Hunting-Aston Basin

Gabbroic dykes of the Hunting-Aston Basin are generally 30–50 m thick, strike both northeast and northwest, and cut the Archean basement and overlying Mesoproterozoic sedimentary rocks on the Prince of Wales and Somerset islands (Figure 1; Dixon, 1974; Mayr et al., 2004). These crosscutting relationships, reported Neoproterozoic ages and paleomagnetic data (ca. 702 ± 25 Ma, K-Ar dating; Dixon, 1974; Jones and Fahrig, 1978) are consistent with the Franklin igneous event.

Eastern Arctic

Mafic sills and dykes occur in the Fury and Hecla Basin area and the Pituffik area in northwestern Greenland (Figure 1; Dawes, 1997; Mayr et al., 2004; Dufour et al., 2020). Additional dykes in southwestern Greenland, known as the Ataa Sund dykes, may represent the continuity of the Franklin dykes from eastern Baffin Island (Buchan et al., 2006; Halls et al., 2010). A subswarm of dykes is tangential to the main radiating swarm and includes the north-striking Clarence Head dykes on Ellesmere Island and the Strathcona dykes on northern Baffin Island (Pehrsson and Buchan, 1999; Denyszyn et al., 2009a). The Clarence Head dykes have yielded a U-Pb baddeleyite age of 716–713 Ma (Denyszyn et al., 2009a) and are thus slightly younger than the main Franklin dyke swarm at ca. 720 Ma but remain considered as part of the Franklin igneous event. A coeval sill (see ‘Steensby Land sill complex’ section below) in the Granville Fjord area (northwestern Greenland) has yielded a U-Pb baddeleyite age of 712 Ma (Denyszyn et al., 2009b) and is likely related to this subswarm.

Franklin dykes and Dybbol sill, Fury and Hecla Basin

Southeast-striking Franklin dykes cut both the Mesoproterozoic Fury and Hecla Basin and the Archean basement rocks (Figure 1; Chandler, 1988; Dufour et al., 2020). The Dybbol sill, also in the Fury and Hecla Basin, is located on the Autridge peninsula (near Autridge Bay) and covers the top of the Mesoproterozoic stratigraphy. Both the dykes and sill are gabbroic rocks, usually fine to medium grained in the chilled margin and medium to coarse grained in the interior (Dufour et al., 2020). Chandler and Stevens (1981) reported K-Ar ages of 631 ± 43 Ma for a dyke, and

716 ±166 Ma and 746 ±87 Ma for the Dybbol sill in the Fury and Hecla Basin, and tentatively correlated these intrusions to the Franklin igneous event.

Franklin dykes, Borden Basin

Northwest-striking mafic dykes in the Milne Inlet area (northwestern Baffin Island; Figure 1) of the Borden Basin are medium to coarse grained and subophitic with a mineralogy consisting of plagioclase, clinopyroxene and olivine (+Fe-amphibole, biotite, quartz, albite, chlorite, apatite, baddeleyite, zircon; Christie and Fahrig, 1983; Pehrsson and Buchan, 1999). Pehrsson and Buchan (1999) report a U-Pb baddeleyite age of 720–716 Ma for one of these dykes, thus clearly linking them with the Franklin igneous event. The age correlation is supported by geochemical studies indicating that the dykes of the Borden Basin are comparable to Franklin dykes located elsewhere on Baffin Island (Pehrsson and Buchan, 1999; Jackson, 2000).

Thule dykes, Thule Basin

West-southwest–striking gabbroic dykes cut the Steensby Land sill complex (SLSC) of the Thule Basin in Greenland and are referred to as the Thule dykes (Figure 1; Dawes, 2006, 2009). The dykes form a dense swarm and are preserved as prominent ridges (Dawes, 1997, 2006). Chilled margins of the dykes have fine-grained textures and dyke centres have an aphanitic–porphyritic texture. The rocks have a black–grey colour on fresh surfaces and a brown–greenish weathered face. The dykes are composed of plagioclase, pyroxene and ilmenite (±quartz, olivine).

The Thule dykes are correlated with the Franklin igneous event based on similar age and similar strike to Franklin dykes on Baffin Island (Oakey, 2005; Dawes, 2006; Oakey and Damaske, 2006). Denyszyn et al. (2009b) report a U-Pb age of 721 Ma for a dyke north of Steensby Land, in the vicinity of Qaanaaq, which is parallel to the Thule dykes in Granville Fjord (Steensby Land) area. Denyszyn et al. (2009b) have also reported a 712 Ma age for an SLSC intrusive body at Granville Fjord, however, Dawes (1997) has shown that Thule dykes cut the SLSC. This year's fieldwork in Granville Fjord, supported by detailed satellite imagery, confirms Dawes (1997) observation that west-southwest striking Thule dykes cut the SLSC. It is noted, however, that the 712 Ma 'sill' sampled on the eastern shore of Granville Fjord (Denyszyn et al., 2009b) lies along strike from a northwest-striking dyke that appears to cut the west-southwest-striking Thule dykes. One possible explanation is that the dated 712 Ma sample is from a younger dyke. Additional samples of Thule dykes and the SLSC were collected to help resolve this uncertainty and will be analyzed at a future date.

Steensby Land sill complex, Thule Basin

The SLSC corresponds to a swarm of tabular Neoproterozoic gabbroic sills, which intrude the stratigraphy of the

Mesoproterozoic Thule Basin in Greenland (Figure 1; Dawes, 2006, 2009). The tabular intrusions are 20–50 m thick and are mostly found within the Mesoproterozoic sandstone and carbonate of the Dundas Group (former settlement of Moriusaq to Pituffik [Thule Air Base] area). Locally the sills are subdivided, with upper parts of the sills (diorite) containing minor quartz and K-feldspar (Wolstenholme Fjord) and lower parts of the sills (ferrogabbro) containing abundant ilmenite. Ilmenite concentrations in the rocks of the SLSC and Franklin dykes of the Thule Basin can reach as high as 15% (Dawes, 2006). A sill analyzed in the Granville Fjord area yielded a U-Pb baddeleyite age of 712 ±2 Ma (Denyszyn et al., 2009b; but see section 'Thule dykes, Thule Basin').

Samples and analytical methods

Presented in this paper are new geochemical data for 24 samples from the Fury and Hecla Basin collected during the 2018 summer field season (Dufour et al., 2020). Fine- to coarse-grained samples were collected from the centres and the chilled margins of the dykes. Fine-grained samples were taken for the Nyeboe Formation basalts, fine- to medium-grained samples for the Hansen sill and medium- to coarse-grained samples for the Dybbol sill. Weathered surfaces were removed before crushing. Representative rock powders were analyzed by Activation Laboratories Ltd. (Ancaster, Ontario). Major elements were analyzed on a Thermo Jarrell-Ash Enviro II inductively coupled plasma–emission spectrometer (ICP-ES) or a Varian Vista 735 ICP-ES and trace elements were analyzed on a Perkin Elmer Sciex Elan 6000/6100/9000-type inductively coupled plasma–mass spectrometer.

Results

Mackenzie igneous suite

The total alkali-silica (TAS) diagram (Figure 2) shows that most of the Mackenzie-related mafic rocks fall within the basalt field (tholeiitic basalts) with a lesser number of samples falling in the tephrite, trachyandesite and andesite fields. The compositions of the Hansen samples from the Fury and Hecla Basin and the Savage Point sill from the Hunting-Aston Basin plot largely in the basalt field of mid to upper alkaline compositions. Mesoproterozoic sills from the Nares Strait Group (Thule Basin) show a large variation in the TAS diagram from basalt (gabbro) to basaltic trachyandesite (monzodiorite). The Mackenzie dykes and Coppermine River Group volcanic rocks are primarily in the basalt field. The Nauyat (Borden Basin), Northumberland (Thule Basin) and Nyeboe (Fury and Hecla Basin) formations fall in the basaltic trachyandesite–trachybasalt fields with a few in the basalt field.

Figure 3 depicts the TiO₂ versus MgO concentrations of the Mackenzie-related rocks. Mesoproterozoic gabbros and

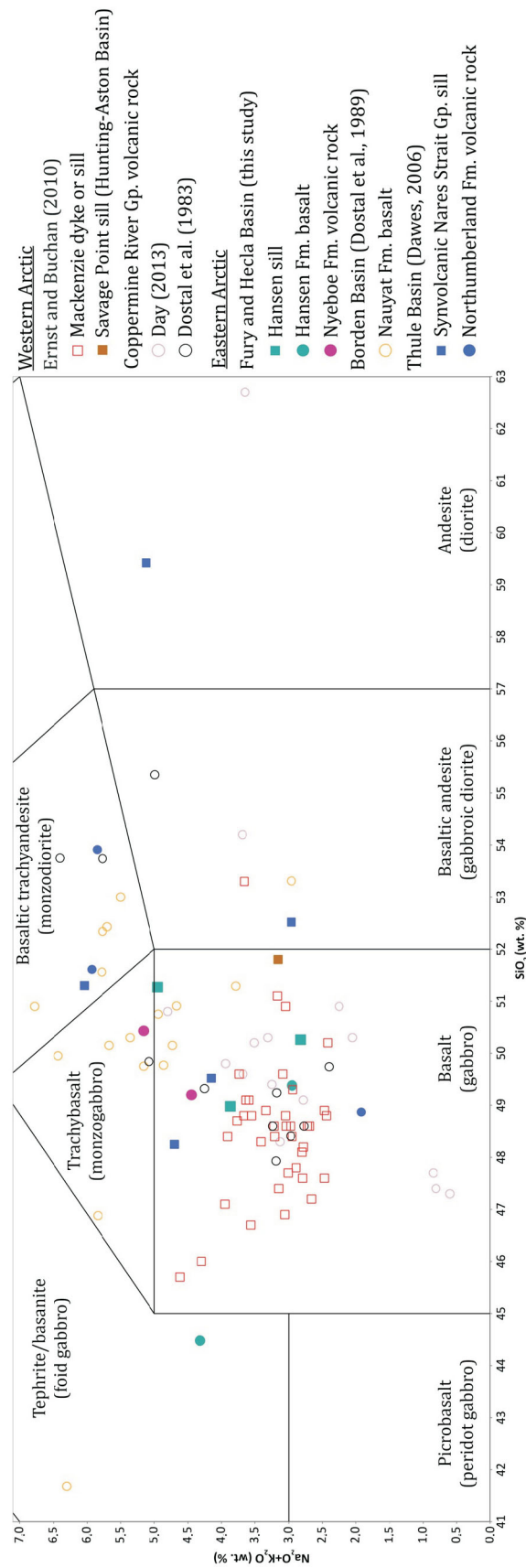


Figure 2: Total alkali-silica (TAS) diagram (after LeMaitre, 1989) of Mackenzie-related rocks, Canadian Arctic and northwestern Greenland: $\text{Na}_2\text{O}+\text{K}_2\text{O}$ versus SiO_2 (in wt. %). The majority of the Mackenzie-related rocks plot as tholeiitic compositions. The compositions of the Fury and Hecla Basin samples are comparable to the Coppermine River Group volcanic rocks and Nauyat Formation basalts.

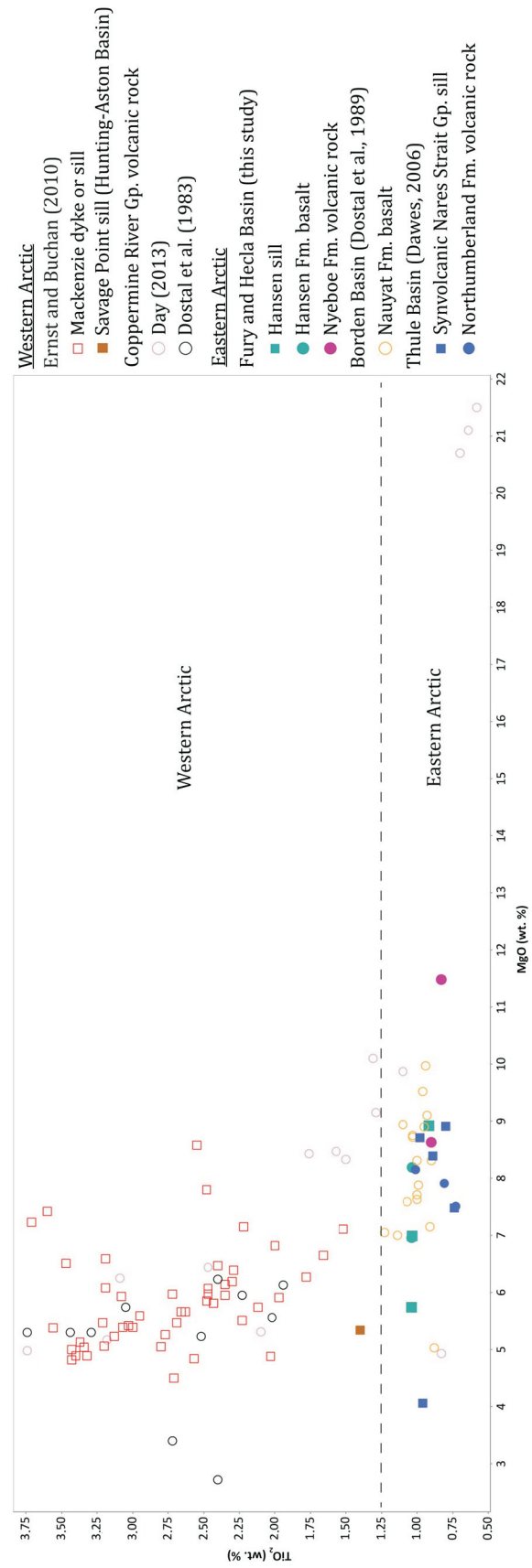


Figure 3: Diagram of TiO_2 versus MgO for Mackenzie-related rocks, Canadian Arctic and northwestern Greenland. Note the higher TiO_2 concentrations of the western Arctic (>1.25 wt. % TiO_2) compared to the mafic rocks of the eastern Arctic (<1.25 wt. % TiO_2).

basalts of the eastern Arctic have TiO_2 concentrations of <1.25 wt. % and the rocks of the western Arctic have TiO_2 concentrations of >1.25 wt. %. Based on this classification, it appears that the Savage Point sill sample is likely a western Arctic rock. Two samples from the Nyeboe Formation have high MgO (>8.5 wt. %) concentrations. Basalts from the Nauyat and Northumberland formations also have low TiO_2 (<1.2 wt. %) concentrations and MgO concentrations between 5 and 10 wt. %. A sill from the Nares Strait Group and the Hansen sill, with 4 and 9 wt. % MgO concentrations, respectively, are both TiO_2 -poor. In contrast, the Mackenzie dykes and volcanic rocks from the Coppermine River Group of the western Arctic are characterized by relatively higher TiO_2 concentrations and a similar range of MgO concentrations (4–9 wt. %). High MgO concentrations of ~21 wt. % in a few samples of basalts of the Coppermine River Group likely represent olivine accumulations.

Figure 4 is a diagram after Pearce (2014) depicting variations in the Nb/Yb and Th/Yb values of basalts from different tectonic environments (volcanic arcs, mid-ocean ridges, hot spots). The variations in the ratios reflect the different tectonic environments, but also fingerprint crustal input (high Th/Yb) and the degree of melting/source composition (Nb/Yb). The samples of the eastern Arctic are closely grouped together between 3.5–4 Nb/Yb and ~1 Th/Yb in the continental arcs field, whereas the rocks of the western Arctic are more scattered along the enriched mid-ocean-ridge basalt (E-MORB) trend. The similar ratios of the tholeiitic basalts of the eastern Arctic could reflect a similar degree of contamination of these rocks. The lower Th/Yb values of the rocks of the western Arctic suggest a lower level of crustal contamination. The Savage Point sill sample from the western Arctic plots slightly apart from the eastern Arctic samples in the continental arcs field as it has a slightly lower Nb/Yb ratio.

Franklin igneous suite

On a TAS diagram, the Franklin-related rocks plot mostly within the gabbro field with a lesser number lying in the alkalic gabbro–monzodiorite fields (Figure 5). The Neoproterozoic dykes of the Fury and Hecla Basin and the sills and dykes of the Thule Basin have higher $\text{Na}_2\text{O}+\text{K}_2\text{O}$ (>3 wt. %) than the majority of the samples from the western Arctic.

The Franklin-related rocks (Figure 6) range from 3–10 wt. % MgO and up to 5.25 wt. % TiO_2 , although most samples have <3.5 wt. % TiO_2 . The dykes of the Fury and Hecla Basin may be more differentiated than most of the other dykes and sills, in so far as they have lower MgO abundances (3–6.5 wt. %). The dykes and the Steensby Land sills of the Thule Basin and some dykes from eastern Baffin Island (Ernst and Buchan, 2010) have the highest

TiO_2 concentrations of the Franklin-related rocks and plot mostly above 3.5 wt. %. The Dybbol sill sample and samples with MgO concentrations of >10 wt. % from the western Arctic (Natkusiak sills) may reflect an accumulation of olivine.

The trace element discrimination diagram of Figure 7 indicates that most of the Franklin-related rocks yield similar Nb/Yb (1.4–2.8) and Th/Yb (0.15–0.4) ratios, although some of the Franklin dykes from eastern Baffin Island yield higher Nb/Yb ratios.

Discussion

Mackenzie igneous suite geochemistry

The overall geochemistry of the different Mackenzie-related igneous rocks is relatively homogeneous with most samples plotting in the basalt domain of Figure 2. However, geochemical differences occur between the Mackenzie-related rocks of the western Arctic and the eastern Arctic. The TiO_2 concentrations of the Mackenzie-related rocks of the Thule, Borden (Nauyat Formation basalts) and Fury and Hecla basins are lower compared to those rocks from the western Arctic, including the Savage Point sill of the Hunting-Aston Basin (Figure 3). In Figure 4, the eastern Arctic rocks fall within the continental arc domain, which likely reflects assimilation of older arc-derived crust or metasomatized lithospheric mantle. The higher Nb/Yb ratios along with documented negative Nb anomalies, low TiO_2 and high Zr concentrations among the basalts of the Borden and Fury and Hecla basins are consistent with an origin from tholeiitic basalts that were contaminated by continental crust (Galley et al., 1983; Chandler, 1988; Dostal et al., 1989). Dostal et al. (1989) also suggested that the depleted Nb and high incompatible element concentrations of the Nauyat Formation basalts suggests that they could be derived from a subcontinental lithosphere mantle source, which includes depleted mantle and recycled crustal components. In contrast, the Savage Point sill of the Hunting-Aston Basin may be slightly less contaminated than Mackenzie-related rocks of the other Bylot basins.

Geochemical variations have also been observed among the Mackenzie dykes of the western Arctic. The dykes have been divided into two subswarms based on the alkaline character of the dykes (normative quartz versus olivine; Gibson et al., 1987; Baragar et al., 1996). LeCheminant and Heaman (1989) suggested that the more alkaline dykes might come from an earlier and deeper (plume) source versus a shallower source for the less alkaline dykes. Similarly, some of the observed geochemical variations between the Mackenzie-related volcanic rocks of the western Arctic (e.g., Coppermine River Group volcanic rocks) and the eastern Arctic (volcanic rocks of the Fury and Hecla, Borden and Thule basins) may reflect the nearness of the Coppermine River Group lavas to the proposed Mackenzie

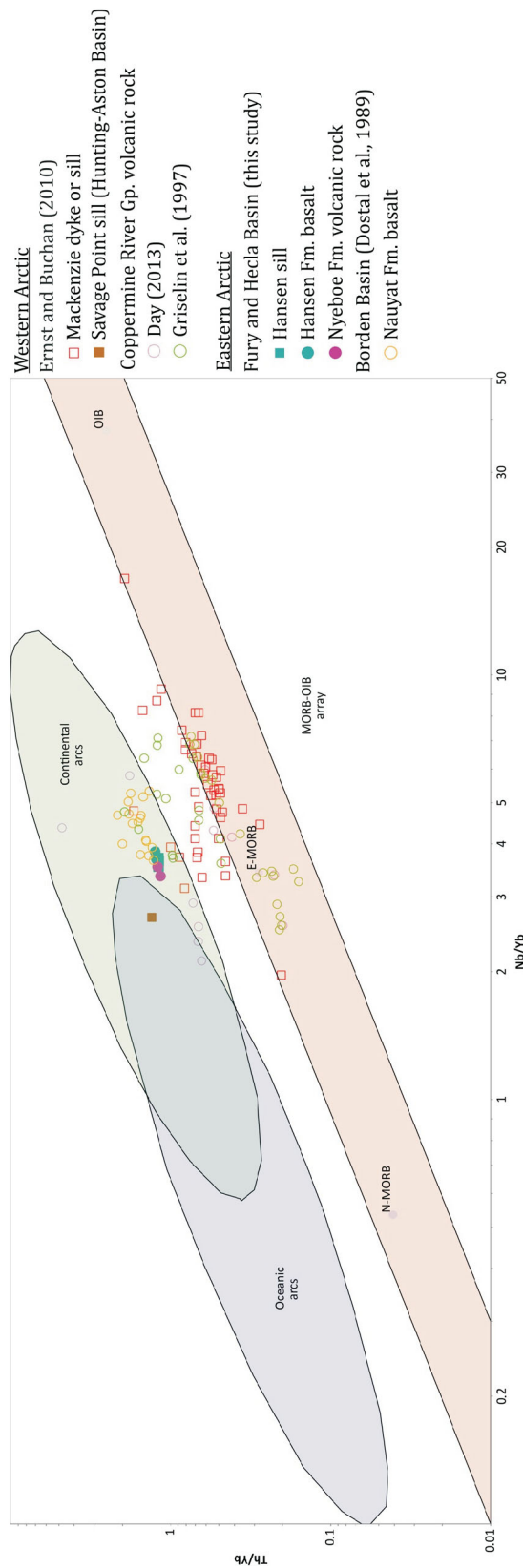


Figure 4: A Th/Yb versus Nb/Yb discrimination diagram (after Pearce, 2014) of Mackenzie-related rocks, Canadian Arctic, indicating the possible tectonic sources of the magmas. The igneous mafic rocks of the Hansen Formation, Nyeboe Formation and Nauyat Formation of the eastern Arctic are tightly grouped whereas the data of the western Arctic is more dispersed. The arrow indicates the direction of differentiation. Abbreviations: E-MORB, enriched mid-ocean-ridge basalt; MORB, mid-ocean-ridge basalt; N-MORB, normal mid-ocean-ridge basalt; OIB, oceanic-island basalt.

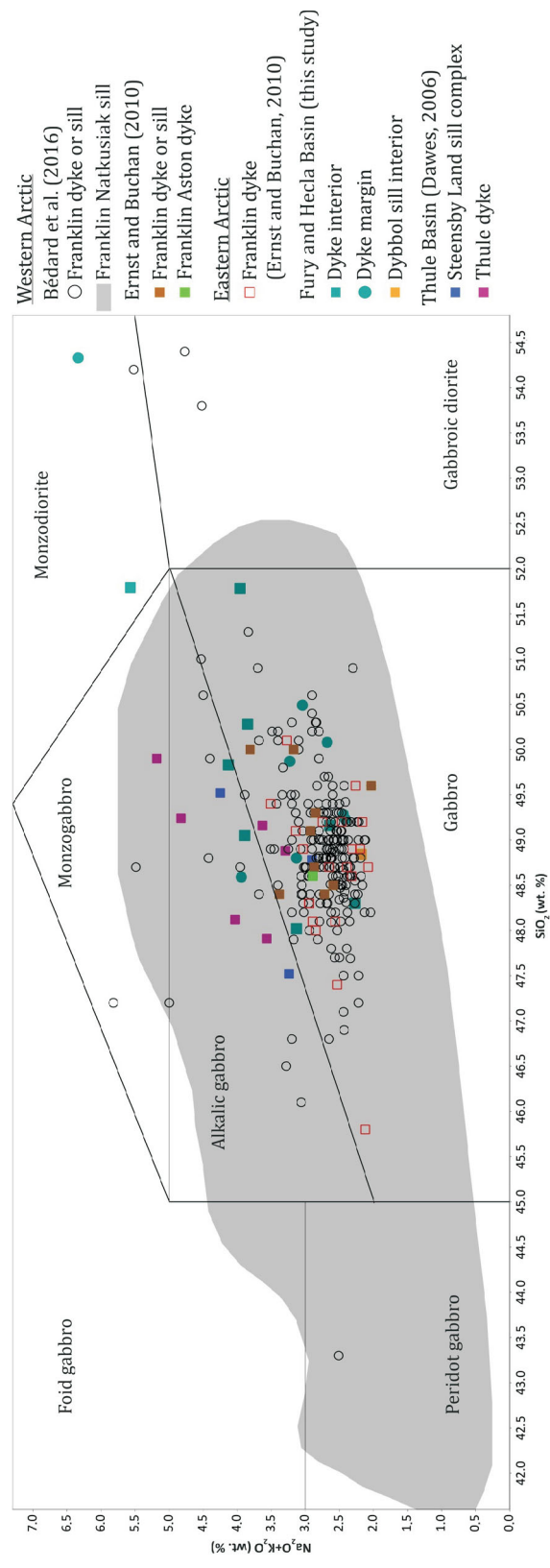


Figure 5: Total alkali-silica (TAS) diagram (after Middlemost, 1994) of Franklin-related rocks, Canadian Arctic and northwestern Greenland: $\text{Na}_2\text{O}+\text{K}_2\text{O}$ versus SiO_2 (in wt. %). The compositions of the Franklin-related intrusions of the Fury and Hecla Basin are somewhat scattered but most plot in the gabbro field.

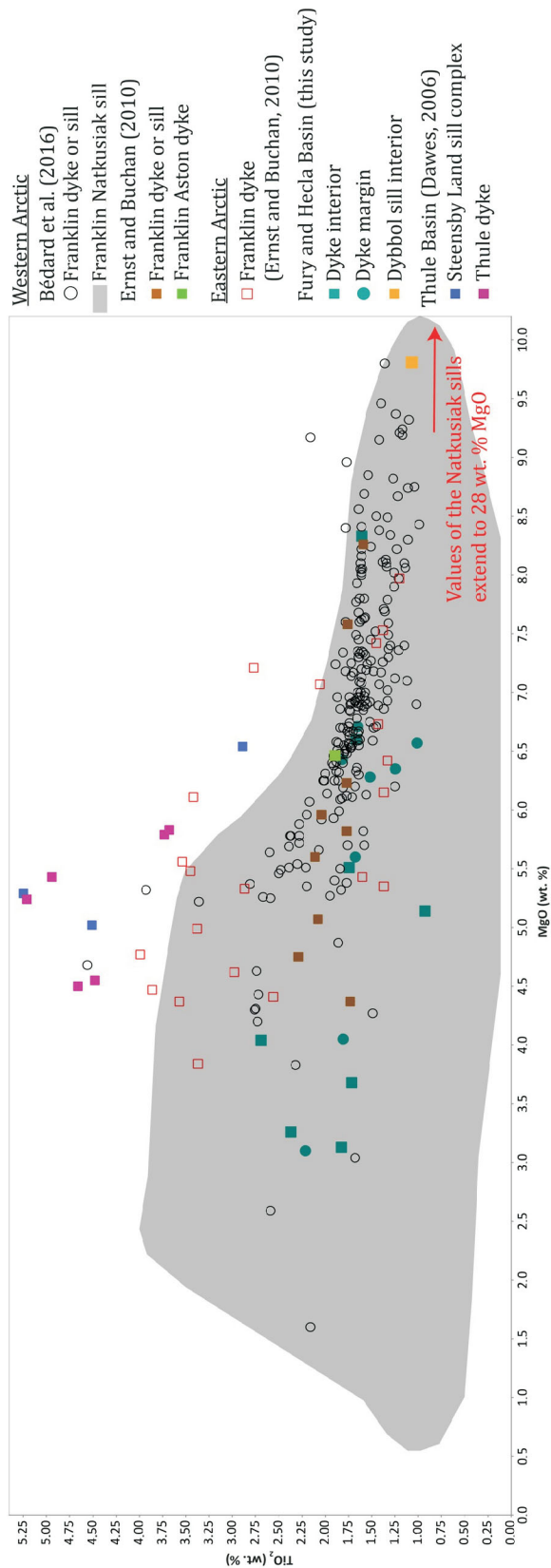


Figure 6: Diagram of TiO_2 versus MgO for Franklin-related rocks, Canadian Arctic and northwestern Greenland. Most of the Franklin-related intrusions lie along a trend of increasing TiO_2 with decreasing MgO, indicating that TiO_2 increases with magmatic differentiation. The Fury and Hecla Basin dykes plot at the lower end of the MgO concentration range, possibly indicating a greater degree of differentiation. The Thule Basin intrusions are characterized by high TiO_2 contents.

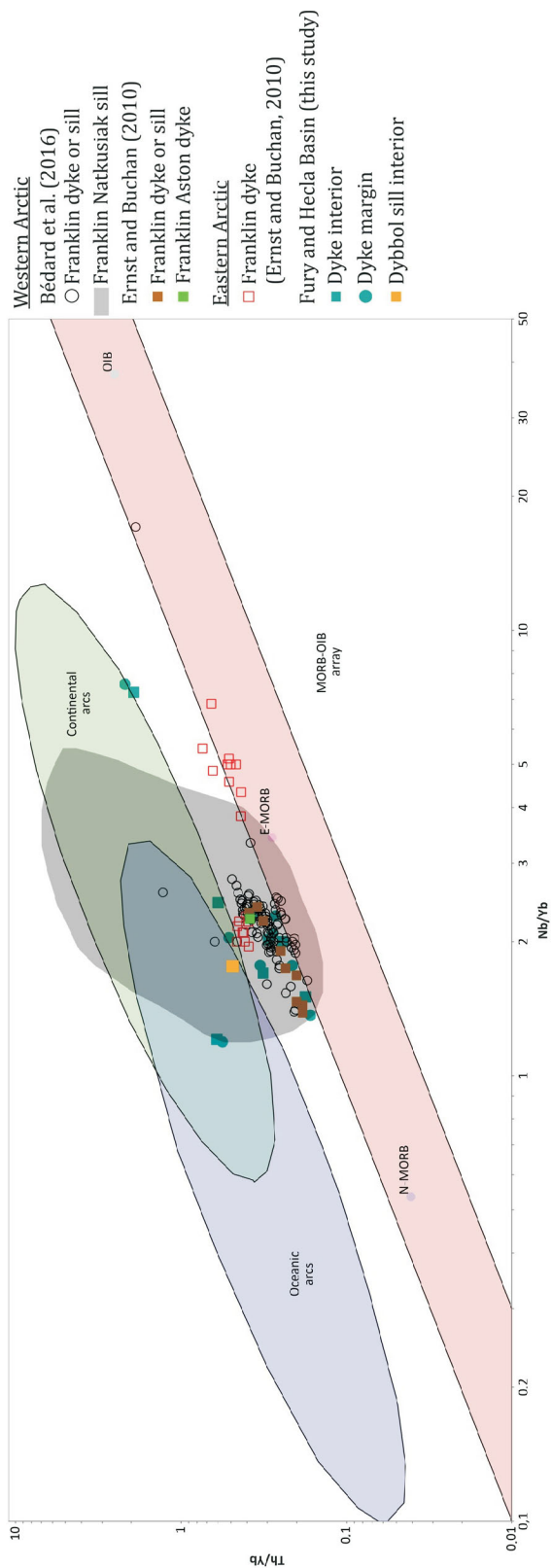


Figure 7: A Th/Yb versus Nb/Yb discrimination diagram (after Pearce, 2014) of Franklin-related rocks, Canadian Arctic, indicating the possible tectonic sources of the magmas. The Fury and Hecla Basin dykes and Dybbol sill are mostly grouped with the rest of the Franklin-related rocks of the western Arctic.

plume centre on Victoria Island relative to some of the more distal Bylot basins volcanic rocks (LeCheminant and Heaman, 1989). Griselin et al. (1997) also proposed that lavas of the Copper Creek Formation of the Coppermine River Group basalts formed from deep-seated melting and were subsequently contaminated in a crustal magma chamber. Thus, it is possible that Mackenzie-related rocks for three of the Bylot basins, including the Fury and Hecla Basin, may have experienced similar crustal contamination during emplacement.

Franklin igneous suite geochemistry

The Franklin-related rocks form a largely homogeneous group in the gabbro field of Figure 5. For example, the Natkusiak sills of Victoria Island (Beard et al., 2018) have some compositions similar to the Franklin-related rocks of the eastern and western Arctic. The Natkusiak sills are considered to be typical continental tholeiites, consisting of both low-TiO₂ (type 1) and high-TiO₂ (type 2) basalts (Dostal et al., 1986; Heaman et al., 1992; Bédard et al., 2016).

The majority of the Franklin-related rocks follow a trend of increasing TiO₂ with decreasing MgO (Figure 6). The higher TiO₂ concentrations of the SLSC and Franklin dykes from the Thule Basin (Dawes, 2006) may indicate a greater degree of differentiation and/or differences in the magma sources.

The Nb/Yb versus Th/Yb variations for the Fury and Hecla Basin mafic intrusions (Figure 7) extend from near E-MORB compositions to within the continental arc domain. Rather than representing arc magmas, these compositions likely reflect crustal contamination of the tholeiitic magmas as was demonstrated for the Natkusiak Formation volcanic rocks by Beard et al. (2018). The data for the western Arctic lie mostly along and slightly above the E-MORB trend in Figure 7. However, the data field for the Natkusiak sills cuts across the Fury and Hecla Basin data and the basalts are interpreted to have evolved from plume-related magmas (E-MORB), which have assimilated continental crustal components (Heaman et al., 1992; Shellnutt et al., 2004; Jowitt and Ernst, 2013; Beard et al., 2018). The Franklin-related mafic rocks of the Fury and Hecla Basin are likely the product of similar sources.

Economic considerations

The overall chalcophile nature and associated crustal contamination of the Mackenzie- and Franklin-related mafic rocks make these rocks interesting exploration targets for Ni-PGE-Cu mineralization (Naldrett, 2004; Jowitt and Ernst, 2013).

Numerous examples of base-metal mineralization have been documented in the Coppermine River Group (Baragar, 1969; Skulski et al., 2018). Disseminated and na-

tive copper is present in faults, veins and amygdulites of the Copper Creek Formation and Ni-PGE associated with sulphides are present in the Muskox intrusion. The emplacement of the Mackenzie magmas may also have provoked hydrothermal circulation and mineralization, such as arsenopyrite, barite and copper-uranium ores in the Paleoproterozoic Lady Nye Formation (Northwest Territories) based on a 1284 ± 11 Ma age from a hydrothermal xenotime (Davis et al., 2008; Skulski et al., 2018).

The Neoproterozoic Thule Basin mafic rocks are TiO₂-rich, yielding high-grade ilmenite concentrations in raised-beach black sands found along the coastline of the Thule Basin (Dawes, 2006). Occurrences of sulphides such as pyrite and chalcopyrite (up to 2%) and trace pyrrhotite and sphalerite have also been documented in fractures/veins within the SLSC and Thule dyke swarm.

Conclusions

The Mackenzie igneous suite of the western Arctic is characterized by higher TiO₂ concentrations (>1.25 wt. %) and lower Th/Yb ratios compared to Mackenzie-related rocks from the three Bylot basins in the eastern Arctic (<1.25 wt. %). This may indicate that the Mackenzie-related rocks of the eastern Arctic are more differentiated and may have interacted with different crustal components.

Franklin-related rocks in the Fury and Hecla Basin have slightly higher Th/Yb ratios relative to their western Arctic counterparts. This may reflect differences in their mantle source and/or in the extent to which they interacted with continental crust.

Both the Mackenzie and Franklin igneous events are characterized as large igneous provinces that formed intrusive sills, dyke swarms and extrusive lava flows over a great distance. Progressive geochemical differentiation and/or source contamination exhibited by the magmas appears to correlate with distance from the inferred plume source and may be related to thermal doming and plume uplift for both large igneous provinces.

Acknowledgments

The authors would like to thank H. Steenkamp and the crew for their help while collecting the samples during the 2018 field season. Thanks also to L. Lebeau and the team for organizing the 2019 summer field season in the Fury and Hecla Basin.

The Fury and Hecla Geoscience Project is funded by the Canadian Northern Economic Development Agency's Strategic Investments in Northern Economic Development program and through a Strategic Partnership Grant (#506660) from the Natural Sciences and Engineering Research Council of Canada. A grant for the analytical costs of

this research was provided by the Natural Sciences and Engineering Research Council of Canada. The Canada-Nunavut Geoscience Office (CNGO) is gratefully acknowledged for providing logistical support in the field. The authors thank J. Bédard and K. Buchan for a thoughtful review of an earlier version of this manuscript.

References

- Baragar, W.R.A. 1969: The geochemistry of Coppermine River basalts; Geological Survey of Canada, Paper 69-44, 43 p.
- Baragar, W.R.A., Ernst, R.L., Hulbert, L. and Peterson, T. 1996: Longitudinal petrochemical variation in the Mackenzie dyke swarm, northwestern Canadian Shield; *Journal of Petrology*, v. 37, p. 317–359.
- Beard, C.D., Scoates, J.S., Weis, D., Bédard, J.H. and Dell’Oro, T.A. 2018: Geochemistry and origin of the Neoproterozoic Natkusiak flood basalts and related Franklin sills, Victoria Island, Arctic Canada; *Journal of Petrology*, v. 58, issue 11, p. 2191–2220.
- Bédard, J.H., Hayes, B., Hryciuk, M., Beard, C., Williamson, N., Dell’Oro, T.A., Rainbird, R.H., Prince, J., Baragar, W.R.A., Nabelek, P., Weis, D., Wing, B., Scoates, J.S., Naslund, H.R., Cousens, B., Williamson, M.-C., Hulbert, L.J., Montjoie, R., Girard, E., Ernst, R. and Lissenberg, C.J. 2016: Geochemical database of Franklin sills, Natkusiak basalts and Shaler Supergroup rocks, Victoria Island, Northwest Territories, and correlatives from Nunavut and the mainland; Geological Survey of Canada, Open File Report 8009, 11 p., URL <<https://doi.org/10.4095/297842>>.
- Bédard, J.H., Naslund, H.R., Nabelek, P., Winpenny, A., Hryciuk, M., MacDonald, W., Hayes, B., Steigerwaldt, K., Hadlari, T., Rainbird, R., Dewing, K. and Girard, É. 2012: Fault-mediated melt ascent in a Neoproterozoic continental flood basalt province, the Franklin sills, Victoria Island, Canada; *Bulletin of the Geological Society of America*, v. 124, no. 5–6, p. 723–736, URL <<https://doi.org/10.1130/B30450.1>>.
- Blackadar, R.G. 1970: Precambrian geology northwestern Baffin Island, District of Franklin; Geological Survey of Canada, Bulletin 191, 89 p.
- Blanchard, J.A., Ernst, R.E. and Samson, C. 2017: Gravity and magnetic modelling of layered mafic-ultramafic intrusions in large igneous province plume centre regions: case studies from the 1.27 Ga Mackenzie, 1.38 Ga Kunene–Kibaran, 0.06 Ga Deccan, and 0.13–0.08 Ga high Arctic events; *Canadian Journal of Earth Sciences*, v. 54, no. 3, p. 290–310.
- Buchan, K.L. and Ernst, R.E. 2013: Diabase dyke swarms of Nunavut, Northwest Territories and Yukon, Canada; Geological Survey of Canada, Open File 7464, 24 p., 1 map, scale 1:3 000 000, URL <<https://doi.org/10.4095/293149>>.
- Buchan, K.L., Ernst, R.E., Bleeker, W., Davis, W.J., Villeneuve, M., van Breeman, O., Hamilton, M.A. and Söderlund, U. 2010: Proterozoic magmatic events of the Slave craton, Wopmay orogen and environs; Geological Survey of Canada, Open File 5985, 26 p., 1 sheet, 1 CD-ROM, URL <<https://doi.org/10.4095/285383>>.
- Buchan, K.L., Ernst, R.E., Hanski, E., Mertanen, S., Rämö, T. and Vuollo, J. 2006: Giant dyke swarms and the reconstruction of the Canadian Arctic islands, Greenland, Svalbard and Franz Josef Land; in *Dyke Swarms: Time Markers of Crustal Evolution*, E. Hanski, S. Mertanen, T. Rämö and J. Vuollo (ed.), CRC Press, Boca Raton, Florida, p. 27–48.
- Campbell, F.H.A. 1978: Geology of the Helikian rocks of the Bathurst Inlet area, Northwest Territories; in *Current Research, Part A*, Geological Survey of Canada, Paper 78-1A, p. 97–106.
- Chandler, F.W. 1988: Geology of the late Precambrian Fury and Hecla Group, northwest Baffin Island, District of Franklin; Geological Survey of Canada, Bulletin 370, 30 p.
- Chandler, F.W. and Stevens, R.D. 1981: Potassium-argon age of the late Proterozoic Fury and Hecla Formation, northwest Baffin Island, District of Franklin; Geological Survey of Canada, Paper 81-1A, p. 37–40.
- Christie, K.W. and Fahrig, W.F. 1983: Paleomagnetism of the Borden dykes of Baffin Island and its bearing on the Grenville Loop; *Canadian Journal of Earth Sciences*, v. 20, no. 2, p. 275–289.
- Cox, G.M., Halverson, G.P., Denyszyn, S., Foden, J. and Macdonald, F.A. 2018: Cryogenian magmatism along the northwestern margin of Laurentia: plume or rift?; *Precambrian Research*, v. 319, p. 144–157.
- Cox, G.M., Strauss, J.V., Halverson, G.P., Schmitz, M.D., McClelland, W.C., Stevenson, R.S. and Macdonald, F.A. 2015: Kikiktat volcanics of Arctic Alaska—melting of harzburgitic mantle associated with the Franklin large igneous province; *Lithosphere*, v. 7, no. 3, p. 275–295.
- Davis, W.J., Rainbird, R.H., Gall, Q. and Jefferson, C.J. 2008: In situ U-Pb dating of diagenetic apatite and xenotime: paleo-fluid flow history within the Thelon, Athabasca and Hornby Bay basins; *Geochimica et Cosmochimica Acta, Supplement*, v. 72, p. A203.
- Dawes, P.R. 1997: The Proterozoic Thule supergroup, Greenland and Canada: history, lithostratigraphy and development; *Geology of Greenland Survey, Bulletin 174*, 150 p.
- Dawes, P.R. 2006: Explanatory notes to the geological map of Greenland, 1:500 000, Thule, Sheet 5; Geological Survey of Denmark and Greenland, Map Series 2, 97 p.
- Dawes, P.R. 2009: Precambrian–Palaeozoic geology of Smith Sound, Canada and Greenland: key constraint to palaeogeographic reconstructions of northern Laurentia and the North Atlantic region; *Terra Nova*, v. 21, issue 1, p. 1–13.
- Day, J.M. 2013: Hotspot volcanism and highly siderophile elements; *Chemical Geology*, v. 341, p. 50–74.
- Day, J.M., Pearson, D.G. and Hulbert, L.J. 2008: Rhenium–osmium isotope and platinum-group element constraints on the origin and evolution of the 1.27 Ga Muskox layered intrusion; *Journal of Petrology*, v. 49, issue 7, p. 1255–1295.
- Denyszyn, S.W., Davis, D.W. and Halls, H.C. 2009a: Paleomagnetism and U-Pb geochronology of the Clarence Head dykes, Arctic Canada: orthogonal emplacement of mafic dykes in a large igneous province; *Canadian Journal of Earth Sciences*, v. 46, no. 3, p. 155–167.
- Denyszyn, S.W., Halls, H.C., Davis, D.W. and Evans, D.A. 2009b: Paleomagnetism and U-Pb geochronology of Franklin dykes in High Arctic Canada and Greenland: a revised age and paleomagnetic pole constraining block rotations in the Nares Strait region; *Canadian Journal of Earth Sciences*, v. 46, no. 9, p. 689–705.
- Dixon, J. 1974: Revised stratigraphy of the Hunting Formation (Proterozoic), Somerset Island, Northwest Territories; *Canadian Journal of Earth Sciences*, v. 11, no. 5, p. 635–642.
- Dixon, O.A., Williams, S.R. and Dixon, J. 1971: The Aston Formation (? Proterozoic) on Prince of Wales Island, Arctic

- Canada; Canadian Journal of Earth Sciences, v. 8, no. 7, p. 732–742.
- Dostal, J., Baragar, W.R.A. and Dupuy, C. 1983: Geochemistry and petrogenesis of basaltic rocks from Coppermine River area, Northwest Territories; Canadian Journal of Earth Sciences, v. 20, no. 5, p. 684–698.
- Dostal, J., Baragar, W.R.A. and Dupuy, C. 1986: Petrogenesis of the Natkusiak continental basalts, Victoria Island, Northwest Territories, Canada; Canadian Journal of Earth Sciences, v. 23, no. 5, p. 622–632.
- Dostal, J., Jackson, G.D. and Galley, A. 1989: Geochemistry of Neohelikian Nauyat plateau basalts, Borden rift basin, northwestern Baffin Island, Canada; Canadian Journal of Earth Sciences, v. 26, no. 11, p. 2214–2223.
- Dufour, F., Stevenson, R. and Halverson, G.P. 2020: Timing of emplacement of mafic rocks of the Fury and Hecla Group and younger mafic intrusions, northwestern Baffin Island, Nunavut; *in* Summary of Activities 2019, Canada-Nunavut Geoscience Office, p. 27–36, URL <https://m.cngo.ca/wp-content/uploads/Summary_of_Activities_2019-Paper_03.en_.pdf> [January 2021].
- Ernst, R. and Buchan, K.L. 2010: Geochemical database of Proterozoic intraplate mafic magmatism in Canada; Geological Survey of Canada, Open File 6016, 1 CD-ROM, URL <<https://doi.org/10.4095/261831>>.
- Fahrig, W.F. and Jones, D.L. 1969: Paleomagnetic evidence for the extent of Mackenzie igneous events; Canadian Journal of Earth Sciences, v. 6, no. 4, p. 679–688.
- Fahrig, W.F., Christie, K.W. and Jones, D.L. 1981: Paleomagnetism of the Bylot basins: evidence for Mackenzie continental tensional tectonics; *in* Proterozoic Basins of Canada, F.H.A. Campbell (ed.), Geological Survey of Canada, Paper 81-10, p. 303–312.
- French, J.E., Heaman, L.M. and Chacko, T. 2002: Feasibility of chemical U–Th–total Pb baddeleyite dating by electron microprobe; Chemical Geology, v. 188, p. 85–104.
- Galley, A.G. 1978: The petrology and chemistry of the Nauyat Formation volcanics, Borden Peninsula, northwestern Baffin Island; B.Sc. thesis, Carleton University, Ottawa, Ontario.
- Galley, A.G., Jackson, G.D. and Iannelli, T.R. 1983: Neohelikian subaerial basalts with ocean-floor type chemistry, northwestern Baffin Island; *in* Geological Association of Canada, Program with Abstracts, v. 8, p. A25.
- Geological Survey of Denmark and Greenland 2016: Geological map of Greenland; Geological Survey of Denmark and Greenland, Esri ArcGIS package, scale 1:500 000, URL <http://maps.greenmin.gl/geusmap/?mapname=greenland_portal&lang=en#baslay=baseMapGI&optlay=&extent=-5418170.925925926,5337598.96412037,6246-180.925925926,10710491.03587963&layers=northpole_graticule,grl_geus_500k_geology_map> [March 2020].
- Gibson, T.M., Shih, P.M., Cumming, V.M., Fischer, W.W., Crockford, P.W., Hodgskiss, M.S.W., Wörmle, S., Creaser, R.A., Rainbird, R.H., Skulski, T.M. and Halverson, G.P. 2018: Precise age of Bangiomorpha pubescens dates the origin of eukaryotic photosynthesis; Geology, v. 46, no. 2, p. 135–138.
- Gibson, I.L., Sinha, M.N. and Fahrig, W.F. 1987: The geochemistry of the Mackenzie dyke swarm, Canada; *in* Mafic Dyke Swarms, H.C. Halls and W.F. Fahrig (ed.), Geological Association of Canada, Special Paper 34, p. 109–121.
- Greenman, J.W., Patzke, M., Halverson, G.P. and Ielpi, A. 2018: Refinement of the stratigraphy of the late Mesoproterozoic Fury and Hecla Basin, Baffin Island, Nunavut, with a specific focus on the Agu Bay and Autridge formations; *in* Summary of Activities 2018, Canada-Nunavut Geoscience Office, p. 85–96, URL <https://m.cngo.ca/wp-content/uploads/Summary_of_Activities_2018-P08-Greenman.pdf> [January 2021].
- Griselin, M., Arndt, N.T. and Baragar, W.R.A. 1997: Plume–lithosphere interaction and crustal contamination during formation of Coppermine River basalts, Northwest Territories, Canada; Canadian Journal of Earth Sciences, v. 34, no. 7, p. 958–975.
- Halls, H.C., Hamilton, M.A. and Denyszyn, S.W. 2010: Paleomagnetism and U–Pb baddeleyite dating of the Melville Bugt and Ataa Sund dykes, Greenland; Sixth International Dyke Conference, February 4–7, 2010, Varanasi, India, abstracts volume.
- Harrison, J.C., Lynds, T., Ford, A. and Rainbird, R.H. 2016: Geology, simplified tectonic assemblage map of the Canadian Arctic Islands, Northwest Territories – Nunavut; Geological Survey of Canada, Canadian Geoscience Map 80, scale 1:2 000 000, URL <<https://doi.org/10.4095/297416>>.
- Hayes, B., Bédard, J.H., Hryciuk, M., Wing, B., Nabelek, P., MacDonald, W. and Lissenberg, C.J. 2015a: Sulfide immiscibility induced by wallrock assimilation in a fault-guided basaltic feeder system, Franklin Large Igneous Province on Victoria Island, Arctic Canada; Economic Geology, v. 110, p. 1697–1717, URL <<https://doi.org/10.2113/econgeo.110.7.1697>>.
- Hayes, B., Bédard, J.H. and Lissenberg, C.J. 2015b: Olivine-slurry replenishment and the development of igneous layering in a Franklin sill, Victoria Island, Arctic Canada; Journal of Petrology, v. 56, no. 1, p. 83–112, URL <<https://doi.org/10.1093/petrology/egu072>>.
- Hayes, B., Lissenberg, C.J., Bédard, J.H. and Beard, C. 2015c: The geochemical effects of olivine slurry replenishment and dolostone assimilation in the plumbing system of the Franklin Large Igneous Province, Victoria Island, Arctic Canada; Contributions to Mineralogy and Petrology, v. 169, art. 22, URL <<https://doi.org/10.1007/s00410-015-1117-8>>.
- Heaman, L.M. and LeCheminant, A.N. 1993: Paragenesis and U–Pb systematics of baddeleyite (ZrO₂); Chemical Geology, v. 110, issues 1–3, p. 95–126.
- Heaman, L.M., LeCheminant, A.N. and Rainbird, R.H. 1992: Nature and timing of Franklin igneous events, Canada: implications for a Late Proterozoic mantle plume and the breakup of Laurentia; Earth and Planetary Science Letters, v. 109, p. 117–131.
- Hoffman, P.F. 1988: Geology and tectonics, East Arm of Great Slave Lake, Northwest Territories; Geological Survey of Canada, Map 1628A, scale 1:250 000 (geology) and 1:500 000 (tectonics).
- Hulbert, L., Williamson, B. and Thériault, R. 1993: Geology of Middle Proterozoic Mackenzie diabase suites from Saskatchewan: an overview and their potential to host Noril'sk-type Ni–Cu–PGE mineralization; Saskatchewan Energy and Mines, Miscellaneous Report 93-4, p. 112–126.
- Irvine, T.N. 1970: Crystallization sequences in the Muskox intrusion and other layered intrusions, 1. olivine–pyroxene-

- plagioclase relations; Geological Society of South Africa, Special Publication 1, p. 441–476
- Jackson, G.D. 2000: Geology of the Clyde-Cockburn land map area, north-central Baffin Island, Nunavut; Geological Survey of Canada, Memoir 440, 316 p.
- Jackson, G.D. and Iannelli, T.R. 1981: Rift-related cyclic sedimentation in the Neohelikian Borden Basin, northern Baffin Island; *in* Proterozoic Basins of Canada, F.H.A. Campbell (ed.), Geological Survey of Canada, Paper 81-10, p. 269–302.
- Jones, D.L. and Fahrig, W.F. 1978: Paleomagnetism and age of the Aston dykes and Savage Point sills of the Boothia Uplift, Canada; Canadian Journal of Earth Sciences, v. 15, no. 10, p. 1605–1612.
- Jowitt, S.M. and Ernst, R.E. 2013: Geochemical assessment of the metallogenic potential of Proterozoic LIPs of Canada; Lithos, v. 174, p. 291–307.
- Kindle, E.D. 1973: Classification and description of copper deposits, Coppermine River Area, District of Mackenzie; Geological Survey of Canada, Bulletin 214, 109 p.
- LeCheminant, A.N. and Heaman, L.M. 1989: Mackenzie igneous events, Canada: Middle Proterozoic hotspot magmatism associated with ocean opening; Earth and Planetary Science Letters, v. 96, issues 1–2, p. 38–48.
- LeCheminant, A.N. and Heaman, L.M. 1991: U-Pb ages for the 1.27 Ga Mackenzie igneous events, Canada: support for a plume initiation model; Geological Association of Canada, Abstracts, v. 16, p. A73.
- LeMaitre, R.W. (ed.) 1989: A Classification of Igneous Rocks and Glossary of Terms, Recommendations of the IUGS Commission on the Systematics of Igneous Rocks; Blackwell, Oxford, England, 193 p.
- Long, D.G. and Turner, E.C. 2012: Tectonic, sedimentary and metallogenic re-evaluation of basal strata in the Mesoproterozoic Bylot basins, Nunavut, Canada: are unconformity-type uranium concentrations a realistic expectation?; Precambrian Research, v. 214, p. 192–209.
- Macdonald, F.A., Schmitz, M.D., Crowley, J.L., Roots, C.F., Jones, D.S., Maloof, A.C., Strauss, J.V., Cohen, P.A., Johnston, D.T. and Schrag, D.P. 2010: Calibrating the Cryogenian; Science, v. 327, p. 1241–1243.
- Mackie, R.A., Scoates, J.S. and Weis, D. 2009: Age and Hf–Nd isotopic constraints on the origin of marginal rocks from the Muskox layered intrusions (Nunavut, Canada) and implications for the evolution of the 1.27 Ga Mackenzie large igneous province; Precambrian Research, v. 172, p. 46–66.
- Max Planck Institute for Chemistry, comp. 2019: GEOROC, geochemistry of rocks of the oceans and continents; Max Planck Institute for Chemistry, database, URL <<http://georoc.mpch-mainz.gwdg.de/georoc/>> [October 2019].
- Mayr, U., Brent, T.A., de Freitas, T., Frisch, T., Nowlan, G.S. and Okulitch, A.V. 2004: Geology of eastern Prince of Wales Island and adjacent smaller islands, Nunavut; Geological Survey of Canada, Bulletin no. 574, 88 p., 1 CD-ROM, URL <<https://doi.org/10.4095/215690>>.
- Middlemost, E.A.K. 1994: Naming materials in the magma/igneous rock system; Earth-Science Reviews, v. 37, p. 215–224.
- Naldrett, A.J. 2004: Ore deposits associated with flood basalt volcanism; *in* Magmatic Sulfide Deposits, A.J. Naldrett (comp.), Springer, Berlin, Heidelberg, p. 137–278.
- Oakey, G.N. 2005: Cenozoic evolution and lithosphere dynamics of the Baffin Bay-Nares Strait region of Arctic Canada and Greenland; Ph.D. thesis, Vrije Universiteit Amsterdam, Amsterdam, The Netherlands, 233 p.
- Oakey, G.N. and Damaske, D. 2006: Continuity of basement structures and dyke swarms in the Kane Basin region of central Nares Strait constrained by aeromagnetic data; Polarforschung, v. 74, no. 1–3, p. 51–62.
- Palmer, H.C. and Hayatsu, A. 1975: Paleomagnetism and K-Ar dating of some Franklin lavas and diabases, Victoria Island; Canadian Journal of Earth Sciences, v. 12, no. 8, p. 1439–1447.
- Patzke, M., Greenman, J.W., Ielpi, A. and Halverson, G.P. 2018: Sedimentology of the sandstone-dominated units in the Fury and Hecla Basin, northern Baffin Island, Nunavut; *in* Summary of Activities 2018, Canada-Nunavut Geoscience Office, p. 75–84, URL <https://m.cngo.ca/wp-content/uploads/Summary_of_Activities_2018-P07-Patzke.pdf> [January 2021].
- Pearce, J.A. 2014: Immobile element fingerprinting of ophiolites; Elements, v. 10, p. 101–108.
- Pehrsson, S.J. and Buchan, K.L. 1999: Borden dykes of Baffin Island, Northwest Territories: a Franklin U-Pb baddeleyite age and a paleomagnetic reinterpretation; Canadian Journal of Earth Sciences, v. 36, p. 65–73.
- Schwab, D.L., Thorkelson, D.J., Mortensen, J.K., Creaser, R.A. and Abbott, J.G. 2004: The Bear River dykes (1265–1269 Ma): westward continuation of the Mackenzie dyke swarm into Yukon, Canada; Precambrian Research, v. 133, issues 3–4, p. 175–186.
- Sevigny, J.H., Cook, F.A. and Clark, E.A. 1991: Geochemical signature and seismic stratigraphic setting of Coppermine basalts drilled beneath the Anderson Plains in northwest Canada; Canadian Journal of Earth Sciences, v. 28, no. 2, p. 184–194.
- Shellnutt, J.G., Dostal, J. and Keppie, J.D. 2004: Petrogenesis of the 723 Ma Coronation sills, Amundsen Basin, Arctic Canada: implications for the break-up of Rodinia; Precambrian Research, v. 129, issues 3–4, p. 309–324.
- Skulski, T., Rainbird, R.H., Turner, E.C., Meek, R., Ielpi, A., Halverson, G.P., Davis, W.J., Mercadier, J., Girard, E. and Loron, C.C. 2018: Bedrock geology of the Dismal Lakes–lower Coppermine River area, Nunavut and Northwest Territories: GEM-2 Coppermine River Transect, report of activities 2017–2018; Geological Survey of Canada, Open File 8522, 37 p.
- Steenkamp, H.M., Bovingdon, P.J., Dufour, F., G  n  reux, C.-A., Greenman, J.W., Halverson, G.P., Ielpi, A., Patzke, M. and Tinkham, D.K. 2018: New regional mapping of Precambrian rocks north of Fury and Hecla Strait, northwestern Baffin Island, Nunavut; *in* Summary of Activities 2018, Canada-Nunavut Geoscience Office, p. 47–62, URL <https://m.cngo.ca/wp-content/uploads/Summary_of_Activities_2018-P04-Steenkamp.pdf> [January 2021].
- St-Onge, M.R., Harrison, J.C., Paul, D., Tella, S., Brent, T.A., Jauer, C.D. and Maclean, B.C. 2015: Tectonic map of Arctic Canada; Geological Survey of Canada, Canadian Geoscience Map 187, 1 sheet, URL <<https://doi.org/10.4095/295945>>.
- Williamson, N., Ootes, L., Rainbird, R.H., B  dard, J.H. and Cousens, B. 2016: Initiation and early evolution of a continental flood basalt province preserved in the 720 Ma Natkusiak Formation, Victoria Island, Canadian Arctic; Bulletin of Volcanology, v. 78, no. 3, art. 19, URL <<https://doi.org/10.1007/s00445-016-1012-9>>.



Geochemistry and mineralogy of glacial sediments and geomorphology of the Jungersen River area, northwestern Baffin Island, Nunavut

T. Tremblay¹

¹Canada-Nunavut Geoscience Office, Iqaluit, Nunavut, tommy.tremblay@canada.ca

The Fury and Hecla Geoscience Project (FHGP) was led by the Canada-Nunavut Geoscience Office in collaboration with Crown-Indigenous Relations and Northern Affairs Canada, and researchers and students from Laurentian University, McGill University and Université du Québec à Montréal. The multiyear project involved mapping and sampling of Archean, Proterozoic and Paleozoic rocks, and Quaternary surficial deposits and features. The study area comprised all or parts of nine 1:250 000 scale NTS map areas north and south of Fury and Hecla Strait on Baffin Island and Melville Peninsula, respectively (NTS 37C, F, 47C–H and 48A).

Tremblay, T. 2021: Geochemistry and mineralogy of glacial sediments and geomorphology of the Jungersen River area, northwestern Baffin Island, Nunavut; in Summary of Activities 2020, Canada-Nunavut Geoscience Office, p. 47–62.

Abstract

In the summer of 2019, fieldwork was conducted in the Jungersen River area located on northwestern Baffin Island, Nunavut, to document glacial dynamics at a regional scale and mineral prospectivity using till sampling. Field-based glacial geomorphology observations have been integrated with elements from previous surficial geology maps and field observations, and the analysis of pebble lithology in till samples. Laboratory work was performed on the till samples, including geochemical, heavy minerals and sedimentological analyses. Mineral exploration potential was found for diamonds in the study area and for white and translucent corundum south of the study area. The geochemical and mineralogical data will complement existing baseline data to guide any potential future mineral exploration and infrastructure studies in the region.

Introduction

In the summer of 2019, fieldwork was conducted in the Jungersen River area on northwestern Baffin Island, Nunavut (Figure 1). This work is the surficial geology component of the Fury and Hecla Geoscience Project and the objective is to reconstruct the glacial history and evaluate the mineral potential from the study of glacial sediments in this large underexplored territory. Ice-flow indicators were recorded and till samples were collected for geochemical, sedimentological and heavy mineral analyses. For the glacial geomorphology mapping, field and remote sensing data were used. The geochemical and mineralogical data from till samples collected for this project will provide additional baseline data to guide potential future mineral exploration and infrastructure studies (permafrost and geotechnical) in the region. This survey is a continuation of fieldwork started in 2018 for which two reports have already been published (Tremblay and Godbout, 2018; Tremblay et al., 2020).

Regional setting

The study area is located on northwestern Baffin Island, 100 km south of the Hamlet of Arctic Bay and 200 km northwest of the Hamlet of Igloolik, between southern

Borden and Brodeur peninsulas (Figure 1). The majority of the region lies below 200 m above sea level (asl); there are several lowlands with generally undulating relief that are interconnected between the major marine water bodies, and there are a few Quaternary sediment-filled flat valleys, especially near the mouths of major rivers (Magda River, Jungersen River) that drain into Jungersen Bay. The plateaus on Brodeur and Borden peninsulas are generally between 200 and 400 m asl, with a maximum elevation of 501 m asl north of Moffet Inlet (Figure 2).

The bedrock geology of the study area (Figure 3; Chandler, 1980; de Kemp and Scott, 1998; Steenkamp et al., 2018; Lebeau et al., 2020) primarily consists of basement lithologies of the Archean and Paleoproterozoic Rae domain (felsic orthogneiss, mafic-ultramafic and felsic intrusive bodies, metasedimentary rocks, volcanic rocks and banded iron formation rocks), unconformably overlain by Mesoproterozoic rocks of the Fury and Hecla Group (quartzitic sandstone, sandstone, mudstone, carbonate and volcanic rocks). Neoproterozoic mafic dykes and sills intrude older Precambrian rocks. Paleozoic carbonate rocks and quartzitic sandstones overlie basement rocks on the Borden and Brodeur peninsulas.

This publication is also available, free of charge, as colour digital files in Adobe Acrobat® PDF format from the Canada-Nunavut Geoscience Office website: <https://cngo.ca/summary-of-activities/2020/>.

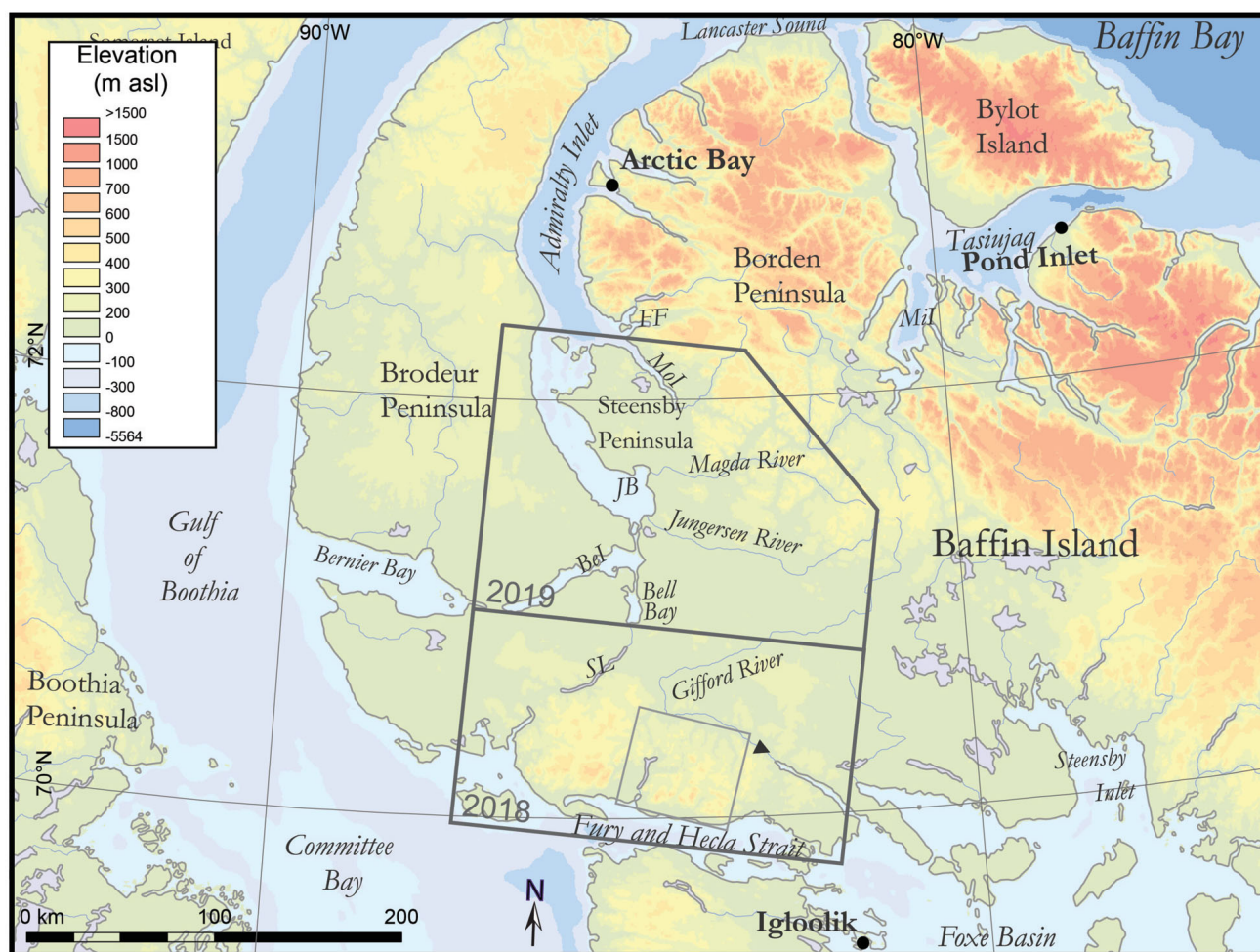


Figure 1: Location of study area on northwestern Baffin Island, Nunavut. Digital elevation model and bathymetry from GEBCO (GEBCO Compilation Group, 2014). Location of study areas in 2018 and 2019 outlined in dark grey, and location of Figure 7 outlined in light grey. Triangle indicates base camp location. Abbreviations: Bel, Berlinguet Inlet; FF, Fabricius Fiord; JB, Jungersen Bay; Mil, Milne Inlet; Mol, Moffet Inlet; SL, Saputing Lake.

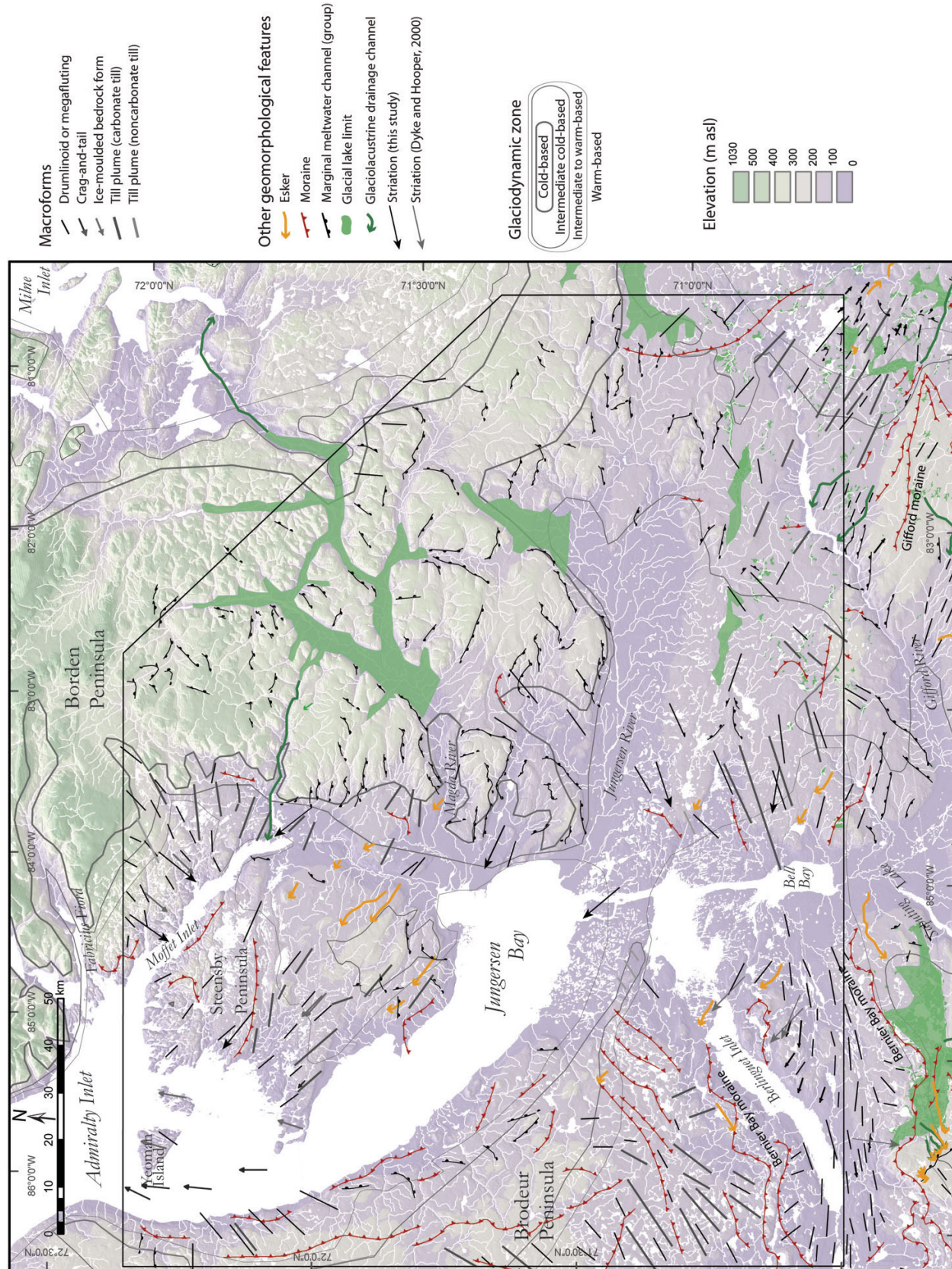
Previous work

Glacial and postglacial marine histories of the area between Berlinguet Inlet and Fury and Hecla Strait are described in Hooper (1996), whereas ice-flow directions (including striae) and till composition (texture analysis, petrographic counts, geochemical and heavy minerals analyses) are published in de Kemp and Scott (1998), Dyke and Hooper (2001) and Utting et al. (2008). The ice-flow chronology for the study area, based on striations, macroforms and glacial dispersion evidence, is documented in Tremblay and Godbout (2018) and Tremblay et al. (2020). Surficial geology mapping was completed at a scale of 1:250 000 over the entire study area (Dyke, 2000a, b, 2004; Dyke and Hooper, 2000; Hooper and Dyke, 2000). More recently, De Angelis (2007) and Margold et al. (2015) used satellite imagery to map macroforms, glaciodynamic settings (some cold-based zones) and ice streams. During the last glacial cycle, ice streams were present over northern Melville Peninsula, and in Fury and Hecla Strait, Bernier Bay, Admiralty Inlet and Steensby Inlet (Hooper, 1996; Dredge, 2000; Dyke,

2008; Tremblay and Paulen, 2012; Tremblay and Godbout, 2018). Local ice divides persisted on the Saputing Lake–Gifford River plateau (Gifford-Saputing ice divide; Tremblay and Godbout, 2018), Brodeur Peninsula and Borden Peninsula (Dyke and Prest, 1987). Previous work provided radiocarbon dating data on shells, which helped to document the ice retreat and the chronology of the last deglaciation in the region (Hooper, 1996; Dyke and Hooper, 2001; Dyke et al., 2003; McNeely et al., 2006; Dalton et al., 2020). The economic geology of the region, based on till studies, was published in de Kemp and Scott (1998), Utting et al. (2008), Tremblay et al. (2020) and in various mineral exploration industry reports (Craigie, 2001, 2006; Winzar and McKenzie, 2005), and highlighted mineral potential for iron, diamonds, uranium and corundum (white and translucent, from an unknown source).

Methods

In July 2019, helicopter-supported (Bell Helicopter Textron 206 LR) fieldwork was conducted during seven



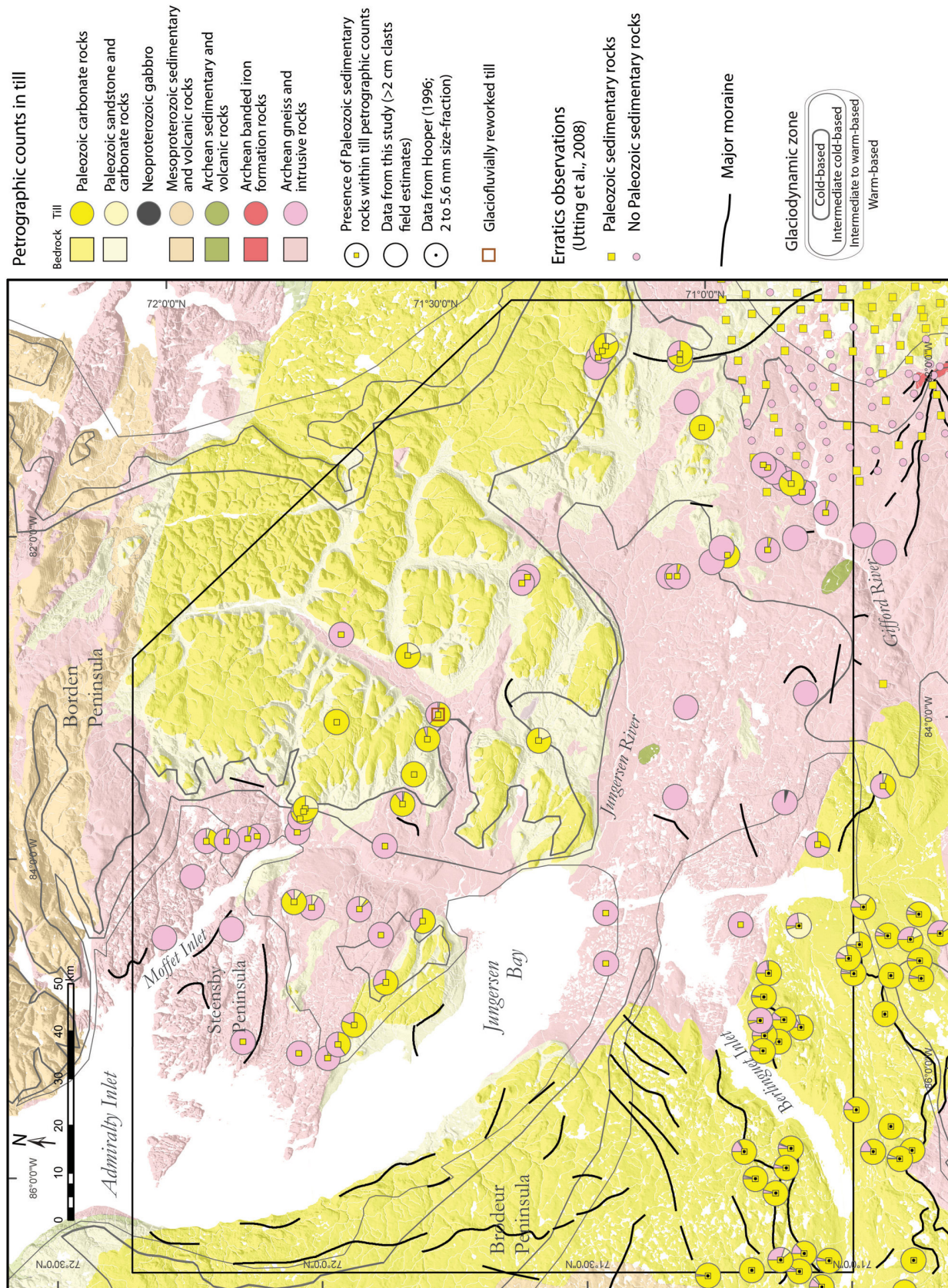


Figure 3: Bedrock geology (modified from de Kemp and Scott, 1998, and Lebeau et al., 2020) and till clast petrography, Jungersen River area, northwestern Baffin Island. Study area outlined in black.

days in the Jungersen River area from a base camp located along the Gifford River (Figure 1). Numerous geomorphological elements were documented from air and ground observations (Figure 2), striations were measured at eight sites and till was sampled from frost boils, between 0 and 30 cm from the surface, at 47 sites. For each till sample, about 2 kg of material was recovered for geochemical and sedimentological analyses, and for 42 samples about 8 kg was recovered for heavy minerals analysis. Till pebble lithologies (>2 cm size-fraction) were counted in the field at surface sample sites (Figure 3) to complement provenance studies.

Till geochemical and sedimentological analyses

The till samples (n=47) were processed at the Geological Survey of Canada (GSC) Sedimentology Laboratory in Ottawa (Ontario) following the protocol described in McClenaghan et al. (2020). Each sample was air dried and split to recover the <63 µm fraction for geochemical analysis. Another portion was used for grain-size analysis, and for the determination of inorganic carbon content, loss-on-ignition (LOI), carbonate content and Munsell colour. Finally, a third portion was saved for archival purposes.

The grain-size distribution (sand, silt, clay) of the till sample was documented using a Beckman Coulter, Inc. LS 13 320 laser particle-sizing analyzer on the <63 µm fraction (see Girard et al., 2004 for details on laboratory protocols). The grain size of fractions between 63 µm and 2 mm was determined by wet sieving on the >45 µm and <2 mm fraction, and by dynamic digital image processing using a HORIBA, Ltd.'s CAMSIZER particle size and shape analysis system. Inorganic carbon content and LOI were determined with a LECO® Corporation CR412 carbon analyzer and the carbonate content was determined by titration with UIC Inc.'s CM5015 CO₂ coulometer with CM5230 acidification module on the <63 µm fraction, on a (maximum) 2 g sample. The colour of the dry sediment was measured using X-Rite, Incorporated's SP64 portable sphere spectrophotometer.

A split of the <63 µm fraction was shipped to Bureau Veritas Minerals in Vancouver (British Columbia) for geochemical analysis. A 30 g split was digested with modified aqua regia and analyzed by inductively coupled plasma-mass spectrometry (ICP-MS) for 65 elements, including gold, base metals, platinum and rare-earth elements. Another 2 g split was analyzed using a lithium metaborate-tetraborate fusion and digestion in nitric acid followed by inductively coupled plasma-emission spectrometry (ICP-ES) for major oxides and ICP-MS for trace elements. Analytical accuracy and precision were monitored by including GSC CANMET-certified standards (TILL-2 and TILL-4) inserted into the sample batch at the GSC Sedimentology Laboratory and additional quality control samples inserted by Bureau Veritas Minerals (laboratory duplicates of sam-

ples, blanks, reference standards and analytical duplicates). For some till samples, the <2 µm fraction was geochemically analyzed using the methods described above. The <2 µm size-fraction of the till samples from de Kemp and Scott (1998) and Utting et al. (2008) were analyzed with ICP-ES and ICP-MS, respectively, after aqua-regia digestion.

Heavy mineral analysis

The bulk till samples (8 kg average total weight, n=42) were collected to produce heavy mineral concentrates (HMC) for the recovery of indicator minerals, including kimberlite-indicator minerals (KIMs), sulphides, platinum-group minerals, gold, gemstones and other minerals of interest using methods described in Plouffe et al. (2013). Samples were sent to Overburden Drilling Management Limited (ODM; Ottawa, Ontario) for heavy mineral analysis.

A standard pre-analysis treatment was applied to all samples, which included initial sieving of pebbles (>2 mm fraction; the 4–8 mm fraction was separated for lithological counts) and preconcentration of heavy minerals on a shaking table. The table concentrate was panned to recover gold grains and metallic-indicator minerals, which were counted, described and returned to the preconcentrate. The heavy mineral preconcentrate was then further refined using heavy liquid separation (methylene iodide, specific gravity of 3.2) and ferromagnetic separation. The >0.25 mm fraction of the nonferromagnetic heavy mineral concentrate (NFHMC) was examined with a binocular microscope and various distinctive mineral species including KIMs and metamorphic massive-sulphide indicator minerals (MMSIMs), which included gahnite, red rutile, pyrite, chalcopyrite, arsenopyrite and other minerals (Averill, 2001), were visually identified.

The mineralogical picking was performed on three different size fractions (0.25–0.5 mm, 0.5–1 mm, 1–2 mm) of the NFHMC. Following further preparation, binocular microscope identification of MMSIMs and KIMs was undertaken and supported in specific cases by scanning electron microscope (SEM) analysis. The indicator mineral abundances in the NFHMC reported by ODM were subsequently normalized to 10 kg of the <2.0 mm material (table feed) prior to the interpretation of the data.

Results and discussion

Glacial geomorphology

The regional glacial geomorphology of the study area is presented in Figure 2 (nomenclature used is similar to that of Tremblay and Godbout [2018]). Landforms were generalized from airphotos and previous surficial geology maps and datasets (see 'Previous work' section), and updated with information from observations and interpretations

based on new field data, petrographic analysis and interpretations from satellite imagery (SPOT 6), georeferenced field photographs, digital elevation models (DEMs; ArcticDEM [Porter et al., 2018], Canadian digital elevation model [CDEM; Natural Resources Canada, 2016], high-resolution digital elevation model [HRDEM; Natural Resources Canada, 2018]) and high-definition multibeam data from the Canadian Coast Guard Ship *Amundsen* (Ocean Mapping Group, 2019). Figure 2 shows geomorphological features indicative of ice-flow dynamics (macroforms and striations), ice-retreat patterns (eskers, proglacial lakes and locations of the glaciolacustrine drainage channels [Figure 4a]) and ice-front positions (ice-marginal moraines, ice-marginal channels). In some areas, the configuration (orientation) of the retreating ice-margin dammed proglacial lakes in confined topographic lows (valleys). Some macroforms are the result of direct bedrock erosion by the ice, whereas others are the result of ice streamlining forms in till (drumlinoids and megaflutings), or bedrock and till (crag-and-tail features). Linear glacial landforms (macroforms) likely of subglacial origin, identified as till plumes, can be >10 km in length and are subdivided into those formed in mostly carbonate till versus those formed in mostly noncarbonate till (typical shield till; Figure 2). On the ground, they commonly appear as patches of a thicker or finer grained till and visually contrast with the surrounding boulder fields and till areas.

Glaciodynamic zones

The mapping of glaciodynamic zones aims at characterizing the amount of glacial activity (degree of erosion and transport) that took place during the recent Quaternary in a specific area (Figure 2). The mapping system used here is similar to the one employed in previous CNGO projects (Tremblay and Paulen, 2012; Tremblay et al., 2014) and in a recent synthesis paper on glacial geomorphology in central Nunavut (McMartin et al., 2020), in which they are termed ‘glacial landscapes’. Glaciodynamic zones are delineated primarily from field observations, airphotos, satellite imagery and DEM interpretations.

Cold-based zone

Cold-based zones (CBs) correspond to areas where signs of glacial erosion (e.g., striae, macroforms, glacially eroded outcrops, etc.) are virtually absent from the landscape (Figure 2). These zones are characterized by the scarcity or absence of small lakes and by an increased proportion of dendritic river systems versus deranged river systems. The analysis of cosmogenic isotopes (^{10}Be , ^{26}Al) in samples from a similar setting on a cold-based plateau on nearby Melville Peninsula shows that the surface sediments date or predate the last interglacial period (Tremblay and Gosse, 2019) and are usually composed of regolith (i.e., in situ bouldery diamictic material; Figure 4a–c), which may have been minimally transported by ice. Precambrian crystalline

rock outcrops are moderately to extensively weathered. Paleozoic rocks are often present as tors (Figure 4c, e). In the study area, CBs are frequently located on plateaus, which suggests a strong topographic control. The bedrock morphology and structure are not commonly reflected in the overall cold-based terrain topography. Ice-marginal parallel channels are frequently observed in association with subaerial or marginal meltwater sediments and landforms. The degree of glacial erosion associated with the dispersion of erratics is very restricted (see ‘Glacial dispersal studies’ section). The unerosive character of ice suggests the surface till and regolith cover, as well as the glacial transport of erratics, might have occurred incrementally during the Wisconsinian and previous glaciations.

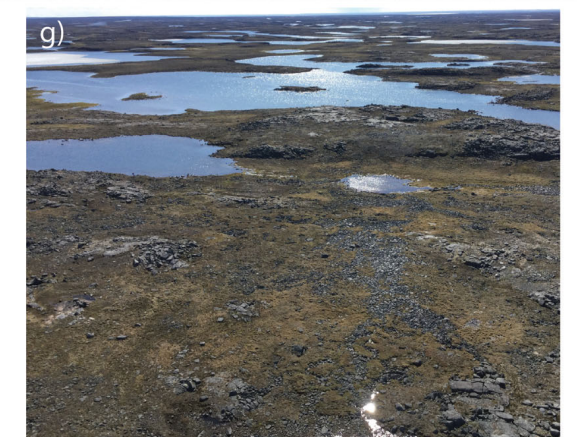
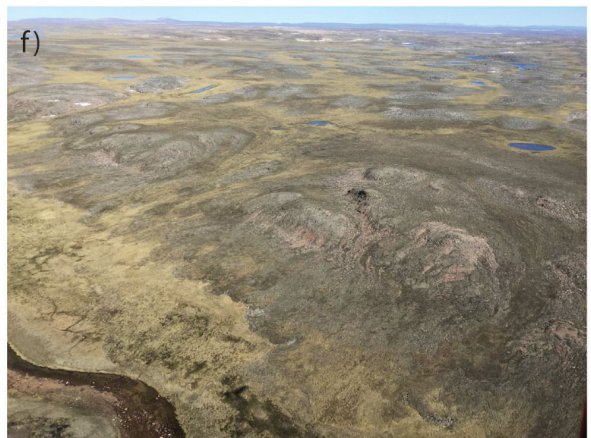
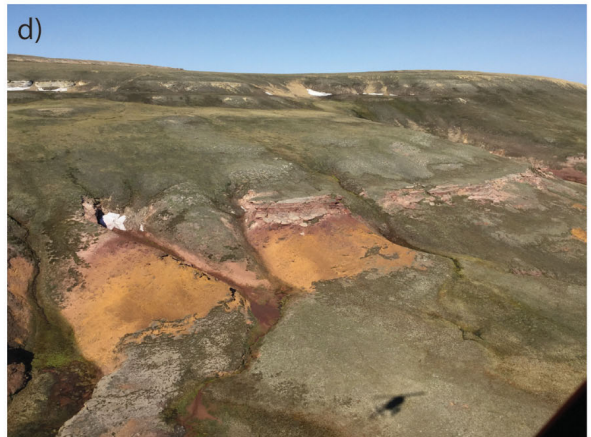
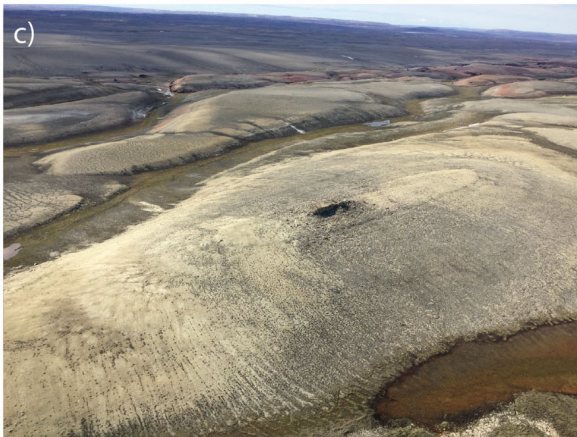
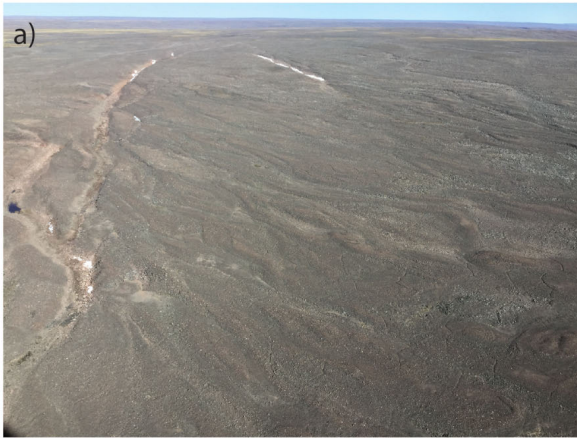
Intermediate cold-based zone

The intermediate cold-based zone (IB) represents a transition area where at least one or more of the criteria for a cold-based glaciation are not fulfilled. Starting from its contact with the cold-based zone, signs of glacial erosion gradually appear in the intermediate cold-based landscape as more lakes, bedrock outcrops devoid of regolith, macroforms and ultimately streamlined outcrops are observed. Near the border of the IB-CB, striae and roches moutonnées are rare and, if present, occur on the most prominent outcrops composed of weather-resistant lithologies, such as gabbro dykes. The greater abundance of striations toward the IB–warm-based zone (WB) border corresponds to a similar increase in the number of poorly to well-defined roches moutonnées. Meltwater channels are still relatively abundant in places compared to CBs.

Intermediate to warm-based zone

The transition between intermediate cold-based and warm-based zones is highly diffuse in some areas and consequently a zone identified as intermediate to warm-based was mapped (see McMartin et al., 2020; Figure 4f). In this zone, several indications of warm-based glacial erosion are present but the bedrock is still weathered and not striated enough to fall under the warm-based zone category.

Figure 4: Photographs of geomorphological features in different glaciodynamic settings, Jungersen River area, northwestern Baffin Island: **a)** ice-marginal channels cut into regolith/till terrain over Precambrian crystalline rocks, in cold-based zone; **b)** regolith (and thin till?) terrain over Paleozoic sandstone and carbonate rocks, in cold-based zone; **c)** regolith and thin till terrain over Paleozoic sandstone and carbonate rocks, with tor on top of hill, in cold-based zone; **d)** gossan in Paleozoic sandstone, in intermediate cold-based zone; **e)** tor in Paleozoic sandstone, in intermediate cold-based zone; **f)** bedrock, regolith and till (with 10% carbonate content) mix over Precambrian crystalline rocks, in intermediate to warm-based zone; **g)** till overlying and bedrock outcrops of Precambrian crystalline rocks, in warm-based zone; **h)** till (with about 50% Precambrian crystalline rocks content) overlying Paleozoic carbonate rocks, in warm-based zone.



Warm-based zone

The warm-based zone (WB) landscapes are characterized by a variable boulder cover and, from the IB-WB contact inward, display increasing signs of glacial erosion, such as streamlined outcrops and bedrock hills (Figure 4g), linear glacial erosion corridors, macroforms (drumlins, flutings, ice-moulded bedrock forms), abundant lakes and prevalent deranged drainage system. Striae are abundant on outcrops that are relatively resistant to permafrost action and weathering whereas they are typically absent from mudstone and carbonate rock outcrops. Till thickness is variable over both Precambrian crystalline rocks and Paleozoic rocks (Figure 4h) with significant glacial transport distances documented (over 10 km).

Ice-flow chronology

Figure 5 shows an ice-flow chronology for the study area, which was synthesized from striations, macroforms (Figure 2) and glacial dispersion evidence (see ‘Glacial dispersal studies’ section). During the last glaciation, local ice divides persisted on central Brodeur and central Borden peninsulas. The main regional ice flow, probably during Last Glacial Maximum (LGM) and part of the deglaciation, was influenced by the presence of ice streams flowing toward Admiralty Inlet (Admiralty Inlet ice stream) and toward Bernier Bay (Figure 1; Bernier Bay ice stream). Abundant elongated streamlined glacial landforms present on the seafloor of Admiralty Inlet and Bernier Bay, as revealed by multibeam imaging (Ocean Mapping Group, 2019), and on Yeoman Island (Figure 2) are interpreted as evidence of ice streams. A strong converging pattern of ice flow is also found in Moffet Inlet, perhaps suggesting a late ice-stream pattern. Subsequent ice-flow deflection linked with restrained flows existed in the Foxe Basin (to the southeast of the study area; Figure 1) and Fury and Hecla Strait (to the south; Figure 1), the most prominent being a southeastward ice flow toward Steensby Inlet (Figure 1; Steensby Inlet ice stream), which was probably active for only a few centuries around 7 cal. ka BP (Dyke, 2008). Noticeable deflections in the ice-retreat configuration occurred toward the Bernier Bay moraine (Figure 2), as well as in a few localities north of Fury and Hecla Strait. The orientation of the ice margin during ice retreat, as indicated by the configuration of short eskers, moraines, marginal channels and proglacial lakes (Figure 5), was probably associated with sluggish (mostly cold-based?) ice flow during deglaciation. The ice pushed material at the glacier front, accounting for the deposition of most of the moraines (e.g., Gifford moraine, moraines on Steensby and Brodeur peninsulas; Figure 2). Deglaciation of the Admiralty Inlet area took place between 11.0 cal. ka BP (10.3 cal. ka BP in this study area) and 8.1 cal. ka BP (Dyke et al., 2003; Dalton et al., 2020). Numerous samples were collected to refine the deglaciation chronology in the study area: shells for radiocarbon dating, sandy sediments for infrared stimulated lu-

minescence (IRSL) dating and bedrock outcrops/boulders for surface exposure dating.

Glacial dispersal studies

The till petrographic compositions shown in Figure 3 represent ground counts of clasts >2 cm from this study, counts from the 2 to 5.6 mm size-fraction by Hooper (1996) and his original field notes on airphotos, and occurrence of carbonate cobbles and boulders at the surface by De Beers Canada Exploration Inc. and A. Dyke (Geological Survey of Canada) as reported by Utting et al. (2008). The combination of these past results with present observations provide essential information about the regional glacial transport processes and ice-flow history, even though data presented in Figure 3 represent results from different size-fractions of till.

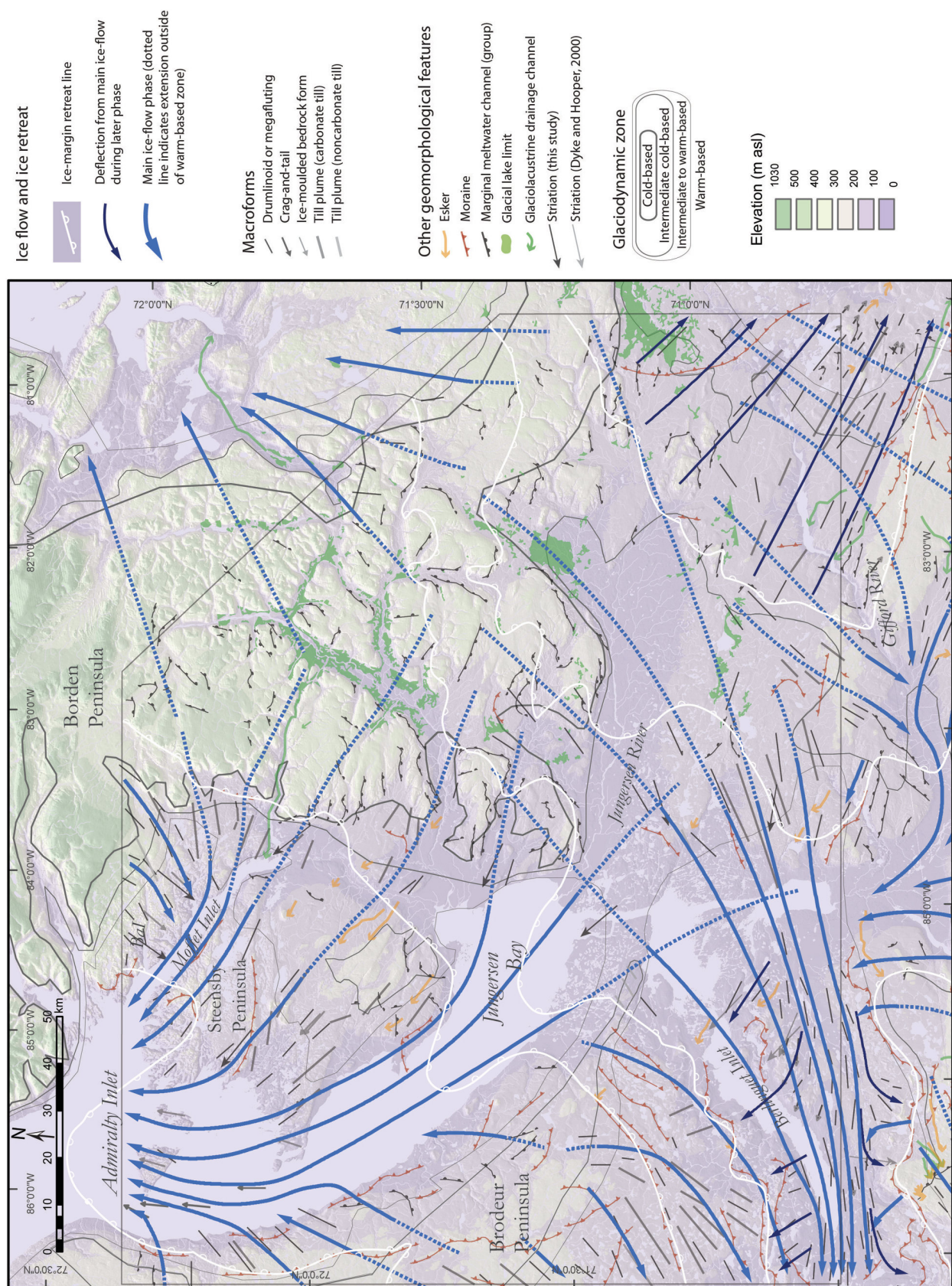
The glaciodynamic zones (Figure 2) have an important impact on the distance of glacial transport. Warm-based ice is characterized by long distance transport of Precambrian rocks over Paleozoic rocks (frequently more than 10 km), notably in the Berlinguet Inlet area and west of Moffet Inlet. Between Moffet Inlet and Jungersen Bay, the complex geometry of Paleozoic outcrops explains the diverse patterns observed in the erratic composition of the regional till. On the CB located south of the Jungersen River, the scarcity of erratic clasts near contacts between contrasting rock units (Paleozoic sedimentary rocks versus Precambrian crystalline rocks) indicates short distances of glacial transport, less than 1 km, with generally less than 1% erratic content after a few hundred metres of transport in the direction of ice flow. The presence of scattered Paleozoic carbonate clasts found immediately south of Jungersen Bay indicates a northward transport of about 15 km across an intermediate to warm-based area, and therefore suggests that these erratics were transported there during the early phase of the main ice flow. In the large valley north of Magda River, the results show a mix of Precambrian and Paleozoic rocks, although glaciofluvial input might explain most of this diversity of rock types in the surface sediments. Overall, these glacial transport distances compare broadly with those obtained on similar glaciodynamic terrains on Melville Peninsula (Tremblay and Paulen, 2012) and immediately south of the study area (Tremblay and Godbout, 2018).

Analytical results

Complete geochemistry and heavy mineral results are presented in Tremblay (2021)².

Elemental concentrations based on the <63 µm fraction of samples from this study (aqua-regia digestion, ICP-MS

²CNGO Geoscience Data Series GDS2021-001, containing the data or other information sources used to compile this paper, is available online to download free of charge at <https://cngo.ca/summary-of-activities/2020/>.



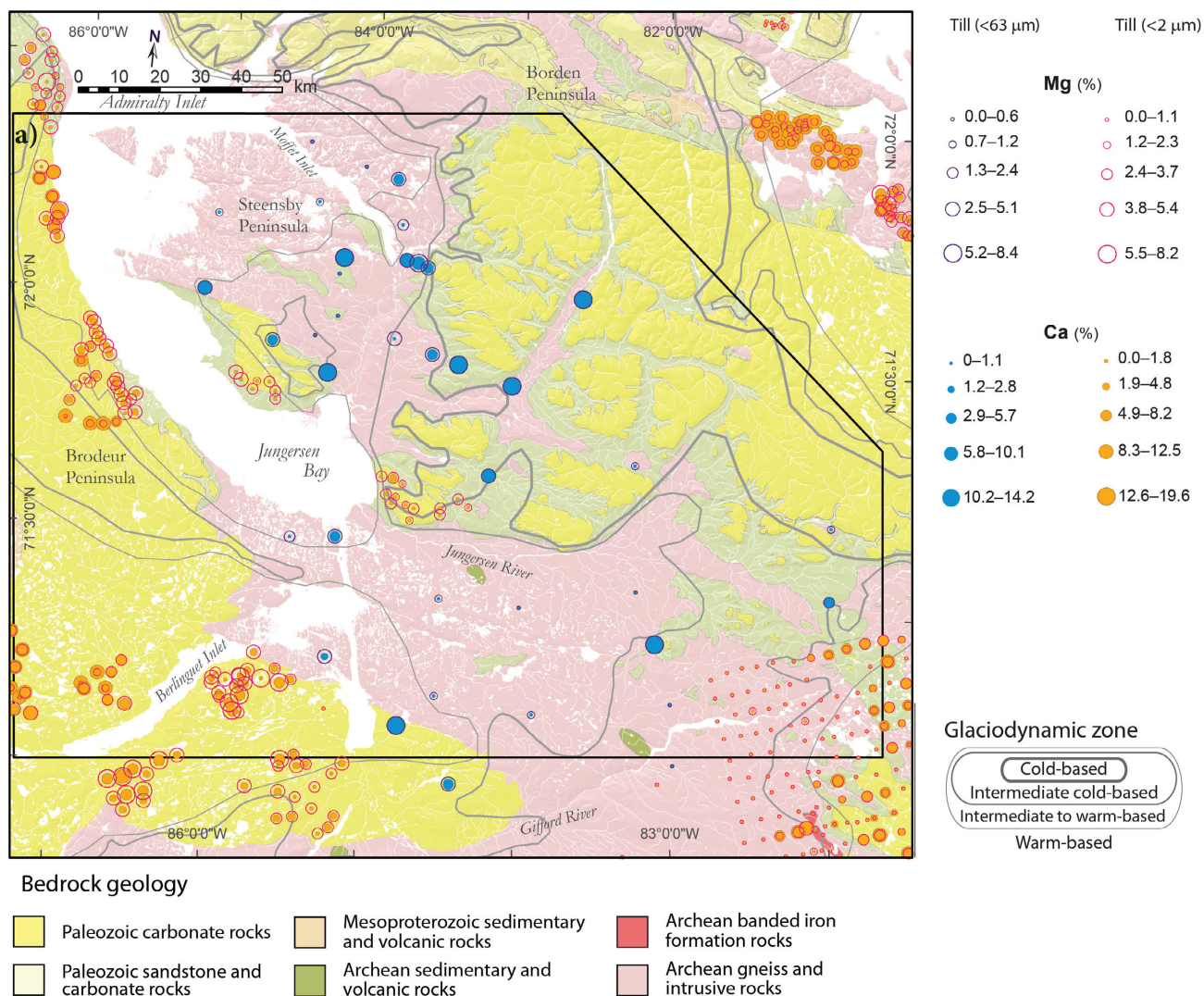


Figure 6: Sedimentology, geochemistry and heavy minerals results from till sampling programs, Jungersen River area, northwestern Baffin Island. Study area outlined in black. Background bedrock geology modified from de Kemp and Scott (1998) and Lebeau et al. (2020). **a)** Mg and Ca. Geochemical results are from the <63 µm fraction (blue full and dark blue outline circles; samples from this study) and from the <2 µm fraction (orange full and red outline circles; samples from de Kemp and Scott, 1998, and Utting et al., 2008).

analysis) and the <2 µm fraction of samples from de Kemp and Scott (1998; aqua-regia digestion, ICP-ES analysis), and Utting et al. (2008; aqua-regia digestion, ICP-MS analysis) and selected HMC minerals are shown on Figure 6. Even though the results of the till geochemistry analyses for both the <63 µm and <2 µm fractions are presented in Figure 6, the following interpretations are based only on the <63 µm fraction analysis due to the partitioning effect between both grain sizes (Shilts, 1993).

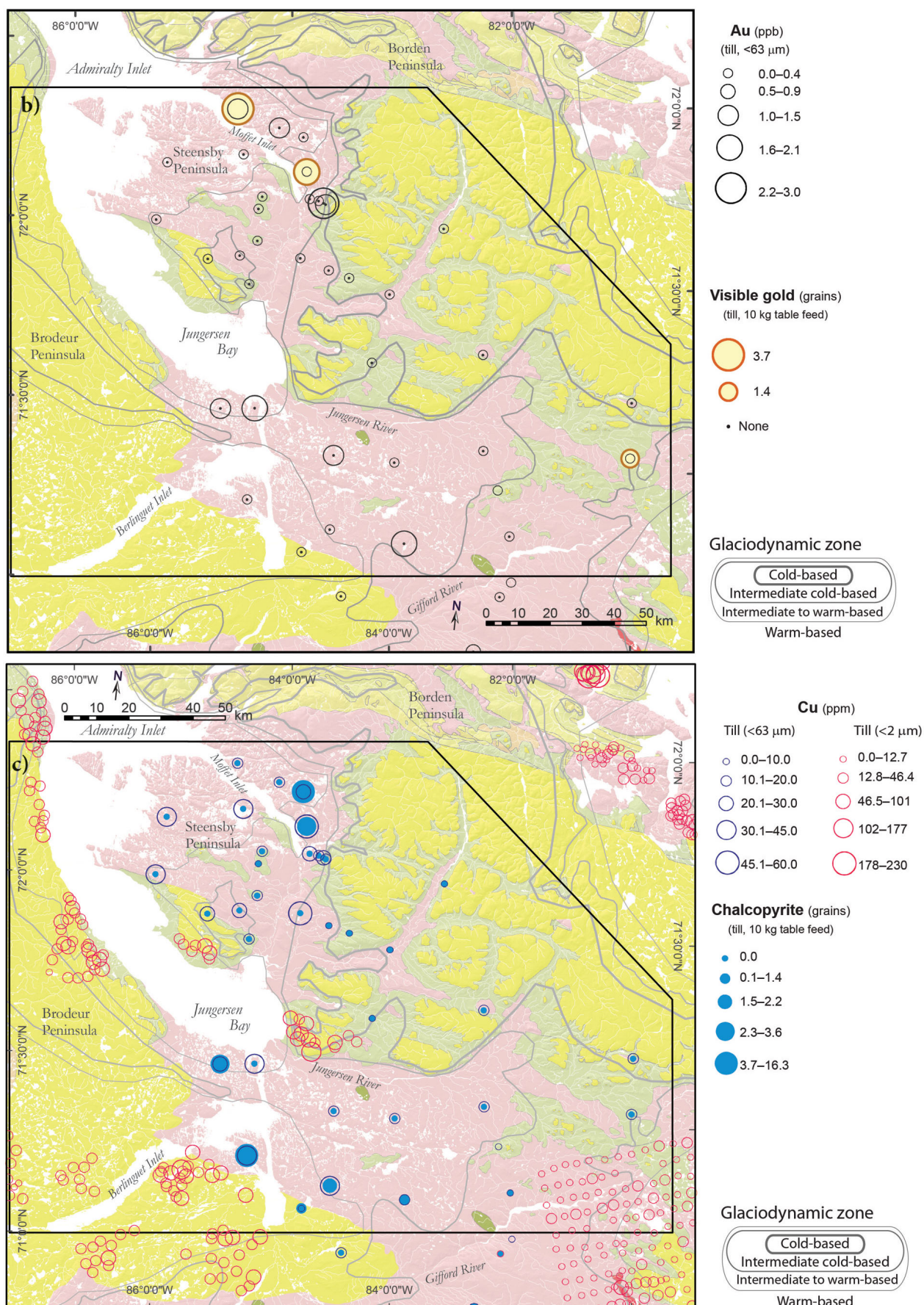
Figure 6a shows the samples with high Ca and Mg concentrations are associated with high Paleozoic sediment clast concentrations (Figure 3), which is expected since the concentrations of Ca and Mg in till (<63 µm fraction) over Precambrian crystalline rocks are typically <1% for both elements and typically around 12% for Ca and 8% for Mg over Paleozoic carbonate rocks. These results are similar to

those presented by Tremblay (2019). The other elements and minerals will be discussed in the next section.

Economic considerations

This surficial geological mapping and sampling program added new data about glacial transport paths and important geomorphological processes, which are critical compo-

Figure 6 (continued): Sedimentology, geochemistry and heavy minerals results from till sampling programs, Jungersen River area, northwestern Baffin Island. **b)** Au and gold grains normalized to 10 kg table feed (samples from this study). All grains are re-shaped (Averill, 2001). **c)** Cu and chalcopryrite grains from nonferromagnetic heavy mineral concentrate (NFHMC) normalized to 10 kg table feed. Geochemical results for Cu are from the <63 µm fraction (dark blue outline circles; samples from this study) and from the <2 µm fraction (red outline circles; samples from de Kemp and Scott, 1998, and Utting et al., 2008). See this page for background geology legend.



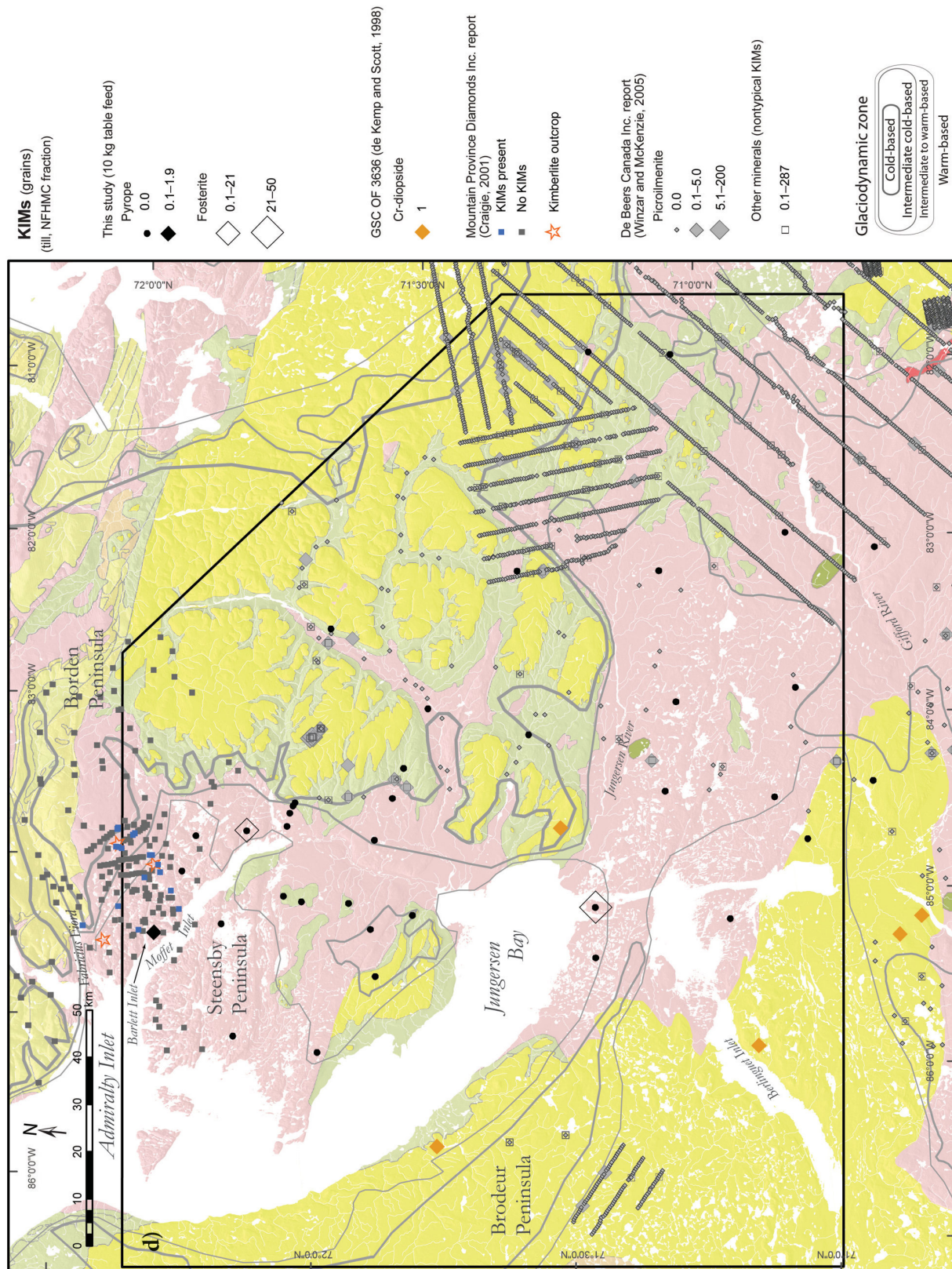


Figure 6 (continued): Sedimentology, geochemistry and heavy minerals results from till sampling programs, Jungersen River area, northwestern Baffin Island. **d)** kimberlite-indicator mineral (KIM) grains from nonferromagnetic heavy mineral concentrate (NF-HMC) normalized to 10 kg table feed, samples from this study, and KIM results from other studies. See page 56 for background geology legend. Abbreviations: Bal, Bartlett Inlet; GSC, Geological Survey of Canada; OF, Open File.

nents in interpreting the provenance of the surficial sediments and determining the significance of the geochemical and mineralogical data derived from these surficial sediments. These analyses will provide additional baseline information to guide future mineral exploration and infrastructure studies (permafrost conditions, granular aggregate sources) in the region. The sampling grid is widely spaced (about 15 km between sites) and the existence of undetected narrow till dispersal trains between sample sites cannot be excluded. In some regions of the study area, moderately elevated values for base and precious metals in till are indicative of a relatively low potential for mineral exploration. The highest anomalies in the study area are located around Moffet Inlet, with till samples showing anomalous values for gold grains (less than 4 grains/10 kg; Figure 6b), Au (less than 3.0 ppb; Figure 6b), chalcopyrite (less than 13 grains/10 kg; Figure 6c), Cu (less than 53 ppm; Figure 6c), Zn (less than 144 ppm; see Tremblay, 2021) and Pb (less than 24 ppm; see Tremblay, 2021). Around the eastern part of Berlinguet Inlet, other small anomalies are found in till for chalcopyrite (less than 16 grains/10 kg; Figure 6c), Cu (less than 42 ppm; Figure 6c) and Au (less than 1.7 ppb, with no associated gold grains; Figure 6b). The origins of these anomalies are unknown, but could be linked to small, unmapped, Archean–Paleoproterozoic supracrustal rocks (mafic–ultramafic and metasedimentary rocks), or rusty beds within the basal Paleozoic sandstone (Figure 4d). Immediately south of the study area (Tremblay, 2019), Au and gold grains values are found in metasedimentary rocks. Lebeau et al. (2020) also reported copper mineralization associated with paragneiss bedrock about 25 km east of study area.

Between Moffet Inlet and Fabricius Fiord, the work of several diamond exploration companies between 1999 and 2006, including Mountain Province Diamonds Inc., First Strike Diamonds Inc. and Patriotic Diamonds Inc. (Craigie, 2001, 2006), found several till samples (and a few stream sediment samples) with KIMs (including pyrope, chromite, picroilmenite, Cr-diopside and olivine; Figure 6d). This led to the discovery of 12 kimberlite occurrences (in bedrock or boulder regolith) with at least one containing microdiamonds. One till sample presented in this study contains 1.9 grains/10 kg pyrope grains (Figure 6d), significant KIMs, possibly within the dispersal train from the Bartlett Inlet anomalies or one of the Moffet Inlet region kimberlite outcrops. Two samples with high counts of fosterite (16 and 45 grains/10 kg samples) were

found near southern Moffet Inlet and southern Jungersen Bay, respectively; their origins might be linked to either kimberlite or ultramafic rocks. Additionally, three sites with Cr-diopside grains were found in the southwestern quadrant of the study area (Figure 6d; de Kemp and Scott, 1998). These Cr-diopside grains might have been transported a potentially considerable distance from the northeast due to the presence of an ice stream in the region (Bernier Bay ice stream). Diamond exploration using glacial sediments was conducted by De Beers Canada Inc. in northwestern Baffin Island (Winzar and McKenzie, 2005). The KIM data from that report indicate that picroilmenite is abundant in four samples (from 10 to 55 grains; Figure 6d) in this study area. These picroilmenites are sometimes associated with possibly unidentified KIMs, which were labelled as ‘other’. These picroilmenites occurring with other KIMs could potentially, but with low confidence, lead to undiscovered KIMs, although the absence of typical garnets, chromite and olivine do not support such interpretation. The Winzar and McKenzie (2005) report also indicates the presence of spinel in the study area, which seems to have a different source, probably nonkimberlitic (these results are not shown on Figure 6d).

In 2019, corundum grains were found in four till samples collected from the 2018 study area, in addition to the two corundum-bearing samples collected in 2018 (Figure 7; Tremblay et al., 2020). The corundum are white and translucent and relatively abundant in the 2019 samples (similar to the two samples from Tremblay et al., 2020). Among the combined 2019 and Tremblay et al. (2020) samples, the corundum counts are between 25 and 208 grains/10 kg with an average value of 112 grains/10 kg (17%) in the 0.25–0.5 mm NFHMC fraction. Additionally, two of the samples

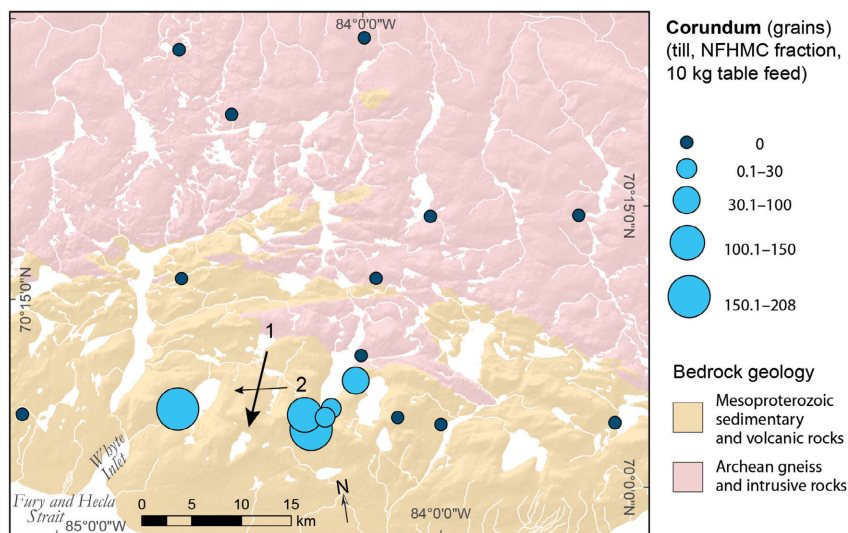


Figure 7: Corundum (white and translucent) from the nonferromagnetic heavy mineral concentrate (NFHMC) fraction (0.25–0.5 mm) of till samples, normalized to 10 kg table feed. Till samples were collected in 2018 and 2019 in the 2018 study area, near Whyte Inlet, northwestern Baffin Island. No corundum were found in 2019 study area. Arrows indicate simplified chronology of ice flow (1 being the oldest). See Figure 1 for location.

have anomalous values of scheelite grains with 2 and 9 grains/10 kg. There is no association with monazite and barite in the samples collected in 2019, compared to those collected in 2018 (Tremblay et al., 2020). The grains are of angular shape, which is indicative of a short distance of transport (see Tremblay et al., 2020). The absence of corundum in the sample located immediately north of the contact between the base of the Mesoproterozoic sedimentary and volcanic rocks (Fury and Hecla Group) and the granite and gneiss (Rae domain) to the north indicates that corundum probably originates from intrusive or metasomatized rocks near that contact, or from the basal Fury and Hecla Group rocks, including the Nyeboe Formation (conglomerate, breccia, sandstone, dolostone and basalt; Greenman et al., 2020) or the Sikosak Bay Formation (quartz arenite). The mechanism of mineralization or mineral concentration is uncertain and could be linked with late intrusive rocks, contact metamorphism or placer deposits. Additional potential for a preferential accumulation of corundum grains exists in both fluvial and glaciofluvial sedimentary settings due to their high density (4.0 g/cm³). The economic potential of the corundum as gemstones depends on the size of the crystals in the host rock and on whether their colour and saturation could be enhanced by thermal treatment (Nassau, 1981; Shor and Weldon, 2009).

Acknowledgments

Funding for the Fury and Hecla Project has been provided by the Canadian Northern Economic Development Agency (CanNor) under the Strategic Investments in Northern Economic Development program delivered through the Government of Nunavut to the Canada-Nunavut Geoscience Office (CNGO). Funding was also provided through a Strategic Partnership Grant (#506660) from the Natural Sciences and Engineering Research Council of Canada. L. Lebeau, S. Basso, C. Gilbert, S. Zhang and L. Ham from CNGO are thanked for their administrative and fieldwork collaboration. This project benefited from the support of the Hamlet of Igloolik and the Qikiqtani Inuit Association. Polar Continental Shelf Project staff are thanked for logistical services. The ArcticDEM was provided by the Polar Geospatial Center, under National Science Foundation–Office of Polar Programs awards 1043681, 1559691 and 1542736. Special thanks to the pilots at Prairie Helicopters Inc., Discovery Mining Services and support personnel from the Igloolik community. P.-M. Godbout (Geological Survey of Canada) is thanked for reviewing this paper.

Natural Resources Canada, Lands and Minerals Sector contribution 20200672

References

Averill, S.A. 2001: The application of heavy indicator mineralogy in mineral exploration with emphasis on base metal indica-

tors in glaciated metamorphic and plutonic terrains; Geological Society of London, Special Publication 185, p. 69–81.

Chandler, F.W. 1980: Geology of the late Precambrian Fury and Hecla Group, northwest Baffin Island, District of Franklin; Geological Survey of Canada, Bulletin 370, 30 p. and 1 sheet.

Craigie, E.R. 2001: Evaluation report, 2000 exploration program, Baffin Island project, Territory of Nunavut; Crown-Indigenous Relations and Northern Affairs Canada Assessment Report 084449 submitted by Mountain Province Diamonds Inc., 32 p. and 2 maps.

Craigie, E.R. 2006: Report of an airborne magnetic survey, Borden Peninsula project; Crown-Indigenous Relations and Northern Affairs Canada Assessment Report 085068 submitted by Patrician Diamonds Inc., 129 p.

Dalton, A.S., Margold, M., Stokes, C.R., Tarasov, L., Dyke, A.S., Adams, R.S., Allard, S., Arends, H.E., Atkinson, N., Attig, J.W., Barnett, P.J., Barnett, R.L., Batterson, M., Bernatchez, P., Borns, H.W., Jr., Breckenridge, A., Briner, J.P., Brouard, E., Campbell, J.E., Carlson, A.E. et al. 2020: An updated radiocarbon-based ice margin chronology for the last deglaciation of the North American Ice Sheet Complex; *Quaternary Science Reviews*, v. 234, art. 106223.

De Angelis, H. 2007: Palaeo-ice streams in the north-eastern Laurentide Ice Sheet; Ph.D. thesis, Stockholm University, Stockholm, Sweden, 123 p.

de Kemp, E.A. and Scott, D.J. 1998: Geoscience compilation of northern Baffin Island and northern Melville Peninsula, Northwest Territories; Geological Survey of Canada, Open File 3636, 2 CD-ROMs, URL <<https://doi.org/10.4095/210027>>.

Dredge, L.A. 2000: Carbonate dispersal trains, secondary till plumes, and ice streams in the west Foxe Sector, Laurentide Ice Sheet; *Boreas*, v. 29, no. 2, p. 144–156.

Dyke, A.S. 2000a: Surficial geology, Milne Inlet, Baffin Island, Nunavut; Geological Survey of Canada, “A” Series Map 1962A, scale 1:250 000, URL <<https://doi.org/10.4095/211528>>.

Dyke, A.S. 2000b: Surficial geology, Moffet Inlet and Fitzgerald Bay, Baffin Island, Nunavut; Geological Survey of Canada, “A” Series Map 1963A, scale 1:250 000, URL <<https://doi.org/10.4095/211527>>.

Dyke, A.S. 2004: Surficial geology, Erichsen Lake, Baffin Island, Nunavut; Geological Survey of Canada, “A” Series Map 2066A, scale 1:250 000.

Dyke, A.S. 2008: The Steensby Inlet ice stream in the context of the deglaciation of northern Baffin Island, eastern Arctic Canada; *Earth Surface Processes and Landforms*, v. 33, p. 573–592.

Dyke, A.S. and Hooper, J.M.G. 2001: Deglaciation of northwest Baffin Island, Nunavut; Geological Survey of Canada, Map 1999A, scale 1:500 000.

Dyke, A.S. and Hooper, M.J.G. 2000: Surficial geology, Berlinguet Inlet and Bourassa Bay, Baffin Island, Nunavut; Geological Survey of Canada, “A” Series Map 1960A, scale 1:250 000, URL <<https://doi.org/10.4095/211873>>.

Dyke, A.S. and Prest, V.K. 1987: Late Wisconsinan and Holocene retreat of the Laurentide Ice Sheet; Geological Survey of Canada, “A” Series Map 1702A, scale 1:5 000 000.

- Dyke, A.S., Moore, A. and Robertson, L. 2003: Deglaciation of North America; Geological Survey of Canada, Open File 1574, 2 sheets, 1 CD-ROM.
- GEBCO Compilation Group 2014: GEBCO 2014 Grid; International Hydrographic Organization and Intergovernmental Oceanographic Commission, gridded global bathymetry data, URL <<http://www.gebco.net>> [August 2018].
- Girard, I., Klassen, R. and Laframboise, R. 2004: Sedimentology Laboratory manual, Terrain Science division; Geological Survey of Canada, Open File 4823, 137 p.
- Greenman, J.W., Patzke, M., Halverson, G.P. and Ielpi, A. 2020: Updated stratigraphy of the Fury and Hecla Group of Melville Peninsula and northwestern Baffin Island, Nunavut; *in* Summary of Activities 2019, Canada-Nunavut Geoscience Office, p. 37–50, URL <https://m.cngo.ca/wp-content/uploads/Summary_of_Activities_2019-Paper_04.en_.pdf> [January 2021].
- Hooper, J.M.G. 1996: Glacial history and Holocene sea level regression in the Foxe/Baffin sector of the Laurentide Ice Sheet, northwest Baffin Island, Arctic Canada; Ph.D. thesis, University of Alberta, Calgary, Alberta, 195 p.
- Hooper, J.M.G. and Dyke, A.S. 2000: Surficial geology, Agu Bay and Easter Cape, Baffin Island, Nunavut; Geological Survey of Canada, “A” Series Map 1959A, scale 1:250 000.
- Lebeau, L.E., Russer, M., Therriault, I., Bovingdon, P.J., Dufour, F., Greenman, J.W. and Patzke, M. 2020: Regional Precambrian bedrock mapping of the Jungersen River area, northwestern Baffin Island, Nunavut; *in* Summary of Activities 2019, Canada-Nunavut Geoscience Office, p. 11–26, URL <https://m.cngo.ca/wp-content/uploads/Summary_of_Activities_2019-Paper_02.en_.pdf> [January 2021].
- Margold, M., Stokes, C.R., Clark, C.D. and Kleman, J. 2015: Ice streams in the Laurentide Ice Sheet: a new mapping inventory; *Journal of Maps*, v. 11, issue 3, p. 380–395, URL <<https://doi.org/10.1080/17445647.2014.912036>>.
- McClenaghan, M.B., Spirito, W.A., Plouffe, A., McMartin, I., Campbell, J.E., Paulen, R.C., Garrett, R.G., Hall, G.E.M., Pelchat, P. and Gauthier, M.S. 2020: Geological Survey of Canada till-sampling and analytical protocols: from field to archive, 2020 update; Geological Survey of Canada, Open File 8591, 73 p., URL <<https://doi.org/10.4095/326162>>.
- McMartin, I., Godbout, P.-M., Campbell, J.E., Tremblay, T. and Behnia, P. 2020: A new map of glacial features and glacial land systems in central mainland Nunavut, Canada; *Boreas*, URL <<https://doi.org/10.1111/bor.12479>>.
- McNeely, R., Dyke, A.S. and Southon, J.R. 2006: Canadian marine reservoir ages, preliminary data assessment; Geological Survey of Canada, Open File 5049, 3 p.
- Nassau, K. 1981: Heat treating ruby and sapphire: technical aspects; *Gems & Gemology*, v. 17, issue 3, p. 121–131.
- Natural Resources Canada 2016: Canadian digital elevation model (CDEM); Natural Resources Canada, URL <ftp://ftp.geogratis.gc.ca/pub/nrcan_rncan/elevation/cdem_mnec/> [April 2018].
- Natural Resources Canada 2018: High resolution digital elevation model (HRDEM)-CanElevation Series; Natural Resources Canada, URL <<https://open.canada.ca/data/en/dataset/957782bf-847c-4644-a757-e383c0057995>> [April 2018].
- Ocean Mapping Group 2019: Multibeam bathymetric data; Ocean Mapping Group, University of New Brunswick, URL <<http://www.omg.unb.ca/Projects/Arctic/>> [July 2020].
- Plouffe, A., McClenaghan, M.B., Paulen, R.C., McMartin, I., Campbell, J.E. and Spirito, W.A. 2013: Processing of unconsolidated glacial sediments for the recovery of indicator minerals: protocols used at the Geological Survey of Canada; *Geochemistry: Exploration, Environment, Analysis*, v. 13, p. 303–316.
- Porter, C., Morin, P., Howat, I., Noh, M.-J., Bates, B., Peterman, K., Keesey, S., Schlenk, M., Gardiner, J., Tomko, K., Willis, M., Cloutier, M., Husby, E., Foga, S., Nakamura, H., Platson, M., Wethington, M. J., Williamson, C., Bauer, G., Enos, J., Arnold, G., Kramer, W., Becker, P., Doshi, A., D’souza, C., Cummins, P., Laurier, F. and Bojesen, M. 2018: ArcticDEM; Harvard Dataverse, version 1, URL <<https://doi.org/10.7910/DVN/OHHUKH>>.
- Shilts, W. 1993: Geological Survey of Canada’s contributions to understanding the composition of glacial sediments; *Canadian Journal Earth Sciences*, v. 30, p. 333–353.
- Shor, R. and Weldon, R. 2009: Ruby and sapphire production and distribution: a quarter century of change; *Gems & Gemology*, v. 45, issue 4, p. 236–259.
- Steenkamp, H.M., Bovingdon, P.J., Dufour, F., G  n  reux, C.-A., Greenman, J.W., Halverson, G.P., Ielpi, A., Patzke, M. and Tinkham, D.K. 2018: New regional mapping of Precambrian rocks north of Fury and Hecla Strait, northwestern Baffin Island, Nunavut; *in* Summary of Activities 2018, Canada-Nunavut Geoscience Office, p. 47–62, URL <https://m.cngo.ca/wp-content/uploads/Summary_of_Activities_2018-P04-Steenkamp.pdf> [January 2021].
- Tremblay, T. 2019: Surficial geology in the Fury and Hecla Strait area; Nunavut Mining Symposium Society, Nunavut Mining Symposium 2019, April 2–4, 2019, Iqaluit, Nunavut, presentation.
- Tremblay, T. and Godbout, P.M. 2018: Surficial geology of the north coast of Fury and Hecla Strait, northwestern Baffin Island, Nunavut; *in* Summary of Activities 2018, Canada-Nunavut Geoscience Office, p. 107–120, URL <https://m.cngo.ca/wp-content/uploads/Summary_of_Activities_2018-P10-Tremblay.pdf> [January 2021].
- Tremblay, T. and Gosse, J.C. 2019: Cosmogenic isotopes transect on the northeastern Laurentide ice sheet cold-based plateaus; INQUA Congress 2019, July 25–31, Dublin, Ireland, abstract.
- Tremblay, T. and Paulen, R. 2012: Glacial geomorphology and till geochemistry of central Melville Peninsula, Nunavut; Geological Survey of Canada, Open File 7115, 47 p.
- Tremblay, T., Leblanc-Dumas, J., Allard, M., Ross, M.A. and Johnson, C. 2014: Surficial geology of central Hall Peninsula, Baffin Island, Nunavut: summary of the 2013 field season; *in* Summary of Activities 2013, Canada-Nunavut Geoscience Office, p. 103–114, URL <<https://m.cngo.ca/wp-content/uploads/Summary-of-Activities-2013-P12.pdf>> [January 2021].
- Tremblay, T., Sasseville, C. and Godbout, P.M. 2020: Geochemistry and mineralogy of glacial sediments, north of Fury and Hecla Strait, northwestern Baffin Island, Nunavut; *in* Summary of Activities 2019, Canada-Nunavut Geoscience Office, p. 51–64, URL <https://m.cngo.ca/wp-content/uploads/Summary_of_Activities_2019-Paper_05.en_.pdf> [January 2021].
- Tremblay, T. 2021: Data tables on geochemistry and mineralogy of glacial sediments from Jungersen River area (northwestern Baffin Island) and northeastern Baffin Island, Nunavut; Canada-Nunavut Geoscience Office, Geoscience Data Se-

ries GDS2021-001 Microsoft® Excel® file, URL <<https://cngo.ca/summary-of-activities/2020/>>.

Utting, D.J., Little, E.C., Young, M.D., McCurdy, M.W., Dyke, A.S. and Girard, I. 2008: Till, stream-sediment and bedrock analyses, North Baffin Island, Nunavut (NTS 37E, F, G, H and 47E); Geological Survey of Canada, Open File 5742, 14 p., 1 CD-ROM.

Winzar, D. and McKenzie, J. 2005: Assessment report on the 2003, 2004 and 2005 till and stream sampling, geophysics and drill programmes on the Baffin property, Nunavut; Crown-Indigenous Relations and Northern Affairs Canada, Assessment Report 084940 submitted by De Beers Canada Inc.



Ground temperature, active-layer thickness and ground-ice conditions in the vicinity of Rankin Inlet, Nunavut

A.-M. LeBlanc¹ and G.A. Oldenborger²

¹Natural Resources Canada, Geological Survey of Canada, Ottawa, Ontario, anne-marie.leblanc@canada.ca

²Natural Resources Canada, Geological Survey of Canada, Ottawa, Ontario

The Western Hudson Bay Project is a Canada-Nunavut Geoscience Office-led geoscience compilation project in the Kivalliq Region of Nunavut, along the western coast of Hudson Bay from the Manitoba border to Rankin Inlet (NTS 55D–F, K, L). The project objective is to compile all existing aggregate, mineral potential, surficial geology, land cover and permafrost data for this area. The project also involves the development of methods for regional characterization of permafrost conditions by integrating observations from different sources across different scales, from site-based data to remote sensing.

LeBlanc, A.-M. and Oldenborger, G.A. 2021: Ground temperature, active-layer thickness and ground-ice conditions in the vicinity of Rankin Inlet, Nunavut; in *Summary of Activities 2020*, Canada-Nunavut Geoscience Office, p. 63–72.

Abstract

The Kivalliq Region of Nunavut is undergoing significant infrastructure development, for which information on permafrost is required to ensure resilience in the context of climate change. Measurements of ground temperature and observations of ground-ice conditions are critical for permafrost characterization but are sparse in the Kivalliq Region. This paper reports on shallow (<3 m) and deep (>6 m) ground-temperature measurements made in the vicinity of Rankin Inlet since 2016. Study site locations were chosen to represent a variety of conditions, including developed and undeveloped land, and different geological settings. Ground-ice conditions are reported upon, where observed. The top of permafrost is ice rich in near-shore marine polygons and in poorly drained alluvial and marine sediments. Although thick lenses of segregated ice are present near the top of permafrost in till, the first decimetres may not be particularly ice rich. The mean annual ground temperature (MAGT) at the top of permafrost ranges between -9.5 and -5.5°C . The MAGT at a depth of close to 7 m is approximately -6.7°C in undisturbed ground and approximately -5.5°C in developed land within the Hamlet. Active-layer thickness (ALT) ranges between 0.6–0.7 m, under a thick organic layer overlying alluvial-marine sediments, and 1.6 m in marine and till sediments. Surface conditions, including soil moisture, drainage and snow cover, are the main factors explaining the ground-temperature differences across the sites. The cold but wet year of 2018–2019 contributed to higher ground temperatures and a thicker active layer. Current MAGT and ALT are both greater than those measured in 1974–1976.

Introduction

Information on ground temperatures and ground-ice conditions is important for understanding the response of permafrost to warming and for predicting the behaviour of permafrost as an engineering substrate. Such knowledge is important in the Kivalliq Region of Nunavut, where temperatures are increasing, and significant infrastructure development is occurring in a context of achieving natural resource and community sustainability. Biskaborn et al. (2019) provided evidence and analysis of permafrost warming at a global scale, and Smith et al. (2010) synthesized the thermal state of permafrost and ground warming from sites across North America. However, there is a scarcity of permafrost data along the western coast of Hudson Bay and the Kivalliq Region of Nunavut (Figure 1), which limits understanding of local conditions and prohibits the

characterization of trends in ground temperature for Central Canada (Smith et al., 2010).

Community-based permafrost monitoring sites are improving the ability to evaluate the thermal state of permafrost in Nunavut (Smith et al., 2013; Ednie and Smith, 2015). Other temperature data are often collected specifically for natural-resource projects and records but are limited in duration and availability. The objective of this paper is to present ground-temperature measurements made in the region of Rankin Inlet since 2016. Site locations were chosen to represent a variety of terrain conditions, including developed and undeveloped land, and different geological settings. Thermistor arrays were installed in both shallow cored boreholes and pits, and in deeper air-rotary-drilled boreholes. Cored drilling allowed for some observations of

This publication is also available, free of charge, as colour digital files in Adobe Acrobat® PDF format from the Canada-Nunavut Geoscience Office website: <https://cngo.ca/summary-of-activities/2020/>.

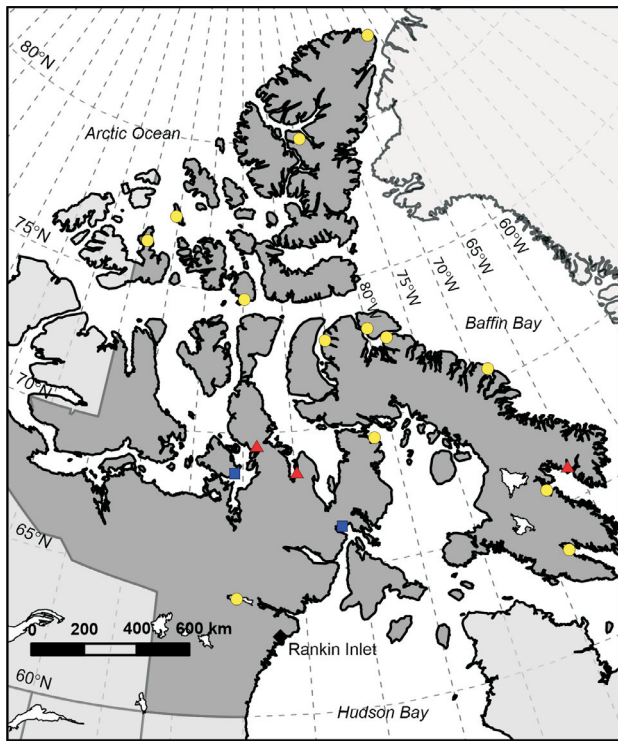


Figure 1: Ground-temperature monitoring boreholes in Nunavut; the monitoring sites are represented as circles (Smith et al., 2010), triangles (Smith et al., 2013) and squares (Ednie and Smith, 2015).

ground-ice conditions. Results provide valuable baseline information in the Kivalliq Region of Nunavut.

Study area

The Hamlet of Rankin Inlet is located on the western coast of Hudson Bay in the Kivalliq Region of Nunavut, Canada (Figure 1). The region was covered by the Laurentide Ice Sheet during the Wisconsin Glaciation (Dyke, 2004). After deglaciation, the postglacial Tyrrell Sea extended as much as 150 km inland from the current coastline over the isostatically depressed land surface, reaching an elevation of approximately 170 m above present sea level (Dyke, 2004; Randour et al., 2016). Postglacial isostatic rebound and emergence resulted in the formation of subaerial permafrost that continues to evolve.

The surficial geology consists of glacial, glaciofluvial, marine, alluvial and organic deposits over bedrock

(McMartin, 2002). The glacial deposits are unsorted to poorly sorted tills with a silty sand matrix. The postglacial sea resulted in deposition of marine, nearshore and beach sediments, along with reworking of glacial sediments. In many locations, wave washing resulted in isolation of coarse till components and accumulation of fine silt and sand at lower elevations as nearshore marine deposits. The topography consists of undulating bedrock hills, eskers, moraines and drumlins, with a network of rivers draining the area toward Hudson Bay. Small lakes are abundant in depressions related to bedrock basins and glacial landforms. Most of the study area is covered with tundra vegetation typical of the low-arctic region (mosses, herbaceous plants, shrubs and alpine-arctic plants).

Rankin Inlet is within the continuous permafrost zone, where 90% to 100% of the land area is underlain by permafrost (Heginbottom et al., 1995), with the potential for low to medium abundance of segregated ice (O'Neill et al., 2019). Periglacial features such as ice-wedge polygons, mud boils, palsas, gelifluction lobes and active-layer detachments are abundant (McMartin, 2002; Oldenborger et al., 2018), indicating the presence of ground ice. In the area of Rankin Inlet, permafrost salinities of 3.0–30.6 parts per mil have been reported at depths of 2.4–6.1 m (Hivon, 1991).

Climate

Average mean annual air temperature (MAAT) for Rankin Inlet was -10.3°C from 1981 to 2019, with an average increase of approximately $0.05^{\circ}\text{C}/\text{year}$ (Environment and Climate Change Canada, 2019). Ground temperatures were measured during three climatic years (October to September) with different air-temperature and precipitation conditions: 2016–2017 was warm and dry, 2017–2018 was cold and precipitation was normal, and 2018–2019 was cold and wet, corresponding to the historical record (1981–2019) of total rain (Table 1).

Methods

Ground-temperature measurement sites in the vicinity of Rankin Inlet were planned to cover a representative suite of surficial geological units and land-cover types. Tentative site locations were established after considering field ob-

Table 1: Rankin Inlet climate from 2015 to 2019, based on climatic year (October to September).

Climatic year	MAAT ($^{\circ}\text{C}$)	Total rain (mm)	Total snow (cm)	Total precipitation (mm)	FDD	TDD	Climate
2015–2016	-9.7	121.0	113.6	224.8	4561	1039	Warm and dry
2016–2017	-8.8	103.8	78.6	171.5	4220	1058	Warm and dry
2017–2018	-11.0	173.7	136.2	303.1	4734	843	Cold and normal
2018–2019	-11.1	336.2	149.9	482.1	4744	819	Cold and wet
Normal 1981–2019	-10.3	184.0	130.6	310.7	4654	909	

Abbreviations: FDD, freezing degree-days (or freezing index, sum of days with negative mean daily air temperature over a climatic year); MAAT, mean annual air temperature; TDD, thawing degree-days (or thawing index, sum of days with positive mean daily air temperature over a climatic year)

servations and land access, and after engaging in community consultation (Oldenborger et al., 2016). Two sites (RI01, RI02) were chosen for permanent monitoring of the thermal regime of Rankin Inlet for developed and undeveloped land use scenarios (Figure 2). Both sites are on marine washed till several metres thick, adjacent to marine littoral sediments (Oldenborger et al., 2017). Washed till and marine sediments are considered to be representative of large portions of the western coast of Hudson Bay. Boreholes at RI01 and RI02 were drilled in March 2017 using a track-mounted air-rotary drill. The borehole at RI01 was drilled to a depth of 14.1 m without encountering bedrock. The borehole at RI02 was drilled to a depth of 7.0 m, with bedrock reported at approximately 3.5 m depth based on resistance and cuttings. Both holes were cased with polyvinyl-chloride tube, filled with silicone oil, and instrumented in June 2017 with multi-thermistor cables connected to 16-channel data loggers.

In addition to the permanent ground-temperature monitoring boreholes, eight sites were selected as shallow permafrost-monitoring stations. At these sites, shallow boreholes were drilled and/or sediment pits were dug in the active layer, and permafrost cores and sediment samples were extracted. Instrumentation, including thermistors, thaw tubes and cameras, were installed to measure ground and surface

temperature, ground heave, thaw depth, moisture content and snow thickness (RI03–RI08; Figure 2). Sites were chosen to represent different terrain types, including a raised beach ridge (RI03a) characterized by large-scale ice-wedge troughs (RI03b); nearshore marine sediments with a well-developed ice-wedge polygon network (RI05a, b, c); littoral and offshore marine sediments (RI06); transitional till/nearshore sediments characterized by hummocky ground and mud boils (RI07); and alluvial/marine valley sediments (RI08). Sediments and ground-ice conditions encountered at each site are summarized in Table 2 (soil descriptions apply to cored sites only). Direct observations of ground ice include an ice-rich top of permafrost (ToP) in marine and alluvial sediments, along with ice wedges in beach sediments (Oldenborger et al., 2017).

Ground temperatures were recorded using loggers developed by RBR Ltd. with a resolution of $\pm 0.01^\circ\text{C}$ (RI01, RI02, RI03b, RI05c, RI07, RI08) and 4-channel Onset temperature loggers (HOBO® U12 model with TMC-HD sensors) with a resolution of $\pm 0.03^\circ\text{C}$ (RI03a, RI05a, b, RI06). Single-channel Onset temperature loggers (HOBO® Water Temperature Pro v2 model) were located within a few centimetres of some thermistor cables (RI05b, c, RI07, RI08) and 2–5 cm below the ground surface to measure

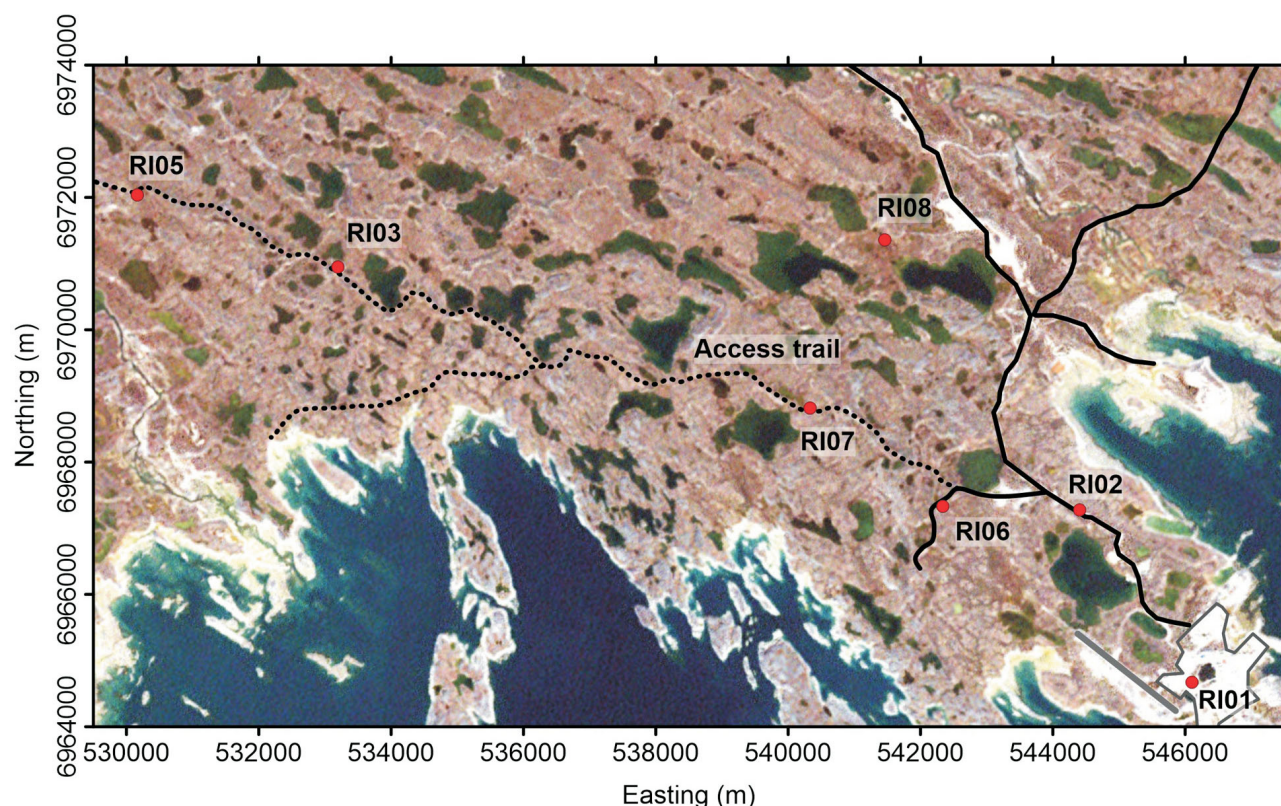


Figure 2: Site locations near Rankin Inlet, where deep (RI01, RI02) and shallow (RI03–08) ground-temperature measurements were made. Site RI04 is not shown and no data (ground-surface temperature for one summer only) are reported at this stage. Rankin Inlet hamlet and airstrip are shown by the grey polygon and line, respectively; some roads and access trails are shown by the continuous and dotted black lines (GeoBase®, 2020). All co-ordinates are in UTM Zone 15N, NAD 83.

Table 2: Rankin Inlet study site descriptions, including primary surficial geology (McMartin, 2002; Geological Survey of Canada, 2017), active-layer volumetric grain-size summaries and descriptions from shallow permafrost coring, where available.

Site	Sediments and ground-ice conditions
RI01	T.M(w)/Mr: beach sediments over till, marine washed; thin layer of coarse brown sand over marine-washed till; average 52% sand, 46% silt, 2% clay; >14 m thick; developed land within Rankin Inlet; negligible snow cover (March 2017), potentially subject to snow drifting and clearing; disturbed vegetation.
RI02	T.M(w): till, marine washed; till reworked by marine wave and current action; poorly sorted, coarse-grained with boulder lag; >3 m thick; patches of nearshore and littoral marine sediments; hummocky to flat; some mudboils; undeveloped land along all-season Rankin Inlet access road; variable snow cover <0.5 m thick (March 2017).
RI03	Mr: beach sediments; derived from reworking of upland glacial and glaciofluvial deposits; generally well-sorted sand and gravel; 98% sand, 2% silt, 0% clay with 12–38 wt. % pebbles; 1–5 m thick; orthogonal frost cracks or ice-wedge polygons. Active layer: 0.05–0.1 m organic, 1.25 m coarse brown sand with shells; ToP: ice-bonded to poorly ice-bonded coarse brown sand, ice-bonded grey silt below 2 m, no visible ice, ice wedges from 1.16 m depth in polygon trough. Snow cover 0.25–0.45 m in ice-wedge trough (winter-spring 2019).
RI05	Mn: nearshore marine sediments; derived from reworking of surficial deposits and accumulation of winnowed fines in low-lying areas; well-sorted sand to silty sand; 11–48% sand, 46–81% silt, 6–8% clay with 2–15 wt. % pebbles; 1–5 m thick; abundant ice-wedge polygons. RI05c active layer: 0.05 m organic, 0.86 m ice-bonded medium brown sand with shells, 0.06 m grey silty sand with millimetre-scale irregular reticulate cryostructure (transient layer ¹); ToP: 0.5 m massive ice (segregated) with suspended cryostructure of sand aggregates above grey silt (soil slurry, saline permafrost; Oldenborger et al., 2020). RI05b: low-lying area; wet sedge. RI05c: snow cover 0.05 m (winter-spring 2019).
RI06	T.M(w)/Mr/Mn/A.M: retrogressive alluvial sand over shell lag with grey clay/silt layers and ice-rafted debris; 52% sand, 44% silt, 5% clay with 11 wt. % pebbles; some nearby peat/palsas.
RI07	T.M: till and marine sediments, undifferentiated; till, glacial marine diamicton and patches of nearshore and littoral marine sediments, commonly grading to nearshore marine or alluvial and marine sediments; unsorted to poorly sorted with silty sand matrix; 46–94% sand, 6–49% silt, 0–5% clay with 47–63 wt. % pebbles; 1–5 m thick; common mudboils; rare ice-wedge polygons. Active layer: 0.04 m organic, 1.2 m ice-bonded grey silty sand with shells; ToP: < 0.1 m grey silty sand with millimetre-scale lenticular layered cryostructure, 0.2 m soil slurry, 0.1 m grey silt with 0.01–0.05 m lenticular layered cryostructure, 0.95 m grey silt with millimetre- to centimetre-scale lenticular layered cryostructure. Potentially saline permafrost (Hivon, 1991). Snow cover 0.3–0.4 m (winter-spring 2019).
RI08	A.M: alluvial and marine sediments, undifferentiated; modern alluvium mixed with fine-grained sediments washed from slopes by wave action; sand and silt; 1–5 m thick; nearby perennial frost blisters; rare ice-wedge polygons. Active layer: ice rich, 0.4 m organic with injection ice (0.04 m), 0.2 m silty sand with irregular reticulate cryostructure; ToP: 1 m ice-rich grey-brown silty sand with shells, millimetre- to centimetre-scale lenticular layered cryostructure.

¹The transient layer is the upper part of the transition zone, which alternates in status between seasonally frozen ground (active layer) and permafrost over subdecadal to centennial time scales; the transition zone encompasses the transient layer and the intermediate layer (Shur et al., 2005). The latter is often called the ice-rich top of permafrost.

hourly near-surface temperatures with a resolution of $\pm 0.03^{\circ}\text{C}$.

Mean annual ground temperature (MAGT) was calculated at each depth using daily averages from the thermistor cables. As with air temperatures, a climatic year (October to September) was used instead of the calendar year to include one complete freezing and thawing season. Some years are incomplete because of long-term thermistor malfunctioning and were removed from the analysis. Thawing and freezing n-factors (ratio of the surface freezing or thawing index to the air freezing or thawing index; Harris et al.,

1988) were calculated based on the near-surface temperature records at RI05b, RI05c, RI07 and RI08.

Active-layer thickness (ALT, maximum summer thaw depth) was estimated by linear interpolation of the temperature profile close to 0°C and/or by linear extrapolation from sensors located on the unfrozen side of the 0°C isotherm (Riseborough, 2008), especially for sites having only active-layer ground temperatures. The accuracy of interpolation and extrapolation is approximately 0.05 and 0.1 m for thermistor spacings of 0.25 and 0.5 m, respectively.

For each site, the annual freeze-back period was estimated from ground temperatures at the deepest thermistor in the

active layer. Freeze-back corresponds to the period during which a nearly constant temperature, close to the freezing point, persists during refreezing of the active layer (Harris et al., 1988); the moment temperatures drop below the freezing point marks the end of this freeze-back period. This period (also called the zero curtain) results from the dissipation of the latent heat of fusion of water during freezing (or thawing) of the active layer. During freezing, the latent-heat effect protects the active layer and the permafrost from rapid cooling (e.g., Romanovsky and Osterkamp, 2000). In the thawed active layer, high water content is commonly associated with a long freeze-back period and, therefore, warmer permafrost.

Results

Ground temperatures

The MAGT profiles are grouped by climatic year (Figure 3a, b) and terrain type (Figure 4a–c). The range of MAGT for 2018–2019 varies from -8.8 to -3.9°C , depending on the local surface conditions, whereas ToP temperatures range between -9.5 and -5.5°C (Figure 3b). In 2017–2018, the range is similar, but reduced due to fewer active monitoring sites (Figure 3a). The MAGT at the depth of zero annual amplitude (depth at which the annual temperature fluctuation is $<0.1^{\circ}\text{C}$; Harris et al., 1988) of 13 m is -5.63°C at RI01 in till (Figure 3a). At the depth of 7 m (annual amplitude of about 1°C), the MAGT at RI01 is -5.36°C (Figures 3a, 4c), whereas it varies from -6.56 to -6.85°C at RI02 for 2017–2018 and 2018–2019, respectively (Figure 4c). For a given site, temperatures in the first metres of permafrost are lower in 2017–2018 than 2018–2019, whereas the only profile of 2016–2017 (RI03a) had the highest active-layer temperatures of the three years (Figure 4b).

Active-layer characteristics

Active-layer thicknesses ranged mostly between 1 m at sites with an ice-rich ToP (RI05a, c) and 1.6 m in a low-lying wet area of the polygonal network at RI05b (Figure 5). One exception was the ice-rich alluvial and marine sediments, where ALT was estimated to be between 0.6 and 0.7 m under a thick, surface organic layer (RI08). In general, for a given site, the active layer was thickest in 2017, followed by 2019, and then 2018. The maximum depth of the thaw front was typically reached between August 29 and September 6 at the sites, with extremes of August 20 and September 17. The freeze-back period duration (Table 3), influenced by the presence of water, ranged from less than 10 days at RI07 and RI05c to 63 days at RI05b. However, the freeze-back period duration was quite variable for a given terrain type and surface condition. For example, it was 34 and 46 days at RI05a, a site similar to RI05c, where freeze back lasted only 10 days. The thawing

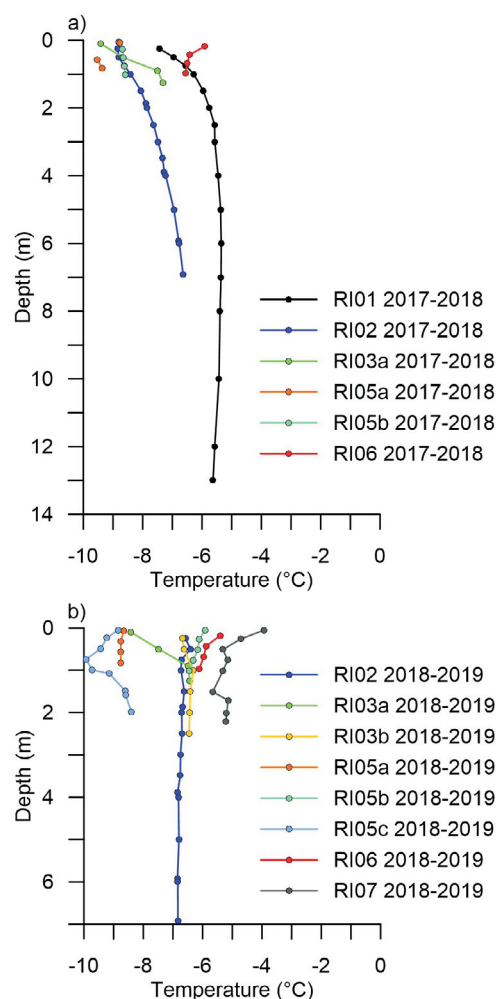


Figure 3: Mean annual ground temperature profiles across the different study sites in the vicinity of Rankin Inlet for climatic years **a)** 2017–2018 and **b)** 2018–2019.

and freezing n-factors, and seasonal thaw settlement, are also shown in Table 3.

Discussion

Interannual ground temperatures and variability across sites

For a given site, the warmer active layer in 2016–2017 compared with 2017–2018 and 2018–2019 is consistent with the higher MAAT of 2016–2017, and the above normal thawing degree-days (TDD) and freezing degree-days (FDD), despite a dry winter (Table 1). Warmer permafrost in 2018–2019 compared with 2017–2018 is likely due to higher winter precipitation despite lower TDD and slightly higher FDD in 2018–2019. Snow cover, due to its low thermal conductivity and insulating effect, is known to be one of the main factors contributing to warmer permafrost (Goodrich, 1982). The decrease in freezing n-factor for 2018–2019 at site RI05b (Table 3) is indicative of a thicker insulating snow cover. Except at sites with very thin snow cover (RI05a, c; Table 2), the ground temperatures in win-

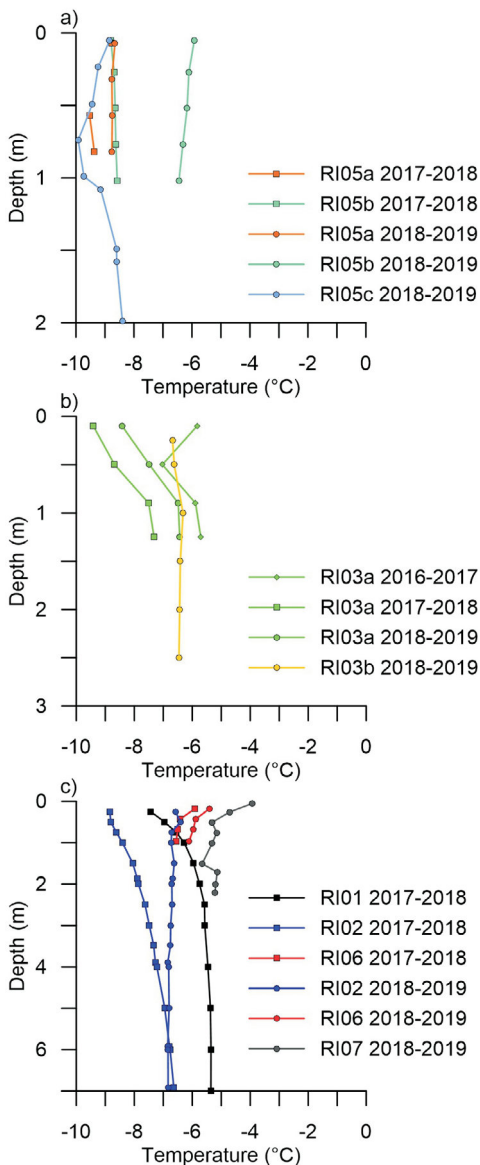


Figure 4: Mean annual ground temperature profiles across the different study sites in the vicinity of Rankin Inlet for climatic years 2017–2018 and 2018–2019 by terrain type: **a)** nearshore marine sediments; **b)** raised beach ridge (including 2016–2017); **c)** undifferentiated till and marine sediments.

ter 2018–2019 at all sites are considerably higher than winter 2017–2018, due to this insulating snow cover (e.g., 2.5 to 4°C higher at 1 and 0.25 m below the surface at site RI02; results not shown). In contrast, active-layer temperatures were only slightly higher (0.5°C) in summer 2019 compared to 2018 (e.g., at RI02). At RI02, the thermal effect of the snow cover is noticeable up to a depth of 6 m (Figure 4c).

The presence of a recurring thick (>1 m) snow cover adjacent to RI01 may explain why the MAGT at 7 m depth was about 1.2°C higher than at RI02 (Figure 3a). In June 2018, a snowdrift from road clearance was found adjacent to the site, but not immediately above the RI01 instrument.

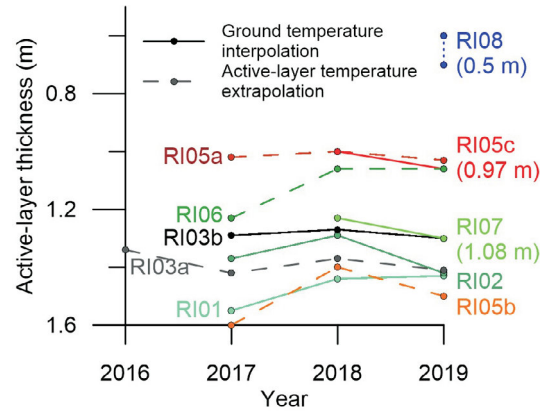


Figure 5: Variation in active-layer thickness at the different study sites in the vicinity of Rankin Inlet between 2016 and 2019 (values in parentheses are from measurements made using a frost probe in September 2019).

Freeze-back duration between the two sites in 2017 was similar (Table 3), suggesting that this factor does not explain the difference in ground temperature between the two sites. The disturbed environment of RI01 (being adjacent to a road and power pole) may also complicate the interpretation of the profile. The surface conditions could have been disturbed through time leading to warmer permafrost temperatures.

Permafrost temperatures were highest at RI07 among the study sites (Figure 3b). During winter 2018–2019, the snow cover was 40 cm (Table 2), with a corresponding freezing n-factor of 0.46 (Table 3). Study site RI07 is located on a gentle slope between two small water tracks and the vegetation is sparse. The surface was wet at the beginning and end of the summers, but it was never flooded. Wet ground surfaces absorb more solar radiation, which agrees with the high thawing n-factors close to unity (Table 3). In 2018, this site had a relatively short freeze-back period (Table 3) that would generally contribute to lower ground temperatures. However, the air temperature in fall 2018 was relatively high up to the beginning of November, hindering the ground from cooling. Unless it is highly variable from one year to another, the duration of the freeze-back period of the active layer may not account for warmer ground at RI07. Therefore, the low freezing n-factor at this site is likely the main factor explaining the high MAGT compared with other sites.

In contrast, the centres of ice-rich polygons in nearshore marine sediments (RI05a, c) were underlain by the coldest permafrost among the terrain types investigated (Figure 3b). Winds are likely very strong in this valley and particularly at the centre of high polygons, limiting the snow cover at RI05c to <5 cm throughout the winter of 2018–2019 (Table 2). This allows heat in the ground to effectively dissipate into the atmosphere in winter, leading to ground cooling (freezing n-factor of 0.81; Table 3). The freeze-back period at RI05c was relatively short compared with

Table 3: Active-layer characteristics, including freeze-back period, thawing and freezing n-factors, and seasonal thaw settlement, observed at the different study sites in the vicinity of Rankin Inlet.

Site	Freeze-back period (days)			Thawing n-factor			Freezing n-factor		Seasonal thaw settlement (cm)	
	2016	2017	2018	2017	2018	2019 ¹	2017–2018	2018–2019	2018	2019
RI01		22	24							
RI02		25	15							
RI03a	37	22	26							
RI03b		36	43							
RI05a		34	46							
RI05b		37	63	0.87	0.9	0.98	0.83	0.6		
RI05c			10		0.81	0.95		0.81	6.8	7.8
RI06		50	38							
RI07			7		0.99	1.05		0.46	4.5	6
RI08			n/a			0.93				12.5

¹Up to mid-September 2019

Abbreviation: n/a, not available

RI05a and RI05b (Table 3). The change in slope of the MAGT profile at RI05c is likely due to the heterogeneous stratigraphy (coarse sediments, ice-rich ToP and fine-grained soils below) and related thermal properties.

The three sites at RI05, within the same terrain unit but different surface conditions and degree of ground wetness, show how the ground temperatures can vary at an exceedingly small scale. At RI05a, which presumably also had thin snow cover as at RI05c, the longer freeze-back period may explain why the active layer was warmer (Figure 4a). At site RI05b, the thicker snow cover (lower freezing n-factor than RI05c; Table 3), the wet to flooded ground surface and the long freeze-back period in 2018 (Table 3) explain the higher active-layer temperatures compared with sites at the centre of polygons and compared to the previous year. The two sites at RI03 are another example of small-scale variability; located a few metres apart, they shared the same terrain unit. However, the isothermal profile at RI03b (Figure 4b) is due to a combination of thicker snow conditions in the ice-wedge trough (Table 2), a longer freeze-back period (Table 3) and ice wedge at depth.

Active-layer thickness and ground ice at the top of permafrost

Warmer summers and higher TDD (2016 and 2017; Table 1) generally lead to a thicker active layer (e.g., Jorgensen et al., 2006). The only site for which ALT measurements made in 2016 are available is RI03a. At this site, the higher TDD in 2016 compared with 2018 and 2019 did not result in a thicker active layer. Other factors such as previous summer and winter precipitation (Iijima et al., 2010), and FDD (Zhang et al., 1997) have also been associated with active-layer dynamics. Although some of these factors can be ruled out (by comparing values in Table 1 for the different years), there is a lack of evidence to explain why RI03a has a thinner ALT compared with other years, especially as the available measurements were made at only one site in summer 2016. Recently, Douglas et al. (2020) found that increased rainfall was the only factor related to deeper

thaw across 2750 maximum thaw depths over several sites in Alaska. For Rankin Inlet dry soils, the extremely wet summer of 2019 likely contributed to a thicker active layer than drier previous summers, despite lower TDDs compared to 2017. The thawing n-factors also increased in 2019 compared with 2018 for dry-, wet- and flooded-surface conditions (Table 3), with the greater increase associated with the dry surface. At sites RI05b and RI06, where local drainage often results in flooded surfaces (even during dry summers), thick active layers in 2017 (Figure 5) were consistent with both high TDD and wet conditions and may explain why the difference was greater between 2017 and 2019 compared with that observed in relatively dry soils (e.g., RI02).

Also, at RI05a, RI05c and RI03b, ALT and its interannual variation were likely limited by the high latent-heat requirement to melt the ice-rich ground at the sites, which included an ice wedge and massive ice at the ToP (Figure 5). At sites where the ALT exhibited greater interannual variability, such as RI05b in wet sedge and all till sites, the ToP was likely not as enriched with ice. Study site RI05b had the thickest active layer among the sites, likely explained by the lack of ice-rich ToP, wet sand, and flooded ground surface at the site. Flooded surface provides a source of heat to the ground and saturated-soil conditions enhance heat flow to depth by increasing soil thermal conductivity (e.g., Iijima et al., 2010). In till, cores of permafrost were retrieved only at site RI07. A fine-grained slurry (mud) was collected near the ToP (around 1.3 m) underlying <0.1 m of ground with a lenticular cryostructure and ice lenses of 0.01 m, followed by 0.01–0.05 m of lenticular layered cryostructure at depth greater than 1.6 m (Table 2). During drilling, ice-rich soil, if present, will not result in a soil slurry; instead, intact cores are likely to be collected as was the case at RI03b, RI05c and RI08. Although the ToP is not particularly ice rich in its first decimetres, the undifferentiated till and marine sediments are associated with lake expansion and medium to high seasonal and annual ground-surface displacements inferred by the interferometric synthetic aperture radar tech-

nique (LeBlanc et al., 2020; Oldenborger et al., 2020), which suggests that the base of the active layer and/or ToP includes sufficient ice content to cause the ground to subside upon thawing. Some of the sites, where ALT was determined solely from active-layer temperature measurements, exhibited high variability in interannual ALT. The mean difference between extrapolation and interpolation of ALT at sites where both calculations were possible was similar from year to year and ranged between $\Delta 0.01$ (at RI07 and RI05c) and $\Delta 0.04$ m (at RI02). These differences are smaller than the interannual variability at sites where massive ice is believed to be absent at the ToP.

Study site RI08 had the thinner active layer among the sites due to the thick (0.4 m) organic layer at the surface (Table 2), which provides better thermal insulation than mineral soil. The range of 0.6 to 0.7 m for the ALT in 2019 is due to the large uncertainty in ALT estimate resulting from interpolating between sensors at ground surface and in permafrost and extrapolating from sensors located in permafrost only (Figure 5).

Finally, the estimation of ALT from ground-temperature data does not account for the settlement that usually accompanies thawing of ice-rich ground. For example, thaw settlement in 2019, measured from heave sleeves, was 6.0, 7.8 and 12.5 cm, at RI07, RI05c and RI08, respectively (Table 3). These values are consistent with the frost probing of the thaw front in September 2019 (Figure 5) such that ALT determined from frost probing was comparable to that based on ground temperatures less the seasonal thaw settlement. At RI05c, the extremely wet summer of 2019 was sufficient to thaw the transient layer from 0.91 to 0.97 m based on frozen core (Table 2).

Comparison with past permafrost-temperature records

Brown (1978) reported on the ground temperatures and ALT of four unknown locations near Rankin Inlet over the period of 1974 to 1976; however, the terrain type in which

each of the cables was installed was noted. The MAGT profiles from Brown (1978) are reproduced in Figure 6 for units described as bedrock, esker (gravel) and till (silt-clay-stones). Mean annual air temperature in 1974–1976 was estimated to be around -11.6°C , based on the Chesterfield Inlet air-temperature record (Brown, 1978), 92 km northeast of Rankin Inlet. The warmer permafrost at one of the esker sites was under a thick (0.91–0.99 m) snow cover in the winters of 1974 to 1976, whereas the other sites had thin snow covers (0.08–0.30 m) and similar MAGT profiles. Although a direct comparison with currently instrumented sites is not possible, the deeper MAGTs from 1974–1976 at sites with thinner snow cover are lower than the current MAGTs at depth in till at RI02 and RI01 (Figure 6). The profile for study site RI02 can be tentatively compared with the Brown (1978) profiles because of similar substrate and surface conditions. The ALT in till from 1974–1976 varied between 1.07 and 1.31 m (average of 1.17 m) compared with a range of 1.29 to 1.42 m (average 1.36 m) at RI02. This may also suggest ground warming and an increase in ALT since 1974–1976.

Economic considerations

Land-based infrastructure projects could significantly affect the local economy and community welfare along the western coast of Hudson Bay (e.g., Varga, 2014; Rogers, 2015). Permafrost and ground ice are important features of this landscape and can significantly affect ground stability and infrastructure. This new ground-temperature data and permafrost information for Rankin Inlet will be useful for land-use planning and risk mitigation associated with infrastructure management. These data will also fill a gap in coverage from a national permafrost monitoring perspective and will support efforts to enhance resilience of Canadians to climate change.

Conclusions

The focus of this paper was on shallow (<3 m) and deep (>6 m) ground temperatures recorded near Rankin Inlet between 2016 and 2019. Site locations were chosen to represent a variety of conditions. These included developed land and undeveloped areas with different geological settings, such as marine coarse- and fine-grained sediments; alluvial and marine sediments; and till and marine undifferentiated sediments. The different sites encompass a variety of surface conditions from relatively dry to wet and flooded surfaces, as well as thin and thick snow cover. Active-layer thicknesses based on ground-temperature measurements, along with ground-ice conditions at the top of permafrost observed during shallow (<3 m)

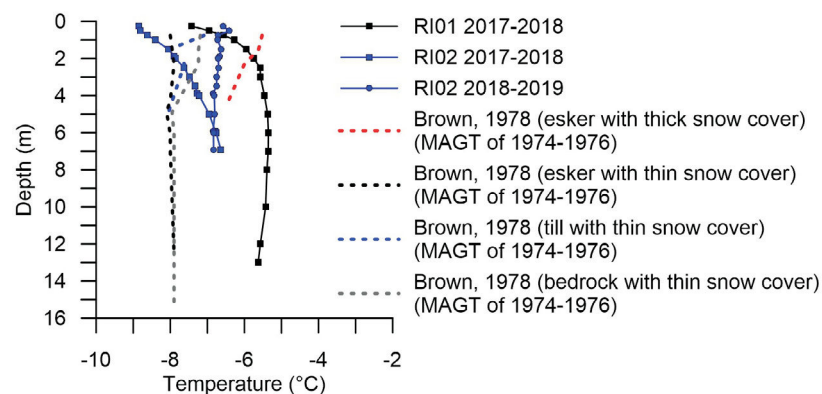


Figure 6: Comparison between historical (1974–1976; Brown, 1978) and current mean annual ground temperature (MAGT) profiles at the study sites in the vicinity of Rankin Inlet.

cored drilling, are also presented. Results indicate that the MAGT at the ToP varies between -9.5 and -5.5°C , whereas the MAGT close to a depth of 7 m is approximately -6.7 and -5.5°C in undisturbed ground and developed land within the Hamlet, respectively. As expected, for a given site, the MAGT and ALT vary according to interannual MAAT, including TDD, FDD and snow conditions, but the extremely wet summer of 2019 also led to a relatively warm and thick active layer, despite the higher FDD of the previous winter and its lower TDD compared with other years. This wet summer likely induced the thawing of the transient layer at one site with ice-rich ToP. For a given year, spatial variability in the MAGT and ALT are linked to the surface conditions, active-layer soil moisture and ToP ground-ice conditions. Ice-rich active layer and/or ice-rich ToP, observed in alluvial and marine sediments and in nearshore marine sediments, have the lowest ALT (0.6 and 1 m, respectively), whereas a thicker active layer among the study sites (1.6 m) is likely found where ice-rich ToP is absent, under flooded surfaces. Till may not be particularly ice rich in its first decimetres, despite the presence of thick lenses of segregated ice near the ToP. Current MAGT at depth and ALT are both greater than those measured in 1974–1976.

Acknowledgments

This work was supported by the Natural Resources Canada Climate Change Geoscience Program and through funding to the Canada-Nunavut Geoscience Office from the Canadian Northern Economic Development Agency's (CanNor) Strategic Investments in Northern Economic Development (SINED) program. Valuable assistance was provided by R. Connelly of the Government of Nunavut, Department of Economic Development and Transportation, and S. Napier and A. Netser of the Nunavut Arctic College. Fieldwork assistance was provided by O. Bellehumeur-Génier. Critical review by B. O'Neill.

Natural Resources Canada, Lands and Minerals Sector contribution 20200673

References

- Biskaborn, B.K., Smith, S.L., Noetzli, J., Matthes, H., Vieira, G., Streletskiy, D.A., Schoeneich, P., Romanovsky, V.E., Lewkowicz, A.G., Abramov, A., Allard, M., Boike, J., Cable, W.L., Christiansen, H.H., Delaloye, R., Diekmann, B., Drozdov, D., Eitzelmüller, B., Grosse, G., Guglielmin, M. et al. 2019: Permafrost is warming at a global scale; *Nature Communications*, v. 10, art. 264, URL <<https://doi.org/10.1038/s41467-018-08240-4>>.
- Brown, R.J.E. 1978: Influence of climate and terrain on ground temperatures in the continuous permafrost zone of northern Manitoba and Keewatin district, Canada; *in* Proceedings of the Third International Conference on Permafrost, July 10–13, 1978, Edmonton, Alberta, p. 15–22.
- Douglas, T.A., Turetsky, M.R. and Koven, C.D. 2020. Increased rainfall stimulates permafrost thaw across a variety of Interior Alaskan boreal ecosystems; *Climate and Atmospheric Science*, v. 3, art. 28, URL <<https://doi.org/10.1038/s41612-020-0130-4>>.
- Dyke, A.S. 2004: An outline of North American deglaciation with emphasis on central and northern Canada; *Developments in Quaternary Science*, v. 2, p. 373–424, URL <[https://doi.org/10.1016/S1571-0866\(04\)80209-4](https://doi.org/10.1016/S1571-0866(04)80209-4)>.
- Ednie, M. and Smith, S.L. 2015: Permafrost temperature data 2008–2014 from community based monitoring sites in Nunavut; Geological Survey of Canada, Open File 7784, 18 p., URL <<https://doi.org/10.4095/296705>>.
- Environment and Climate Change Canada 2019: Historical climate data; Environment and Climate Change Canada, URL <<http://climate.weather.gc.ca>> [November 2019].
- GeoBase® 2020: Landsat 7 orthorectified imagery over Canada (1999–2003); Natural Resources Canada, URL <<http://geogratis.gc.ca/api/en/nrcan-rncan/ess-sst/-/%28urn:iso:series%29canimage-landsat-7-orthoimages-of-canada-150-000?sort-field=relevance>> [December 2020].
- Geological Survey of Canada 2017: Surficial geology, Rankin Inlet, Nunavut, NTS 55-K/16; Geological Survey of Canada, Canadian Geoscience Map 68 (preliminary, Surficial Data Model v. 2.2 conversion of Open File 4116), 1:50 000 scale, URL <<https://doi.org/10.4095/299616>>.
- Goodrich, L.E. 1982: The influence of snow cover on the ground thermal regime; *Canadian Geotechnical Journal*, v. 19, p. 421–432, URL <<https://doi.org/10.1139/t82-047>>.
- Harris, S.A., French, H.M., Heginbottom, J.A., Johnston, G.H., Ladanyi, B., Sego, D.C. and van Everdingen, R.O. 1988: Glossary of permafrost and related ground-ice terms; National Research Council of Canada, Associate Committee on Geotechnical Research, Technical Memorandum no. ACGR-TM-142, 159 p., URL <<https://doi.org/10.4224/20386561>>.
- Heginbottom, J.A., Dubreuil, M.H. and Harker, P.T., comp. 1995: Canada, Permafrost; Natural Resources Canada, Geomatics Canada, National Atlas of Canada, 5th ed., MCR 4177, scale: 1 750 000, URL <<https://doi.org/10.4095/294672>>.
- Hivon, E.G. 1991: Behaviour of saline frozen soils; Ph.D. thesis, University of Alberta, Calgary, Alberta, 435 p.
- Iijima, Y., Fedorov, A.N., Park, H., Suzuki, K., Yabuki, H., Maximov, T.C. and Ohata, T. 2010: Abrupt increases in soil temperatures following increased precipitation in a permafrost region, central Lena River basin, Russia; *Permafrost and Periglacial Processes*, v. 21, p. 30–41, URL <<https://doi.org/10.1002/ppp.662>>.
- Jorgenson, M.T., Shur, Y.L. and Pullman, E.R. 2006: Abrupt increase in permafrost degradation in Arctic Alaska; *Geophysical Research Letters*, v. 33, art. L02503, 4 p., URL <<https://doi.org/10.1029/2005GL024960>>.
- LeBlanc, A.-M., Bellehumeur-Génier, O., Oldenborger, G.A. and Short, N. 2020: Lake area and shoreline changes due to climate and permafrost-related drivers, Rankin Inlet area, Nunavut; *in* Summary of Activities 2019, Canada-Nunavut Geoscience Office, p. 79–92, URL <https://m.engo.ca/wp-content/uploads/Summary_of_Activities_2019-Paper_07.en_.pdf> [January 2021].
- McMartin, I. 2002: Surficial geology, Rankin Inlet, Nunavut; Geological Survey of Canada, Open File 4116, scale 1:50 000, URL <<https://doi.org/10.4095/213219>>.
- Oldenborger, G.A., Bellehumeur-Génier, O. and LeBlanc, A.-M. 2018: Performance of a consumer-grade unmanned aerial

- vehicle for imaging, elevation modelling and ground displacement mapping in permafrost terrain, Rankin Inlet area, southern Nunavut; *in* Summary of Activities 2018, Canada-Nunavut Geoscience Office, p. 153–166, URL <https://m.cngo.ca/wp-content/uploads/Summary_of_Activities_2018-P14-Oldenborger.pdf> [January 2021].
- Oldenborger, G.A., Bellehumeur-Génier, O., Short, N., Tremblay, T. and LeBlanc, A.-M. 2017: Ground temperatures and permafrost conditions, Rankin Inlet, southern Nunavut; *in* Summary of Activities 2017, Canada-Nunavut Geoscience Office, p. 117–128, URL <https://m.cngo.ca/wp-content/uploads/Summary_of_Activities_2017-P10-Oldenborger.pdf> [January 2021].
- Oldenborger, G.A., LeBlanc, A.-M., Bellehumeur-Génier, O., Grosset, C., Holzman, S., Masson, C. and Tremblay, T. 2016: Community workshop on permafrost and landscape change, Rankin Inlet, Nunavut; Geological Survey of Canada, Open File 8057, 31 p., URL <<https://doi.org/10.4095/298806>>.
- Oldenborger, G.A., Short, N. and LeBlanc, A.-M. 2020: Electrical conductivity and ground displacement in permafrost terrain; *Journal of Applied Geophysics*, v. 181, art. 104148, URL <<https://doi.org/10.1016/j.jappgeo.2020.104148>>.
- O'Neill, H.B., Wolfe, S.A. and Duchesne, C. 2019: New ground ice maps for Canada using a paleogeographic modelling approach; *The Cryosphere*, v. 13, p. 753–773, URL <<https://doi.org/10.5194/tc-13-753-2019>>.
- Randour, I., McMartin, I. and Roy, M. 2016: Study of the post-glacial marine limit between Wager Bay and Chesterfield Inlet, western Hudson Bay, Nunavut; *in* Summary of Activities 2016, Canada-Nunavut Geoscience Office, p. 51–60, URL <https://m.cngo.ca/wp-content/uploads/Summary_of_Activities_2016-P06-Randour.pdf> [January 2021].
- Riseborough, D. 2008: Estimating active layer and talik thickness from temperature data: implication for modeling results; *in* Proceedings of the Ninth International Conference on Permafrost, D.L. Kane and K.M. Hinkel (ed.), Institute of Northern Engineering, University of Alaska Fairbanks, June 29–July 3, 2008, Fairbanks, Alaska, v. 2, p. 1487–1492.
- Rogers, S. 2015: Manitoba-Nunavut hydro link is economically viable: study; *Nunatsiaq News*, October 6, 2015.
- Romanovsky, V.E. and Osterkamp, T.E. 2000: Effects of unfrozen water on heat and mass transport processes in the active layer and permafrost; *Permafrost and Periglacial Processes*, v. 11, p. 219–239, URL <[https://doi.org/10.1002/1099-1530\(200007/09\)11:3<219::AID-PPP352>3.0.CO;2-7](https://doi.org/10.1002/1099-1530(200007/09)11:3<219::AID-PPP352>3.0.CO;2-7)>.
- Shur, Y., Hinkel, K.M. and Nelson, F.E. 2005: The transient layer: implication for geocryology and climate-change science; *Permafrost and Periglacial Processes*, v. 16, p. 5–17, URL <<https://doi.org/10.1002/ppp.518>>.
- Smith, S.L., Riseborough, D.W., Ednie, M. and Chartrand, J. 2013: A map and summary database of permafrost temperatures in Nunavut, Canada; Geological Survey of Canada, Open File 7393, 20 p., URL <<https://doi.org/10.4095/292615>>.
- Smith, S.L., Romanovsky, V.E., Lewkowicz, A.G., Burn, C.R., Allard, M., Clow, G.D., Yoshikawa, K. and Throop, J. 2010: Thermal state of permafrost in North America: a contribution to the international polar year; *Permafrost and Periglacial Processes*, v. 21, no. 2, p. 117–135, URL <<https://doi.org/10.1002/ppp.690>>.
- Varga, P. 2014: GN renews commitment to Manitoba road and hydro link; *Nunatsiaq News*, November 3, 2014.
- Zhang, T., Osterkamp, T.E. and Stamnes, K. 1997: Effects of climate on the active layer and permafrost on the North Slope of Alaska, U.S.A.; *Permafrost and Periglacial Processes*, v. 8, p. 45–67, URL <[https://doi.org/10.1002/\(SICI\)1099-1530\(199701\)8:1<45::AID-PPP240>3.0.CO;2-K](https://doi.org/10.1002/(SICI)1099-1530(199701)8:1<45::AID-PPP240>3.0.CO;2-K)>.



Preliminary assessment of the distribution of submarine slope failures in Baffin Island fiords, Nunavut

R. Bennett¹, A. Normandeau² and D.C. Campbell²

¹Natural Resources Canada, Geological Survey of Canada–Atlantic, Dartmouth, Nova Scotia, robbie.bennett@canada.ca

²Natural Resources Canada, Geological Survey of Canada–Atlantic, Dartmouth, Nova Scotia

This work is part of the Baffin Bay Geohazards Activity of the Landslides and Marine Geohazards Project of Natural Resources Canada's Public Safety Geoscience Program (PSGP). This program undertakes research across Canada to support risk reduction from the effects of hazardous natural conditions (i.e., space weather, earthquakes, tsunamis, volcanoes and landslides). The program develops authoritative scientific knowledge and tools to reduce future economic, social and environmental losses from these hazards. Additional funding for this research was provided by the Government of Canada's Program of Energy Research and Development (PERD), Crown-Indigenous Relations and Northern Affairs Canada, and ArcticNet.

Bennett, R., Normandeau, A. and Campbell, D.C. 2021: Preliminary assessment of the distribution of submarine slope failures in Baffin Island fiords, Nunavut; in Summary of Activities 2020, Canada-Nunavut Geoscience Office, p. 73–80.

Abstract

Natural Resources Canada (NRCan) has been conducting research into hazardous marine geological conditions (or geohazards) in Baffin Bay, Nunavut, since 2013. In 2020, part of NRCan's geohazard research was aimed at mapping the distribution of submarine slope failures in the fiords of eastern Baffin Island using all available multibeam echosounder and sub-bottom profiler data. Submarine slope failures (also known as submarine landslides) are a type of geohazard that occurs when sediments become unstable on an angled seabed and these sediments move downslope due to gravity. The volume of material moved by a slope failure has the potential to be immense (e.g., the 1929 submarine landslide offshore Newfoundland displaced more than 100 km³ of sediment), so it is important to investigate these features. Although long recognized, the distribution of slope failures in fiords of Baffin Bay is not well understood. Preliminary mapping shows 273 slope failures observed within 22 fiords, with 86% of the fiords examined having at least one slope failure. It is important to understand the distribution of slope failures, as they have the potential to damage seabed infrastructure (e.g., underwater fibre-optic cables and pipes) and cause tsunamis.

Introduction

Fiords are deep estuaries located at high latitudes of both hemispheres that have been modified by the action of glacial ice. Canada has more fiords than the rest of the world combined, with more than 50% of its fiords being located in the Canadian Arctic Archipelago (Syvitski et al., 1987). Baffin Island's eastern coastline is incised by fiords throughout the study area (Figure 1). Slope failures are common within fiord settings due to the fiords' characteristic steep sides and potential for very high sedimentation rates—key factors for failure development (Syvitski et al., 1987). Slope failures have the potential to damage seabed infrastructure and, in some cases, these failures are able to generate tsunamis. Fiords can be characterized by under-consolidated sediments lying on steep slopes that could fail under their own weight, or be easily triggered by external factors (i.e., earthquakes, waves, delta progradation or subaerial failures). New research shows that many fiords of

Baffin Island are affected by submarine slope failures (Broom et al., 2017; Brouard and Lajeunesse, 2019; Deering et al., 2019; Normandeau et al., work in progress) and that their triggers are likely different than those of lower latitude failures (Normandeau et al., 2021). Fiord sediments can be highly variable in their composition due to the numerous input sources and diverse glacial histories. This sediment variability can lead to discontinuities and unconformities that are potential failure surfaces (Syvitski et al., 1987).

In order to assess the hazard associated with slope failures in Baffin Island fiords, it is necessary to understand the recurrence of such events, preconditioning factors and likely locations of future events. The distribution of past events preserved as slope-failure deposits may provide insight into future events. This study used all available multibeam

This publication is also available, free of charge, as colour digital files in Adobe Acrobat® PDF format from the Canada-Nunavut Geoscience Office website: <https://cngo.ca/summary-of-activities/2020/>.

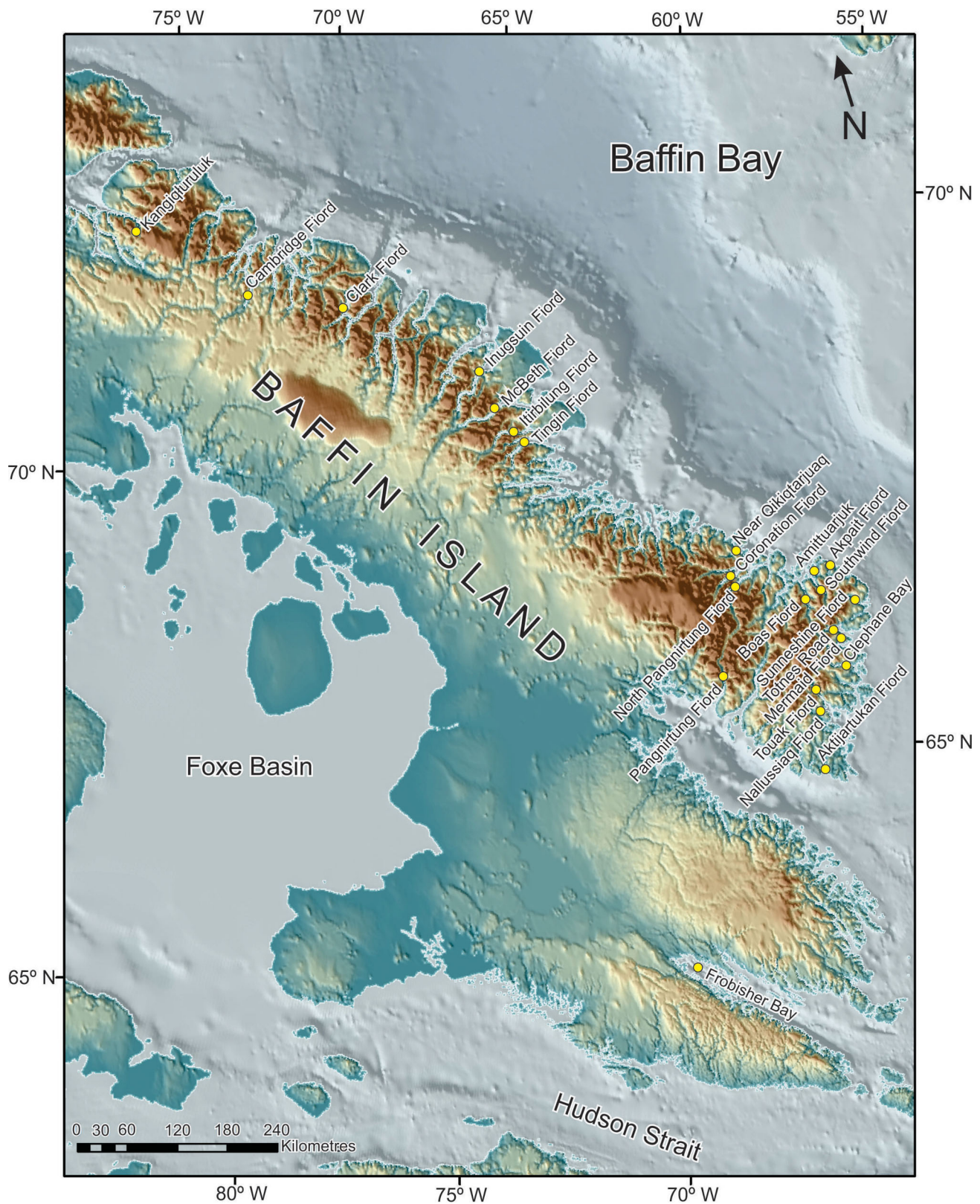


Figure 1: Study area on eastern Baffin Island, with yellow dots indicating fiord areas that were examined for the presence of slope failures.

and sub-bottom profiler data to determine the distribution of slope failures within the fiords of Baffin Island.

Methods

Two data types were used during this research for mapping slope failures: a) multibeam echosounder data collected by either the Canadian Coast Guard Ship (CCGS) *Amundsen* and *CSL Heron* through the ArcticNet program or Geological Survey of Canada (GSC) personnel onboard the Government of Nunavut's Research Vessel (RV) *Nuliajuk*; and b) Hunttec deep-tow high-resolution seismic sub-bottom profiler data collected by the GSC onboard the CCGS *Hudson* in 1982 (GSC cruise #82031). Multibeam data were first assessed for quality and then reprocessed to 2 m resolution and 4x vertical exaggeration. The multibeam and navigation components of the Hunttec data were imported into a Geographic Information System (GIS). All seabed features interpreted as slope failures were mapped in the GIS, given a unique identification number, and measured and classified in a database using the seven parameters highlighted in bold below. The data type, fiord name and any comments from the interpreter were also recorded in the database.

The following information was recorded in the database for each slope failure:

- **Id:** unique identifier number for each mapped slope failure
- **Morphology:** interpretation of how well defined the feature is on geophysical records
- **Type:** identifies if the feature is a single failure or a group of two or more failures (i.e., failure complex; after "Object type" in Clare et al., 2019)
- **Debris:** denotes if a debris deposit is visible at the downslope termination of the feature
- **Rmax:** maximum runout length of the failure in metres (includes the debris field [Figure 2]; after "total length" in Clare et al., 2019)
- **Wmax:** maximum width of the failure in metres (includes the debris field [Figure 2]; after "scar width" in Clare et al., 2019)
- **Hmax:** maximum head scarp width in metres (see Figure 2)
- **Scour:** observations of ice scours near the head scarp of the failure (within ~300 m)
- **Fiord:** name of the fiord where the feature is located
- **Source:** source of the data used to make the interpretation
- **Comments:** any comments by the interpreter

To date, 22 fiord areas have been mapped to determine the distribution of slope failures. The fiord areas that were mapped for slope failures using multibeam data were Frobisher Bay, Pangnirtung Fiord, Mermaid Fiord, Totnes Road, Akpait Fiord, Southwind Fiord, Boas Fiord, near Qikiqtarjuaq, Touak Fiord, Nallussiaq Fiord, Aktijartukan

Fiord, Clephane Bay and Amittuarjuk. Hunttec data were used in Sunneshine Fiord, Coronation Fiord, North Pangnirtung Fiord, Tingin Fiord, Itirbilung Fiord, McBeth Fiord, Inugsuin Fiord, Clark Fiord and Cambridge Fiord (see Figure 1 for locations).

Discussion

Slope failures are located in almost all Baffin Island fiords that were mapped during this study (Figure 3). To date, 273 slope failures have been mapped in the 22 Baffin Island fiord areas specified in the previous paragraph. Several different styles of failure were interpreted from the multibeam echosounder and Hunttec seismic data, including slides, debris flows and evidence of turbidity currents.

Slides are commonly observed in the Baffin Island fiords and are characterized by the rough or blocky texture of their debris fields (Figure 4). Most slides appear to be translational due to the smooth appearance of their failure surfaces (Figure 5). A smaller number of slides show a rough, folded texture of their failure surface in multibeam echosounder data due to frontal thrusting (Figure 6). The slope failure in Figure 6 appears to have a headscarp and a side-scarp roughly perpendicular to each other. It is not clear if both of these scarps were active at the same time or if failure from the headscarp led to the creation of the side-scarp along the margin of the original failure.

Debris flows generally have higher water content and greater mobility than slide failures. In multibeam echosounder data, debris flows have a long run-out length and smooth-textured debris fields, and are more likely to have a nonlinear shape than slides. Figure 7 shows four slope failures in Frobisher Bay that are interpreted to be debris flows. Each debris flow follows the contours of the seafloor to a deep basin where they terminate in a smooth, low-relief terminal lobe. Debris flow 1 in Figure 7 is interpreted to be the oldest, as it is overlain by debris flows 2 and 3. Debris flows 1, 2, and 3 are then truncated by the youngest debris flow, number 4. Debris flow 4 occurred in two phases, as the headscarp of 4a is no longer visible and was either overprinted by 4b or they originated from the same headscarp. Debris flow 4b is also observed incising into 4a. The sediments that form the terminal lobe are likely a mixture of material from all four debris-flow events.

Turbidity currents are not directly observed in the Baffin Island fiords but are inferred from the presence of sediment waves in multibeam echosounder data (Figure 8). Normandeau et al. (2019) showed that sediment waves on fiord deltas are due to recurring turbidity currents. Sediment waves were observed in multibeam data in about 70% of the fiords mapped during this study (Frobisher Bay, Clephane Bay, Pangnirtung Fiord, Mermaid Fiord, Totnes Road, Akpait Fiord, Southwind Fiord, Boas Fiord and Nallussiaq Fiord). Normandeau et al. (2019) also observed sediment waves in

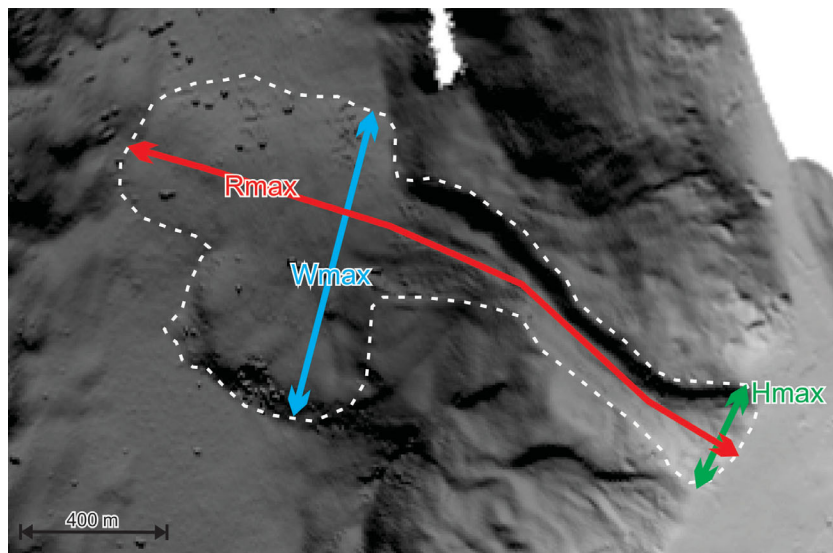


Figure 2: Example measurements of the Rmax, Wmax and Hmax parameters, Southwind Fiord.

Kangiqłuruluk (formerly Oliver Sound). Thirteen of the fifteen (87%) instances of sediment waves observed during this study are located on fiord-head deltas.

Future studies

At the time this paper was prepared, not all of the available multibeam data had been analyzed for slope-failure distribution. Future work will complete the analysis of these data and the results will be released in a GSC open file or similar publication. A database of measurements on all identified slope failures, accompanied by distribution maps, will be included in this publication.

Economic considerations

Slope failures can be damaging to all marine infrastructure and must therefore be considered during project planning. Understanding the distribution, magnitude and frequency of slope failures is essential for design of nearby infrastructure in a safe and cost-effective manner. One specific type of marine infrastructure that is being considered for Nunavut is submarine fibre-optic cables. These cables are very susceptible to the impacts of slope failures and would require expensive and time-consuming repairs if damaged. This research is a first step in understanding slope failures in Baffin Bay fiords and can help with the safe and efficient installation of submarine cables or other marine construction projects.

Conclusions

At this time, 86% (19 of 22) of the fiords examined show evidence of slope failures. The types of failures observed are slides, debris flows and turbidity currents, with 273 features identified so far. Slides and debris flows are the most

abundant failure types. Since slope failures are so widespread in Baffin Island fiords, it is important that they are considered during seabed infrastructure projects or when making decisions regarding public safety and the environment. As other data are analyzed and new data are collected, future research will continue to refine and improve the understanding of these features.

Acknowledgments

This research would not have been possible without the financial support provided by the Government of Canada's Program of Energy Research and Development (PERD), and Crown-Indigenous Relations and Northern Affairs Canada (CIRNAC). The authors also thank ArcticNet, the Government of Nunavut's Department of Environment (Fisheries and Sealing Division), the Fisheries and Marine Institute of Memorial University of Newfoundland, and the officers and crew of the CCGS *Hudson*, CCGS *Amundsen* and RV *Nuliajuk*.

Natural Resources Canada, Lands and Minerals Sector contribution 20200573

References

- Broom, L.M., Campbell, D.C. and Gosse, J.C. 2017: Investigation of a Holocene marine sedimentary record from Pond Inlet, northern Baffin Island, Nunavut; in Summary of Activities 2017, Canada-Nunavut Geoscience Office, p. 93–104, URL <<http://cngo.ca/summary-of-activities/2017/>> [November 2020].
- Brouard, E. and Lajeunesse, P. 2019: Glacial to postglacial submarine landform assemblages in fiords of northeastern Baffin Island; *Geomorphology*, v. 330, p. 40–56, URL <<https://doi.org/10.1016/j.geomorph.2019.01.007>>.

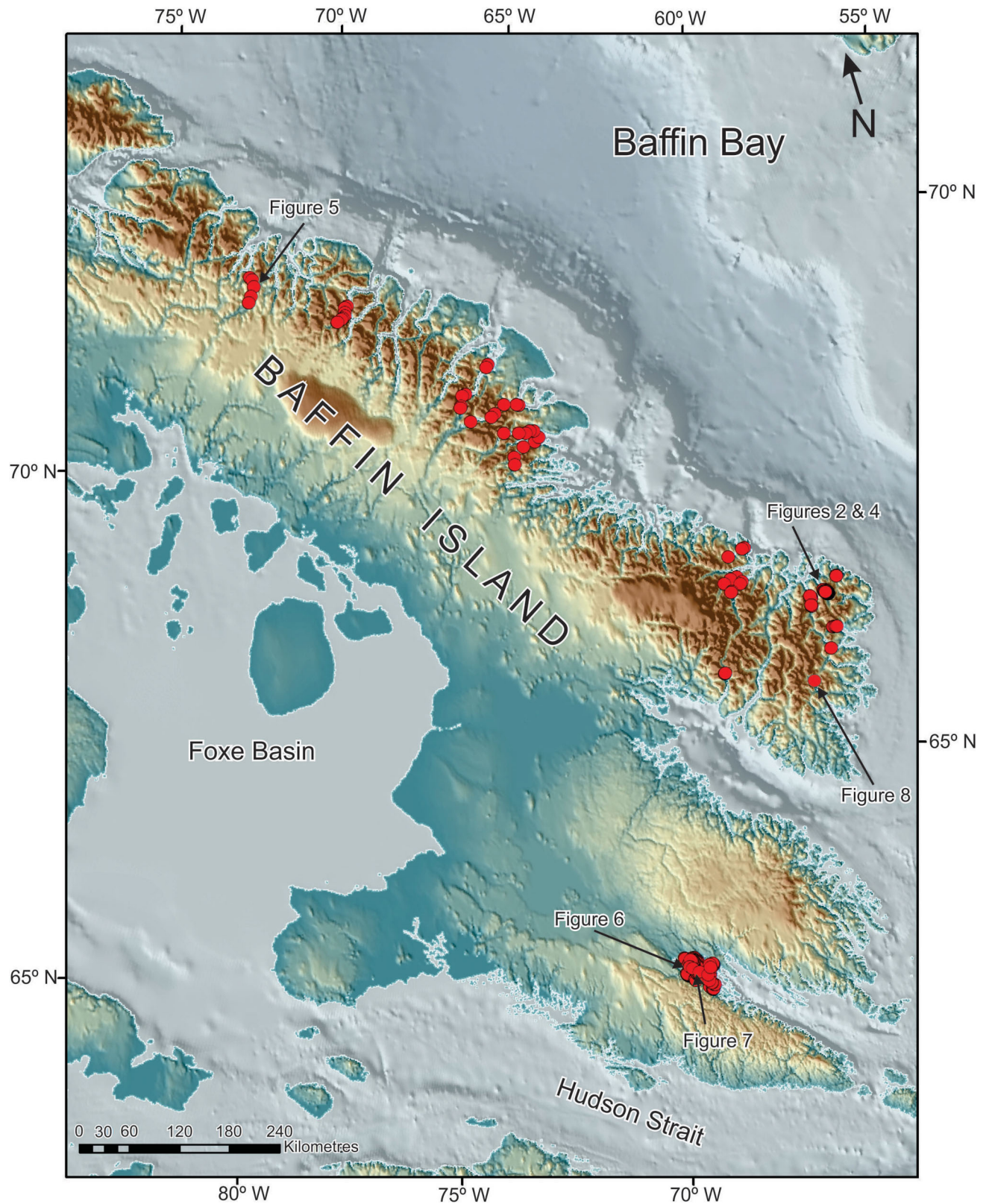


Figure 3: Distribution of slope failures in Baffin Island fiords (red circles indicate failure positions).

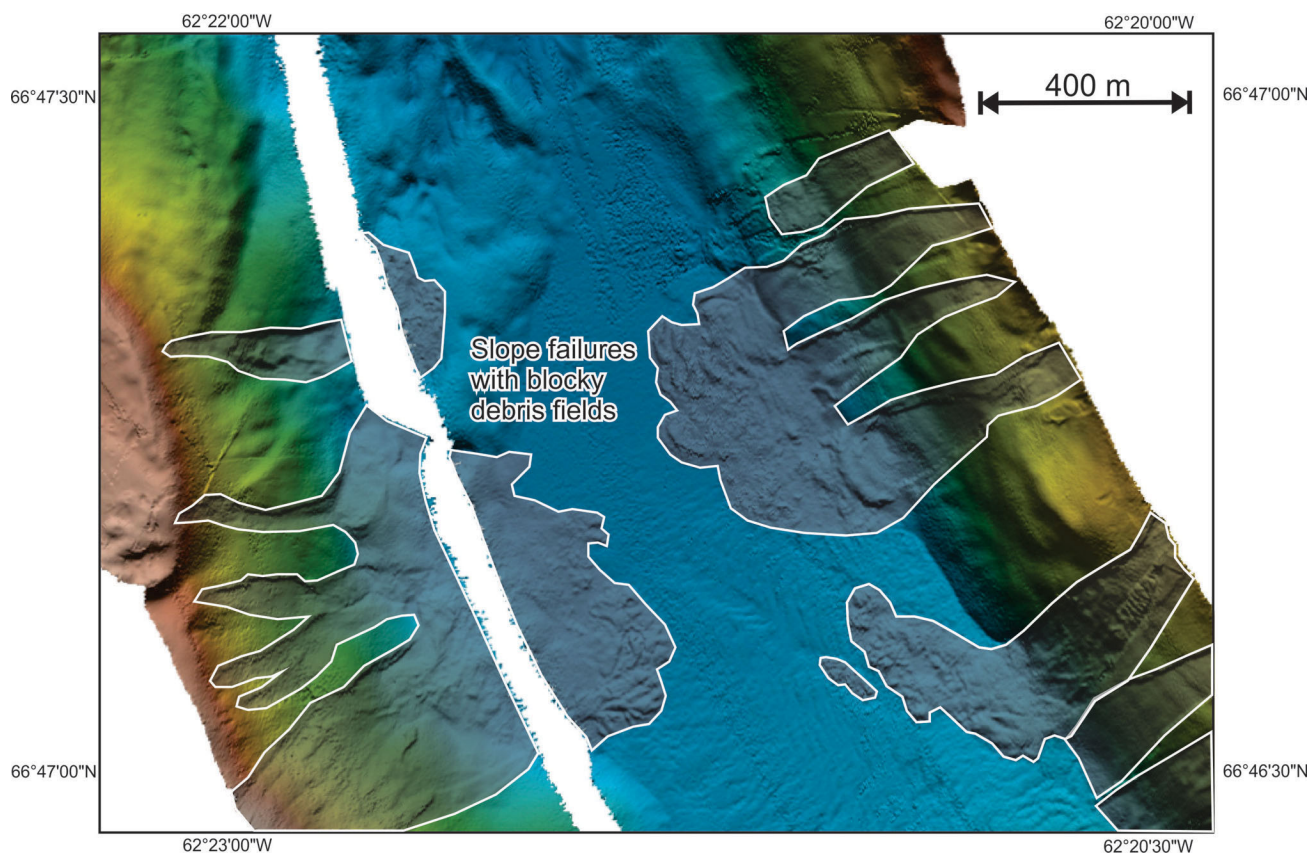


Figure 4: Slope failures in Southwind Fiord with a rough blocky texture in their debris fields.

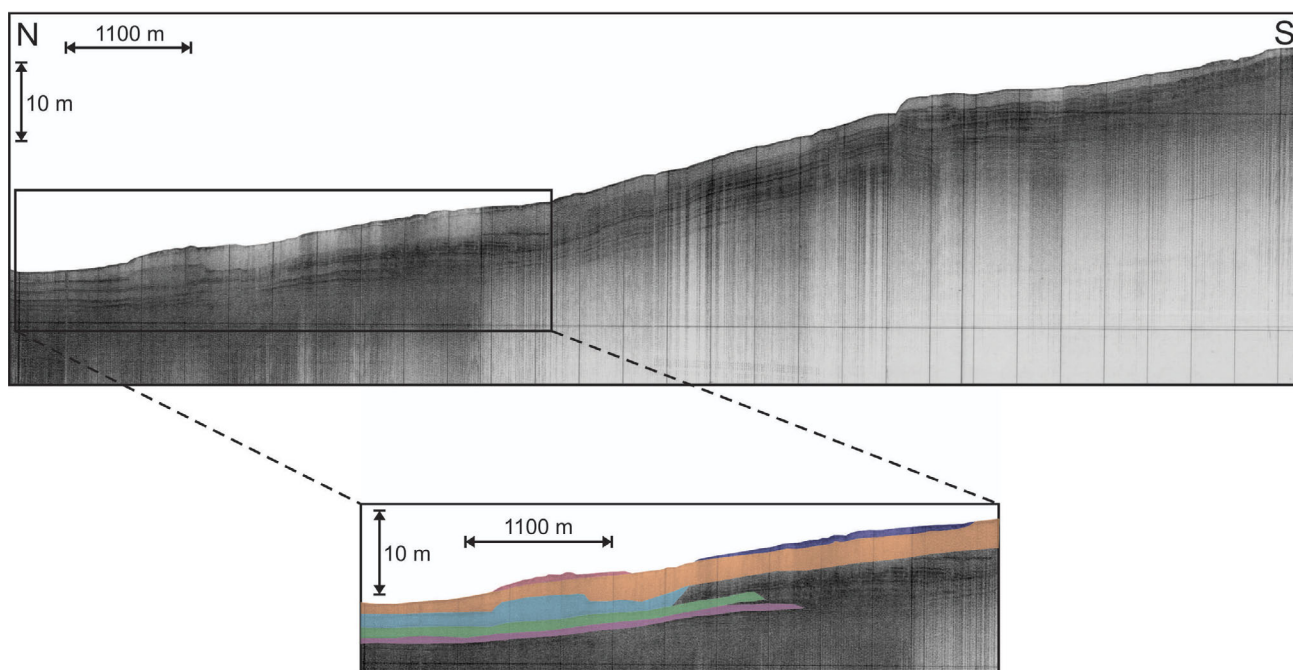


Figure 5: Stacked slope failures in Cambridge Fiord observed from Hunttec seismic sub-bottom profiler data. The zoomed-in inset image shows the individual slope failures, each shaded in a different colour.

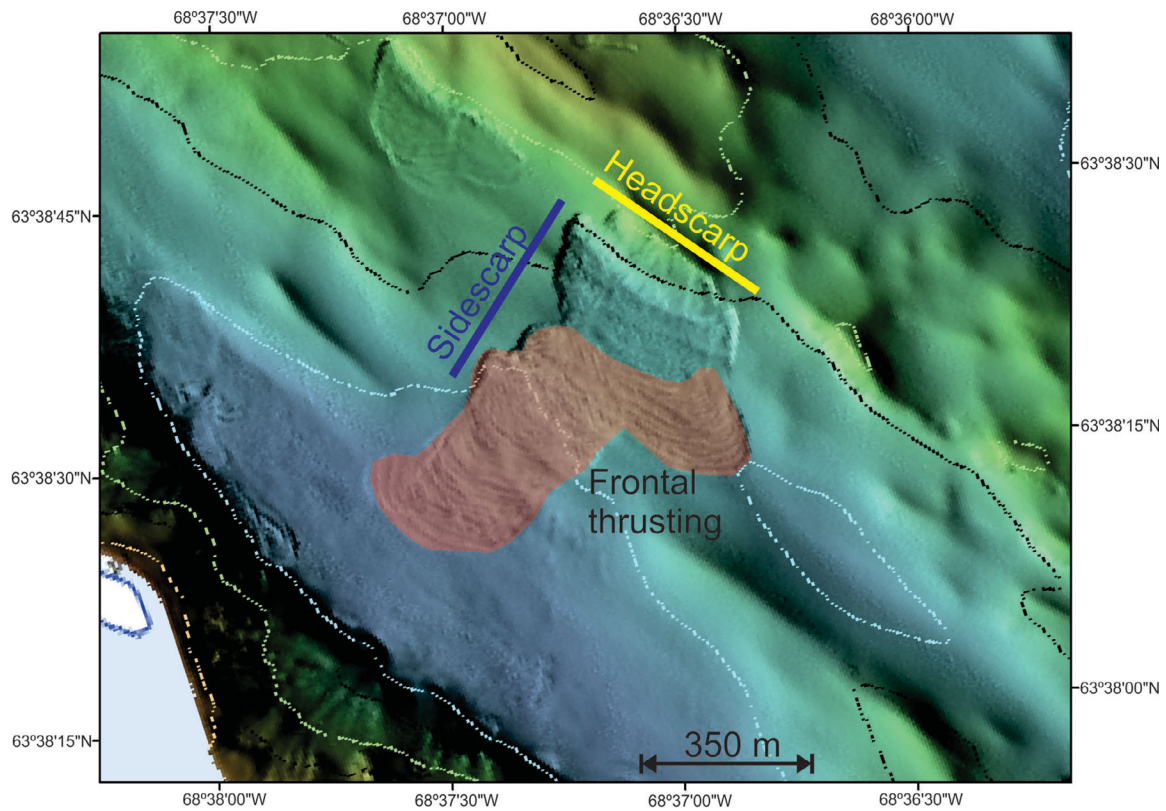


Figure 6: Slope failure in Frobisher Bay displaying characteristics of frontal thrusting in its lower section. This failure also appears to have a main headscarp and a steep sidescarp.

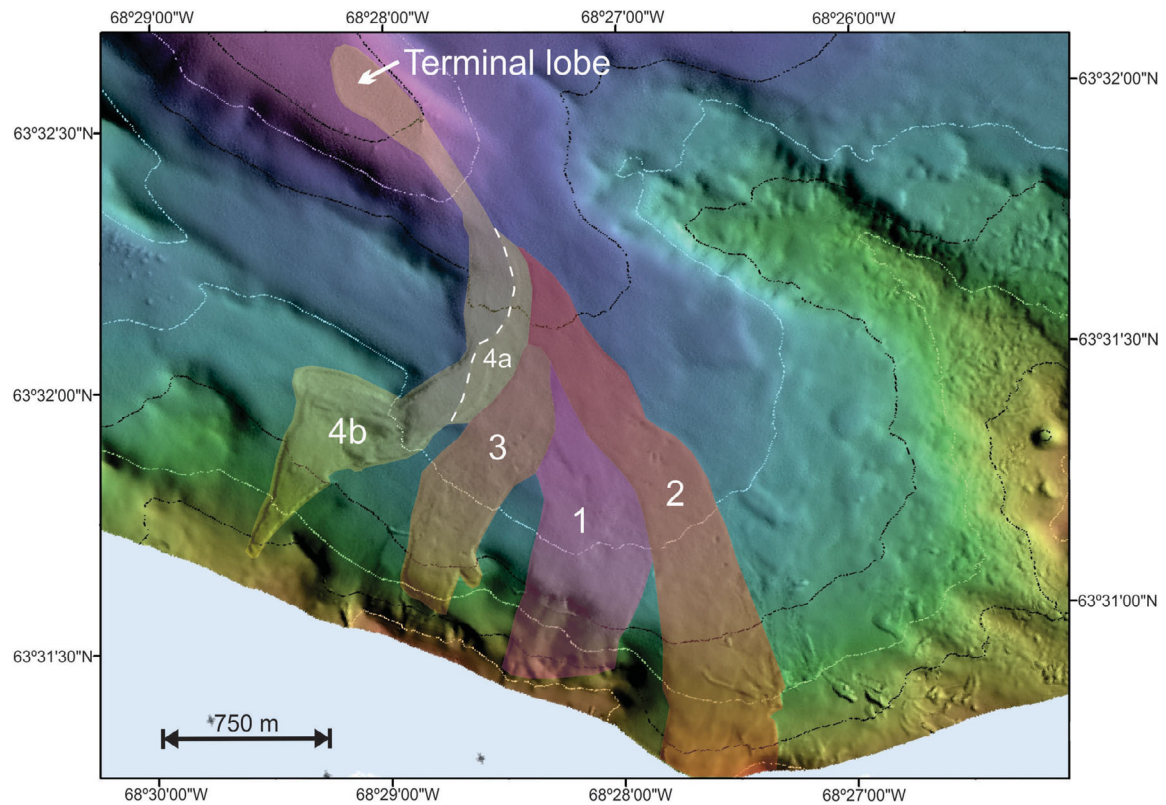


Figure 7: Multiple debris flows from Frobisher Bay depositing sediments in a small basin. Numbers show the order of deposition: 1, oldest, 4, youngest. Interpretation modified from Deering et al. (2019).

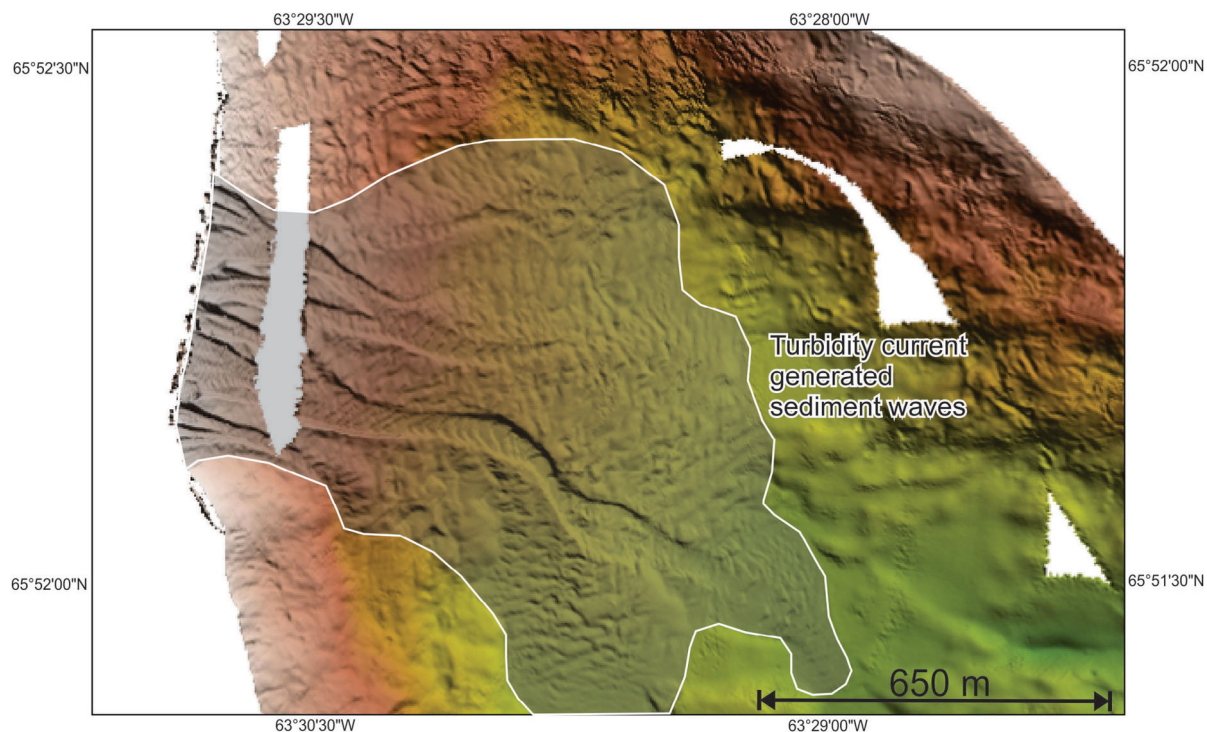


Figure 8: Sediment waves and channels in Touak Fiord caused by turbidity currents.

Clare, M., Chaytor, J., Dabson, O., Gamboa, D., Georgiopoulou, A., Eady, H., Hunt, J., Jackson, C., Katz, O., Krastel, S., León, R., Micallef, A., Moernaut, J., Moriconi, R., Moscardelli, L., Mueller, C., Normandeau, A., Patacci, M., Steven-ton, M., Urlaub, M. et al. 2019: A consistent global approach for the morphometric characterization of subaqueous land-slides; Geological Society of London, Special Publications, v. 477, p. 455–477, URL <<https://doi.org/10.1144/SP477.15>>.

Deering, R., Bell, T., Forbes, D.L., Campbell, D.C. and Edinger, E. 2019: Morphological characterization of submarine slope failures in a semi-enclosed fjord, Frobisher Bay, eastern Cana-dian Arctic; Geological Society of London, Special Publi-cations, v. 477, p. 367–376, URL <<https://doi.org/10.1144/SP477.35>>.

Normandeau, A., Dietrich, P., Hughes-Clarke, J., Van Wychen, W., Lajeunesse, P., Burgess, D. and Ghienne J.-F. 2019: Re-

treating pattern of glaciers controls the occurrence of turbidity currents on high-latitude fjord deltas (eastern Baffin Island); *Journal of Geophysical Research: Earth Surface*, v. 124, no. 6, p. 1559–1571, URL <<https://doi.org/10.1029/2018JF004970>>.

Normandeau, A., Mackillop, K., Macquarrie, M., Philibert, G. and Bennett, R. 2021: Southwind Fiord, Baffin Island, Nunavut: a natural laboratory to explore modern turbidity currents, submarine landslides and iceberg scouring in an Arctic envi-ronment; *in* Summary of Activities 2020, Canada-Nunavut Geoscience Office, p. 81–92, URL <<https://cngo.ca/summary-of-activities/2020/>>.

Syvitski, J., Burrell, D. and Skei, J. 1987: *Fjords: Processes and Products*; Springer Verlag, New York, New York, 379 p., URL <<https://doi.org/10.1007/978-1-4612-4632-9>>.



Southwind Fiord, Baffin Island, Nunavut: a natural laboratory to explore modern turbidity currents, submarine landslides and iceberg scouring in an Arctic environment

A. Normandeau¹, K. Mackillop², M. Macquarrie², G. Philibert² and R. Bennett²

¹Natural Resources Canada, Geological Survey of Canada–Atlantic, Dartmouth, Nova Scotia, alexandre.normandeau@canada.ca

²Natural Resources Canada, Geological Survey of Canada–Atlantic, Dartmouth, Nova Scotia

This work is part of the Baffin Bay Geohazards Activity of the Landslides and Marine Geohazards Project of Natural Resources Canada's Public Safety Geoscience Program (PSGP). This program undertakes research across Canada to support risk reduction from the effects of hazardous natural conditions (i.e., space weather, earthquakes, tsunamis, volcanoes and landslides). The program develops authoritative scientific knowledge and tools to reduce future economic, social and environmental losses from these hazards. Additional funding for this research was provided by the Government of Canada's Program of Energy Research and Development (PERD), Crown-Indigenous Relations and Northern Affairs Canada, and ArcticNet.

Normandeau, A., MacKillop, K., Macquarrie, M., Philibert, G. and Bennett, R. 2021: Southwind Fiord, Baffin Island, Nunavut: a natural laboratory to explore modern turbidity currents, submarine landslides and iceberg scouring in an Arctic environment; in Summary of Activities 2020, Canada-Nunavut Geoscience Office, p. 81–92.

Abstract

The Geological Survey of Canada has a long history of regional assessment of marine geohazards in Arctic environments. Regional mapping allows identification of the distribution of hazards on the seafloor and is a critical part of hazard assessments. However, it does not shed light on understanding the recurrence and triggers of marine geohazards because it consists of one static view of the seafloor. In order to better understand the dynamic nature of seafloor environments, an experiment in Southwind Fiord, Nunavut began by monitoring and recording active marine geohazards. The preliminary data allowed recording of the effect of active turbidity currents and iceberg groundings in the fiord. Both these processes have led to erosion and deposition of sediment on the seafloor. A submarine landslide recorded in the fiord in 2018 appeared to have been triggered by an iceberg grounding on the fiord slope. A submarine landslide triggered by iceberg grounding is a significant discovery, as icebergs ground in many fiords and across the continental margin of Baffin Bay, therefore representing a previously unknown hazard on the seafloor. These results show that Arctic environments are areas of active seafloor processes that can have consequences on future marine infrastructure. Understanding the triggers of marine geohazards, in combination with standard regional assessments performed by the Geological Survey of Canada, will allow stakeholders and decision-makers to properly manage seabed infrastructure in a changing and active marine environment.

Introduction

Marine geohazards occur in most marine environments; however, the causes, frequency and risk they pose are largely unknown, especially in Arctic environments (Broom et al., 2017; Deering et al., 2020). Historically, the Geological Survey of Canada (GSC) has focused targeted research on regional mapping of marine geohazards. This led to the discovery of numerous hazards on the seafloor, the existence of which forms the basis of hazard assessments. Regional mapping commonly does not, however, allow a thorough understanding of the processes responsible for these hazards and the evaluation of their modern activity. Regional mapping offers only a static view of the seafloor, while its

dynamic nature is not understood. Unlike terrestrial landscapes where satellites can help map changes in the environment every few days, the seafloor is more commonly mapped only once, from which its dynamic nature is interpreted rather than directly observed. Therefore, without repeat mapping or monitoring, this single view of the seafloor does not display its changing nature.

In the last decade, monitoring of seafloor hazards in Canada has greatly improved, mostly through detailed studies offshore British Columbia (e.g., Ayranci et al., 2012; Hill, 2012; Hughes Clarke, 2016; Lintern et al., 2016) and, more recently, southeastern Canada (Normandeau et al., 2020a). However, these detailed studies are currently limited to

This publication is also available, free of charge, as colour digital files in Adobe Acrobat® PDF format from the Canada-Nunavut Geoscience Office website: <https://cngo.ca/summary-of-activities/2020/>.

southern Canada, where the processes responsible for seafloor hazards are likely to be different from those occurring in Arctic environments. The predominant role of glaciers and ice sheets in delivering sediments (Normandeau et al., 2019) is likely to contribute to seafloor geohazards. Without repeat seafloor mapping and monitoring of Arctic environments, these processes are not well understood. Therefore, although regional mapping is an important component of hazard assessments, it has been recently recognized that there is a need for targeted monitoring of Arctic seafloor processes to better understand the triggers of marine geohazards and the processes acting on the seabed.

In 2018 and 2019, taking advantage of GSC scientific cruises, a short monitoring program was implemented to understand specific processes and marine geohazards activity in one Arctic fiord. This monitoring program was planned in conjunction with a more regional assessment of seafloor sediment failures (Bennett et al., 2021). This paper presents the approach used during this ongoing monitoring program and preliminary results that help in understanding marine geohazards in Arctic environments.

Regional setting

Baffin Bay is a 1300 km long by 450 km wide, elongated ocean basin connecting the Arctic Ocean to the Atlantic Ocean. Eastern Baffin Island's offshore can be divided into four distinct morphological settings: 1) the inner fiords, which trap most of the sediment supplied by the rivers and have steep-sided walls; 2) the continental shelf, 40–60 km wide with numerous U-shaped transverse troughs that reach 700 m deep; 3) the continental slope, dissected by submarine channels and submarine landslides; and 4) the Baffin Bay basin, accumulating sediment from both the Greenland and Baffin Bay margins and reaching a depth of 2300 m.

The occurrence and recurrence of marine geohazards have been shown to roughly follow the retreat of glacial ice from the region (Normandeau et al., 2020b). Therefore, fiords where glacial ice is present in their watersheds are more likely to rapidly accumulate sediment and be prone to natural hazards. In 2013 and 2014, an ArcticNet mapping program led by Hughes Clarke et al. (2015) mapped numerous fiords around Cumberland Peninsula, which led to the identification of potential hazards. From these data, Southwind Fiord (Figure 1a) stood out because of the number of submarine landslides and the presence of a long channel on the fiord bottom (Figure 1b). Therefore, Southwind Fiord represented an opportunity to monitor seafloor processes in an Arctic environment.

Sediment supply to Southwind Fiord is mainly from a river located at the fiord head. This river is part of an ~265 km² watershed that is composed of 50% glaciers (Normandeau et al., 2019). A glacial tongue 9 km from the fiord head sup-

plies the river with sediment, thus providing a short connection between sediment production from glacial erosion and sediment supply to the fiord (Ghienne et al., 2021). Glacial lakes are a minor component of the watershed, representing only 0.5% of the area. Therefore, there is little sediment trapped in the watershed by lakes and most of the sediments are transported by river to the fiord-head delta.

Southwind Fiord data and methodology

Field-data acquisition

Building on initial seafloor-mapping work done by Hughes Clarke et al. (2015), a thorough study of marine geohazards in Southwind Fiord began in 2018 (Figure 2a). This study included

- 1) repeat seafloor mapping of the fiord bottom to capture changes on the seafloor related to marine geohazards (Figure 2b). Seafloor mapping was carried out in 2018 from the Canadian Coast Guard Ship (CCGS) *Hudson* and in 2019 from the Government of Nunavut's Research Vessel (RV) *Nuliajuk*. These multibeam data were collected with a Reson 7160 (2018) and an EM-2040 (2019), and were then gridded at 5 m and 2 m resolution, respectively, using the Teledyne CARIS HIPS and SIPSTM software suite. Tide data were extracted from the Webtide prediction model (Collins et al., 2011) from Fisheries and Oceans Canada (DFO). The final gridded surfaces were compared to the 2013 and 2014 seafloor maps collected by Hughes Clarke et al. (2015).
- 2) sub-bottom profiles collected from CCGS *Hudson* and RV *Nuliajuk* using a 3.5 kHz sub-bottom profiler. These data allowed the identification of sub-seafloor processes (Figure 2c) and were used for targeted sediment coring.
- 3) three different types of seafloor samples: a) piston cores (Figure 2d) collected from the CCGS *Hudson* in 2018 and targeting landslide scars and undisturbed sediment for slope stability analysis; b) gravity and box cores collected from CCGS *Hudson* and CCGS *Amundsen*, and targeting mass-transport deposits for assessment of their age; and c) grab samples from Van Veen and IKU grab samplers to understand channel sedimentary processes (Ghienne et al., 2021).
- 4) a downward-looking Acoustic Doppler Current Profiler (ADCP) mooring (Figure 2e) to directly measure turbidity currents triggered on the delta front. The mooring was placed at 120 m water depth, at the mouth of the submarine channel. The water depth of the mooring is deeper than the depth of the sill mid-fiord (90 m), which prevents icebergs from coming into the fiord and damaging the mooring.
- 5) a conductivity, temperature and depth (CTD) rosette with water collection to measure suspended sediment concentrations in the fiord along a proximal to distal transect.

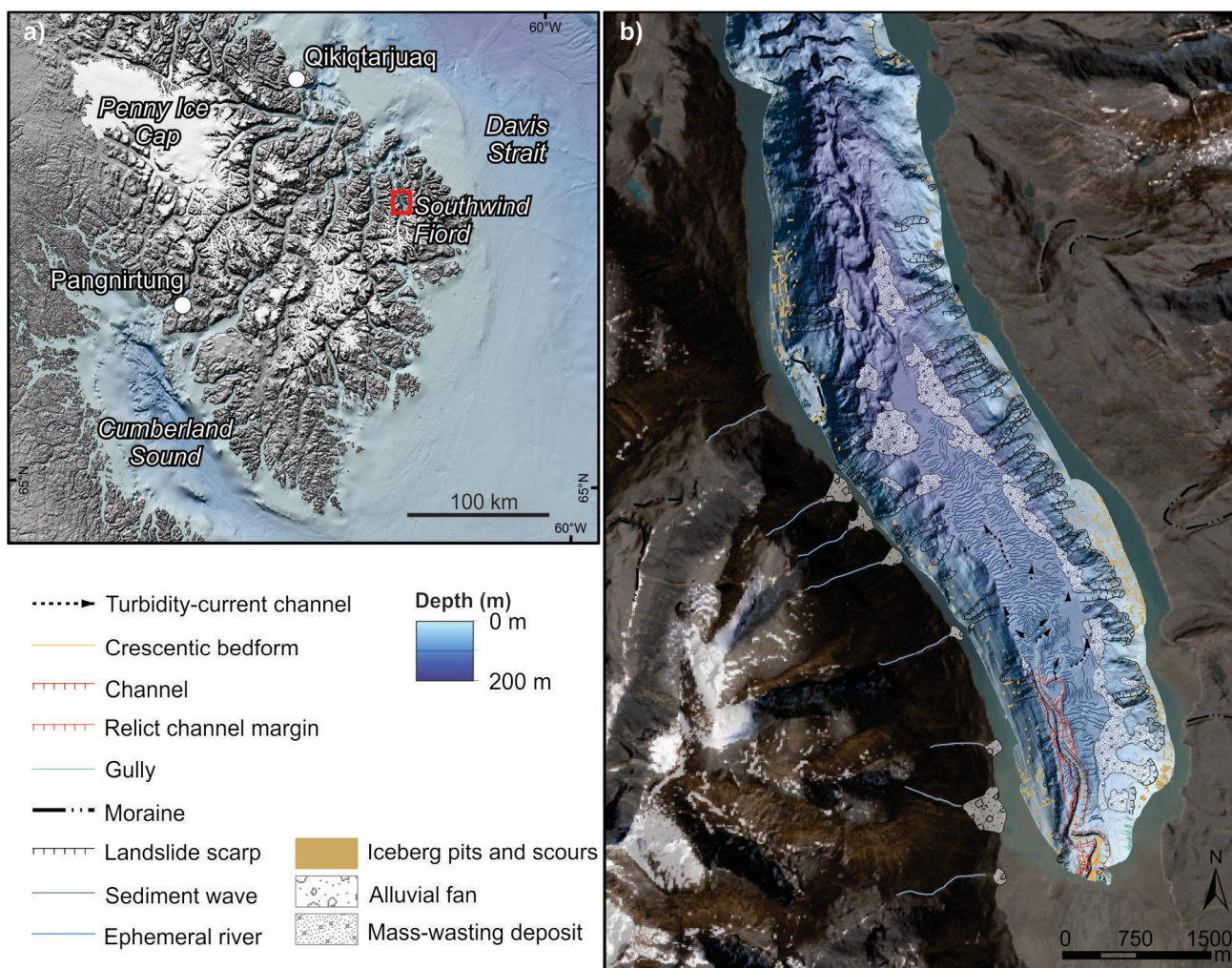


Figure 1: a) Location of Southwind Fiord on southeastern Baffin Island, Nunavut. b) Geomorphology of Southwind Fiord environment.

Although all these types of data were collected, only data from repeat multibeam surveys and seafloor samples are presented in this preliminary overview of the Southwind Fiord experiment.

Laboratory analysis on sediment cores

Laboratory analyses were conducted on the sediment cores collected. The cores were first X-rayed, split, photographed and described. They were then put through a multisensor core logger (MSCL) for measurements of bulk density, magnetic susceptibility and colour-reflectance. In addition, discrete shear-strength measurements were taken at 10 cm intervals along the core using a miniature vane shear, following ASTM D4648/D4648M-16 (2016). Advanced geotechnical testing was also conducted on the sediment cores, but those results are not presented here.

Turbidity currents

Turbidity currents are known to be damaging to subsea infrastructure. Most often, they are triggered at river mouths

because of large volumes of incoming fluvial sediment. In Southwind Fiord, a 2.5 km long submarine channel is present at the mouth of the fiord-head river (Figure 1b). This channel consists of crescent-shaped bedforms that evolve in wavelength from ≤ 25 m near the head of the channel to > 50 m farther downslope (Ghienne et al., 2021). The crescent-shaped appearance is due to the interaction of the bedforms with the channel walls. The centre of the channel represents higher rates of bedform migration compared to the area interacting with the sidewalls, leading to the crescent shape. Where the channel becomes unconfined, the morphology of the sediment waves becomes more sinuous or linear and much wider, no longer being affected by channel sidewalls. The wavelength of the sediment waves becomes 25–50 m and the waves extend more than 2.3 km in the basin. Near the channel mouth, and in the middle of the sediment-wave field, there is some indication of channel formation where small knickpoints are followed by incisions (Figure 1b).

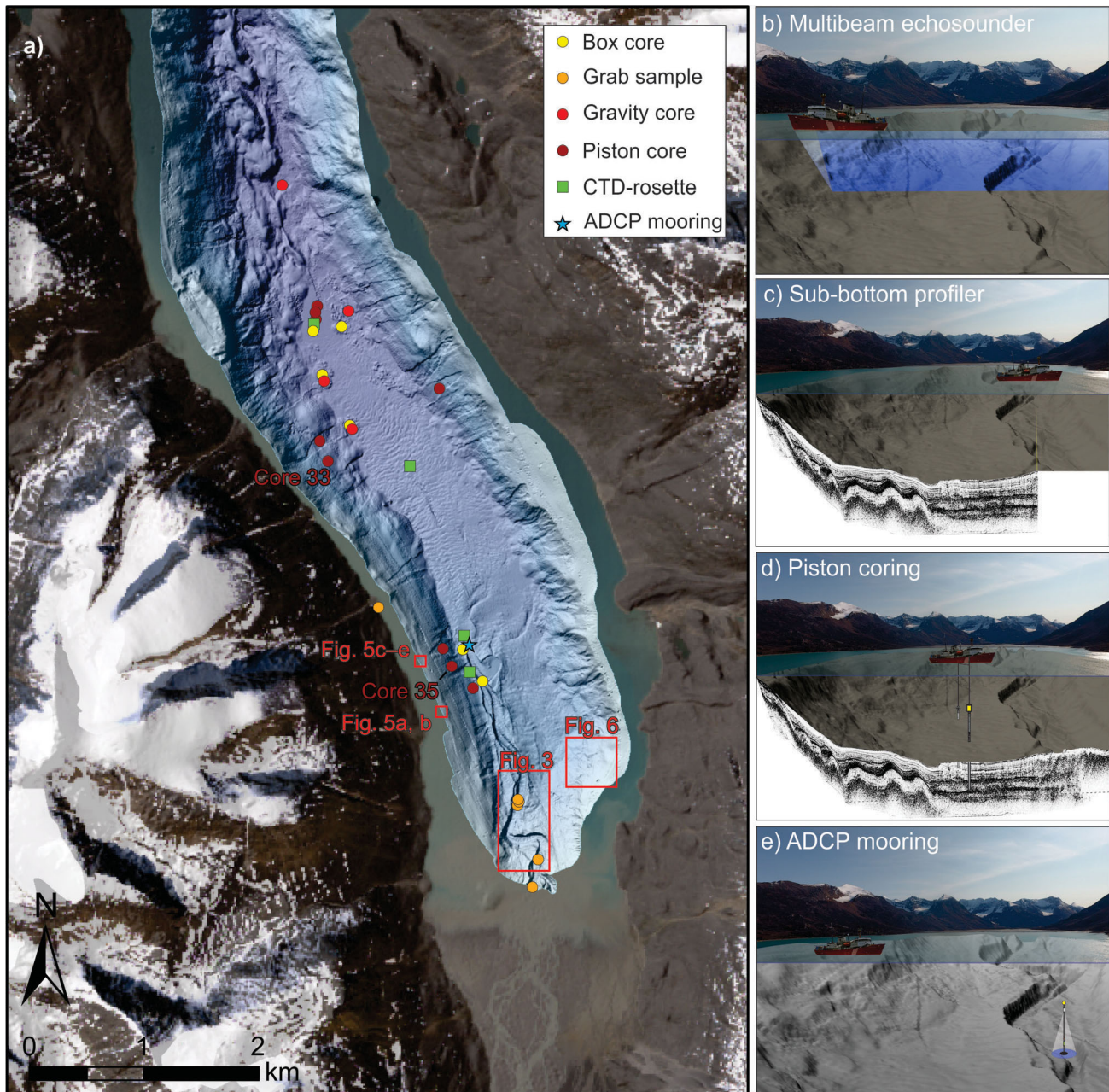


Figure 2: a) Samples collected in Southwind Fiord from three different cruises. Data-acquisition methods used in Southwind Fiord: b) multibeam bathymetry, c) sub-bottom profiling; d) piston coring; and e) ADCP mooring at the end of the channel extending from the mouth of the fiord-head river.

Repeat seafloor mapping conducted from 2013 to 2019 reveals significant changes on the seafloor, most of which have occurred in the channel, along its entire length. These changes are characterized by both sediment accumulation and sediment erosion. Erosion occurs mostly on the steep (lee) side of the bedforms, whereas accumulation occurs mostly on the low-gradient (stoss) side of the bedforms (Figure 3a–d).

The repetitive changes of erosion and deposition on the crescentic bedforms in the channels correspond to the now widely observed pattern in other channel/canyon systems

(Smith et al., 2005; Mazières et al., 2014; Hughes Clarke, 2016; Normandeau et al., 2020a). This repetitive pattern is often attributed to cyclic step processes where turbidity currents erode the lee side of bedforms and deposit sediment on the stoss side. This repetitive pattern leads to the upstream migration of bedforms. These types of processes are known to damage instrumentation installed in their path (Paull et al., 2010; Hughes Clarke et al., 2014) and thus represent a hazard on the seafloor.

The exact timing of turbidity currents remains, to this day, unknown. A downward-looking ADCP deployed at the

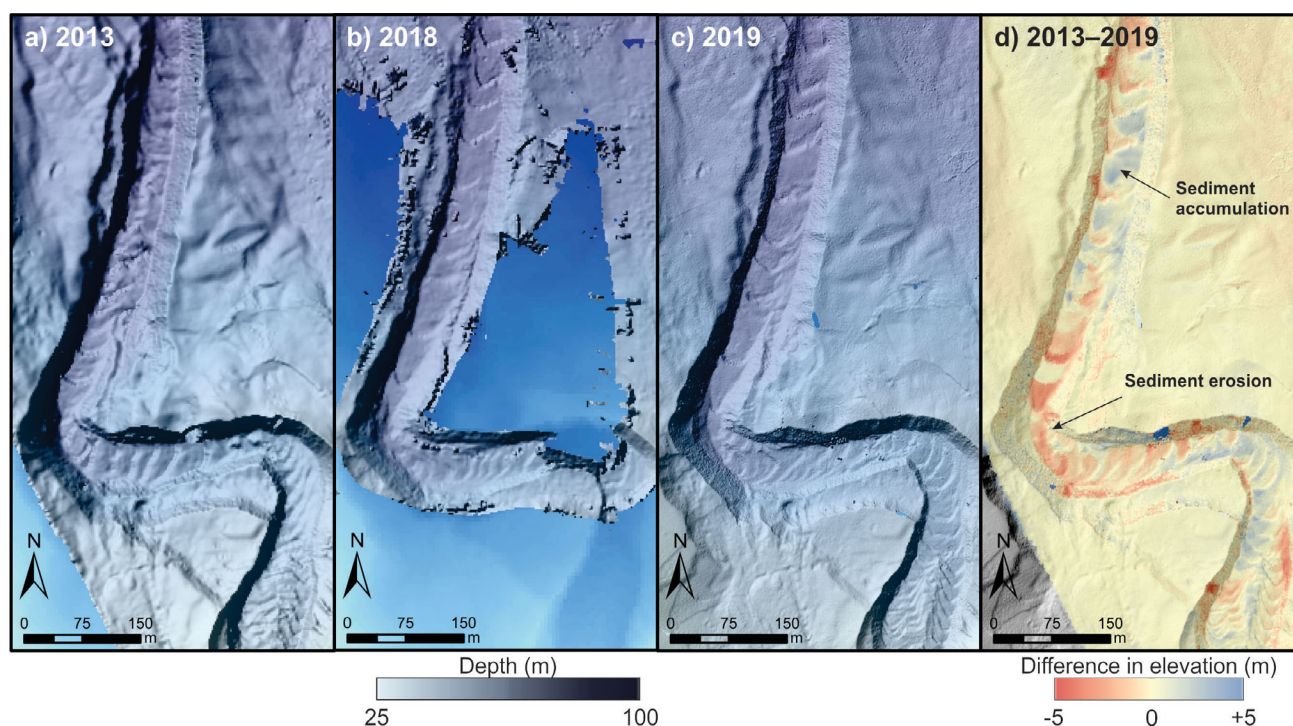


Figure 3: Multibeam bathymetry images showing seafloor evolution in Southwind Fiord from 2013 (a) to 2018 (b) and 2019 (c). The difference in elevation of the seafloor between 2013 and 2019 (d) illustrates the dynamic nature of the channel and the occurrence of turbidity currents.

mouth of a submarine channel in 2019 will shed light on the exact timing and recurrence of turbidity currents, as well as their internal structure. This mooring is expected to be recovered in 2021. Nonetheless, a preliminary analysis of satellite imagery and a comparison to similar fiords makes it possible to estimate the timing of turbidity-current activity. For example, satellite imagery from 2018 shows that the fiord became ice free in early July, as temperatures consistently rose above 5–10°C (Figure 4a, b). As soon as the sea ice melted, sediment plumes were observed extending from the fiord-head river on all imagery from July and August. These plumes did not necessarily create turbidity currents, but it is likely that these density currents occurred mostly during these months. As temperatures began dropping, as seen in early September 2018, sediment plumes were no longer observed at the fiord head, indicating a rapid reduction of sediment supply to the fiord.

The satellite imagery indicates that turbidity currents are likely to be limited to 2 months or less during the summer, although episodic events may occur later in the season. Since glaciers are the main driver for river flow and sediment export, it is likely that glacial melt during summer high temperatures increases river discharge; this, in turn, favours the triggering of turbidity currents. Sediment plumes at the delta front begin to form in early July, when sea ice breaks up and warm temperatures increase glacial melt. In 2018, sediment plumes could be observed until late August. In early September, the absence of sediment

plumes suggests that turbidity currents can no longer be triggered by the supply of sediment on the delta. Therefore, turbidity-current season appears to be limited to July and August, although the recurrence of these events will only be fully understood once the downward-looking ADCP is recovered in 2021.

Iceberg scouring

At least 500 iceberg pits and scours were detected on the seafloor of Southwind Fiord. Iceberg pits can be distinguished on the seafloor by their centre depression and berms on each side, which are higher than the surrounding seafloor. Most of these pits are located in water depths of <40 m, but some extend down to a maximum water depth of about 90 m. The mean pit depth is 30 m, but that does not include the unmapped shallow water of the fiord, meaning that the real mean depth is shallower than 30 m. The mean areal extent of the observed pits is 290 m², which corresponds to iceberg keels measuring approximately 17 m across.

Repeat bathymetry between 2014 and 2019 shows that at least three icebergs created pits on the seabed of Southwind Fiord during the 5-year period. These new pits are identified by erosion at the centre of the pit and accumulation on its sides (berm; Figure 5). In two cases in the fiord, satellite imagery identified precisely which iceberg created the pits (Figure 5a, b): they grounded in early August and early September of 2018 (Figure 5a, b). The iceberg that created

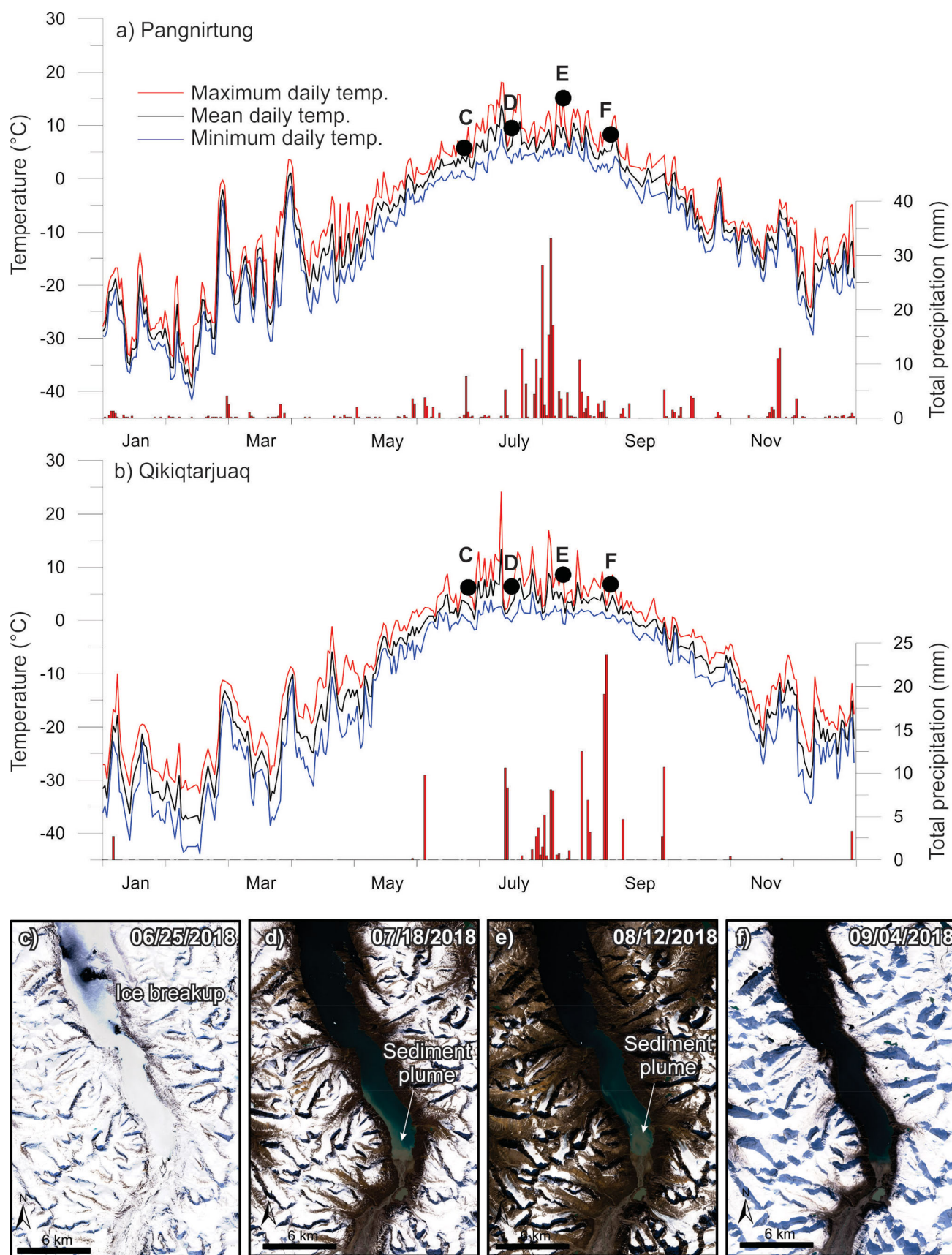


Figure 4: a) and b) Daily temperature in Pangnirtung and Qikiqtarjuaq in 2018. c) to f) Satellite images illustrating the sediment supply from the delta at the head of Southwind Fiord during the warm summer months.

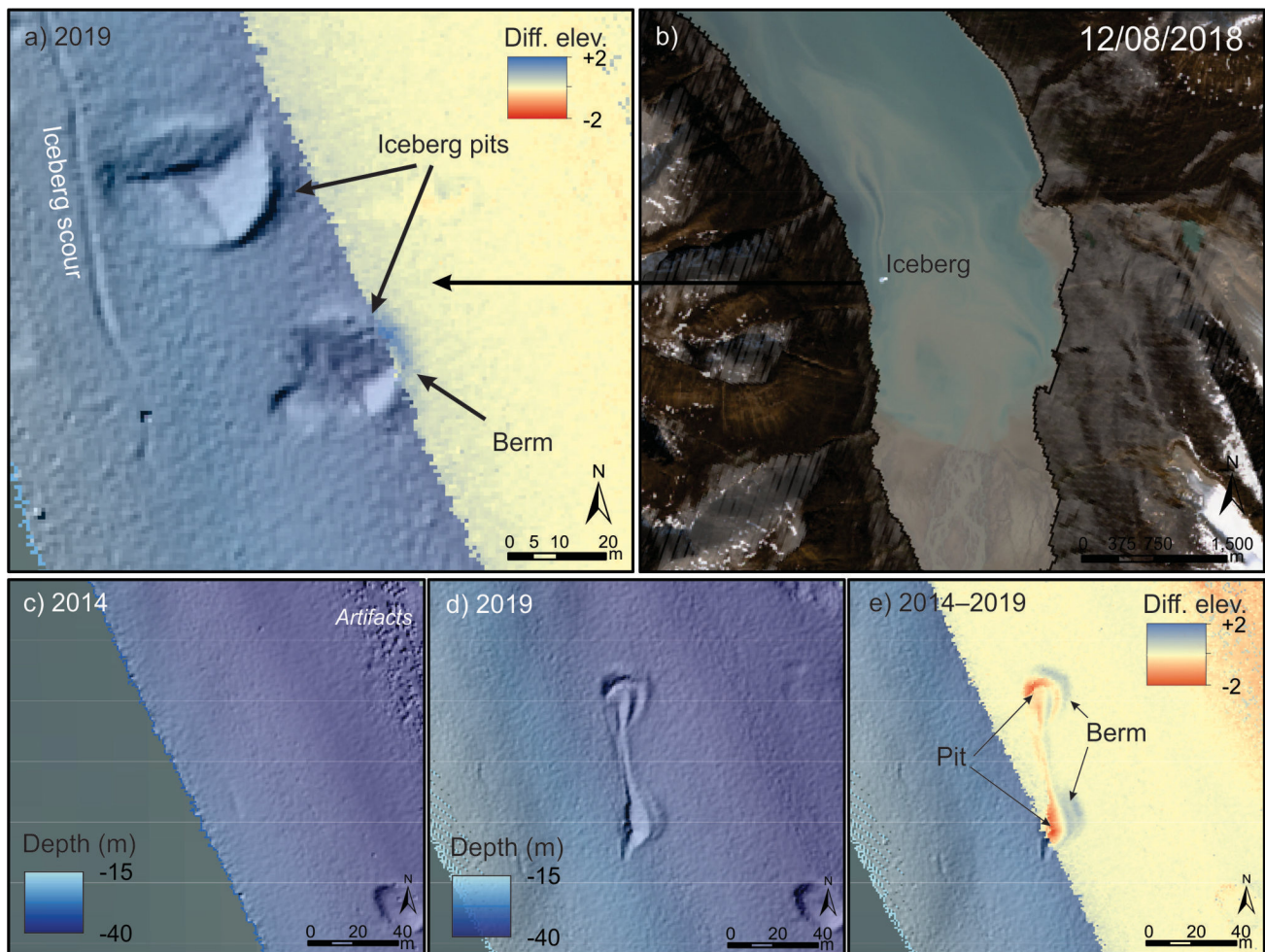


Figure 5: Iceberg pits and scour in Southwind Fiord created between 2014 and 2019: **a)** new iceberg pits created in August 2018 when an iceberg grounded at this location; **b)** and **c)** undisturbed seafloor in 2014; **d)** iceberg pits and scour in 2019; **e)** difference in elevation between 2014 and 2019, showing the erosion of the pit and the formation of a berm by a grounded iceberg. Abbreviation: Diff. elev., difference in elevation.

the third iceberg pit could not be found on satellite imagery (Figure 5c–e).

Mass-transport deposits

A total of 57 landslide scarps were mapped on the slopes of Southwind Fiord (Figure 1b). Many scarps coalesce, which probably leads to an underestimation of the number of landslide events. For example, reactivation of previously failed sediment might not be captured by this descriptive exercise. Most landslides occur within 7 km of the fiord head, are 140 ± 117 m (1σ) wide and have a mean run-out distance of 370 ± 188 m (1σ). About half of them have a visible deposit at their base (Figure 1b), while others, mostly those close to the fiord head, have no visible deposit. The absence of deposits indicates that these failures are older and that the deposits were likely buried or washed away by turbidity currents originating from the fiord head.

Repeat bathymetric surveys between 2014 and 2019 indicate that a landslide was triggered in 2018 (Figure 6a–c).

This new landslide, as well as two new scarp reactivations, are described by Normandeau et al. (work in progress). The main new landslide was triggered at a depth of 28 m and has a scar depth of about 3 m (Figure 6b). The landslide appears to have been triggered by a grounded and potentially cap-sized iceberg impacting the headscarp location (details in Normandeau et al., work in progress).

Sediment cores collected on the fiord sidewall are composed primarily of homogeneous to finely laminated mud. Bulk density and shear strength are relatively low, between 1.6 and 1.8 g/cm³ and between 6 and 12 kPa, respectively. These two physical properties are used to calculate the factor of safety of the slope. The static factor of safety (FS) for total stress conditions was calculated under undrained conditions using the infinite slope analysis equation:

$$FS = \frac{S_u}{\gamma' h \sin \beta \cos \beta}$$

where S_u is the undrained shear strength (kPa), β is the slope angle ($^\circ$), γ' is the effective unit weight (kN/m³) of the sedi-

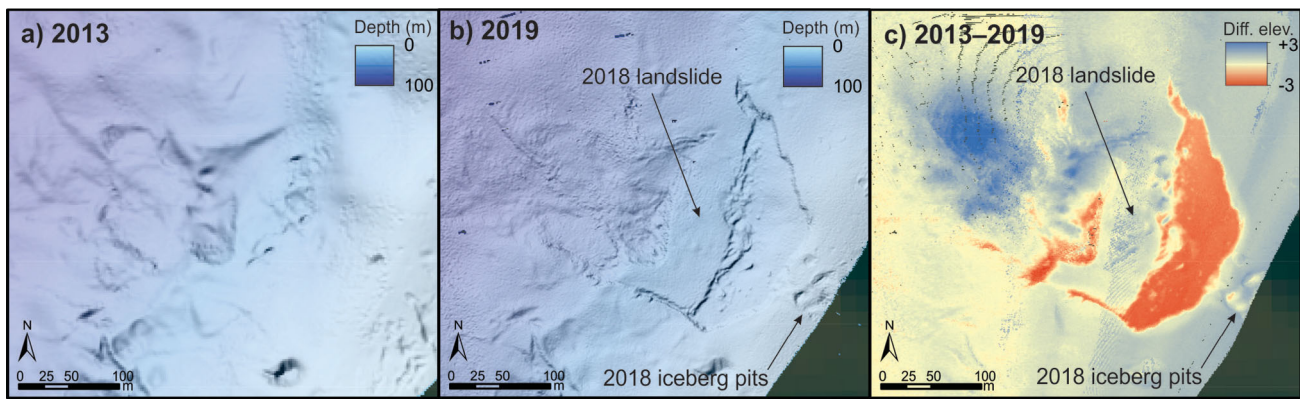


Figure 6: Landslide triggered in 2018 by an iceberg grounding in Southwind Fiord: **a)** 2013 multibeam data illustrating a relatively smooth slope; **b)** 2019 multibeam data showing the presence of a new landslide; **c)** difference in elevation between 2013 and 2019, showing the erosion and deposition associated with the new landslide.

mentary column and h is the height of the effective overburden (depth below seafloor in metres). The FS values presented in Figure 7 were calculated using a slope angle of 13° , which is the slope of the pre-failure surface from the 2018 landslide described previously (Figure 6). The FS reaches 1.7–1.8 at 3 m below the seafloor in cores 33 and 35 (see Figure 2a for locations). The additional load required for failure is between 10 kN/m^2 (core 33) and 17 kN/m^2 (core 35), which is reached at a depth similar to the landslide failure planes observed in the fiord. Iceberg grounding and capsizing can easily produce the additional load

needed and thus is likely a major trigger for landslides in this fiord (Normandeau et al., work in progress, 2021).

The critical slope angle, which is the slope angle under which sediment would naturally fail, is about 24° at a depth of $\sim 3 \text{ m}$ below the seabed, based on physical properties of cores 33 and 35 (Figure 8a). A slope-angle map of Southwind Fiord (Figure 8b) shows that angles $>24^\circ$ occur relatively frequently along the upper part of the fiord sidewalls. Although factors of safety will vary between locations, this slope-angle map indicates that the fiord sidewalls are easily

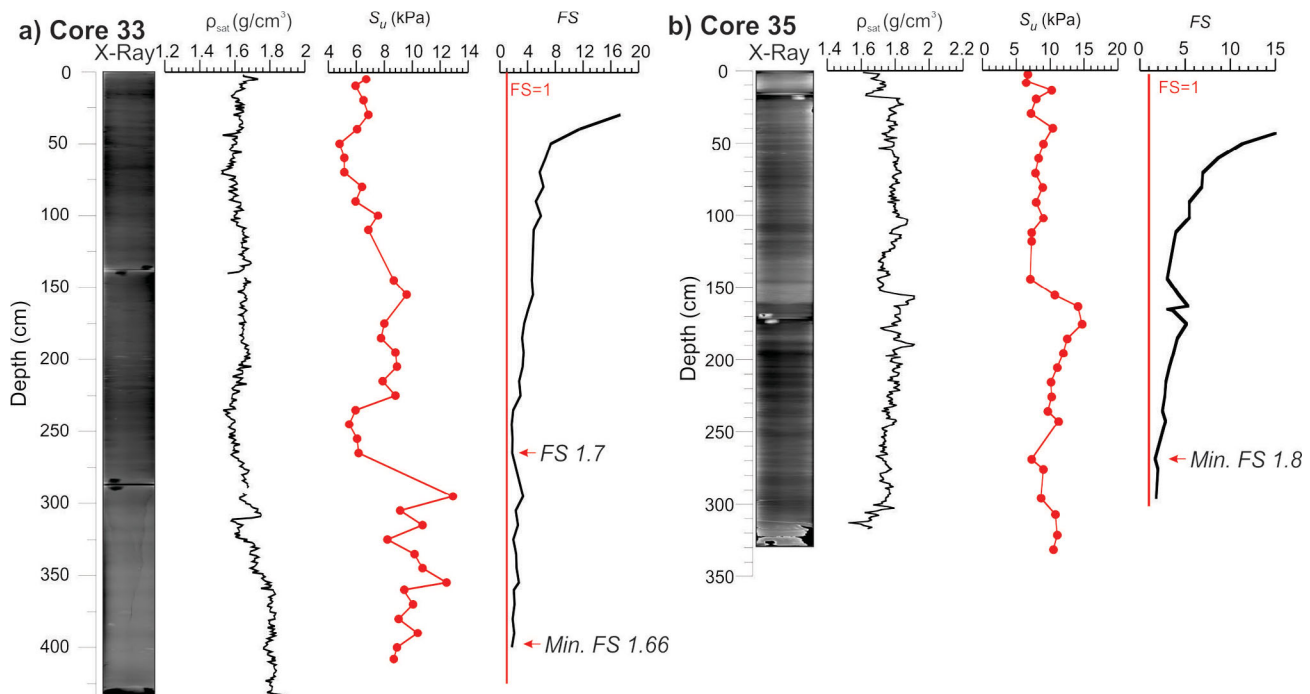


Figure 7: Physical properties of **a)** core 33, distal to the fiord-head delta in Southwind Fiord; **b)** core 35, proximal to the fiord-head delta. See text for details and Figure 2 for location of cores. Abbreviations: Diff. elev., difference in elevation; FS, factor of safety for a slope of 13° ; ρ_{sat} , bulk density; S_u , shear strength.

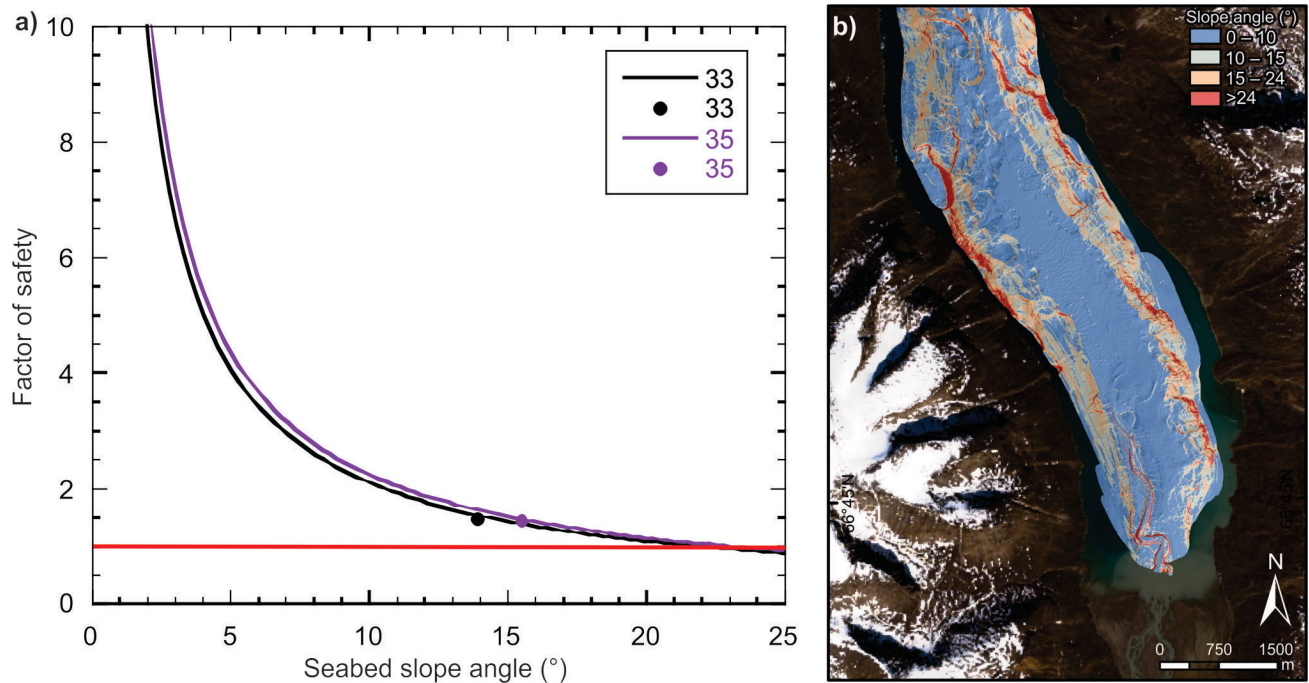


Figure 8: **a)** Factor of safety (FS) for cores 33 and 35 as a function of seabed-slope angle; red line indicates $FS = 1$, where sediments are statically unstable at about 24° ; dots are minimum FS measured on cores 33 and 35 for a slope angle of 13° ; **b)** Slope-angle map of Southwind Fiord.

susceptible to failure, and explains the large number of landslides present on the fiord sidewalls.

Marine geohazards in Arctic fiords: preliminary implications

Iceberg scours and turbidity currents were known recurring hazards in the fiords of eastern Baffin Island (Bennett et al., 2014; Normandeau et al., 2019). However, the recurrence of these processes remains elusive, especially for turbidity currents, as monitoring data do not yet exist. The Southwind Fiord experiment will attempt to bridge that gap once the ADCP mooring is recovered.

The most important implication of the experiment so far is the discovery of a new landslide triggered by a grounding iceberg in 2018. Large submarine landslides in fiords are commonly attributed to earthquake shaking or delta progradation (Stacey et al., 2019). However, the current detailed study of Southwind Fiord indicates that landslides in Arctic fiords with active glaciers and icebergs appear more likely to have been triggered by other processes, such as iceberg groundings. To date, no submarine landslides in Baffin Island fiords were correlated to known earthquakes. For example, the 1933 magnitude 7.3 earthquake offshore Pond Inlet did not lead to any apparent deposit to date (Broom et al., 2017). In addition, on the eastern Baffin Island coastline, a small subset of dated subaerial landslides occurring over glaciers show that these landslides are located in a seismically active area but could not—yet—be

directly related to specific earthquakes (Gosse et al., 2020). It is therefore suggested that icebergs may be a more likely trigger of submarine landslides in Baffin Island fiords because of their prevalence throughout the eastern Arctic. Most submarine landslides in Baffin Bay fiords are located on steep sidewalls and originate from shallow water, which could be affected by iceberg grounding. Other nearshore processes, such as multiyear and shore-fast sea ice moving with the tide and subaerial debris flows extending into the marine environment, may be responsible for other observed landslide deposits. For example, submarine landslides in Frobisher Bay could be due to sea ice grounding in shallow water (e.g., Deering et al., 2020), which likely compares to the mechanism of iceberg grounding observed in Southwind Fiord.

These data from Southwind Fiord represent a crucial step forward in understanding what triggers submarine landslides in Arctic environments. Further studies will need to quantify the role played by icebergs, sea ice, subaerial debris flows and earthquakes in generating these hazards. Although a landslide triggered by iceberg grounding has been observed in Southwind Fiord, it is not possible, at this stage, to assess the prevalence of this trigger compared with others mentioned previously.

Economic considerations

Submarine landslides have known consequences for coastal populations through the generation of tsunamis. One

such tsunami triggered by a submarine landslide occurred in an Alaskan fiord in 1964 (Brothers et al., 2016). In Baffin Bay, there is no record to date of such events caused by submarine landslides. However, the large number of landslides mapped over the years suggests that some of them may have had consequences for the shoreline, but this theory remains to be assessed.

Other consequences of such marine geohazards as submarine landslides, turbidity currents and iceberg scouring are the damage they can cause to seafloor infrastructure. Underwater fibre-optic internet cables have been deemed important to connect northern communities; therefore, a proper understanding of the occurrence and recurrence of seafloor hazards is critical. Damage to seafloor cables can cost millions of dollars in repairs. As Baffin Bay is remote, it can also take time to repair cables underwater, leaving communities without reliable communication for some time. Therefore, before subsea cables are to be laid on the seafloor, the information provided by seafloor mapping and the occurrence and recurrence of seafloor geohazards can be used to properly plan cable-layout routes.

Conclusions

The Geological Survey of Canada has a history of providing regional maps and understanding of seafloor geohazards. In order to document the processes responsible for marine geohazards, an experiment in Southwind Fiord was initiated to monitor and record active geohazards. Although the experiment is ongoing, preliminary results show that turbidity currents, iceberg groundings and submarine landslides have occurred in the last two years in Southwind Fiord, illustrating the dynamic nature of Arctic fiords. A critical observation of this experiment is that iceberg grounding can, under the right circumstances, trigger submarine landslides. Therefore, the extent to which icebergs affect the seafloor extends well beyond their keel depth if they trigger landslides. A proper understanding of the distribution of these hazards will be important to mitigate their effects should there be infrastructure laid on the seafloor.

Acknowledgments

The authors thank the officers, crew and scientific staff on board the CCGS *Hudson*, CCGS *Amundsen* and RV *Nuliajuk* during the 2018 and 2019 field programs. Financial support for this study was provided by the Government of Canada's Program of Energy Research and Development (PERD), ArcticNet and Crown-Indigenous Relations and Northern Affairs Canada. The authors also thank the Government of Nunavut's Department of Environment (Fisheries and Sealing Division) and the Fisheries and Marine Institute of Memorial University of Newfoundland for their support during this project. J. Hughes Clarke (University of New Hampshire) and ArcticNet are thanked for col-

lecting the original 2013–2014 multibeam datasets. Thanks also go to the many collaborators who helped on different aspects of this research: C. Campbell (Geological Survey of Canada), C. Richards (Fisheries and Oceans Canada), D. Bourgault (Université du Québec à Rimouski–Institut des sciences de la mer de Rimouski), J.-F. Ghienne (Université de Strasbourg), J. Hughes Clarke (University of New Hampshire), V. Maselli (Dalhousie University) and M. Cartigny (Durham University).

Natural Resources Canada, Lands and Minerals Sector contribution 20200643

References

- ASTM D4648/D4648M-16 2016: Standard test methods for laboratory miniature vane shear test for saturated fine-grained clayey soil; ASTM International, West Conshohocken, Pennsylvania, URL <<https://www.astm.org/search/fullsite-search.html?query=D4648/D4648M-16>> [December 2020].
- Ayranci, K., Lintern, D.G., Hill, P.R. and Dashtgard, S.E. 2012: Tide-supported gravity flows on the upper delta front, Fraser River delta, Canada; *Marine Geology*, v. 326–328, p. 166–170 <<https://doi.org/10.1016/j.margeo.2012.09.007>>.
- Bennett, R., Campbell, D.C. and Furze, M.F.A. 2014: The shallow stratigraphy and geohazards of the northeast Baffin Shelf and Lancaster Sound; *Bulletin of Canadian Petroleum Geology*; v. 62, p. 217–231, URL <<https://doi.org/10.2113/gscpgbull.62.4.217>>.
- Bennett, R., Normandeau, A. and Campbell, D.C. 2021: Preliminary assessment of the distribution of submarine slope failures in Baffin Island fiords, Nunavut; *in* Summary of Activities 2020, Canada-Nunavut Geoscience Office, p. 73–80, URL <<https://cngo.ca/summary-of-activities/2020/>>.
- Broom, L.M., Campbell, D.C. and Gosse J.C. (2017): Investigation of a Holocene marine sedimentary record from Pond Inlet, northern Baffin Island, Nunavut; *in* Summary of Activities 2017, Canada-Nunavut Geoscience Office, p. 93–104 URL <https://m.cngo.ca/wp-content/uploads/Summary_of_Activities_2017-P08-Broom.pdf> [December 2020].
- Brothers, D.S., Haeussler, P.J., Liberty, L., Finlayson, D., Geist, E., Labay, K. and Byerly, M. 2016: A submarine landslide source for the devastating 1964 Chenega tsunami, southern Alaska; *Earth and Planetary Science Letters*, v. 438, p. 112–121, URL <<https://doi.org/10.1016/j.epsl.2016.01.008>>.
- Collins, A.K., Hannah, C.G. and Greenberg, D. 2011: Validation of a high resolution modelling system for tides in the Canadian Arctic Archipelago; *Canadian Technical Report of Hydrography and Ocean Sciences*, v. 273, 72 p.
- Deering, R., Bell, T., Forbes, D.L., Campbell, D.C. and Edinger, E. 2020: Morphological characterization of submarine slope failures in a semi-enclosed fjord, Frobisher Bay, eastern Canadian Arctic; *Geological Society of London, Special Publications*, v. 477, p. 367–376.
- Ghienne, J., Normandeau, A., Dietrich, P., Bouysson, M., Lajeunesse, P. and Schuster, M. 2020: The depositional signature of cyclic steps: a late Quaternary analogue compared to modern active delta slopes; *Sedimentology*, URL <<https://doi.org/10.1111/sed.12806>>.

- Gosse, J.C., Tremblay, T., Broom, L.A., Campbell, D.C., Wenzel, G., Nedimović, M.R. and Forget Brisson, L. 2020: Initial results from the ULINNIQ seismicity and tsunami hazard project, northeastern Baffin Island, Nunavut; *in* Summary of Activities 2019, Canada-Nunavut Geoscience Office, p. 101–124, URL <https://m.cngo.ca/wp-content/uploads/Summary_of_Activities_2019-Paper_09.en_.pdf> [December 2020].
- Hill, P.R. 2012: Changes in submarine channel morphology and slope sedimentation patterns from repeat multibeam surveys in the Fraser River delta, western Canada; *in* Sediments, Morphology and Sedimentary Processes on Continental Shelves, M.Z. Li, C.R. Sherwood and P.R. Hill (ed.), International Association of Sedimentologists, Special Publication 44, p. 47–70.
- Hughes Clarke, J.E. 2016: First wide-angle view of channelized turbidity currents links migrating cyclic steps to flow characteristics; *Nature Communications*, v. 7, 11896, URL <<https://doi.org/10.1038/ncomms11896>>.
- Hughes Clarke, J.E., Muggah, J., Renoud, W., Bell, T., Forbes, D.L., Cowan, B. and Kennedy, J. 2015: Reconnaissance seabed mapping around Hall and Cumberland peninsulas, Nunavut: opening up southeastern Baffin Island to nearshore geological investigations; *in* Summary of Activities 2014, Canada-Nunavut Geoscience Office, p. 133–144, URL <<https://m.cngo.ca/wp-content/uploads/Summary-of-Activities-2014-P15.pdf>> [December 2020].
- Hughes Clarke, J.E., Vidiera Marques, C.R. and Pratomo, D. 2014: Imaging active mass-wasting and sediment flows on a fjord delta, Squamish, British Columbia; *in* Submarine Mass Movements and their Consequences: Advances in Natural and Technological Hazards Research, S. Krastel, J.-H. Behrmann, D. Völker, M. Stipp, C. Berndt, R. Urgeles, J. Chaytor, K. Huhn, M. Strasser and C.B. Harbitz (ed.), Springer, Berlin, p. 249–260.
- Lintern, D.G., Hill, P.R. and Stacey, C. 2016: Powerful unconfined turbidity current captured by cabled observatory on the Fraser River delta slope, British Columbia, Canada; *Sedimentology*, v. 63, p. 1041–1064, URL <<https://doi.org/10.1111/sed.12262>>.
- Mazières, A., Gillet, H., Castelle, B., Mulder, T., Guyot, C., Garlan, T. and Mallet, C. 2014: High-resolution morpho-bathymetric analysis and evolution of Capbreton submarine canyon head (southeast Bay of Biscay–French Atlantic coast) over the last decade using descriptive and numerical modeling; *Marine Geology*, v. 351, p. 1–12, URL <<https://doi.org/10.1016/j.margeo.2014.03.001>>.
- Normandeau, A., Bourgault, D., Neumeier, U., Lajeunesse, P., St-Onge, G., Gostiaux, L. and Chavanne, C. 2020a: Storm-induced turbidity currents on a sediment-starved shelf: insight from direct monitoring and repeat seabed mapping of upslope migrating bedforms; *Sedimentology*, v. 67, p. 1045–1068, URL <<https://doi.org/10.1111/sed.12673>>.
- Normandeau, A., Campbell, D.C., Bennett, R., Macquarrie, M., Mackillop, K., Philibert, G., Sedore, P., Maselli, V. and Jenner K.A. 2020b: Holocene and active marine geohazards offshore eastern Baffin Island, Nunavut; *in* Summary of Activities 2019, Canada-Nunavut Geoscience Office, p. 93–100, URL <https://m.cngo.ca/wp-content/uploads/Summary_of_Activities_2019-Paper_08.en_.pdf> [December 2020].
- Normandeau, A., Dietrich, P., Hughes Clarke, J., Van Wychen, W., Lajeunesse, P., Burgess, D. and Ghienne, J.-F. 2019: Retreat pattern of glaciers controls the occurrence of turbidity currents on high-latitude fjord deltas (eastern Baffin Island); *Journal of Geophysical Research: Earth Surface*, v. 124, p. 1–13.
- Paull, C.K., Ussler, W., III, Caress, D.W., Lundsten, E., Covault, J.A., Maier, K.L., Xu, J. and Augenstein, S. 2010: Origins of large crescent-shaped bedforms within the axial channel of Monterey Canyon, offshore California; *Geosphere*, v. 6, p. 755–774, URL <<https://doi.org/10.1130/ges00527.1>>.
- Smith, D.P., Ruiz, G., Kvitek, R. and Iampietro, P.J. 2005: Semianual patterns of erosion and deposition in upper Monterey Canyon from serial multibeam bathymetry; *Geological Society of America Bulletin*, v. 117, no. 9–10, p. 1123–1133, URL <<https://doi.org/10.1130/b25510.1>>.
- Stacey, C.D., Hill, P.R., Talling, P.J., Enkin, R.J., Hughes Clarke, J. and Lintern, D.G. 2019: How turbidity current frequency and character varies down a fjord-delta system: combining direct monitoring, deposits and seismic data; *Sedimentology*, v. 66, p. 1–31.



Compiling data from the analysis of surficial materials in Nunavut into a database at the Canada-Nunavut Geoscience Office

T. Tremblay¹ and S. Basso²

¹Canada-Nunavut Geoscience Office, Iqaluit, Nunavut, tommy.tremblay@canada.ca

²Canada-Nunavut Geoscience Office, Iqaluit, Nunavut

Tremblay, T. and Basso, S. 2021: Compiling data from the analysis of surficial materials in Nunavut into a database at the Canada-Nunavut Geoscience Office; in *Summary of Activities 2020*, Canada-Nunavut Geoscience Office, p. 93–100.

Abstract

The Canada-Nunavut Geoscience Office (CNGO) is currently developing a database for data from the analysis of surficial materials in Nunavut. The data preprocessing structure presented in this paper outlines the organization of the geochemical, mineralogical and sedimentological data, which will facilitate its scripted import into a SQLite relational database. This paper focuses on explaining the data preprocessing stage, and the terminology used in the construction of the database.

Introduction

Data from geochemical, mineralogical and sedimentological analyses of surficial materials in Nunavut are available within documents from a variety of sources including the Canada-Nunavut Geoscience Office (CNGO), the Geological Survey of Canada (GSC), academia and the mineral industry. Analyzing geological data from different sources is difficult because the user must make assumptions regarding how comparable the data are; therefore, the complete metadata needs to be catalogued to allow such comparisons between different data. From source to source, and within sources, data are organized in a variety of ways, which makes it difficult to process the data programmatically. Furthermore, in order to succeed in establishing a sound database, the structure and terminology of the data needs to be established; such establishment includes the relationships between sample names, publications, surveys and other published data from the same samples. In particular, naming of the samples is critical, as different names can be used for the same sample in different publications. All this data needs to be correlated. Also, the question of quality assurance–quality control (QA/QC) duplicates and standards must be accurately sorted out, in particular, as to whether the sample is a field or laboratory duplicate. Overall, the metadata attributed to the sample has to be captured as completely and accurately as possible during the preprocessing and processing stages, to allow for complete, successful and precise analyses of the data. The approach should have a solid universal basis, to facilitate its use in the future for data from any type of analysis of any type of geological material.

There is a list, but not a compilation, of numerous surveys and publications (with downloadable datasheets) for Nunavut in the Canadian Database of Geochemical Surveys (Natural Resources Canada, 2020a; see also Adcock et al., 2013; Spirito et al., 2013); this list can be downloaded from GEOSCAN (Natural Resources Canada, 2020b) and the CNGO's website (<https://cngo.ca/>). However, the Canadian Database of Geochemical Surveys takes a complex approach to capturing data that does not fit well with the CNGO's approach, which requires a more flexible data structure to accommodate a wider variety of data and allow for greater ease in writing scripts. This paper presents the methodology for collecting (herein called preprocessing), aggregating (processing) and analyzing (postprocessing) datasets, including all data and metadata. This paper will focus primarily on the preprocessing stage, which is the most advanced stage to date.

Data terminology and structure

Presented in Figure 1 is the data structure showing the various entities and relationships used to capture almost any type of surficial material analytical data. This structure is the basis for the directory of Microsoft[®] Excel[®] files and the SQLite database produced in the preprocessing and processing stages, respectively.

Dataset

The resulting intermediate structure for the surficial material analytical data from a particular document is referred to as a dataset. The name of a dataset is based on the document to which it is related and should be globally unique. For

This publication is also available, free of charge, as colour digital files in Adobe Acrobat[®] PDF format from the Canada-Nunavut Geoscience Office website: <https://cngo.ca/summary-of-activities/2020/>.

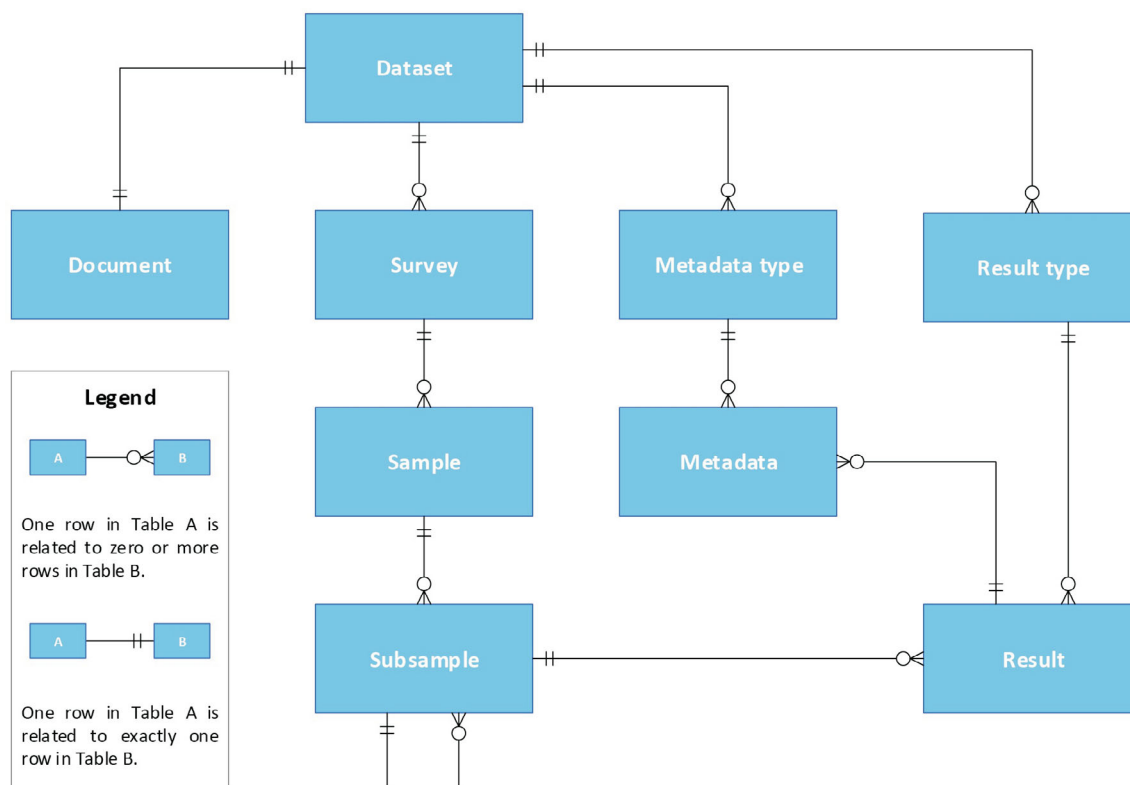


Figure 1: Diagram of data structure for the directory of Microsoft® Excel® files and the SQLite database of analytical data from the surficial materials of Nunavut.

this, reverse domain name notation (Wikipedia, 2020) is used, and this will permit datasets to be uniquely named based on their organization of origin. For example, the dataset name ‘ca.gc.nrcan.gsc.OF1575’ refers to Open File 1575 from the Geological Survey of Canada of Natural Resources Canada of the Government of Canada.

Document

Documents of interest are those that contain geochemical, mineralogical or sedimentological data; these documents can be published (CNGO datasets, GSC open files, scientific journals, etc.) or unpublished (laboratory analysis data sheets, etc.). A document has a one-to-one relationship with a dataset, meaning a dataset must be related to only one document and vice versa.

Survey

Surveys refer to the specific geological effort within a specific region and at a specific time when samples were collected. A survey is identified by its dataset and title. Multiple datasets may reference the same survey, so care should be taken to ensure that these datasets have the same survey name included. In some cases, a survey might also relate to a specific GSC survey number, which is contained within the Canadian Database of Geochemical Surveys. There can be more than one survey related to a single dataset.

Sample

A sample is geological material collected in the field, and is related to a single survey. A sample is identified by its survey, station name, earth material name (e.g., if there is bed-rock present at station 09TIAT001, the sample could have an associated earth material name of 09TIAT001A and if till is also present, it could also have an earth material name of 09TIAT001B) and sample name. A sample also has associated location information (e.g., latitude and longitude) and earth material type.

Subsample

A subsample is named as stated in an analytical report, or as reported in a document. As shown in Figure 1, a subsample has a self-referential relationship allowing for deeper sub-sampling (e.g., sub-subsample of a subsample), if needed. For example, a sample was collected in the field, subsampled for heavy mineral analysis, and within this subsample, a mineral grain was collected and analyzed for trace geochemistry (sub-subsample).

Metadata type and metadata

Together, the metadata type and metadata entities characterize a specific result. For example, a result could have a metadata type of ‘method of analysis’ with a value of ‘ICP-MS’. The structure allows for results to be associated with values for many different metadata types. The metadata

type entity is simply a lookup table that maps IDs (unique integers) to metadata types serving to normalize the data structure, whereas the metadata entity enables the many-to-many relationship between metadata type and result.

Result type

The result type is the quantity or quality analyzed or observed for a specific subsample (e.g., copper concentration). The result type entity is a lookup table similar to the metadata type entity, but in this case, mapping IDs to result types.

Result

The result is the value for the given result type, subsample or metadata (e.g., 56). There is a one-to-many relationship between the result type entity and the result entity whereas a result can have only one result type.

Methodology

The methodology for data compilation is divided into three stages: preprocessing (preparation of the raw data), processing (creation of a single-file relational database from the preprocessed data) and postprocessing (querying the data). This paper focuses on the preprocessing stage as opposed to the two subsequent stages, which are not as advanced. The overall process will be refined and detailed in future papers.

Preprocessing

Geochemical and other types of geological data typically arrive in multiple formats, with unrelated metadata hidden in reports and tables; these factors necessitate conversion to a common structured format. The preprocessing methodology is aimed at capturing all the necessary information, in a normalized manner, and with an ease of manipulation sufficient to allow a large range of users. The format adopted at the CNGO uses a series of directories and Microsoft Excel files, a convenient format in widespread use. The methodology presented in the following outline is based on the data structure presented earlier in this paper:

- 1) Creating an appropriately named directory that represents a dataset. As mentioned in the 'Data terminology and structure' section, a dataset is named based on its associated document using reverse domain name notation.
- 2) Creating a subdirectory named 'ORIGINAL' that contains the original document and any associated data files.
- 3) Populating the dataset directory with the following required files:
 - a) **DOCUMENT.xlsx**
This is a mandatory file containing one worksheet with one data row (see Table 1).
 - b) **SURVEYS.xlsx**
This is a mandatory file containing one worksheet

with zero or more data rows (see Table 2). Zero data rows in this file would mean zero data rows in **SAMPLES.xlsx** and zero data rows in the analysis files.

c) **SAMPLES.xlsx**

This is a mandatory file containing one worksheet with zero or more data rows (see Table 3). Zero data rows in this file would mean zero data rows in the analysis files. Data rows in this file are related to data rows in **SURVEYS.xlsx** through the use of the survey title as a foreign key. Original geographic co-ordinates must be batch-converted to latitude and longitude with NAD83 as the ellipsoid reference.

- 4) Populating the dataset directory with zero or more analysis files (e.g., **BULK.xlsx**, **HMC.xlsx** or **GRAINS.xlsx**). These are optional files containing one or more worksheets. These files contain the actual surficial material analytical data. The name of the file refers to the specific subfraction (object) linked to the metadata and results within the table. For example, **BULK** refers to analysis of the whole material, **HMC** to the heavy mineral content fraction and **GRAINS** to individual grains; other subfraction file names could also exist (e.g., if interstitial water is analyzed, this file could be named **INTERSTITIAL_WATER.xlsx**). Within each file, the composition of the worksheets must adhere to the standard format presented in Table 4.
- 5) Performing quality control using a Python library in development at the CNGO, which provides a programmed interface to the dataset directory; this interface verifies that all of the aforementioned criteria are met, prior to initiating the next stage (processing).

Processing

Processing involves taking all of the Microsoft Excel files from a single dataset, produced in the previous step, and combining them into an SQLite database, with a single file for each dataset. SQLite has been chosen because of its openness, portability and applicability of popular data analysis programming languages (e.g., Python and R) and GIS software (e.g., ArcGIS and QGIS), and the inherent power of SQLite as a relational database. The advantages are discussed in greater detail in SQLite developers (2020). The adoption of SQLite will allow for better quality control measures due to the inherent benefits of a relational data-

Table 1: An example of a worksheet in **DOCUMENT.xlsx**.

RECOMMENDED_CITATION
Tremblay, T., Sasseville, C. and Godbout, P.M. 2020: Data table accompanying "Geochemistry and mineralogy of glacial sediments, north of Fury and Hecla Strait, northwestern Baffin Island, Nunavut"; Canada-Nunavut Geoscience Office, Geoscience Data Series GDS2020-001, Microsoft® Excel® file.

Table 2: An example of a worksheet in SURVEYS.xlsx.

TITLE	ORGANIZATION	YEAR_BEGIN	YEAR_END	PARTY_LEADER	DESCRIPTION	GSC_CATALOG_NUMBER
2018, Till sampling in Fury and Hecla area. Canada-Nunavut Geoscience Office.	Canada-Nunavut Geoscience Office	2018	2018	Tommy Tremblay		210292
2018, Till sampling in Isortoq Lake area. Canada-Nunavut Geoscience Office.	Canada-Nunavut Geoscience Office	2018	2018	Tommy Tremblay		210293

Table 3: An example of a worksheet of SAMPLES.xlsx.

SURVEY_TITLE	STATION	EARTHMAT	SAMPLE	LAT_NAD27	LONG_NAD27	LAT_NAD83	LONG_NAD83	X_NAD27	Y_NAD27	X_NAD83	Y_NAD83	ZONE	EARTHMAT_TYPE
2018, Till sampling in Fury and Hecla area. Canada- Nunavut Geoscience Office.	18TIAT115	18TIAT115A	18TIAT115A1			70.334809	-86.178963						diamicton
2018, Till sampling in Isortoq Lake area. Canada-Nunavut Geoscience Office.	18TIAT168	18TIAT168A	18TIAT168A1			70.194582	-76.452538						diamicton

Table 4: An example of a worksheet in HMC.xlsx.

SAMPLE	SUBSAMPLE	METADATA_TYPE	chalcopryite	pyrite	corundum
		FRACTION_MIN_MM	0.25	0.25	0.25
		FRACTION_MAX_MM	0.5	0.5	0.5
		THRESHOLD			
		UNIT	grains	grains	grains
		METHOD	heavy mineral analysis	heavy mineral analysis	heavy mineral analysis
		LAB_PREPARATION	ODM	ODM	ODM
		YEAR	2018	2018	2018
		PRECONCENTRATION_METHOD	shaking table	shaking table	shaking table
		METHOD_GOLD_GRAINS	shaking table	shaking table	shaking table
		LIQUID_DENSITY	3.3g/cm3	3.3g/cm3	3.3g/cm3
		FERROMAGNETIC_SEPARATION	hand magnet	hand magnet	hand magnet
		PARAMAGNETIC_SEPARATION	yes	yes	yes
		MINERAL_IDENTIFICATION_METHODS	visual picking, SEM	visual picking, SEM	visual picking, SEM
		LAB_PICKING	Overburden Drilling Management	Overburden Drilling Management	Overburden Drilling Management
		NORMALIZATION_METHOD	No	No	No
18T1AT115A1	18T1AT115		0	1	1
18T1AT168A1	18T1AT168		0	0	1

SAMPLE/SUBSAMPLE NAMES
METADATA_TYPE
METADATA
RESULT_TYPE
RESULT

base, which include data integrity (enforcing relational and value constraints), normalization (reduced data redundancy compared to a pile of Excel files), accessibility (querying with SQL) and flexibility (easily restructured to accommodate new requirements). The structure of the database is based on the data structure summarized in Figure 1. Unlike the format in the preprocessing stage, the format in the processing stage will more closely map to the data structure. In the simplest case, one entity in Figure 1 represents one table in the database. In addition to the Python library used to interface with the dataset directory presented in the ‘Preprocessing section’, another library is in development to interface with the SQLite database. Once completed, these libraries will be used in the development of a script to perform the processing stage.

Postprocessing

The postprocessing stage deals with how to query and report the data, in order to analyze or publish the data. With a SQLite database, this step can be performed using various programming languages and GIS software.

At this point, there are individual SQLite databases, each containing one dataset. A single dataset database can be opened in a user’s software or programming language of choice and queried using SQL. With a bit of additional effort, all of the individual SQLite databases can be combined into a single SQLite database, allowing queries across multiple datasets.

With a combined SQLite database, one could execute a query such as:

```
SELECT s.*, ss.*, r.*
FROM samples s,
     subsamples ss,
     metadata_type mt,
     result_type rt,
     metadata m,
     results r
WHERE s.earthmat_type = "diamicton"
AND ss.sample_id = s.id
AND rt.value = "corundum"
AND m.metadata_type_id = mt.id
AND mt.value = "FRACTION_MIN_MM"
AND m.result_id = r.id
AND m.value = "0.25"
AND r.subsample_id = ss.id
AND r.result_type_id = rt.id
AND r.object_type = "HMC";
```

This query would select all results across all datasets for samples with an earth material type of diamicton, with a result type of corundum, a metadata value of 0.25 for the minimum grain size of the subsample (FRACTION_MIN_MM) and an object type of heavy mineral content (HMC). Once selected, the results can be reported in table format, or as cartographic representations. This

data can be published as downloadable files, or as a published or online queryable database file. Postprocessing quality control steps are important, and would include standardizing (e.g., removal of less than symbols affecting numerical values) or normalizing (e.g., dealing with background corrections or missing values) the data.

Using the libraries mentioned in the ‘Preprocessing’ and ‘Processing’ sections, a script will be developed that combines the individual SQLite databases (each containing one dataset) into a single SQLite database (one containing all of the datasets) and performs additional quality control checks.

Summary

The Canada-Nunavut Geoscience Office is in the process of developing a database of analytical data for surficial materials in Nunavut. This paper details the preprocessing of geochemical, mineralogical and sedimentological data that will facilitate its scripted import into a relational database (processing stage) and subsequent querying and reporting (postprocessing stage). The latter two stages are currently in the initial stages of development using Python and SQLite. This is an important step in data management for Nunavut, and has numerous important implications for future data collection and program development.

Economic considerations

The Canada-Nunavut Geoscience Office’s surficial material analytical data structure is a powerful tool for compiling mineral exploration and environment baseline geological data. The quality of data compilation is key to the value of the data for the intended users, which range from geological researchers to applied geological companies. Once compiled, the surficial materials analytical data can help users to a) find significant geochemical or mineralogical anomalies of specific elements or commodities within a large portion of Nunavut, b) understand the significance of geochemical anomalies found by surficial sediment sampling surveys not included in the database, and c) interpret sedimentary transport processes (e.g., glacial, colluvial, alluvial) as an aid to mineral exploration in surficial sediments.

Acknowledgments

This paper benefited from discussions with A. Plouffe, D. Kerr, I. McMartin, D. Mate, W. Spirito and S. Adcock. Those who assisted with data compilation included R. Baines, T. Rowe, C. Mayer, I. Randour and C. Gilbert. The authors thank S. Adcock for reviewing the manuscript.

Natural Resources Canada, Lands and Minerals Sector contribution 20200676

References

- Adcock, S.W., Spirito, W.A. and Garrett, R.G. 2013: Geochemical data management – issues and solutions; *Geochemistry: Exploration, Environment, Analysis*, v. 13, p. 337–348.
- Natural Resources Canada 2020a: Canadian Database of Geochemical Surveys; Natural Resources Canada, URL <https://geochem.nrcan.gc.ca/cdogs/content/main/home_en.htm> [November 2020].
- Natural Resources Canada 2020b: GEOSCAN database; Natural Resources Canada, URL <<https://geoscan.nrcan.gc.ca>> [November 2020].
- Spirito, W.A., Adcock, S.W. and Paulen, R. 2013: Managing geochemical data: challenges and best practices; *in* *New Frontiers for Exploration in Glaciated Terrain*, R.C. Paulen and M.B. McClenaghan (ed.), Geological Survey of Canada, Open File 7374, p. 21–26.
- SQLite developers 2020: SQLite; Hipp, Wyrick & Company, Inc., URL <<https://www.sqlite.org/appfileformat.html>> [November 2020].
- Wikipedia 2020: Reverse domain name notation; Wikipedia, URL <https://en.wikipedia.org/wiki/Reverse_domain_name_notation> [November 2020].



The **Canada-Nunavut Geoscience Office** conducts new geoscience mapping and research, supports geoscience-capacity building, disseminates geoscience information and develops collaborative geoscience partnerships for Nunavut.



www.cngo.ca